

H124/3489

MONASH UNIVERSITY
THESIS ACCEPTED IN SATISFACTION OF THE
REQUIREMENTS FOR THE DEGREE OF
DOCTOR OF PHILOSOPHY

ON.....29 July 2003


.....
Sec. Research Graduate School Committee

Under the Copyright Act 1968, this thesis must be used only under the normal conditions of scholarly fair dealing for the purposes of research, criticism or review. In particular no results or conclusions should be extracted from it, nor should it be copied or closely paraphrased in whole or in part without the written consent of the author. Proper written acknowledgement should be made for any assistance obtained from this thesis.

46

VAL

CADES
e of
for

may

or in

wing

ds to
s the

.02

rding
to the

/02

SIMULATION OF 3-DIMENSIONAL AEROELASTIC EFFECTS IN TURBOMACHINERY CASCADES

This thesis is submitted in fulfillment of the
requirements for the degree of Doctor Philosophy.

Department of Mechanical Engineering

Monash University

Clayton, Australia

October 2002

by

Ivan McBean

Declaration of Originality

I, Ivan William McBean declare that this thesis is my own work and has not been submitted in any form for another degree or diploma at any university or other institute of tertiary education. Information derived from the published and unpublished work of others has been acknowledged in the text and a list of references is provided.

Ivan McBean

Ivan William McBean 28th October 2002.

This manuscript was type-set using lyx and L^AT_EX on a linux workstation. All 2-dimensional graphs were generated by Grace, figures were by Xfig and 3-dimensional graphs by Tecplot (R).

Copyright ©Ivan McBean 2002

Abstract

Blade aeroelasticity is an important problem in turbomachinery. In this study the interaction between the gas dynamics and the turbine blades is considered. A computational tool is developed and the phenomenon is investigated through simulations of vibrating turbomachinery cascades. In particular, the nature of 3-dimensional, viscous effects on aeroelastic behaviour is examined.

The implementation of the fluid model involves a dual time method coupled with a finite volume discretisation of the Favre averaged Navier-Stokes equations and the $k-\omega$ turbulence model. A moving mesh capability is implemented to accommodate the moving structure and a basic structural model is also incorporated. A parallel and multiple block approach allows for time efficient simulations. The new implementation is validated through the simulation of a number of fundamental cases, with comparison with both experiment and theory. A simple, coupled airfoil model is simulated for both Euler and Navier-Stokes flow models.

The turbomachinery cascade simulations involve two different configurations, both of which are modelled on experimental apparatus. The first case is a linear cascade at low subsonic outlet Mach number, in almost incompressible flow. The nature of tip gap flow is discussed, as well as the effect of variation in tip gap size on the aeroelastic characteristics of the cascade. Comparisons are also made between the simulation results and experiment. The variation of tip gap results in significant local variations in blade unsteady surface pressure. An analysis of aeroelastic stability is included using the energy method.

The second turbomachinery case considered is the Standard Configuration 4 annular cascade involving both high subsonic and transonic flow conditions. Once again the energy method is used in the analysis of aeroelastic stability, at a number of different inter-blade phase angles. Euler and Navier-Stokes simulations are compared, as were 2-dimensional and 3-dimensional geometries. Simulations with and without the tip gap model exhibit differences in unsteady loading. Whilst 2-dimensional inviscid flow simulations are adequate in simulating the aeroelastic configuration for the high subsonic flow case, significant differences exist between the Navier-Stokes and Euler simulations, and 2-dimensional and 3-dimensional geometries for the case with transonic flow conditions.

Contents

| | |
|---|------------|
| Abstract | i |
| Acknowledgements | v |
| List of Figures | vii |
| Nomenclature | xii |
| 1 Introduction | 1 |
| 2 Aspects of Aeroelasticity in Axial Turbines | 6 |
| 2.1 The Physics of the Aeroelastic Response in Axial Turbines | 6 |
| 2.1.1 Aeroelasticity | 6 |
| 2.1.2 Turbomachinery Cascade Geometry | 7 |
| 2.1.3 Fluid Dynamics | 8 |
| 2.1.4 Structural Vibration Dynamics | 10 |
| 2.1.5 Forced Response | 11 |
| 2.1.6 Flutter | 12 |
| 2.1.7 Acoustic Resonance | 13 |
| 2.1.8 Structural Mistuning | 14 |
| 2.1.9 Damping Effects | 14 |
| 2.2 Experiments in Aeroelasticity | 15 |
| 2.2.1 Two-dimensional Measurements | 16 |
| 2.2.2 Three-dimensional Measurements | 17 |
| 2.3 Theoretical Modelling | 18 |
| 2.3.1 Methods of Analysis | 18 |
| 2.3.2 The Energy Method | 21 |
| 2.3.3 Simplification of the Model Geometry | 22 |
| 2.3.4 Simplification of Fluid Model | 24 |
| 2.3.5 Simplification of Structural Model | 29 |

| | | |
|----------|---|-----------|
| 3 | Mathematical Model | 31 |
| 3.1 | Fluid Model | 31 |
| 3.1.1 | Navier-Stokes Equations | 31 |
| 3.1.2 | Favre averaged Navier Stokes Equations | 33 |
| 3.1.3 | Closure Approximations | 36 |
| 3.1.4 | The $k-\omega$ Turbulence Model | 39 |
| 3.2 | Structural Model | 42 |
| 3.2.1 | The Equations Governing the Structural Model | 42 |
| 3.2.2 | Modal Equations of Motion | 43 |
| 4 | Computational Implementation | 45 |
| 4.1 | Fluid Model Discretisation | 45 |
| 4.1.1 | Spatial Discretisation of Navier-Stokes Equations | 46 |
| 4.1.2 | Spatial Discretisation of $k-\omega$ Equations | 49 |
| 4.1.3 | Time Discretisation | 50 |
| 4.1.4 | Time Stepping Scheme for Navier-Stokes Equations | 52 |
| 4.1.5 | Time Stepping Scheme for $k-\omega$ Equations | 54 |
| 4.1.6 | Multigrid | 56 |
| 4.1.7 | Artificial Dissipation | 57 |
| 4.1.8 | Residual Averaging | 61 |
| 4.1.9 | Boundary Conditions for Navier-Stokes Equations | 62 |
| 4.1.10 | Boundary Conditions for $k-\omega$ Equations | 66 |
| 4.2 | Structural Model Discretisation | 67 |
| 4.3 | Parallel Computation Strategy | 68 |
| 4.3.1 | Architecture of High Performance Computers | 68 |
| 4.3.2 | Parallel Performance | 70 |
| 4.3.3 | Parallelisation of CFD Codes | 72 |
| 4.3.4 | Implementation of Parallel Solver | 75 |
| 4.3.5 | Data Structure | 76 |
| 4.3.6 | Boundary Conditions | 77 |
| 4.4 | Moving Grid | 78 |
| 4.4.1 | Transfinite Interpolation | 78 |
| 4.4.2 | Multi-block Moving Grid | 81 |
| 4.5 | Coupling and Model Integration | 83 |
| 5 | Validation of Computational Model | 85 |
| 5.1 | Laminar Flat Plate | 85 |
| 5.2 | Turbulent Flat Plate | 86 |
| 5.3 | Isolated cylinder | 88 |

| | | |
|----------|---|------------|
| 5.4 | Isolated Airfoil | 92 |
| 5.4.1 | Steady and Inviscid Simulations | 92 |
| 5.4.2 | Navier-Stokes Simulations | 97 |
| 5.5 | Naca64 in Coupled Simulation | 97 |
| 5.6 | Grid Independence | 103 |
| 5.7 | Parallel Performance | 103 |
| 6 | Turbine Cascade Simulations | 108 |
| 6.1 | Modelling Considerations and Flow Physics | 108 |
| 6.1.1 | Computational Grid | 108 |
| 6.1.2 | Vortex Structures | 111 |
| 6.1.3 | Transonic Flow | 115 |
| 6.1.4 | Aeroelastic Configuration | 117 |
| 6.2 | He Cascade | 117 |
| 6.2.1 | Steady Simulations | 119 |
| 6.2.2 | Aeroelastic Simulations | 132 |
| 6.3 | Standard Configuration 4 | 143 |
| 6.3.1 | Simulation Model | 145 |
| 6.3.2 | High-subsonic Cases | 148 |
| 6.3.3 | Transonic Cascade | 164 |
| 7 | Conclusions and Future Work | 177 |
| | References | 180 |

Acknowledgements

This thesis is a product of collaborative research with Professor Feng Liu at the University of California in Irvine, USA. I spent over 6 months in California in 1999, 8 months in California in 2000 and a week in 2002. I thank Professor Liu for all of his technical assistance, his ideas, for his boundless hospitality and generosity. It will be a great inspiration to me for years to come. Our relationship transcended the normal supervisor - student relationship and he has become a great friend. Providing supervision by telephone and email is challenging at the best of times and I greatly appreciate his selfless commitment to this project.

My supervisors in Australia were Professor Kerry Hourigan and Associate Professor Mark Thompson. Thanks Kerry for helping me with funding for the last 10 months of my research, for your big picture view, for your interest and support. Thanks to Mark for keeping me honest on the technical side of my presentation of method and your other assistance.

My family, particularly my mother, have been a constant and dependable source of financial and moral support, especially when things weren't going so well. Dad thanks for reading over my thesis. Moving in with my sister Elsie must have made it a tough year for her in 2002 -- a single household should only have to finish one of either a PhD thesis or a national monument, not both; so thanks for your perseverance and support (when is Federation Square going to open?).

The Australian Government made available an Australia Postgraduate Award and without the scholarship this work would not have been possible.

The majority of the software used to produce this work was provided free. I owe thanks to all the anonymous computer programmers out there who freely distribute their software and donate their time. Before I began to develop the code in 1999, I attended a super computing workshop in San Diego in California at the National Partnership for Advanced Computational Infrastructure (NPACI). This was funded under the National Science Foundation (NSF) and was a great introduction to parallel computing. The bulk of the computational work for this thesis was performed on the Victorian Partnership for Advanced Computing (VPAC) parallel facility and on the Australian Partnership for Advanced Computing facility (APAC) in Canberra. Having used the Blue Horizon system in California and the APAC system in Australia, I believe we have a world class facility in Canberra. It is extremely well run, it is managed so that it is not over subscribed and the system very reliable -- a great

credit to the staff there. VPAC supplemented my scholarship this year which helped me to finish my work.

There have been a lot of people who have helped me along the way. Kenny Tan assisted me with innumerable computer problems and I thank him for all his time and effort on my behalf. At UCI in California, Carsten Mehring is a great friend and I had some good technical discussions with Mani Sadhegi. The UCI Masters swimming, Monash Water-polo Club and Malvern Marlins swimming all kept me fit and provided me with a great diversion. The coffee group here at Monash kept my sanity with their discourse on world politics and events, and lesser topics. Thanks to my mates in Melbourne for leading me astray when I needed to lighten up.

My studies at Monash have been challenging and rewarding and I leave with a great sense of satisfaction.

Ivan McBean.

30th November 2002

List of Figures

| | | |
|------|---|-----|
| 2.1 | Definition of aeroelasticity (Collar, 1947). | 7 |
| 2.2 | Schematic of a section of a typical annular turbomachinery cascade. | 9 |
| 4.1 | Discretisation in computational space. | 47 |
| 4.2 | Geometry of a typical computational cell. | 47 |
| 4.3 | Transfer of boundary cells. | 73 |
| 4.4 | Communication between blocks and grids in multiblock code. | 75 |
| 4.5 | Deformed mesh for NACA64A010. | 82 |
| 4.6 | Integration of fluid and structure models. | 84 |
| 5.1 | Skin friction coefficient for a flat plate for laminar flow regime. | 87 |
| 5.2 | Boundary layer profile for a flat plate in laminar regime and theory. | 87 |
| 5.3 | Skin friction coefficient for a flat plate with $k-\omega$ turbulence model simulation and theory. | 89 |
| 5.4 | Boundary layer profile for a flat plate with $k-\omega$ turbulence model simulation and theory. | 89 |
| 5.5 | Inner mesh for isolated cylinder of dimensions $384 \times 198 \times 2$ | 90 |
| 5.6 | Time evolution of unsteady lift and unsteady drag for circular cylinder. | 91 |
| 5.7 | Vorticity plot for isolated cylinder at $Re = 190$ | 91 |
| 5.8 | Inner region of mesh used for inviscid simulation of NACA64A010 airfoil. | 93 |
| 5.9 | Validation of moving mesh implementation with NACA64A010 airfoil. | 94 |
| 5.10 | Spatial resolution study for NACA64A010 airfoil. | 95 |
| 5.11 | Spatial resolution study for NACA64A010 airfoil. | 96 |
| 5.12 | Temporal resolution study for NACA64A010 airfoil. | 96 |
| 5.13 | Comparison of smoothing schemes for NACA64A010 airfoil. | 97 |
| 5.14 | Validation of unsteady $k-\omega$ implementation with NACA64A010 airfoil. | 98 |
| 5.15 | Isogai wing model | 98 |
| 5.16 | Coupled simulation for NACA64A010 airfoil – damped configuration $Ma_\infty = 0.825, V_f = 0.530$ | 100 |

| | | |
|------|---|-----|
| 5.17 | Coupled simulation for NACA64A010 Airfoil – stable configuration $Ma_\infty = 0.825$, $V_f = 0.630$ | 101 |
| 5.18 | Coupled simulation for NACA64A010 Airfoil – unstable configuration $Ma_\infty = 0.825$, $V_f = 0.725$ | 101 |
| 5.19 | Flutter boundary for Isogai wing mode with Euler flow model. | 102 |
| 5.20 | Comparison of flutter boundary for Isogai case for different flow models. | 102 |
| 5.21 | Communication time for different flow models. | 104 |
| 5.22 | Traditional speed-up for different flow models. | 107 |
| 5.23 | Other methods of calculating speed-up for different flow models. | 107 |
| 6.1 | Mesh in tipgap region of the He Cascade | 110 |
| 6.2 | O-H grid for Standard Test Case 4 profile for Euler simulations. | 111 |
| 6.3 | Sketch of viscous flow structures in a typical turbine cascade (Sierverding, 1985). | 112 |
| 6.4 | Sketch of viscous flow structures in a typical turbine cascade (Langston, 1980). | 113 |
| 6.5 | Sketch of interaction of passage and horseshoe vortex (Sierverding, 1985). | 114 |
| 6.6 | Sketch of passage flow at different outlet conditions. | 116 |
| 6.7 | Nomenclature for aeroelastic turbomachinery simulations. | 117 |
| 6.8 | Configuration of the cascade of Bell and He (1997). | 118 |
| 6.9 | He Cascade – 2-dimensional simulation test for grid dependency of grid cluster. | 120 |
| 6.10 | He Cascade – 2-dimensional simulation test for grid dependency of grid density. | 121 |
| 6.11 | He Cascade, significance of endwall flows on steady pressure coefficient distribution at mid-span without tip clearance model. | 121 |
| 6.12 | He Cascade, significance of endwall flows on steady pressure coefficient distribution across blade span, without tip clearance model. | 122 |
| 6.13 | He Cascade and stream-lines in horseshoe vortex flow in the hub region. | 123 |
| 6.14 | He Cascade grid dependence study for tip gap configuration – pressure coefficient at 90% span. | 124 |
| 6.15 | He Cascade span-wise pressure coefficient distribution for tip gap of 1.5% chord. | 126 |
| 6.16 | He Cascade comparison of surface pressure coefficient for different tip gaps at 90% span. | 126 |
| 6.17 | He Cascade stream-lines through tip gap region for two different tip gap lengths. | 128 |
| 6.18 | He Cascade velocity profile in tip region and vorticity at exit of tip section at 25% chord. | 129 |
| 6.19 | He cascade, entrainment of passage flow in tip vortex for tip gap of 1.5% chord. | 130 |

| | | |
|------|---|-----|
| 6.20 | He Cascade, classification of different types of tip vortex roll up, with streamlines through tip gap region for tip gap of 1.5 % chord. | 131 |
| 6.21 | He Cascade, type 1 and 2 roll-up with different casing boundary conditions for tip gap of 1.5 % chord. | 133 |
| 6.22 | He Cascade, comparison of steady pressure coefficient on blade. | 134 |
| 6.23 | He Cascade, comparison of magnitude of first harmonic of unsteady pressure coefficient with experiment for suction surface $k_c = 0.125$ | 136 |
| 6.24 | He Cascade, comparison of phase of first harmonic of unsteady pressure coefficient with experiment for suction surface $k_c = 0.125$ | 136 |
| 6.25 | He Cascade, comparison of magnitude of first harmonic of unsteady pressure coefficient with experiment for pressure surface $k_c = 0.125$ | 137 |
| 6.26 | He Cascade, comparison of magnitude of first harmonic of unsteady pressure coefficient with experiment for pressure surface $k_c = 0.125$ | 137 |
| 6.27 | He Cascade, comparison of magnitude of first harmonic of unsteady pressure coefficient at 90% span with experiment for suction surface $k_c = 0.125$ for different tip gaps. | 138 |
| 6.28 | He Cascade, comparison of phase of first harmonic of unsteady pressure coefficient at 90% span with experiment for suction surface $k_c = 0.125$ for different tip gaps. | 139 |
| 6.29 | He Cascade, comparison of magnitude of first harmonic of unsteady pressure coefficient at 90% span with experiment for pressure surface $k_c = 0.125$ for different tip gaps. | 139 |
| 6.30 | He Cascade, comparison of unsteady pressure coefficient magnitude on suction-side of blade, $k_c = 0.125$ for different tip models. | 141 |
| 6.31 | He Cascade, comparison of unsteady pressure coefficient phase on suction-side of blade, $k_c = 0.125$ for different tip models. | 142 |
| 6.32 | Standard Test Case 4 blade from experimental facility (Ott, 2002). | 144 |
| 6.33 | Standard Test Case 4 spring mass assembly in experimental facility (Ott, 2002). | 145 |
| 6.34 | Standard Test Configuration 4 annular cascade assembly (Ott, 2002). | 146 |
| 6.35 | Close up of Standard Test Configuration 4 annular cascade assembly (Ott, 2002). | 146 |
| 6.36 | Typical mesh for a four passage, 3-dimensional Euler simulation. | 149 |
| 6.37 | Steady surface pressure coefficient. | 150 |
| 6.38 | STCF 4 Test 627, Mach number distribution for simulation with Navier-Stokes model in passage at mid-span. | 151 |
| 6.39 | STCF 4, Test 552, $IBPA = 180^\circ$ first harmonic of unsteady pressure coefficient magnitude. | 152 |

| | |
|--|-----|
| 6.40 STCF 4, Test 552, $IBPA = 180^\circ$ first harmonic of unsteady pressure coefficient phase. | 152 |
| 6.41 STCF 4, $IBPA = 180^\circ$, first harmonic magnitude of unsteady pressure coefficient on suction-side at mid-span. | 154 |
| 6.42 STCF 4, $IBPA = 180^\circ$, first harmonic magnitude of unsteady pressure coefficient on pressure-side at mid-span. | 155 |
| 6.43 STCF 4, $IBPA = 180^\circ$, phase of first harmonic of unsteady pressure coefficient at mid-span. | 155 |
| 6.44 STCF 4, $IBPA = 180^\circ$, first harmonic magnitude of unsteady pressure coefficient on suction-side at 10% span. | 156 |
| 6.45 STCF 4, $IBPA = 180^\circ$, phase first harmonic of unsteady pressure coefficient on suction-side at 10% span. | 156 |
| 6.46 STCF 4, $IBPA = 180^\circ$, first harmonic magnitude of unsteady pressure coefficient on suction-side at 90% span. | 157 |
| 6.47 STCF 4, $IBPA = 180^\circ$, phase of first harmonic of unsteady pressure coefficient on suction-side at 90% span. | 157 |
| 6.48 STCF 4, $IBPA = 270^\circ$, first harmonic magnitude of unsteady pressure coefficient on suction-side at mid-span. | 158 |
| 6.49 STCF 4, $IBPA = 270^\circ$, first harmonic magnitude of unsteady pressure coefficient on pressure-side at mid-span. | 159 |
| 6.50 STCF 4, $IBPA = 270^\circ$, phase of first harmonic of unsteady pressure coefficient on suction-side at mid-span. | 159 |
| 6.51 STCF 4, $IBPA = 270^\circ$, phase of first harmonic of unsteady pressure coefficient on pressure-side at mid-span. | 160 |
| 6.52 STCF 4, $IBPA = 180^\circ$, first harmonic magnitude of unsteady pressure coefficient on suction for different models. | 162 |
| 6.53 STCF 4, $IBPA = 180^\circ$, phase of first harmonic of unsteady pressure coefficient on suction for different models. | 163 |
| 6.54 STCF 4, Test 627, damping coefficient for different configurations over a range of inter-blade-phase-angles. | 164 |
| 6.55 Comparison of transonic flow fields for two different mesh geometries. | 166 |
| 6.56 Grid dependency of 2-dimensional grid for Test 628. | 167 |
| 6.57 STCF 4, Test 628, separation region on trailing edge of blade for 2-dimensional simulation. | 167 |
| 6.58 STCF 4, Test 628, comparison of steady pressure coefficient for the 2-dimensional and 3-dimensional simulations. | 168 |
| 6.59 Comparison of pseudo-Schlieren plots. | 170 |

| | | |
|------|--|-----|
| 6.60 | STCF 4, Test 628, steady pressure coefficient and separation bubble on suction-side of the 3-dimensional simulation. | 171 |
| 6.61 | STCF 4, Test 628, the span-wise distribution of steady pressure coefficient on blade surface. | 171 |
| 6.62 | STCF 4, Test 628, $IBPA = 180^\circ$, first harmonic magnitude of unsteady pressure coefficient on suction-side at mid-span. | 172 |
| 6.63 | STCF 4, Test 628, $IBPA = 180^\circ$, first harmonic magnitude of unsteady pressure coefficient on pressure-side at mid-span. | 173 |
| 6.64 | STCF 4, Test 628, $IBPA = 180^\circ$, phase of first harmonic of unsteady pressure coefficient at mid-span. | 173 |
| 6.65 | STCF 4, Test 628, $IBPA = 180^\circ$, blade unsteady surface pressure magnitude distribution. | 174 |
| 6.66 | STCF 4, Test 628, $IBPA = 180^\circ$, blade unsteady surface pressure phase distribution. | 175 |
| 6.67 | STCF 4, Test 628, damping coefficient for different simulations compared with experiment. | 175 |

Nomenclature

English Symbols

| | |
|--|--|
| a | Distance from pitching axis to leading edge. |
| a_0, a_2, a_4 | Coefficients for CUSP artificial viscosity scheme. |
| A | Blending function for mesh interpolation. |
| $b = \frac{c}{2}$ | Semi-chord. |
| B | Blending function for mesh interpolation; constant in law of the wall. |
| c | Sound speed; chord or airfoil or turbine blade. |
| c_f | Friction coefficient. |
| c_h | Moment coefficient. |
| c_i | Modal damping. |
| c_w | Aerodynamic work coefficient. |
| C | Blending function for mesh interpolation. |
| C | Structural damping matrix. |
| C_D | Drag coefficient. |
| C'_D | Fluctuating drag coefficient. |
| C_L | Lift coefficient. |
| C'_L | Fluctuating lift coefficient. |
| C_m | Moment coefficient. |
| C_p | Specific heat at constant pressure. |
| $C_p = \left(\frac{p - p_{ref}}{p_0 - p_{ref}} \right)$ | Time average surface pressure coefficient. |
| $C_{p(n)} = \left(\frac{p^{(n)}}{h_c(p_0 - p_{ref})} \right)$ | n th harmonic of the unsteady pressure coefficient. |
| C_v | Specific heat at constant volume. |
| C_k, C_ω | Convective terms arising from the discretisation of the k and ω equations. |
| dS | Differential element of area. |
| dV | Differential element of volume. |

| | |
|-----------------------------------|---|
| D | Dissipative terms arising from discretisation of Navier-Stokes equations; blending function for mesh interpolation. |
| D_t | Backward time derivative operator. |
| $D^{(2)}$ | First order dissipative derivative vector. |
| $D^{(4)}$ | Third order dissipative derivative vector. |
| E | Total energy; source term in time discretisation. |
| E_n | Parallel efficiency. |
| e | Internal energy. |
| \hat{e} | Favre averaged energy. |
| f | Fraction parallel of total execution time. |
| f_1, f_2 | Blending functions for CUSP artificial viscosity. |
| \mathbf{f}_c | Vector of convective terms for the x Cartesian coordinate direction; convective terms for CUSP artificial viscosity. |
| \mathbf{f}_p | Pressure terms for CUSP artificial viscosity. |
| \mathbf{f}_μ | Vector of viscous terms for the x Cartesian coordinate direction. |
| F | Parameterisation variable for mesh. |
| \mathbf{F} | Force vector. |
| \mathbf{g}_c | Vector of convective terms for the y Cartesian coordinate direction. |
| \mathbf{g}_μ | Vector of viscous terms for the y Cartesian coordinate direction. |
| G | Parameterisation variable for mesh. |
| h | Enthalpy; plunging coordinate; displacement. |
| \dot{h} | Displacement velocity. |
| \ddot{h} | Displacement acceleration. |
| \hat{h} | Favre averaged enthalpy. |
| h_c | bending amplitude, non-dimensional with chord. |
| \mathbf{h}_c | Vector of convective terms for the z Cartesian coordinate direction; |
| \mathbf{h}_μ | Vector of viscous terms for the z Cartesian coordinate direction. |
| H | Total enthalpy; parameterisation variable for mesh. |
| I_α | Moment of inertia about pitching axis. |
| \mathbf{K} | Structural stiffness matrix. |
| k | Coefficient of thermal conductivity; kinetic energy of turbulent fluctuations; mesh stiffness. |
| \mathbf{k} | Vector of k - ω variables. |
| $k^{(2)}, k^{(4)}$ | User specified factors for artificial viscosity. |
| $k_c = \frac{\omega c}{2U_{ref}}$ | Reduced frequency, based on semi-chord. |
| k_h | Spring constant for plunging axis. |
| k_i | Modal stiffness. |

| | |
|-----------------------------------|--|
| k_α | Spring constant for pitching axis. |
| l | Turbulence length scale; characteristic eddy size. |
| L | Length scale; lift force. |
| m_i | Modal mass. |
| M | Local Mach number; moment. |
| \mathbf{M} | Structural mass matrix. |
| Ma | Mach number. |
| Ma_{is2} | Isentropic Mach number at outlet. |
| \mathbf{P} | Structural force matrix due to fluid. |
| n | Number of processors. |
| \mathbf{n} | Unit normal vector. |
| p | Static pressure, mesh stiffness coefficient. |
| p_{ref} | Reference static pressure at a position designated by experiment. |
| $P^{(n)}$ | n th harmonic of unsteady pressure. |
| p_0 | Total pressure; reference total pressure. |
| \bar{p} | Fluctuating static pressure. |
| P_d | Production terms in $k-\omega$ turbulence model equations. |
| Pr_L | Laminar Prandtl number. |
| Pr_T | Turbulent Prandtl number. |
| P_{2h} | Multigrid forcing term. |
| q_j | Heat flux, in tensor notation. |
| q_{Lj} | Laminar heat flux in tensor notation. |
| q_{Tj} | Turbulent heat flux in tensor notation. |
| q_i | Modal displacement. |
| Q | Convective terms arising from discretisation of Navier-Stokes equations. |
| Q_i | Modal force normalised with respect to mass. |
| $Q_{c,ijk}$ | Summation of convective fluxes for cell. |
| $Q_{\mu,ijk}$ | Summation of viscous fluxes for cell. |
| \dot{q}_i | Modal velocity. |
| \ddot{q}_i | Modal acceleration. |
| R | Perfect gas constant; residual; radius of curvature of stream-line. |
| R^* | Modified residual. |
| $Re = \frac{\rho U_{ref} c}{\mu}$ | Reynolds number. |
| R_k | Residual from k equation. |
| R_ω | Residual from ω equation. |
| S | Cell surface; surface element; entropy. |
| SF | Parameterised coordinate. |

| | |
|--|--|
| S_{ij} | Mean strain rate tensor. |
| S_k, S_ω | Source terms in the k and ω equations. |
| S_n | Parallel speed-up. |
| S_x, S_y, S_z | Cartesian projected areas. |
| S_α | Static imbalance. |
| S_ξ, S_η, S_ζ | Areas in the i, j and k coordinate directions. |
| t | Time. |
| t_1 | Execution time for one processor. |
| t_{ij} | Viscous stress tensor. |
| \bar{t}_{ij} | Favre averaged viscous stress tensor. |
| t_p | Parallel execution time. |
| t_s | Serial execution time. |
| t^* | Pseudo time. |
| T | Temperature; characteristic time scale. |
| u | Instantaneous Cartesian velocity. |
| \mathbf{u} | Vector of velocity variables. |
| \hat{u} | Favre averaged Cartesian velocity. |
| $u^* = \sqrt{\frac{\tau_{wall}}{\rho_{wall}}}$ | Friction velocity. |
| u_i | Velocity in tensor notation. |
| u'_i | Fluctuating velocity in tensor notation. |
| \hat{u}_i | Favre averaged velocity in tensor notation. |
| u''_i | Favre averaged velocity in tensor notation. |
| u_{grid} | Cartesian grid velocity. |
| U_i | Time mean velocity in tensor notation. |
| U_{ref} | Velocity at reference position. |
| v | Instantaneous Cartesian velocity. |
| \hat{v} | Favre averaged Cartesian velocity. |
| V | Cell volume; volume element. |
| V_f | Flutter velocity. |
| v_{grid} | Cartesian grid velocity. |
| w | Instantaneous Cartesian velocity. |
| \hat{w} | Favre averaged Cartesian velocity. |
| w_{grid} | Cartesian grid velocity. |
| \mathbf{w} | Vector of conservative variables. |
| x | Cartesian coordinate. |
| x_i | Position vector in tensor notation. |
| \mathbf{x} | Position vector. |
| y | Cartesian coordinate. |

$$y^+ = \frac{y u_*}{\nu}$$

 z z_i

Dimensionless distance, scaled with sub-layer.

Cartesian coordinate.

First order decomposition variables for structural model.

Greek Symbols

| | |
|--|--|
| α | Angle of attack; turbulence closure coefficient; inlet flow angle from x axis in θ plane. |
| α_k | Coefficients for convective residual in Runge-Kutta scheme. |
| β | Turbulence closure coefficient. |
| β^* | Turbulence closure coefficient. |
| β_k | Coefficients for dissipative residual in Runge-Kutta scheme. |
| χ_{CG} | Distance from centre of gravity to pitching axis. |
| δ | Direction of bending amplitude from machine axis. |
| δ_{ij} | Kronecker delta. |
| $\delta x, \delta y, \delta z$ | Block corner displacement. |
| Δ^+ | Negative contribution of source terms in $k-\omega$ model. |
| ΔE | Block edge displacement. |
| ΔS | Block surface displacement. |
| Δt | Time step. |
| Δt^* | Pseudo time step. |
| Δx | Mesh node displacement. |
| $\Delta \tau$ | Time step for structural model. |
| ε | Dissipation per unit mass; smoothing parameter for residual averaging; discretisation error. |
| $\varepsilon^{(2)}$ | Dissipation coefficient for first order dissipation. |
| $\varepsilon^{(4)}$ | Dissipation coefficient for third order dissipation. |
| ε_{ij} | Dissipation tensor. |
| $\varepsilon_x, \varepsilon_y, \varepsilon_z$ | Coefficients for residual averaging. |
| η | Blending function for mesh interpolation; similarity variable. |
| Φ | Structural modal matrix of complex amplitudes; rate of dissipation of mechanical energy. |
| $\Phi_{(n)}$ | Phase of n th harmonic of unsteady pressure coefficient. |
| Φ_i | Structural mode shape or eigenvector. |
| Φ_ε | Modification factor for spectral radius on highly stretched meshes. |
| γ | Ratio of specific heat; inlet flow angle from z axis; stagger angle. |
| $\kappa_{i,j,k}$ | Pressure sensor for time-step for Runge-Kutta scheme in the k coordinate direction. |
| λ | Ratio of pseudo time step to time step. |
| $\Lambda_\varepsilon, \Lambda_\eta, \Lambda_\zeta$ | Estimation of the spectral radius in the i, j and k coordinate directions. |
| κ | Kármán constant. |
| μ | Coefficient of dynamic molecular viscosity. |

| | |
|------------------------|---|
| $\mu_{i,j,k}$ | Pressure sensor for time-step for Runge-Kutta scheme in the j coordinate direction. |
| μ_m | Mass ratio. |
| μ_T | Dynamic eddy viscosity. |
| ν | Coefficient of kinematic molecular viscosity. |
| $\nu_{i,j,k}$ | Pressure sensor for time-step for Runge-Kutta scheme in the i coordinate direction. |
| ν_T | Kinematic eddy viscosity. |
| ρ | Density. |
| ρ' | Fluctuating density. |
| $\bar{\rho}$ | Temporal average density. |
| ρ_{wall} | Density at wall. |
| σ | Turbulence closure coefficient. |
| σ^* | Turbulence closure coefficient. |
| σ_{ij} | Stress tensor. |
| τ | Turbulence dissipation time; time in structural model. |
| τ_{ij} | Specific Reynolds stress tensor. |
| $\hat{\tau}_{ij}$ | Total stress tensor, including turbulence and laminar stresses. |
| τ_{wall} | Shear stress at wall. |
| ω | Specific dissipation rate; angular frequency; vorticity. |
| ω_h | Natural frequency of plunging axis. |
| ω_i | Modal frequency. |
| ω_s | Stream-wise vorticity. |
| ω_{wall} | Specific dissipation rate at wall. |
| ω_α | Natural frequency of pitching axis. |
| Ω | Rotor angular frequency. |
| ξ | Blending function for mesh interpolation. |
| Ξ | Blade aerodynamic damping coefficient. |
| ζ_i | Critical modal damping; blending function for mesh interpolation. |

Chapter 1

Introduction

Through the 20th Century turbomachinery developed to become one of the most important components in air transportation and power generation. The origins of the steam turbine can be traced back to the reaction turbine of the Egyptian philosopher Hero. A great deal of development occurred through the 1800's. One of the first axial flow steam turbines was devised by Parsons of Britain, for which he obtained a patent in 1884. By 1896 Westinghouse Machine Co. in the United States and later Brown Boveri and Co. in Switzerland began manufacturing Parson's turbines in large quantities (Neilson, 1912). Early steam turbines were used for electricity generation, but later they were also used in ship propulsion. By 1910 nearly all British warships were equipped with Parsons type turbines (Richardson, 1911).

By 1898 the French brothers Armangaud developed a working gas turbine engine. Frank Whittle of Britain obtained the first patent for an aero-engine in 1930, and over the seven years that followed developed this into a full scale engine. In the first half of the 20th Century, reciprocating engines were the dominant form of propulsion in aviation. Today however, the gas turbine has displaced the reciprocating engine and is the most widespread and most effective method of aircraft propulsion (Huenecke, 2000).

Turbomachines are classified as those devices in which energy is transferred either to, or from, a continuously flowing fluid by the dynamic action of one or more moving blade rows (Dixon, 1998). A rotating blade row changes the enthalpy of the fluid moving through it by either performing negative or positive work. Enthalpy changes are reflected in pressure changes occurring in the fluid. In the present context axial flow turbines are considered, where the flow at the inlet to the turbine is predominantly parallel to the axis of rotation.

A major difference between the axial flow turbines employed for jet propulsion and those used in power generation is the configuration of the compressor and turbine stages. There is a different objective – in power generation the maximum amount of energy possible is removed from the flow as possible before it is exhausted. In jet propulsion, the exhaust is used for propulsion and the aim is to impart as much kinetic energy to the flow as possible.

There are a number of other important differences. Aeroengines are required to run over

a range of flow rates and rotational speeds, whereas power generation machines run at a constant speed. Material weight is an important in aviation but it is not a consideration for a stationary machine. Power generation turbines also tend to have higher aspect ratio blades particularly at the exhaust of the low pressure stage.

The effect of aeroelasticity in turbomachinery has been recognised as far back as the 1940's when axial flow turbines were initially conceived for aircraft propulsion. Development through the 1950's and 1960's was driven by the need for high performance aircraft in both the military and the civil transport, and increasing demand for efficiency in the power generation industry. These requirements led to higher rotational speeds, thinner blade airfoils, higher pressure ratios per stage, and increased operating temperatures. The resulting dynamic problems influence the structural integrity of the principal components of the engine, particularly the blading (Fleeter, 1977). This area of dynamics is known as aeroelasticity - the study of the interaction of aerodynamics with elastic structures.

Initially, design and development of turbomachinery was based on experimental work and operating experience. This meant that often the turbines were introduced into service that were prone to unpredictable failures. Given the critical nature of the requirement for reliability especially in the case of aeroengines, this type of design process was far from acceptable. The successful operation of a power plant depends largely on the structural integrity of its rotating parts. In turn, the structural integrity depends on the ability of the machine to withstand steady and vibratory stresses. In the case of a jet engines, vibration-induced fatigue failure of rotor blades is a problem of major concern to the designer (Srinivasan, 1997). As a consequence manufacturers have embarked on costly testing programs, in an attempt to simulate operating conditions.

Whilst solutions have been found to many aeroelastic problems, new designs in these areas of industry may be subject to unwanted vibratory response unless their effects are accounted for in the design process. A tool is required to model this response if it is to be avoided. However it is first necessary to understand the mechanisms of the vibration before it may be modelled.

In particular, the understanding and modelling of aeroelastic responses of turbines in power generation is required for the control of vibration of individual blades. The vibration of turbine blades has a number of adverse effects on the turbine. These include a decrease in efficiency due to an increase in the width of blade wakes, dynamic stall and variation in loading due to vibration which can reduce the life of a blade due to cyclic fatigue. The decreased service life of blades requires an increase in the frequency of servicing, at great cost to the operator.

Due to inadequacies in classical and computational models, it is currently difficult to predict the vibratory response of the turbine during the design process and such responses are often found after a prototype has been manufactured. Thus any design tool that can

accurately predict such responses will reduce the requirement for redesign, and may also improve the design and efficiency of the final product.

Over the past couple of decades, airfoil design methods have involved the use of empirical and semi-empirical methods to identify and avoid the highest responding, vibratory modes of turbine blades. This is then followed by an extensive full scale engine test, where strain gauges are used to ascertain the response at operating speed. However the empirical methods have proven to be inadequate in avoiding all critical resonances, where the blades would be prone to failure through high cycle fatigue or flutter. Thus flutter and forced response is an expensive problem that cannot be completely overcome by conventional, empirical means (Hilbert *et al.*, 1997). Clearly, a computational method solving this problem of avoiding blade response could reduce design cost and design lead-time.

Whilst most computational, aeroelastic analysis has been unsuccessful in exactly reproducing experimental conditions, it has provided important insight into aeroelastic mechanisms that may not otherwise be available. For example, it has been established that for certain transonic fans that the major contribution to flutter is the oscillation in the passage shock wave, rather than the stall of blading as first thought (Isomura & Giles, 1998). Thus validated numerical codes can still be useful to the design process, even though physical conditions cannot exactly be reproduced.

Another problem is the determination of the rotor unsteady loading due to the interaction with upstream and downstream stators (in the case of transonic and subsonic turbines) and whether it is sufficient to cause excessive response in any one of these modes. If the response is excessive in any one of the modes, then either the excitation frequency or magnitude must be reduced or the airfoil responsiveness to the excitation reduced. It is not possible to remove all modes from the operating range with significant airfoil thickness increases that would adversely effect performance (Hilbert *et al.*, 1997). The computational tool allows the designer to predict the response in these modes without resorting to the use of full-scale production models.

In turbomachinery design, the aeroelastic response is represented graphically through a Campbell Diagram. The modal frequencies of the airfoil and forms of excitation are plotted versus the rotational speed. Where the lines cross indicates an operating point at which unacceptable vibratory stresses could occur. Thus the computational tool may be useful in determining both the loaded natural frequencies of the blade and the sources of excitation for a particular configuration so that the Campbell diagram may be formulated before physical testing is required. In the case of power generation turbines, the designer may ensure that there are no 'crossings' at or close to the design point.

It has been estimated that for studies on aeroplane wings, an experiment that involves the study of aeroelasticity in a wind tunnel experiment is an order of magnitude more expensive than a similar rigid body experiment involving only aerodynamics (Obayashi & Guruswamy,

1992). Thus even for the simple case of an isolated airfoil, the use of experimentation to investigate aeroelasticity is an expensive exercise. When it is considered that the geometry for a turbine rotor is a great deal more complex, the study of aeroelasticity may be prohibitive, even if it was possible to perform all the measurements necessary.

The present study aims to identify the importance of viscous effects on the aeroelastic stability of turbomachinery blades. It has been noted that in the literature the majority of studies, both computational and experimental, concentrate on a 2-dimensional plane. Thus the effects of hub and casing secondary flows and tip gap regions are usually ignored.

To simulate 3-dimensional effects on aeroelastic stability, a Navier-Stokes code has been developed. The original code was written by Liu (Liu, 1991) and makes extensive use of schemes by Jameson. This code implemented a steady state, Navier-Stokes solver that included the 1988 $k-\omega$ turbulence model by Wilcox (Wilcox, 1988). Convergence acceleration techniques involved residual averaging, multigrid and the use of local time steps. Both Jameson Schmidt Turkel (JST) (Jameson *et al.*, 1981) and Convective Upwind Split-Pressure (Liu *et al.*, 1998b) artificial viscosity schemes were implemented for stability in the transonic regime and to correct odd-even decoupling.

The high demand on computational resources posed by the complexity of the aeroelastic phenomenon prompted the development of a code that could more effectively simulate the problem. A survey of the most powerful computers available indicated that the most common architecture involved a parallel array of multiple processors, or a single very fast processor connected to a large memory. The different types of architecture are discussed in Chapter 4, however the most readily available systems involved an array of processors that were not necessarily connected to the same memory. One of the most common methods of performing simulations on these types of systems is through message passing software using the Message Passing Interface (MPI). A portable version was developed by a research group at the University of Argonne (Gropp *et al.*, 1996; Gropp & Lusk, 1996) to run on most systems. Consequently it was used in the parallel implementation.

Other issues involving the parallel implementation of the code included data structure, the coordination of the moving mesh and the interpolation of the movement of the structure to the movement of the fluid boundary. New routines were introduced for the moving mesh and the unsteady implementation, and routines were adapted from other codes for the structural solver.

The advent of computers and their subsequent development has allowed for the numerical modelling of complex physical systems. Whilst the sophistication of computers continues to develop, the goal of modelling exactly the complexity of the physics found in the interaction between turbine flows and turbine structures still proves to be an elusive one. Thus experimental analysis provides a key role in both validating numerical techniques, and providing results for analysis of characteristics that numerical methods are unable to reproduce.

The thesis is divided into seven chapters. Chapter 2 discusses the nature of aeroelasticity, the configuration of typical turbomachinery cascades and some important forms of aeroelasticity in axial flow turbomachinery. A number of experiments are used in comparisons in later chapters and the nature of experimental measurements is discussed. The various forms of analysis and theoretical approaches are presented in the context of the present investigation.

Chapter 3 presents the mathematical models underlying the simulations of the gas and structural dynamics. This includes the Favre averaged Navier-Stokes equations, the $k-\omega$ turbulence model and modal structural model.

Chapter 4 details the computational approach and the way in which the mathematical model is represented on the computer. The discretisation of both the fluid field and the structure is discussed at length. The method of parallel computation is a major issue in the development of the implementation. Integration of the structural model and moving mesh to accommodate structural displacement are other important issues.

Chapter 5 is a validation of the simulation model. The classical laminar and turbulent regime flat plate cases are used to test the laminar and turbulent multiple block implementations. An isolated cylinder, and an isolated airfoil are used to validate the time accuracy and moving mesh implementation respectively. The behaviour of a simple aeroelastic airfoil flutter model was investigated for both Euler and Navier-Stokes flow models.

Chapter 6 is a presentation of the turbomachinery cascade simulations. The issues regarding the modelling of the configurations are discussed. Typical flow features found in turbomachinery cascades under different flow regimes is presented. The first turbine cascade investigated involves flow in the low subsonic regime. The second is an annular cascade and involves flow in the high subsonic and transonic flow regimes.

Chapter 7 concludes the thesis.

This work seeks to understand and quantify differences between theoretical models and experiment.

Chapter 2

Aspects of Aeroelasticity in Axial Turbines

2.1 The Physics of the Aeroelastic Response in Axial Turbines

One of the most important aeroelastic responses in turbomachinery involves the interaction of the fluid or gas with the turbine blades. This is complex and involves a number of different mechanisms. In the following section, the general nature of aeroelasticity is described then a number of the key mechanisms are presented. Methods of modelling the phenomenon through experimental and analytical means are also examined.

The blades in compressors and turbines of turbomachines are subject to a number of different aeroelastic effects. Two major sources are forced response and flutter, however there are also others such as mistuning which affect the behaviour of the turbine to a lesser extent. Before examining these effects, it is first necessary to consider the typical flow conditions and the modes of vibration found in a rotor or stator.

2.1.1 Aeroelasticity

A general definition for aeroelasticity is provided by Collar (1947) as the study of the mutual interaction that takes place within the triangle of the inertial, elastic, and aerodynamic forces acting on structural members exposed to an airstream, and the influence of this on design. This is illustrated in Figure 2.1. Aeroelastic interactions may have an undesirable effect and are found in many areas of industry and transport. These include helicopter rotors, aeroplane wings, wind turbines, aeroplane propellers, and turbomachinery in both aerospace and power generation. Depending on the particular application, vibratory response decreases efficiency, produces unwanted noise, reduces component life and may affect the control of the transport

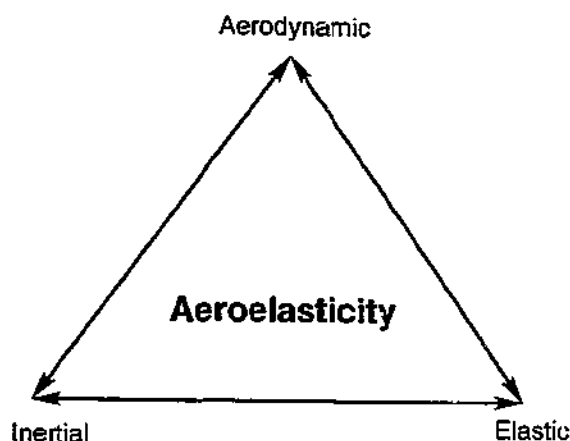


Figure 2.1: Definition of aeroelasticity (Collar, 1947).

vehicle.

One of the most common forms of aeroelasticity is the interaction that results in an oscillating displacement of the structure. If the oscillating displacement does not reach a limit cycle, the amplitude of displacement of the structure may increase until the structural member fails. In the situation where the amplitude is limited, high cycle fatigue may result and the structural member may fail after an extended period.

Aeroelasticity may be considered by subdividing the problem into the two main disciplines that it encompasses, fluid dynamics and structural dynamics. The fluid dynamics tend to be the more sensitive of the two domains. In some cases it is possible to decouple the problem and assume a simplified model for the response of the other domain.

2.1.2 Turbomachinery Cascade Geometry

In the design and modelling of turbomachinery, they are often simplified to annular cascades of turbine blades. This is the type of configuration that is investigated in this work. In particular sections of this work the flow will be described within the cascade. A section of the geometry of a typical turbomachinery cascade is shown in Figure 2.2 with labels for the different regions and axes. For example, the pitch-wise direction is in the circumferential plane between the blades. In this case two blades and 2 passages are shown. The turbine blade on the right of the figure has been removed for clarity.

Different regions have been coloured depending on type. The yellow and blue regions are the inlet and outlet planes respectively – these are orthogonal to the machine axis. The dark green region is the hub of the cascade and the casing of the cascade is not shown, but would be a section of a cylinder spanning the top of the inlet and outlet planes with its axis also at the machine axis. The blade tip is coloured red and rest of the blade is grey. The blade leading edge is the part of the blade closest to the inlet plane and the blade trailing edge is

closest to the outlet plane.

The flow through the turbine moves from inlet to outlet. An annular cascade involves as many blades as required to complete the annulus; there are usually no side-walls in the pitch-wise direction. Often two dimensional flow is investigated – this is done by considering the flow field at a cylindrical plane through the passage, bisecting the blade and its axis coinciding with the machine axis.

In turbine cascades, the blade suction side experiences the largest pressure drop at most chord-wise positions. The blade pressure side typically faces upstream towards the cascade inlet, whereas the blade suction side faces the blade outlet. The hub and casing are also known as endwalls. The axial direction is positive in the major flow direction, moving from cascade inlet to outlet.

2.1.3 Fluid Dynamics

The development of theoretical analyses to predict unsteady flows in axial-flow turbomachines has been motivated primarily by the need to predict the aeroelastic behaviours of the blading. Due to the complexity of the unsteady fluid dynamics, this component of the overall industrial design prediction system has generally been regarded as being the one requiring the most research attention (Verdon, 1993).

Typical gas turbines may be divided into a number of operating units, including a compressor, the combustor stage and a turbine. Steam turbines may also involve multiple cylinders, although the whole turbine is involved in the extraction of energy from the flow. Flow characteristics vary throughout the turbines and range from transonic to low velocity subsonic, depending on the stage involved. The fluid state may be characterised as compressible, turbulent and multiphase (in the case of steam turbines). This is one of the more challenging and difficult fluid regimes to model in both analytical and experimental fields, particularly when it is considered that shock waves, boundary layers, wakes, laminar and turbulent flow may all play important roles in determining flow behaviour.

For example, typical fan compressors operate in the transonic flow region. The flow is mixed in that the flow at the hub may be subsonic and flow at the fan tip is supersonic. In the region in between, the flow varies between the two. However the mixed nature of the flow has a considerable influence on the shock structure at the tips, and consequently on the aeroelastic stability of the rotor (Bendiksen, 1986). Toward the end of a low-pressure turbine stage the flow velocity may approach the speed at which incompressibility may be assumed. In this case, given the absence of shock waves, other flow characteristics dominate aeroelastic interactions such as the potential or pressure effects, vortex shedding and laminar/turbulent transition.

Blade vibration can significantly affect the aerodynamic performance of individual blades.

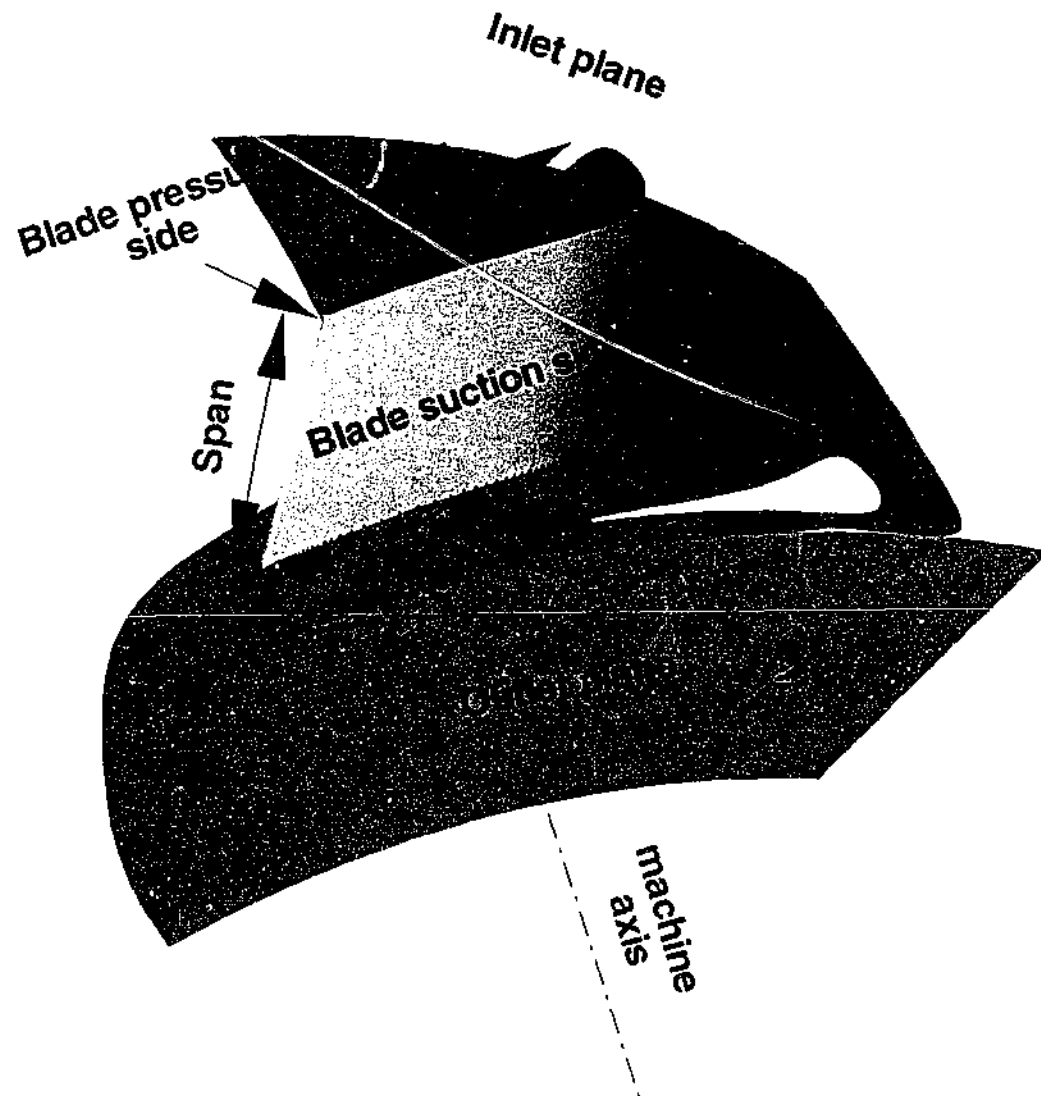


Figure 2.2: Schematic of a section of a typical annular turbomachinery cascade.

Excessive oscillations can cause the airfoil to stall, for example on the suction side of turbine blades where the pressure gradient may be close to the critical value at which separation may occur. This is known as dynamic stall and may be caused by any type of aeroelastic oscillation.

The effect of turbulence can be important in the majority of flow regimes and the modelling of viscous flow at any Reynolds number in practical turbomachinery cases requires a turbulence model. The problem of modelling turbulence is one of the biggest facing those in the scientific community simulating fluid dynamics at moderate Reynolds number. The typical Reynolds number found in a turbine passage is of the order of 10^5 or above, which is orders of magnitude above the Reynolds number threshold in turbulent channel flow. Unfortunately the modelling of turbulence increases the complexity of the mathematical model and computational implementation. Whilst turbulence models exist that provide reasonable predictions of bulk flow behaviour, however they still perform poorly in some cases where effects such as laminar/turbulent transition and shock/boundary layer interactions are important (Wilcox, 2000).

2.1.4 Structural Vibration Dynamics

The nature of the blade vibration can be important in understanding the sources of blade instability. Complex vibrational motion is often simplified by linearisation through the assumption that it may be represented by a number of vibrational modes. Each mode has a particular displacement associated with it, known as a mode shape. A frequency is also ascribed to each mode. By summing all the mode shapes the complete motion may be described. In general there is a single dominant mode of oscillation that is of primary importance to the aeroelastic stability. Often this mode is modelled and the other modes are ignored, resulting in single degree of freedom analysis. Usually modes shapes may be described as bending or torsional modes.

Blades in high performance turbines and compressors are generally complex in geometry. The camber of the blade may vary from hub to tip, the blade usually being twisted from root to tip, may be raked in the axial flow direction and vary in chord length. Thus to closely model these characteristics, 3-dimensional structural and fluid models are required. Despite the complicated geometry of individual blades, in the majority of cases each blade on the rotor may be regarded as being almost identical and this leads to modelling simplifications that are discussed in Section 2.3.3.

Other blade characteristics may have a significant impact on both blade structural integrity and flow pattern. Cooling holes in gas turbines are an added complication, changing the thermodynamics of the structure and hence the profile, the gas dynamics, and also complicating the stress distribution in the structure due to the stress concentrations around the

holes. Shrouded rotors or splitter blades may also change the inter-blade coupling of rotors (Bendiksen, 1986).

Mikolajczak (Mikolajczak *et al.*, 1975) provides a description of the vibration dynamics of rotors in turbomachines. The vibration of a symmetrical rotating system such as a turbine rotor is predominantly characterised by both torsional and bending motion. If the rotor is considered isolated from the rest of the machine and is observed from a viewpoint in the upstream axial direction, nodes of torsional vibration (where deflection from the steady state is zero) will appear as radial lines, also known as travelling nodal diameters. Nodes of bending vibration will appear as concentric circles around the bladed disc. On a rotating stage the radial lines or waves of constant deflection travel around the hub. Adjacent blades experience a relative time delay or phase difference as the wave passes; this is the inter-blade phase angle (IBPA).

2.1.5 Forced Response

The blades in turbomachinery are subject to oscillating forces from a number of different sources. A dynamic oscillation of a structure is described as forced if it occurs at or close to the frequency of the force, rather than at the natural frequency of the structure. The forces may be classified as either mechanically induced vibration due to external factors or internal flow-field induced forces.

There are a number of sources of flow-induced response in the turbine:

- the interaction of blade wakes and tip vortices with following blade rows.
- the effect of the potential field of upstream and downstream blade rows (pressure field). This includes pressure fluctuations of downstream shock bow waves on upstream vanes
- Oscillations in shock wave position - unsteady aerodynamic forces due to shock motion have a pronounced effect on the aeroelastic stability of cascades representative of typical transonic/supersonic rotors (Bendiksen, 1986).
- Distortions of flow at the turbine inlet

Many investigations have been performed into forced response in turbine applications. Shiratori (Shiratori *et al.*, 1998) investigated the behaviour of passage shock waves in both staggered and unstaggered 2 dimensional cascades. They observed self excited shock wave oscillation with a similar frequency to that observed in channel flow. The oscillation in position was observed to be over 40% of the chord length of the blade, which may cause a substantial torsional response.

Rotor stator interaction, or the interaction of blade rows with upstream flow is another important area in research into forced response. Sbardella and Peiro (Sbardella & Peiro,

1997) modelled inter-blade row interaction numerically using an inviscid flow solver. They found that the effect of an oblique shock wave extending from the trailing edge of a stator and impinging on the surface of the following rotor resulted in fluctuations in the local rotor lift as high as 53%. This could cause substantial vibratory effects in the rotor blades. It was also noted that the interaction between the shock wave and the leading edge of the rotor blade could cause temporary separation of the boundary layer in this region.

Tip leakage effects may also contribute to rotor instability in high power turbines (Martinez-Sanchez *et al.*, 1995). The Alford Effect is the name given to the oscillating force due to irregularities either in the casing or shroud that encases the rotor tips, or due to eccentricity in the centre-line of the rotor. Leakage effects may lead to non-uniformity in the casing pressure distribution, a consequence of irregularities in the casing seals. The magnitude of these forces not only depends on the variations with respect to the tip clearance in the circumferential direction, but also on the magnitude of the tip clearance.

The turbomachinery manufacturers invest heavily in research in an attempt to reduce the effects of forced response. There is a major difference between the design issues addressed in flutter and forced response. In flutter stability is required (the correct combination of excitation frequency and natural frequency). In forced response, the amplitude of vibration is important (so the fatigue life may be estimated). Given that there are other factors that are difficult to quantify, such as structural damping, non-linear damping at the blade roots and the forcing itself, forced response is often aimed at ranking potential designs rather than predicting exact vibration levels (Imregun, 1998).

2.1.6 Flutter

The term flutter is applied to the self-excited vibration of turbine blades as a result of the continuous interaction between the fluid and the structure. This is where the external flow around the blade sustains oscillatory motion of the airfoil. It is similar to forced vibration, however the frequency of oscillation is close to the natural frequency of the blade. It occurs because the unsteady aerodynamic forces and moments created by periodic blade vibrations do positive aerodynamic work on the blade during each vibration cycle and the mechanical damping is insufficient to dissipate this work input (Mikolajczak *et al.*, 1975). It may occur in a completely uniform flow-field and the motion is sustained by the extraction of energy from the uniform flow during each vibratory cycle. One notable characteristic of flutter is that it induces high stresses, leading to short term, high cycle fatigue failure. Failure has been observed in both turbines and compressors (Fleeter, 1977). Flutter has also been identified in low pressure and therefore subsonic turbine stages, where shock waves do not exist (Nowinski & Panovsky, 1998).

The major concern with flutter is structural stability. Flutter stability is reduced sharply

for specific narrow speed ranges, a phenomenon known as flutter bite (Marshall & Giles, 1998).

A common correlation parameter that is used to describe flutter is the reduced frequency. This is defined:

$$k_c = \frac{\omega c}{2U_{ref}} \quad (2.1)$$

where ω is the frequency of oscillation, c is the blade chord and U_{ref} a reference velocity.

Until recently it was believed that reduced frequency was the primary design parameter for low pressure turbines. However, Nowinski (Nowinski & Panovsky, 1998) observed in a comparison of a number of different configurations that mode shape (or vibration mode) is primary in the determination of damping. A relationship has also been observed between minimum damping coefficient and reduced frequency – a reduction in reduced frequency leads to a reduction in the minimum damping coefficient. The dominant contribution to the overall stability of low pressure turbine blades was deemed to be the mode shape, followed by reduced frequency, and finally some type of loading parameter. Incidence did not have a major effect on stability.

It has been found from aeroelastic simulations that the shock wave plays a dominant role in flutter, especially at the point where the shock wave becomes detached. The stability of the shock wave is decreased at this point and minor oscillations cause the shock wave to oscillate between attached and detached (Isomura & Giles, 1998).

Both numerical and experimental approaches to flutter analysis are almost identical to those applied to forced response, as they are very similar phenomena. The forcing mechanisms are identical and the difference between the two is due to structural considerations.

2.1.7 Acoustic Resonance

Acoustic resonance is another phenomenon present in turbines. The significance of the effect of these acoustic disturbances on the turbine structure is still not clear, due to the difficulties with modelling this phenomenon both numerically and experimentally. It is usually caused by the shedding of vortices from the trailing edge of stalled blades (Parker, 1997). Turbines in the power generation industry run at close to optimal unstalled conditions, acoustic resonance would usually only occur during start up or shut down, or in the case of dynamic stall. Acoustic resonance may also be caused by the introduction of acoustic waves due to vibration external to the turbine. Consequently the effects of acoustic resonance on the turbine are not as important as flutter, or forced response (Marshall & Imongun, 1996b).

2.1.8 Structural Mistuning

Most analytical and numerical models of flutter and forced response rely on ideally tuned vibrational modes of the blades – this assumes that each blade is identical. The accuracy to which the profiles are shaped is directly related to the cost of machining. Therefore there is a trade-off between profile accuracy and cost. However, variations in profile lead to structural mistuning of the bladings – this can cause unpredictable and serious aeroelastic effects. Small deviations in the blade geometry can lead to a scatter of the blade eigenfrequencies, thus blade interactions become more unpredictable (Kahl, 1998). It is one of the most difficult of the sources of aeroelasticity to model, as the variations are usually random within a certain tolerance. Ideally, a model should be able to predict the combinations of blade profile variation that will provide the most response, however due to the number of combinations possible this poses a difficult problem.

Kahl (1998) examined the effects of blade variations in a comparison between mistuned and tuned calculations for a subsonic low-pressure turbine and transonic compressor rotor. Mistuning is often cited as the source of significant variations of the resonant amplitudes in the individual blades of cascades in test facilities. It was found that in the numerical experiment that mistuning leads to higher resonant amplitudes. It has also been found the mistuning can have a stabilising effect and damp out the aeroelastic response (Nowinski & Panovsky, 1998; Sadeghi & Liu, 2001a). Other types of mistuning includes the uneven spacing of the blades. This has been studied using two whole annulus blade rows by Valdati et al (1999). They found that unsteady excitation increased with the increase in throat width variation.

2.1.9 Damping Effects

Where the turbomachine is subject to oscillating forces, damping plays a significant role in determining not only the amplitude of vibration, but also its frequency. The damping of the aeroelastic system is due to a variety of factors and mechanisms. Predominantly damping is provided by the fluid, with material damping and frictional damping at the blade roots making a lesser contribution. Excitation forces can under certain conditions change to damping forces, as has been mentioned in previous sections. In fact, some authors refer to excitation forces as negative damping.

The sources of aerodynamic damping may be categorised:

- Mean aerodynamic loading
- Shock movement (in the transonic regime)
- Blade wakes and hub and casing vortices

- Mistuning
- Movement of regions of separation
- Movement of turbulence transition region (Mabey *et al.*, 1987)

Structural damping is less complicated in that there are not as many contributing factors:

- Material (hysteric) damping
- Frictional damping at the blade roots, or at the shroud or tip

Damping is possibly one of the more difficult aeroelastic properties to model, as it often involves nonlinear mechanisms. These include frictional damping, large amplitude shock wave oscillation, and turbulence. Thus damping is one characteristic that is most often approximated as linear, or neglected altogether.

2.2 Experiments in Aeroelasticity

Physical experimentation can involve observing systems and taking measurements, or by the observation of a simplified experimental model that is designed to simulate the physical system. Usually a simplified model is created to simplify measurement, increase measurement reliability or decrease system complexity. Turbines are complex rotating machinery and the flow conditions and geometry make measurement of the flow difficult. Experimental measurements provide invaluable data for the validation of the computational model. It is worth reviewing the experimental data presently available as it provides insight into the important characteristics of aeroelasticity and also suggests simplifications and approximations that may be made in a computational model.

Unlike numerical and theoretical analysis, physical experiments are always made in three-dimensional space. However the measurement of 3-dimensional flow phenomena provides a considerable challenge. In many cases measurements are taken across a single plane. So that they may be compared with theoretical models, the effect of 3-dimensional structures is reduced by locating the measurement plane outside regions subject to their effects, such as the hub and casing regions in turbomachinery. Thus the experiments may be characterised by the method of measurement. Where measurements are specifically taken only at mid-span, they may be regarded as being dominated by 2-dimensional effects. If measurements are taken in the hub or tip regions, the flow in these areas is dominated by viscous structures and thus the measurements are investigating 3-dimensional effects. Consequently the experimental studies may be grouped into 2-dimensional and 3-dimensional studies.

Whilst there have been many 3 dimensional numerical calculations performed on turbine cascades and blade rows, it appears that there is a lack of experimental data to validate

numerical simulations. One of the major reasons for this is the huge cost involved in performing such experiments. There is also a considerable problem in the reproduction of blade oscillation in the wind tunnel.

Typical measurements performed on rigs include surface pressure, heat transfer (hot film sensors), whole blade passage and downstream flow field velocity distributions through hot wire measurement, vibration measurement through optical sensors and Schlieren pictures to observe the position and movement of shock waves. Holography has also been used for qualitative analysis and has identified torsional and bending nodes.

The construction of simplified experimental models not only reduces costs but also facilitates measurements that under normal, full scale operating conditions would not be possible. An example of this is an experiment carried out by Bell and He (1998), where aeroelasticity was modelled by hinging the blades at the blade root near the hub and moving the tip with a sinusoidal displacement. This simplifies the experiment and also the numerics – as the blade displacement varies linearly across the span, the grid is more easily adapted to blade movement and no finite element structural modelling is required.

There are a number of common configurations found in experimental aeroelasticity and unsteady flow analysis:

- a single oscillating blade (in first mode bending or torsion only) in a linear cascade of static airfoils
- an annular cascade of linear turbine blades in a turbine configuration, with all blades oscillating.
- full scale engines

Over the past couple of decades, research and development in turbomachinery aeroelasticity has grown into an important field in engineering. The symposium “Aeroelasticity in Turbomachines” was initiated in 1976, which brought together researchers in this area. This event has been a regular forum for the presentation of new research in this area.

2.2.1 Two-dimensional Measurements

In the 1980's it was recognised that research in the area of aeroelasticity in turbomachinery was hindered by a general lack of consistency in the configurations subject to both theoretical and physical experimentation. Another problem exists where research was performed in collaboration with commercial entities. Often the results of such research are highly confidential – whilst the resulting papers may provide physical insight into the mechanisms of the aeroelastic phenomenon, often important details such as geometry specifications are omitted so that the physical or numerical results cannot be reproduced. Therefore any comparisons

with results may only be qualitative which provides little scope for a detailed analysis and evaluation of a numerical solution method.

In 1980, as a result of the symposium, a wide scope of different "standard configurations" was established, and sample cases with different flow conditions within each standard configuration were defined. The objective was to formulate test cases which are repeatable and suitable for code validations of numerical models predicting flutter in viscous flows (Bölcs & Fransson, 1986). It was intended that subsequently they would be better defined and eventually expand or reduce these cases. At the 1987 Symposium, a task force was charged with the collecting of information about experimental and theoretical methods and data in the field of aeroelasticity in turbomachines, and this was presented at the 1991 Symposium with ten standard configurations (Fransson & Verdon, 1991). An 11th configuration has been added more recently (Fransson *et al.*, 1998).

The standard configurations are useful in the validation process of 2 dimensional numerical codes, as there is a large body of experimental, numerical and theoretical results from which to make comparisons.

2.2.2 Three-dimensional Measurements

As noted earlier, there are fewer experiments that concentrate on 3-dimensional aeroelastic flow characteristics in turbomachinery. Compared to flow field measurements, measurements of the blade structure are more common as they may be more easily performed. For example the aeroelastic response of full-scale subsonic turbines has been measured through the application of strain gauges to the blade surfaces. These data have been used to determine the maximum vibrational mode, which has been compared with calculated results (Hilbert *et al.*, 1997). The same maximum mode was determined to be dominant in both the experiment and computation. Non-interference measurements have been conducted on a stage using optical sensors (Watkins & Chi, 1989). Whilst they provide detailed information on the blade vibration modes, they provide little with regard to the flow mechanisms causing the instability. Without knowledge of the source of the aeroelastic interaction it is difficult for designers to eradicate the problem.

A number of researchers have investigated 3-dimensional flow structures in turbomachinery in both stationary and rotating facilities. However these have concentrated on secondary flows or inter-blade row interaction. For example, the tip region of an operating turbine has been investigated recently through unsteady velocity measurements (McCarter *et al.*, 2001a; McCarter *et al.*, 2001b). Whilst the detail of the measurements was limited, all of the major secondary flows were identified in the region of the casing.

However, 3-dimensional flow measurements for aeroelasticity are not common in the literature. The effects of 3-dimensional flow features have been modelled more simply by

a single blade and two-blade passages (Bell & He, 1997; Bell & He, 1998). The bending mode was simulated by hinging the blade at the root. Measurements were taken at a number of span-wise locations. The effect of tip gap on the unsteady aerodynamics was also investigated (Bell & He, 2000).

Data for the inlet and outlet planes and the 3-dimensional mode shape of Standard Test Case 4 (Ott, 1998; Ott, 2002) have been made available and this allows the simulation and comparison of this case in 3-dimensions.

The last two cases are used in this work to investigate viscous flow structures, tip leakage effects and the differences between 2-dimensional and 3-dimensional aeroelastic simulation models.

2.3 Theoretical Modelling

The numerical simulation of engineering systems provides a number of advantages over physical experimentation. One is economic in that in general computer resources are cheaper than experimental facilities. Another is that the fluid dynamics may be represented with a much higher level of detail with a computational model. Whilst experimental analysis is subject to measurement errors, computational simulation is subject to modelling errors and these may be much more difficult to identify than those due to experimental method.

2.3.1 Methods of Analysis

Since the identification of the aeroelasticity as a major problem, a number of different approaches have been applied to analyse the interaction of fluid and structure. Initially the analysis was limited due to the lack of methods for modelling unsteady fluid flow. However over the last couple of decades there has been advancement in the fields of fluid modelling which has led to more sophisticated methods.

The different approaches have been recently classified by Marshall and Imregun (1996b). Principally methods may be divided into two different categories. The first class is classical, whereby the fluid and structural fields are uncoupled and considered completely separately. At present this approach is most commonly used and most widely researched. One reason is that the power of computational facilities have restricted design and research to this more simplified problem. Another is that it has only been recently that the strong integration of personnel between the disciplines of structural and fluid modelling has occurred (Marshall & Imregun, 1996b). The second class is known as an integrated approach, where the coupling of the structure and aerodynamics is considered. Uncoupled procedures have been classed as inadequate in many cases (Marshall & Imregun, 1996a) as the basic assumption relies on splitting an inherently coupled non-linear phenomenon into two separate analyses, which are

often themselves linear.

The various methods of coupling have been classified. Uncoupled solution methods are not integrated, whilst partially coupled methods involve the separate solution of the fluid and structural fields, where the information is passed as boundary conditions at each global time step. Fully integrated methods are where the structural motion is solved simultaneously with the fluid solution in time. This may be achieved by using the same time integration solver for the entire fluid/structural domain. Whilst fully integrated methods may provide a superior model of the energy exchange between the two domains due to the lack of time lag, partially integrated methods allow for the use of structural modal analysis and sub-cycling of the fluid domain, both of which greatly increase the computational efficiency and thus reduce simulation time.

The two domains of solid and fluid may be directly modelled through the same numerical method, however it is found in the majority of cases that it is more efficient to use simulation methods that have been developed specifically for each discipline. Finite element methods are almost exclusively used for the modelling of structures. On the other hand, finite volume methods are most common in the simulation of gas dynamics. The structural and fluid domains are both governed by second order differential equations, however the resolution required for the fluid domain is usually much higher. Given the different resolution requirements for solid and fluid elements, it seems natural to solve the dynamics of the two domains separately, transferring any interactions between the two during the solution process. A major consideration in the modelling of aeroelasticity is the method of coupling these equations and therefore modelling the interaction between two different physical regions.

Usually structural calculations are performed in Lagrangian space, where the computational nodes remain fixed with respect to the material. Fluid calculations are usually performed in Eulerian space, where the nodes are fixed with respect to space. Thus there is a problem at the fluid/structural boundary where the structure is moving with respect to space. To overcome this problem, the most common solution is to adapt the fluid grid to the movement of the structure. It is also possible that the fluid grid may remain stationary, however this introduces complexities at the flow boundaries, where quantities must be then interpolated and the possibility of the boundary in the middle of a computational cell must be taken into account.

The efficiency and accuracy of coupled procedures for the solution of aeroelastic problems has been studied in detail by a number of researchers (Piperno, 1997; Piperno *et al.*, 1995; Farhat *et al.*, 1998). If the solution of the structural and fluid domains are to be found using a partially coupled formulation, the accuracy of the computational model is governed not only by the accuracy of the individual methods for fluid and structure, but the way in which they are coupled. Numerical inaccuracies in the method of coupling may be quantified through the calculation of the energy created at the fluid/structure interfaces. Piperno

(1997) has investigated various schemes and their corresponding accuracy with respect to energy transfer.

The method of sub-cycling has been used widely to increase computational efficiency. It involves the utilisation of different time steps in the structural and fluid solvers. This is useful as in the majority of cases, the fluid solver requires a much smaller time step due to constraints on stability or the requirement for temporal resolution. It has the advantage that it reduces overall simulation CPU time due to the fact that the structural solution is advanced a fewer number of steps. There is also a reduction in the number of transfers between the two solvers, further decreasing solution time. However this is only effective if sub-cycling does not affect the stability of the partitioned algorithm (Farhat *et al.*, 1995).

Within the class of classical approaches there are a number of different methods. Usually they involve reducing the 3-dimensional problem to a single, typical cross-section.

Some early work on actuator disc theory was presented by Whitehead (1959) and then later developed for compressible flow (Adamczyk *et al.*, 1982). This theory predicts the unsteady forces on the blade as a function of the steady flow field entering the cascade and the geometry and dynamic response of the cascade. It is limited to modelling low reduced frequencies and small inter-blade phase angles. Given that instability can occur at relatively large inter-blade phase angles this technique has limited applicability.

A frequency domain approach, also known as the aeroelastic eigensolution method (Marshall & Imregun, 1996b), transforms unsteady aerodynamic data to the frequency domain. These aerodynamic coefficients are calculated for a number of inter-blade phase angles and reduced frequencies. With the inclusion of the force coefficients, the governing equations of motion for the blade structure may be reduced to a complex eigenvalue problem. A stability map may be produced for each reduced frequency which is a locus of eigenvalues. The real axis represents the frequency of the oscillation and the imaginary axis the damping (Srinivasan, 1997).

A time domain approach allows for the detailed investigation of the aerodynamic parameters that contribute to energy loss in turbomachinery designs (Srinivasan, 1997). Also known as the energy method it represents more or less the state of the art in turbomachinery flutter analysis in the aerospace industry because not only their simplicity but also their compatibility with section by section design procedures (Marshall & Imregun, 1996b). The energy method does not include the complexities of a coupled approach in the coupling between structural and fluid fields, nor does it involve the long simulation times required for a number of different structural modes and thus time scales.

Whilst 3-dimensional coupled simulations of turbomachinery have already been performed (for example (Doi & Alonso, 2002; Vahdati *et al.*, 1999)) for compressors, there is still a need for the investigation into the simulation unsteady effects in turbines and 3-dimensional aeroelastic flows. Detailed analysis of uncoupled, unsteady aeroelastic flows

allows for the identification of sources of instability with regard to flow features and their importance in the aeroelastic instability without the added complication of a responding structure.

2.3.2 The Energy Method

One of the first researchers to introduce the energy method (Marshall & Imregun, 1996b) was Carta (1967). He investigated the notion that coupled motion can result in system instability under certain conditions. This instability manifests itself in an extraction of energy of a rotor from the airflow in sufficient quantities to produce an unstable vibratory motion. The approach finds its basis in the most fundamental of analyses due to Collar (1947) briefly discussed in Section 2.1.1.

A particular mode shape and structural eigenfrequency is modelled and the flow response on the surface of the vibrating structure is monitored. This approach is used in both physical experimentation and numerical simulation. The motion of the structure is prescribed and the flow has no effect on the structural mode shape. If the integrated effect of the flow on the structure is to amplify the motion, that is it applies more force to the structure in the direction of oscillation, the configuration is deemed unstable. If the configuration was an elastic system, the force would tend to add energy over time. Without any other damping the amplitude of oscillation would increase in time until the elastic system fails. The integration of work over a displacement cycle provides a direct indication of system stability. The negative of this quantity results in the damping coefficient.

The aerodynamic force coefficient is the integral of the pressure over the blade, resolved in the direction of the oscillation motion,

$$c_h(t) = \int_S \frac{\tilde{p}(x,t)}{h_c(p_0 - p_{ref})} [\mathbf{n} \cdot \mathbf{e}_h] dS,$$

where \mathbf{e}_h is the vector aligned with the blade displacement direction and \mathbf{n} is the surface normal.

The aerodynamic work coefficient may be calculated by integrating the force coefficient over a cycle of oscillation,

$$c_w = \int_h h \cdot c_h(t) dh = \int_0^{t=T} hc_h(t) \cdot h dt. \quad (2.2)$$

The aerodynamic damping is a function of the aerodynamic work and may be expressed in normalised form,

$$\Xi = -\frac{c_h}{\pi h_c^2} \quad (2.3)$$

Given that the blade motion and force coefficient are purely harmonic, the phase between

the two ultimately determines the stability. The damping coefficient may also be calculated through the imaginary part of the force coefficient (Bölcs & Fransson, 1986),

$$\Xi = -\Im(c_h).$$

The phase of the pressure coefficient with respect to the blade motion provides a useful indication of any local flow behaviour that may be leading to configuration instability.

A positive damping coefficient is stable – the phase of the displacement leads the aerodynamic force on the blade and the motion is damped. If the coefficient is negative, the phase of the aerodynamic force leads the displacement function and thus would add energy to an elastic system over time; this system is unstable.

2.3.3 Simplification of the Model Geometry

One method of reducing the demands on computational resources is to simplify the model geometry. Simplifications include reduction of domain size due to the assumption of periodicity and isolation of particular regions from the rest of the machine. Further simplifications include the assumption of 2-dimensionality of the configuration and 1-dimensional vibrational mode shapes.

Given the symmetric nature of a turbine blade row, flow periodicity may be assumed over a certain number of passages – that is the flow pattern is assumed to repeat itself after a certain number of consecutive passages in the annulus. The assumption of flow periodicity coincides with the notion of inter-blade phase angle and a single equivalent blade for the modelling of the blade vibration.

Lane (Lane, 1956) was one of the first to identify and simplify the vibrational characteristics of turbine rotors. He reduced the number of possible system modes to one by considering a single equivalent blade. In this assumption the blade vibrational mode shape for each blade in the rotor is identical, with a phase shift between adjacent blades. The shape of the mode may be quite complex in that it involves a combination of bending and twist. One result of this analysis is that the phase shift between blades, known as the inter-blade phase angle (IBPA) must be a multiple of the circumferential angle between blades. For a finite rotor, there are a finite number of possible IBPA's. This is due to the fact that a single blade must be in phase with itself in sustained vibration. The analysis is applied to compressor blade rows, but may equally be applied to turbine blade rows. It is reasonable to assume that the rotor vibrational modes are identical around the rotor as the blades are intended to be identical in the manufacturing process. Where blades differ in characteristics, this leads to mistuning, a phenomenon discussed in Section 2.1.8.

Due to the complexity of the flow in a full turbine, often different flow mechanisms are decoupled for the purposes of analysis. For example, it may be assumed that the effect of

wakes passing due to upstream blade rows may be considered separately from the unsteadiness caused by blade vibration (Hilbert *et al.*, 1997). This is analogous to the decoupling methods used in potential and Euler linear analysis, where the steady and unsteady flows are decoupled from one another.

Often blade rows are considered individually and are isolated from interactions with the rest of the machine. With Lane's assumption and the assumption of flow periodicity, a blade row may be further reduced to part of the annulus, where only a number of blades and blade passages are included in the analysis. A single dominant mode shape may only be considered, reducing the resolution required for time domain analysis.

A structural model may be used that structurally decouples the blade row and assumes a rigid hub and casing. This simplifies computation whilst still allowing for the aerodynamic coupling of the full blade row model. It does not take into account the effects of inter-blade structural vibrations that would be transmitted through a non-rigid hub, which may damp or further excite instabilities of particular configurations. However it was found by Chew (Chew *et al.*, 1998) through a finite element model that the inclusion of the effect of the elasticity of the fan disc of an aeroengine did not vary the natural frequencies of the blades.

In an analysis of the time histories of a numerical calculation for a full annulus, it has been found that there are interactions taking place between the different assembly modes (Sayma *et al.*, 1998). Thus it may not always be valid to consider the different vibration modes separately in the computational analysis.

A great deal of analysis has been performed on 2-dimensional configurations where the structural mode shape is a harmonic translation or pitching rotation of the turbine blade. However three-dimensional effects are important in the modelling of turbomachinery blades for a number of reasons (Holmes & Lorence, 1998):

- Modern blades, which are designed routinely using inviscid and viscous 3D solvers can have highly 3 dimensional shapes (twist, rake, change in camber, change in chord length over the radial span)
- Three dimensional flow features – hub and tip boundary layers, secondary flows (hub and casing horse-shoe vortices), and tip vortices can occupy a significant portion of the flow field, limiting the flow region in which the flow field can be regarded as two dimensional. This also includes the interactions with upstream blade rows due to secondary flows.
- Transonic flows are inherently 3 dimensional – shocks may only exist in the out board region of the blade where the flow moves from sub to supersonic
- Even where the mean flow is two dimensional, the vibration mode of the blade usually leads to different surface displacements in the radial direction.

2.3.4 Simplification of Fluid Model

Computational demands may also be reduced through the simplification of the mathematical model for the fluid domain. A number of different flow models have been used for the simulation of turbomachinery flows. In general these have been simplifications of the Navier-Stokes equations. The Navier-Stokes equations are presented in Section 3.1.1. The following flow models have been applied or are available to researchers in the simulation of aeroelasticity in turbomachinery.

- Potential flow equations.
- Linearised Euler equations.
- Euler equations.
- Thin Layer Reynolds averaged Navier-Stokes equations (TLRNS).
- Reynolds averaged Navier-Stokes equations (RANS).
- Large Eddy Simulation (LES).
- Direct Numerical Simulation (DNS).

These models are listed from least to most complex with regard to the physics that they are able to capture. For example, LES is a more complex model than DNS, however the complexity of the flow that can be captured is less. Whilst present-day computers are capable of providing useful results with the second last of the fluid models, the others are still appropriate where a large parameter space is to be investigated. Each has limitations in representing physical processes and this should be allowed for in analysis. The solution of the unsteady flow equations imposes considerable demands on computational resources. The solution methods for each model vary. In the case of the more complex governing equations, some researchers have linearised the governing equations in an effort to reduce the computational requirements whilst retaining the ability to model certain phenomena.

Given the lack of knowledge on the importance of different factors in the aeroelastic interaction, the appropriate selection of governing equations can pose a difficult problem. Each simplification has the advantage of a reduction in computation time or complexity over the full implementation, however there are trade-offs in the physical accuracy of the computational model.

The simplest of models is potential flow. Some of the earliest work involving the aerodynamics of oscillating airfoils involved the application of the potential flow equations (for example, Goldstein (1977)). The coupling of the Navier-Stokes equations with an aeroelastic solver typically requires two or three orders of magnitude of computer time for solution

when compared to one which implements the potential flow equations for flow around aircraft wings (Chaderjian & Guruswamy, 1992). In the early development of aeroelastic and unsteady flow analysis, computers were greatly limited by processing speed and memory storage and the potential equations were the only fluid model that could be effectively simulated.

Where potential flow is used to model transonic, unsteady flows, the mean flow is assumed to be steady. The unsteadiness is modelled as linear perturbations from the mean flow. It can be used to analyse the unsteadiness due to wake/blade interaction or incoming potential waves in addition to structural bending or torsion. A major problem is the assumption of steady flow, which does not take account of the effect of mean loading on the steady pressure field. The complexity of extending linear potential methods to 3-dimensions restricts them to the solution of two-dimensional flows. Variations on the method of potential flow analysis include the transonic small disturbance method of Cunningham (1988). This has been applied to the solution of flow about a whole aircraft, and combines simplicity with computational efficiency to the computation of flows in the transonic regime. Another problem with potential, therefore isentropic and irrotational flow is that it does not account for the production of steady and unsteady entropy and vorticity across shock waves. This deficiency can produce under some circumstances serious errors in the predicted unsteady pressure distribution, shock motions, and unsteady blade loading (Hall & Crawley, 1989).

The Euler equations are a simplification of the Navier-Stokes equations with the effects of viscosity neglected and thus the diffusive terms removed. The flow model is isentropic, except for where discontinuities such as shock waves or vortex sheets exist (Hirsch, 1992a).

In the linearisation of the Euler equations, the steady part is regarded as nonlinear, whilst the unsteadiness is regarded as a linear perturbation from the steady flow. A significant advantage offered by the linearised inviscid approximation is that the first-order unsteady fluid motions arising from various Fourier modes of unsteady excitation are not coupled. Hence it is sufficient to develop solution procedures for a single harmonic (in time and space) component of a given excitation. Solutions for arbitrary periodic excitations and arbitrary combinations of such excitations can then be obtained by superposition (Verdon, 1993). Some authors have found that there are some cases where unsteady perturbations are linear, thus a method assuming a linear change in field variables would suffice (Chew *et al.*, 1998). It has been shown by Lindquist (1994) that the use of the linearised Euler equations coupled with shock capturing is a valid means of modelling unsteady shock movement over turbomachinery airfoils, provided that the shock movement is linear. This requires that the length over which the shock moves is small compared to the chord of the airfoil.

However shock fitting is cumbersome and requires a relatively complex implementation, even though it provides sharp resolution. A harmonic method for the linearised Euler equations was developed in combination with a moving grid to model 2-dimensional aeroelastic

flows in turbomachinery (Hall & Clark, 1993). In this analysis, a steady base flow was assumed and the unsteadiness of the flow was assumed to be linear about the steady solution. It was estimated that the solution method requires one to two orders of magnitude less computation time than for a time-integrating method.

This method was later developed to a nonlinear harmonic method to include a time averaged base flow rather than a steady base flow (He & Ning, 1998; Ning & He, 1998). This produces extra terms in the governing equations, similar to the turbulence stress terms found in the RNS equations. The non-linear effects are included in the time-averaged part of the flow and the unsteady perturbations are calculated based on the time-average flow field. The nonlinear effect on the time-averaged flow is only included as the product term of the first order unsteady calculations, thus assuming that the contributions of the first order term is dominant. It was found that the results where moving shocks that were present in the flow-field were considerably better than for the linearised analysis, whilst only increasing the solution time by 60% (less than required by the nonlinear Euler equations). The difference between the results from a time-linear method and those from a nonlinear method strongly depends on the amplitude of movement of the shock oscillation. Whilst the nonlinear harmonic method improved predictions in the case of oscillating shock waves, the non-linearity present in large oscillations still limits the predictive capability when compared to non-linear calculations (He & Ning, 1998).

Shibata (1998) also made a comparison between non-linear and linear Euler calculations. They found that whilst for most transonic flows containing shocks, the linearised Euler analysis was in good agreement with the nonlinear one, the linearised code showed once again poor agreement where the flow includes large shock movement or where shock waves disappear. Even where the leading edge shock is relatively weak, it has been found that in the majority of cases that the nonlinear Euler solution produces a result closer to experimental measurements in comparison to linearised Euler computations (Hwang & Yang, 1995).

Viscous effects have been included in the fluid model without solving the full Reynolds averaged Navier-Stokes equations. For example, the Euler method has been implemented and viscous effects accounted for through the application of integral boundary layer theory (Wolff & Fleeter, 1995). It is reported that this method increases the solution time by 25%, less than the increase required to implement the Navier Stokes equations. It has the advantage that the same grid may be used for both the inviscid and viscous calculations, something not possible in other inviscid-viscous formulations employing the Navier Stokes equations. Thus there is a substantial saving in the memory required to run such a solution. This is due to the fact that the grid does not have to be concentrated at the wall to the same extent, and also that all fluxes of flow variables at the boundary do not have to be stored at every time step. Other authors have also implemented loss models (Chew *et al.*, 1998; Sayma *et al.*, 1998). Given that computational resources are limited, this has allowed for the computational modelling

of the complete rotor or stator annulus. The loss model assumes that a distributed friction force may represent the effect of the shear stresses on motion and may be determined from experimental or calculated data. Sayma et al (1998) define the loss model numerically using data from a previous viscous analysis of a single blade passage on a much finer mesh. The viscous solution is then interpolated onto the coarser mesh that is used for an inviscid analysis of the whole assembly. The viscous stresses of the first solution are used as source terms in the inviscid calculation.

Time linearised viscous methods have been shown to be valid for subsonic cases, where large (closed) separation bubbles exist (He, 1998). Although it was found that local pressure coefficients varied by up to 10 percent from nonlinear calculations, the difference in integrated pressure coefficient was much less. However this was only achieved through the modelling of the separation region and may not be a good method where the form of the separation bubble is not well understood.

Inviscid calculations that employ linearised or non-linear Euler equations require much less computation time and reduce the complexity of implementation, however ignoring viscosity may be neglecting important effects (Shibata & Kaji, 1998). Shock boundary layer interaction or the interaction between the shock wave and the turbulent transition point may play an important role in the aeroelastic interaction, especially where strong shocks exist in the blade passage. It has been found by Grüber and Carstens (1998) that RNS calculations predict an expansion shock position that is much closer to that measured experimentally, when compared with an Euler calculation. They attribute this to a shock induced separation bubble, which effects a sudden thickening of the boundary layer, causing the shock to move upstream, since the pressure gradient in front of the shock is fairly small. Other researchers have identified configurations where viscous effects are important. It has been found that flow separation has an important role in the damping of the effect of shock oscillation (Isumura & Giles, 1998), which cannot be modelled by an inviscid calculation.

Comparisons of some of the simulations involving different flow models applied to aeroelastic turbomachinery flows have been performed by a number of authors. Ayer (1998) compare TLRNS, Euler, Euler first harmonic, and linearised inviscid flow predictions for the 10th Standard Cascade. The research indicated that for subsonic flow conditions, although viscous effects cause a small reduction in the time-averaged or mean pressure loading of the down-stream half of a blade, they have a negligible impact on the unsteady surface pressure fluctuations. In a comparison of work per cycle predictions for subsonic flow, it was found that TLRNS, Euler, Euler first harmonic, and linearised inviscid flow predictions produced very similar results. It was therefore concluded that for subsonic flows, the non-linear and viscous effects only have a small impact on the aeroelastic stability margin. However for transonic flows, non-linear and viscous effects were found to be important in regions traversed by shocks – viscous effects diminish the impulsive unsteady loads due to shock

motion. Relatively large second and higher harmonic pressure variations occur close to the shock, thus degrading the predictions made by the first harmonic Euler calculation.

Fransson (1998) made a comparison between a quasi-3dimensional potential small perturbation model, linearised Euler, 2D nonlinear Euler and quasi-3D nonlinear RNS solver for the 11th Standard Configuration. Meshes were chosen so that the solutions were grid independent. For the steady results, the shock position is best predicted by the RNS result. None of the results predicted well either the position of the passage shock, or its strength. However it was noted that the experimental results were highly sensitive to inlet conditions, especially with regard to the characteristics of the passage shock. Once again it was determined that for the subsonic case, the inviscid linearised methods made sufficiently accurate predictions, whilst also providing high computational efficiency.

The TLRNS equations approximate the RNS equations by neglecting gradients in the stream-wise direction. This is useful if there is little recirculation in the flow and little separation. However the method becomes inaccurate if there is gross separation. A turbulence model is once again required to model the nonlinear unsteady components of the TLRNS equations.

The RANS equations have been applied in 2-dimensional simulations in aeroelastic simulations of power generation turbines (Grüber & Carstens, 1998; He, 1998). The quasi-3dimensional form of the governing equations, where the solution is calculated along a stream surface, has also been implemented (Weber *et al.*, 1998). In this work, a comparison was made between non-linear Euler and RNS calculations, and it was found that the RNS calculations predicted aerodynamic damping closest to that found in experiment.

Linearised, three dimensional RNS equations coupled with the $k-\omega$ turbulence model have also been implemented (Holmes & Lorence, 1998). The authors note that a complete linearisation of the discretised non-linear flow solver may be impossible. Some part of the non-linear flow solver can only be linearised at significant development cost. The degree to which the turbulence model needs to be linearised was identified as an area requiring further research. The turbulence model must be completely linearised for low reduced frequency and higher incidences, close to stall.

It appears that one of the most promising methods of reducing the fluid model equations for periodic types of flows such as those found in aeroelastic turbomachinery applications is the harmonic balance method or time linearisation methods (Hall & Crawley, 1989; Hall & Clark, 1993; Hall *et al.*, 2000; McMullen *et al.*, 2001). This method is particularly useful for multiple blade row simulations where the blade passing frequency requires up to 100 periods of oscillation of a time-accurate solver to resolve the periodic flow features. Harmonic balance techniques effectively transform an unsteady problem in the time domain to a steady problem in the frequency domain (McMullen *et al.*, 2001).

The time harmonic method can provide a substantial reduction in the solution time. However it is difficult to establish for the present application and it depends on the resolution of the simulation that is required. If five temporal modes are included in the case of the low Reynolds number circular cylinder (the number required for temporal convergence) it represents 50% of the effort required for the dual-time method (McMullen *et al.*, 2001). How this compares with the simulation of turbomachinery flows with a two-equation turbulence model is not known. The formulation of the harmonic balance form of the turbulence equations presents a significant challenge and the related convergence issues are not known or understood.

Given the presently available computer resources and numerical methods, the RANS equations are the most suitable for investigating the effects of tip leakage and secondary flows and flows that are potentially under the influence of shock/boundary interaction and separation in aeroelastic turbomachinery configurations. Time linearisation of the fluid model is possible, however this approach is complicated and the linearisation of two-equation turbulence models is not yet well understood. The Wilcox (Wilcox, 1988) $k-\omega$ model was chosen over more simple models for a better prediction of length scales for the turbulence eddy viscosity in the tip gap region. The selection of turbulence model is an important issue and this is discussed further in Section 3.1.3.

2.3.5 Simplification of Structural Model

Finite element methods are traditionally used for simulation and design of dynamic and static structural elements. They are also widely used in aeroelastic calculations where the structure has a complex geometry. The methods of solution are well documented and developed. Compared to computational fluid mechanics, structural analysis is much more reliable and for most applications predictions closely match experimental measurements.

There are two common ways of solving the dynamic structural equations. The first is modal analysis, briefly discussed in section 2.1.4, where a finite number of modes is assumed which reduces the size of the dynamical matrix system. The second are direct integration methods and require no transformation of the dynamic equations. Time is discretised through the finite difference or Newmark methods. Given that the solution time is proportional to the number of time steps required for solution, where there are a large number of time steps to be calculated, it is often more efficient to use modal analysis (Rao, 1989).

Modal analysis finds its basis in the method of Rayleigh. The Rayleigh Ritz Method is an extension of the Rayleigh method. Whilst the method of Rayleigh assumes that the entire integral equation may be satisfied through a single function, the Rayleigh Ritz method assumes that the integral equation may be satisfied by using a summation of functions, each function referred to as a mode or mode shape. Thus the total deflection may be represented

by the sum of the mode shape functions. A solution may be made up of an arbitrary number of mode shapes, however the more modes included in the calculation the more accurate the solution (Rao, 1995).

The solution may be approximated by first assuming a finite number of modes and then calculating the total response from superposition. This allows the reduction of the bandwidth of the stiffness, mass and damping matrices in the aeroelastic equations. Since the number of operations required to solve the problem is proportional to the bandwidth of these matrices, this reduces the computation requirements. For modal analysis, the element displacements must first be transformed to generalised displacements. This transformation must also be performed on stiffness, mass and damping matrices. However the transformation is not time dependent and must only be performed at the start of the solution process.

The transformation matrices are often calculated by only considering the undamped system. Thus small vibrations and therefore linear structural behaviour is assumed. In the present work a modal approach is used for the modelling of an airfoil aeroelastic problem, but this is not extended to turbomachinery configurations.

Chapter 3

Mathematical Model

Traditionally fluids and structures have been widely modelled as continuous media. Equations governing the continuum have been developed and whilst they do not represent matter at a molecular level they provide very good representation when bulk phenomena are considered. These are formulated by applying classical conservation laws of mass, momentum and energy (Hirsch, 1992a).

3.1 Fluid Model

The gas or fluid found in the compressors and turbines of turbomachinery may typically be modelled by the Favre averaged Navier-Stokes equations.

3.1.1 Navier-Stokes Equations

A number of different derivations of the Navier-Stokes equations exist in the literature. One of the more physically intuitive developments of the governing equations is through the construction of a control volume. This relates well to the finite volume method of discretisation used in the present computational method.

Consider an arbitrary control volume V fixed in space and time, conservation of mass requires that the rate of change of mass within the control volume is equal to the mass flux across the surface S of V (Fletcher, 1997).

$$\frac{d}{dt} \int_V \rho dV = - \int_S \rho u_i \cdot n dS \quad (3.1)$$

For a control volume that changes in geometry in time, the normal velocity of the surface must be subtracted from the fluid velocity. Thus the formulation is changed from a purely Eulerian reference frame to the more general arbitrary Lagrangian Eulerian formulation. This may then be applied to configurations involving a fluid domain that is moving, particularly important in aeroelastic simulations.

$$\frac{d}{dt} \int_V \rho dV = - \int_S \rho(u_i - u_{grid}) \cdot n dS \quad (3.2)$$

Since the volume V is arbitrary, this integral formulation reduces to the more commonly known form of the continuity equation

$$\frac{\partial \rho}{\partial t} + \frac{\partial}{\partial x_i} (\rho(u_i - u_{grid})) = 0. \quad (3.3)$$

Newton's second law of motion states that the time rate of change of linear momentum is equal to the sum of forces acting.

$$\frac{d}{dt} \int_V \rho u_i dV = \sum F_i \quad (3.4)$$

The forces on the fluid element involve those acting at its surface and volume forces. In this case the effect of volume forces is neglected, as for aerodynamic applications the density is low enough for the influence of body forces to be of negligible magnitude. Surface forces include a normal pressure force and tangential surface shear stresses due to viscosity. For some of the simulations only the Euler equations are solved thus the effects of viscosity are neglected and the shear stresses are omitted from the governing equations.

In integral form, the Euler momentum equation is

$$\int_V \left(\frac{\partial \rho u_i}{\partial t} + \frac{\partial}{\partial x_j} \rho u_j (u_i - u_{grid}) + \frac{\partial p}{\partial x_i} \right) dV = 0, \quad (3.5)$$

and the Navier-Stokes momentum equation is

$$\int_V \left(\frac{\partial \rho u_i}{\partial t} + \frac{\partial}{\partial x_j} \rho u_j (u_i - u_{grid}) + \frac{\partial p}{\partial x_i} - \frac{\partial t_{ji}}{\partial x_j} \right) dV = 0, \quad (3.6)$$

where t_{ji} is the viscous stress tensor that accounts for tangential stresses in arbitrary directions,

$$t_{ij} = 2\mu \left(S_{ij} - \frac{2}{3}\mu \frac{\partial u_k}{\partial x_k} \delta_{ij} \right), \quad (3.7)$$

and the mean strain rate tensor is defined,

$$S_{ij} = \frac{1}{2} \left(\frac{\partial u_i}{\partial x_j} + \frac{\partial u_j}{\partial x_i} \right). \quad (3.8)$$

The total stress tensor is defined

$$\sigma_{ij} = t_{ij} - \frac{\partial p}{\partial x_i}. \quad (3.9)$$

Where the Mach number exceeds a the limit for incompressible flows $Ma > 0.3$, conservation of energy plays an important role in the fluid governing equations. The first law of

thermodynamics states that the time rate of change of the internal energy and the kinetic energy is equal to the rate of heat transfer less the rate of work done by the system. Combined into a transport equation to account for the movement of the fluid (Fletcher, 1997; Batchelor, 1981),

$$\int_V \left(\frac{\partial pE}{\partial t} + \frac{\partial}{\partial x_j} \rho H(u_i - u_{grid}) \right) dV = \int_S \left(u_i \sigma_{ij} n_j + k \frac{\partial T}{\partial x_i} n_i \right) dS, \quad (3.10)$$

where the terms on the right hand side are the contribution to work of the forces at the volume boundary by the surrounding matter and the transfer of heat or heat flux across the bounding surface S .

The integral equation reduces to the more common differential equation,

$$\frac{\partial pE}{\partial t} + \frac{\partial}{\partial x_j} \rho H(u_i - u_{grid}) = -\frac{\partial p}{\partial x_i} + \Phi + \frac{\partial}{\partial x_i} \left(k \frac{\partial T}{\partial x_i} \right), \quad (3.11)$$

where the rate of dissipation of mechanical energy is defined,

$$\Phi = 2\mu \left(S_{ij} S_{ij} - \frac{1}{3} \left(\frac{\partial u_i}{\partial x_i} \right)^2 \right). \quad (3.12)$$

The first term on the right hand side is the contribution of the work done due to isotropic or expansion part of the rate of strain, the dissipation of mechanical energy is the second term due to the viscosity and this is an irreversible addition of heat. The third term is due to conduction of heat into the element.

To complete the model two equations are required that involve the thermodynamic properties of the fluid or gas (Batchelor, 1981). Local temporal and spatial equilibrium is assumed and the all quantities describing the fluid are a function of two parameters of state. For the ideal gas that is modelled in this work, the temperature is related to pressure and density by the ideal gas equation, or equation of state for an ideal gas,

$$p = R\rho T. \quad (3.13)$$

In the case of a perfect gas with constant specific heats, that is the amount of heat required by to raise the fluid by a unit of temperature, the energy is related to the temperature,

$$e - E = C_v T. \quad (3.14)$$

3.1.2 Favre averaged Navier Stokes Equations

In principal the Navier-Stokes equations apply equally to turbulent and laminar flow (Launder & Spalding, 1972). Typically flow in a turbine passage is of relatively high Reynolds number and the flow is fully turbulent. There is usually a large disparity in the physical

scales that exist in the problem and those that may be resolved by the numerical discretisation. It is estimated that a typical calculation performed in the aerospace industry for an aircraft using the RANS equations requires an operation count in the range of $10^{12} - 10^{13}$ operations. For example, for a simulation of flow over an F16A or the space shuttle in ascent mode requires 8 to 12 hours on a CRAY Y/MP single processor. It is estimated for a direct numerical simulation the number operations required is proportional to Re^3 . If a DNS performed for the same craft then 10^{20} operations is required; this is seven orders of magnitude more than for the RANS case and clearly beyond the capabilities of Teraflop machines (Schiano, 1994). These machines are among the fastest available at the beginning of the 21st Century.

In typical engineering applications the details of turbulence are not required; usually only its time-averaged effects are important even when the mean flow is unsteady (Launder & Spalding, 1972). One of the most common methods of accounting for the effects of turbulence into the fluid governing equations is through some method of averaging in time and space. According to Wilcox (Wilcox, 2000), Reynolds averaging (or Favre averaging) is "a brutal simplification that loses much of the information contained within the Navier-Stokes equation". However at present it is the most common way of dealing with the inadequacies of present computational and numerical methods. Conventional Reynolds time averaging decomposes the independent variables into average and fluctuating parts. For example, for velocity:

$$u_i(\mathbf{x}, t) = U_i(\mathbf{x}, t) + u'_i(\mathbf{x}, t) \quad (3.15)$$

$$U_i(\mathbf{x}) = \frac{1}{T} \int_{t_1}^{t_1+T} u_i(\mathbf{x}, t) dt \quad T_1 \ll T \ll T_2 \quad (3.16)$$

If the compressible fluid governing equations are averaged using Reynolds averaging additional terms are introduced that have no analog in the laminar equations (Wilcox, 2000). For example in the continuity equation, a term is introduced that involves a multiplication of fluctuating parts of density and velocity even in the continuity equation. An approximation to the correlation of these two quantities must be introduced, further complicating the governing equations.

$$\frac{\partial \bar{\rho}}{\partial t} + \frac{\partial}{\partial x_i} (\bar{\rho} U_i + \overline{\rho' u'_i}) = 0 \quad (3.17)$$

To overcome this problem Favre proposed the introduction of a mass averaged velocity. Thus the momentum per unit volume is treated as the dependent variable rather than the velocity in the averaging process. In this case there are no longer terms involving the

fluctuating parts of density and velocity. The mass averaged velocity is represented as:

$$\hat{u}_i = \frac{1}{\bar{\rho}} \int_t^{t+T} \rho(\mathbf{x}, \tau) d\tau \quad (3.18)$$

The conservation of mass in terms of the Favre averaged variables may then be written

$$\frac{\partial \bar{\rho}}{\partial t} + \frac{\partial}{\partial x_i} (\bar{\rho} \hat{u}_i) = 0 \quad (3.19)$$

The Favre averaged Navier-Stokes equations are

$$\frac{\partial \bar{\rho}}{\partial t} + \frac{\partial}{\partial x_i} (\bar{\rho} (\hat{u}_i - u_{i,grid})) = 0 \quad (3.20)$$

$$\frac{\partial}{\partial t} (\bar{\rho} \hat{u}_i) + \frac{\partial}{\partial x_j} (\bar{\rho} \hat{u}_j (\hat{u}_i - u_{i,grid})) = -\frac{\partial P}{\partial x_i} + \frac{\partial}{\partial x_j} [\bar{\tau}_{ji} + \bar{\rho} \tau_{ji}] \quad (3.21)$$

$$\begin{aligned} \frac{\partial}{\partial t} (\bar{\rho} E) + \frac{\partial}{\partial x_j} (\bar{\rho} (\hat{u}_j - u_{j,grid}) H) &= \frac{\partial}{\partial x_j} \left[-q_{Lj} - q_{Tj} + \overline{t_{ji} u_i''} - \overline{\rho u_j'' \frac{1}{2} u_i'' u_i''} \right] + \\ &\frac{\partial}{\partial x_j} [\hat{u}_i (\bar{\tau}_{ij} + \bar{\rho} \tau_{ij})] \end{aligned} \quad (3.22)$$

$$P = \bar{\rho} R \bar{T} \quad (3.23)$$

The total energy E and total enthalpy H include the kinetic energy of the fluctuating energy field k .

$$E = \hat{e} + \frac{1}{2} \hat{u}_i \hat{u}_i + k \quad (3.24)$$

$$H = \hat{h} + \frac{1}{2} \hat{u}_i \hat{u}_i + k \quad (3.25)$$

The terms arising due to viscous stress, the viscous stress tensor $\bar{\tau}_{ji}$ is,

$$\bar{\tau}_{ij} = \mu \left(\frac{\partial \hat{u}_i}{\partial x_j} + \frac{\partial \hat{u}_j}{\partial x_i} \right) - \frac{2}{3} \mu \frac{\partial \hat{u}_k}{\partial x_k} \delta_{ij}.$$

Excluding the energy equation, the difference between the Navier-Stokes equations and the Favre Averaged Navier-Stokes equations is the Reynolds stress tensor,

$$\bar{\rho} \tau_{ij} = -\overline{\rho u_i'' u_j''}, \quad (3.26)$$

appearing in the momentum equations. Further terms appear in the energy equation, including the molecular diffusion $\overline{t_{ji} u_i''}$, the turbulent transport of turbulence kinetic energy

$\overline{\rho u_j'' \frac{1}{2} u_i'' u_i''}$ and the turbulent transport of heat q_{Tj} . These terms reflect the energy transfer that occurs from the smallest turbulent structures to heat.

3.1.3 Closure Approximations

A turbulence model is a mathematical formulation that accounts for the unknowns that arise from the averaging of the Navier-Stokes equations. The Boussinesq eddy viscosity approximation is where the Reynolds stress tensor in equation 3.26, also known as the turbulence shear stress tensor, is assumed to be the product of an eddy viscosity and the mean strain-rate tensor,

$$\bar{\rho} \tau_{ij} = 2\mu_T \left(S_{ij} - \frac{1}{3} \frac{\partial \hat{u}_k}{\partial x_k} \delta_{ij} \right) - \frac{2}{3} k \delta_{ij}, \quad (3.27)$$

where the mean strain rate tensor is defined in terms of the Favre averaged velocities.

This assumes the principal axes of the Reynolds Stress tensor are coincident with the mean strain-rate tensor at all points in the turbulent flow. The eddy-viscosity ν_T varies throughout the flow-field and must be modelled in some manner. The most widely used turbulence models use this approximation as their basis (Wilcox, 2000). Experimental evidence suggests that flow history effects on the stress tensor often persist for long distances in a turbulent flow. This raises questions as to the validity of the assumption of a linear relationship between the mean strain rate tensor and the Reynolds-stress tensor.

The molecular diffusion and transport of turbulent energy terms are commonly approximated,

$$\overline{t_{ji} u_i''} - \overline{\rho u_j'' \frac{1}{2} u_i'' u_i''} = \left(\mu + \frac{\mu_T}{\sigma_k} \right) \frac{\partial k}{\partial x_j}, \quad (3.28)$$

and the turbulent heat flux through Reynolds analogy between momentum and heat transfer, that assumes the proportionality to the mean temperature gradient,

$$q_{Tj} = \overline{\rho u_j'' h''} = - \frac{\mu_T}{Pr_T} \frac{\partial \hat{h}}{\partial x_j}. \quad (3.29)$$

Wilcox lists the applications where the approximations fail to accurately model turbulence. A number of them include:

1. flow over curved surfaces
2. flow in ducts with secondary motions
3. flow in rotating and stratified fluids
4. three-dimensional flows

5. flows with boundary-layer separation
6. transitional flows

Clearly the flow inside a turbomachinery blade passage may be characterised by all of the above applications. There are a number of alternatives to the Boussinesq approximation, however they involve models that are much more complicated both in their mathematical description and numerical solution methods.

There are a range of different turbulence models that may be applied to model turbulent flow. They may be grouped into four different categories (Wilcox, 1994):

1. Algebraic (Zero-Equation) Models
2. One-Equation Models
3. Two-Equation Models
4. Second Order Closure Models

The type of model that is applied will depend on the physics that is characteristic of and therefore important to the fluid and in general there is a correlation between the level of complexity of the model and its implementation and the complexity of the physics that will be represented in the final result. Wilcox (Wilcox, 1994) contends that an ideal model should introduce the minimum amount of complexity while capturing the essence of the relevant physics.

Examples of algebraic models include the Cebeci Smith model (Cebeci & Smith, 1974) or the Baldwin Lomax model (Baldwin & Lomax, 1978). Half equation models include the Johnson King model (Johnson & King, 1985), a development of an algebraic model to handle non-equilibrium flows. A popular one equation model is the Baldwin Barth model (Baldwin & Barth, 1991). A number of comparisons have been made with the zero and one equation models and it has been found that only a modest advantage is gained through the use of the latter.

A major problem with the implementation of Zero and One-Equation models is that a length scale must be calculated (Ekaterinaris & Menter, 1994). In general this usually involves the distance to the closest solid surface which is often ambiguous. In a general multiblock code it is further complicated by that fact that the flow-field domain is spread over a number of processors and the locating of the nearest boundaries is difficult. Wake regions must also be modelled and the locating of these pose another problem. In practical flows, more than one length scale may be important in a particular region and determining a model to determine the importance of each is overly complicated (Launder & Spalding, 1972).

The most commonly employed in aeroelasticity and oscillating airfoil simulations (Kruse *et al.*, 1997; Ayer & Verdon, 1998; Grüber & Carstens, 1998; He, 1998; Abhari & Giles, 1997; Hoehn & Fransson, 1998; Chaderjian & Guruswamy, 1992; Weber *et al.*, 1998) is the Baldwin Lomax algebraic turbulence model (Baldwin & Lomax, 1978). The justification for the use of this simple model is that many researchers believe that the best turbulence models currently available do not model turbulence sufficiently to warrant the extra computation required for their evaluation by the computational method.

Where it has been important that certain mechanisms be modelled, other turbulence models have been applied. For example, shock/boundary layer interaction has been identified as an important effect. Consequently Johnson and King's one half equation model has been applied, with correction from Johnson and Croakley (Isomura & Giles, 1998). This was chosen for its capability to model shock/boundary layer interaction in 2 dimensional calculations.

The transition from laminar flow to turbulent flow has also been identified as important in aeroelastic analysis of airfoils, especially in lower Reynolds number flows. In experiments it has been shown that transition occurs well downstream of the leading edge suction peak, and sometimes in the vicinity of the mid-chord region. Even for a relatively low Reynolds number flow of 4106, it has been found that the transition region has a major effect on the prediction of lift, moment and drag coefficients for oscillating airfoils when compared with experimental measurements (Ekaterinaris & Platzer, 1996). In this investigation, two cases were compared, one in which the transition region was set at the leading edge, the other where it was set to be at a point downstream of the maximum surface pressure gradient.

In the more basic turbulence models the transition region has to be set manually or from experiment (Baldwin Lomax for example). Reliable prediction of the transition region is well beyond the capability of the more sophisticated models; ultimately a good model would find some basis in stability analysis. Transition models are also available for steady computations, for example the e^n method. Some researches have paid a great deal of attention to the issue of turbulence modelling, with particular attention directed towards the movement of the transition region in the unsteady calculation (Isomura & Giles, 1998).

He (He, 1998) assumes Horton's laminar separation model for steady flow to set the transition region of the Baldwin Lomax model. This separation model is employed in a quasi steady manner in that it is applied at each time step. Convergence problems were encountered for the steady solution of an almost incompressible, subsonic cascade calculation. Thus the model had to be altered so that the pressure surface was fully turbulent, and on the suction surface the transition model was applied assuming a laminar boundary layer. If the turbulence model had merely been applied to both surfaces, the effect of reattachment around the separation bubble on the suction side would not have been modelled. Thus the direct application of a turbulence model does not guarantee that the effects of flow separation and reattachment will be simulated.

Turbine flows are complicated by the fact that a number of length scales may exist in particular regions. It has been found that two-equation models, also known as turbulent transport models, result in more physically accurate clearance flow simulations in turbomachinery than the algebraic models (van Zante *et al.*, 2000). There are also advantages in the implementation of two-equation models, in that there is no requirement for the explicit calculation of a length scale that is dependent on the distance from the wall. This is convenient in a multiple block formulation as the turbulent quantities may be evaluated within a computational block requiring only transfer of information at block interfaces. No computation of properties is required on a central processor. The two-equation model results in closure of the flow model governing equations without the assumption of a characteristic length scale within the flow domain and thus should provide a better flow model than the lower order models. However the increase in computational effort required in the calculation may be equivalent to that required to solve the RANS equations themselves. Thus the physical characteristic that imposes the highest level of uncertainty on the numerical model also involves a substantial portion of computation time and the implementation.

The most widely used two equation turbulence model is the k- ϵ model, first developed by Launder and Spalding (Launder & Spalding, 1972). The debate over the best of the two most common two-equation models continues and will continue into the future as these models are developed and additions are made. There have been a number of studies that show that the k- ω model is better for some configurations, such as where there are adverse pressure gradients (Henkes, 1997), yet there are others that show the k- ϵ model to be superior. However comparisons are usually made by applying them to highly simplified geometries and conditions and it is difficult to evaluate their performance under more complex configurations. The advantages of the k- ω model over the k- ϵ is that it does not require damping functions in the viscous sublayer and the equations are less stiff near the wall (Menter, 1992). A numerical model may be described as stiff where there are two different scales in the independent variable on which the dependant variables are changing. This is equivalent to a system having very different eigenvalues. The smallest time scales for the k- ω model tend to occur at solid boundaries where dissipation levels are the highest, ie. $t_{diss} \sim \frac{1}{\omega}$. However in these regions there are algebraic solutions to the turbulence quantity ω , thus rendering the k- ω model more easily integrated to the wall compared to other models such as the k- ϵ .

3.1.4 The k- ω Turbulence Model

The selection of turbulence model for a particular problem will depend on the implementation and the level of physics that are to be modelled. In general it is wise to use a model that is widely used rather than a new model that provides better results for particular cases. This is because the deficiencies of more popular models are better understood than one that has

not undergone the thorough testing of many years of use in industry and research circles.

The $k-\omega$ model was used as it was already implemented in the steady code and has been validated for a number of turbine cases. A comparison of surface pressure coefficient with experimental results provided a good correlation (Liu & Zheng, 1994; Zheng & Liu, 1995; Liu & Zheng, 1996; Liu *et al.*, 1998b). The low Reynolds number of the model has been implemented for quasi-3-dimensional calculations involving a transonic rotor and turbine cascade (Chima, 1996). The results proved adequate in comparison with experiment for surface pressure coefficient, however the spreading rate in the wake was under predicted. The spreading rate behaviour has also been observed for an annular jet and the problem has been rectified in a later version of the model (Wilcox, 2000).

The model has been used to simulate unsteady flows for various airfoils for the thin layer approximation to the Navier-Stokes equations (Ekaterinaris & Menter, 1994), the incompressible 2-dimensional Navier Stokes equations (Queutey, 1998) and the compressible Navier-Stokes equations (Ji & Liu, 1999). It has also been applied in linearised form to turbomachinery aeroelastic configurations (Holmes & Lorence, 1998), although this work dealt more with the linearisation issues rather than an evaluation of results. Smati *et al.* (Smati *et al.*, 1998) applied the $k-\omega$ model to the 7th Standard Test Configuration in a 2-dimensional code. The unsteady calculations for this case appeared to deviate from experiment and it was suggested that the definition of the geometry of the cascade was provided incorrectly in the presentation of experimental results.

The model has been compared to the $k-\epsilon$ and original $k-\omega$ for steady flow (Kim *et al.*, 2000) producing results slightly closer to experiment for the velocity profile, although the plots for surface pressure coefficient were very similar. For time accurate simulations (Ekaterinaris & Menter, 1994) it was found that it better predicted the flow for a stalled airfoil where the standard two equation models tended to suppress the separation of the boundary layer.

An important concept that manifests itself in many turbulence models is the cascade of energy from large structures to small. Turbulence may be regarded as being composed of a collection of eddies of varying sizes. If the spectrum of sizes is considered across a turbulent region, the largest may be of the order of the width of the boundary layer thickness. The size of the smallest structure is attributed to the Kolmogorov length scale.

Kolmogorov's universal equilibrium theory is based on the premise that the rate of receiving energy from the larger eddies is nearly the same as the rate at which energy is dissipated into heat. Thus the behaviour of the smallest scales only depends on the kinematic viscosity and the rate at which they receive energy from the larger scales (Wilcox, 2000). The $k-\omega$ model was first proposed by Kolmogorov in 1942 and was the first model of turbulence without the assumption of a characteristic length scale. This was formulated based on dimensional arguments and involves transport equations. Turbulence was described by

two independent variables; the kinetic energy and the characteristic frequency of the energy containing motions (Launder & Spalding, 1972). Saffman also formulated a k - ω model in 1970 without prior knowledge of Kolmogorov's work (Wilcox, 2000).

The two equation model involves k which is the kinetic energy of the turbulence and ω the dissipation per unit of turbulence kinetic energy. The process of dissipation occurs in the smallest eddies, the rate of dissipation is the rate of transfer of turbulence kinetic energy to the smallest eddies.

The Wilcox 1988 (Wilcox, 1988) model is implemented in the present code, with changes to the inlet boundary condition as proposed by Menter to reduce the dependence of the solution on inlet levels (Menter, 1992).

Wilcox (Wilcox, 2000) also introduces additions to the model that are intended to remove the dependence on free-stream values and improve the performance of the model for other configurations. This includes a cross diffusion term which requires a matrix multiplication of the mean-rotation and mean strain rate tensors which requires a reasonable level of computational effort. However due to the independence in cases tested using Menter's boundary conditions, this was not implemented due to the extra computational work it added to the solution process.

There are five main sets of equations involved in the model.

The eddy viscosity is given

$$\mu_T = \frac{\rho k}{\omega} \quad (3.30)$$

Turbulence kinetic energy

$$\frac{\partial}{\partial t}(\bar{\rho}k) + \frac{\partial}{\partial x_j}(\bar{\rho}(\hat{u}_j - u_{grid})k) = \tau_{ij} \frac{\partial \hat{u}_i}{\partial x_j} - \beta^* \rho k \omega + \frac{\partial}{\partial x_j} \left[(\mu + \sigma^* \mu_T) \frac{\partial k}{\partial x_j} \right] \quad (3.31)$$

Specific dissipation rate

$$\frac{\partial}{\partial t}(\bar{\rho}\omega) + \frac{\partial}{\partial x_j}(\bar{\rho}(\hat{u}_j - u_{grid})\omega) = \alpha \frac{\omega}{k} \tau_{ij} \frac{\partial \hat{u}_i}{\partial x_j} - \beta \rho \omega^2 + \frac{\partial}{\partial x_j} \left[(\mu + \sigma \mu_T) \frac{\partial \omega}{\partial x_j} \right] \quad (3.32)$$

Closure coefficients

$$\alpha = 5/9, \quad \beta = 3/40, \quad \beta^* = 9/100, \quad \sigma = 1/2, \quad \sigma^* = 1/2 \quad (3.33)$$

Auxiliary relations

$$\varepsilon = \beta^* \omega k \quad l = k^{1/2}/w \quad (3.34)$$

3.2 Structural Model

3.2.1 The Equations Governing the Structural Model

Structural dynamics primarily involves three different characteristics, namely mass, damping and elasticity. The dynamic nature of the problem is due to a constant force (in the case of transient analysis), or time varying force. In the case of an aeroelastic problem, the fluctuating pressure exerts time varying distributed loads on the structure.

The equations governing the structure are in general non-linear. There are many different forms of the governing equations used in the analysis of structures in turbomachinery. However for problems involving aeroelasticity, the nonlinear effects are usually ignored due to the complications they add to the solution process and the fact that their influence is regarded as insignificant.

The complete equation of motion governing a structure may be written

$$\mathbf{M}\ddot{h} + \mathbf{C}(\ddot{h}, \dot{h}, h, \Omega)\dot{h} + \mathbf{K}(h, \Omega)h = \mathbf{P}(\dot{h}, h, t) \quad (3.35)$$

Where \mathbf{C} is a function of acceleration, velocity and displacement and rotor angular frequency and \mathbf{K} is a function of displacement and rotor angular frequency.

If it is assumed that the damping matrix is linear, but the stiffness matrix is nonlinear, it may also take the form (Srivastava & Reddy, 1995)

$$\mathbf{M}\ddot{h} + \mathbf{C}\dot{h} + (\mathbf{K}_s + \mathbf{K}(h))h = \mathbf{P}(\dot{h}, h, t) \quad (3.36)$$

where \mathbf{K}_s is the centrifugal softening matrix due to the rotation of the rotor.

Whilst the structural part of the aeroelastic problem may be more accurately modelled compared to the fluid field, the linear equation above does not allow for non-linear characteristics such as frictional damping at the blade roots, shroud interfaces and large deformations under high centrifugal loading (Vahdati & Imregun, 1996). Non-linear interaction may also occur between shroud and blade tip (Marshall & Imregun, 1996a). This displacement-dependent dry friction damping may be an effective means of flutter suppression in turbine and fan blade applications. However the non-linear assumption greatly increases the complexity and time required to compute the structural solution, and is therefore currently avoided by the majority of aeroelastic analyses.

3.2.2 Modal Equations of Motion

Modal analysis is implemented by assuming that the nodal displacements may be represented by a finite sum of modes, with each mode being approximated as complex and harmonic (Zienkiewicz & Taylor, 1991):

$$\mathbf{h} = \Phi e^{\omega t} = \sum_{i=1}^n \Phi_i e^{\omega_i t} \quad (3.37)$$

where ω_i are the eigenvalues, Φ_i are the corresponding eigenvectors and subscript i denotes the mode number. For forced response, it may be assumed that the solution is a linear combination of modes:

$$\mathbf{h} = \sum \Phi_i q_i = [\Phi_1, \Phi_2, \dots] \mathbf{q} \quad (3.38)$$

This may be substituted into the dynamic equation.

$$m_i \ddot{q}_i + c_i \dot{q}_i + k_i q_i = Q_i \quad (3.39)$$

If the modes are normalised with respect to the mass matrix, then

$$\begin{aligned} m_i &= \Phi_i^T \mathbf{M} \Phi_i = 1 \\ c_i &= \Phi_i^T \mathbf{C} \Phi_i \\ k_i &= \Phi_i^T \mathbf{K} \Phi_i \\ Q_i &= \Phi_i^T \mathbf{P} \end{aligned}$$

and

$$\Phi_i^T \mathbf{M} \Phi_j = \Phi_i^T \mathbf{C} \Phi_j = \Phi_i^T \mathbf{K} \Phi_j = 0 \quad \text{when } i \neq j$$

Thus the modes are orthogonal, or decoupled. In general the damping matrix is not diagonal, however it may be assumed that the damping matrix may be formed from a linear combination of mass and stiffness matrices.

The eigenvalues of equation 3.39 may be found by considering the solution of free undamped response.

$$(-\omega^2 \mathbf{M} + \mathbf{K}) \Phi = 0$$

therefore

$$\omega_i^2 \mathbf{M} \bar{a}_i = \mathbf{K} \bar{a}_i$$

Premultiplying by Φ_i^T

$$\omega_i^2 m_i = k_i$$

The damping may be related to its critical value for each mode through

$$c_i = 2\omega_i \zeta_i.$$

The solution may be found for each corresponding eigenvalue, to create a vector of modal displacements that may be transformed back to actual displacements using the transformation equation 3.37.

Where complete assemblies are analysed, the efficiency of the code is critical and often assumptions are made in the structural model. In some cases, the damping of the structure may be considered negligible compared to the damping provided by the aerodynamics and may therefore be neglected (Sayma *et al.*, 1998).

With the normalisation of modes with the mass matrix, the modal equation of motion becomes

$$\ddot{q}_i + 2\zeta_i \omega_i \dot{q}_i + \omega_i^2 q_i = Q_i \quad (3.40)$$

Chapter 4

Computational Implementation

The discretisation refers to the method by which the mathematical formulation is represented on a computer and this will be presented in the following section. Whilst the mathematical formulation assumes a continuum, memory limits and storage methods in the computer require that the flow field or structural field be represented by discrete quantities in space. The state of the continuum may be determined by applying the governing equations in discretised form to the discretised continuum. There are a range of discretisations and numerical methods of applying the model governing equations. The present approach is a cell centred finite volume method on a structured mesh for the fluid and a modal lumped mass representation of the structure.

4.1 Fluid Model Discretisation

In the present analysis the domain of interest is finite in size. The discretisation results in a network of nodes otherwise known as a grid or mesh. Through a solution method the fluid conditions are calculated at the points on the mesh. There are a number of solution methods available for the equations governing the fluid. A good method is one which produces a solution in a time efficient manner and reproduces as accurately as possible the physical characteristics of real fluid phenomena.

As stated in Chapter 3, the simulation of flows is restricted by the size and speed of the available computer hardware and the finite amount of time available to researchers. Over the years solution methods in CFD have been developed and researchers have improved algorithms to produce solutions in a more time efficient manner. Debate remains as to the most appropriate algorithm for CFD and often this is dependant on the type of geometry and flow regime. In the present approach, Jameson type schemes are used. It involves a number of different algorithms that have been previously developed and optimised into an effective method that produces well resolved solutions efficiently.

A survey of numerical solution methods applied by authors in the 1997 International

Symposium of Unsteady Aerodynamics and Aeroelasticity of Turbomachinery (Fransson, 1998) shows that just over half employ Jameson type Runge-Kutta schemes, the rest using implicit time integration methods. The fact that the Jameson type scheme is the most popular scheme does not lead to the conclusion that it is the best method for modelling unsteady aerodynamics in turbomachinery, however it does provide support for its use. Usually implicit methods are coupled with upwind discretisations of the convective terms, whilst central differences or finite volume methods coupled with artificial dissipation are used for the Runge-Kutta schemes.

A range of problems are introduced by the discretisation of a continuum, particularly in high subsonic and transonic flow. This is due to the presence of flow phenomena that may be described as discontinuous. These pose a problem to a discrete representation as the highest resolution that may be achieved is limited by mesh density. The lack of resolution leads to instabilities in the numerical methods and may result in the divergence of the approximation from the physical flow. Many approaches have been proposed to solve the problems due to discretisation of the model gas dynamics equations (for example (Liou & Steffen, 1993)), however it is believed that the present approach provides comparable resolution and numerical efficiency. The other more sophisticated approaches such as Riemann solvers (Toro, 1997) may be warranted where flow conditions are particularly extreme, however none of the cases presently considered involve this type of phenomena.

4.1.1 Spatial Discretisation of Navier-Stokes Equations

The discretisation in space refers to the way in which spatial derivatives in the governing equations are approximated. There are three major methods of discretisation of the fluid field. The finite element method is where approximating functions are used to represent the variation of physical quantities through a finite element. Most implementations involve an unstructured grid that employ pointers to map the computational domain. If the governing equations are represented by the finite difference method, a generalised coordinate transformation is required to apply the governing equations to complex geometries. In the present approach the finite volume method is used for the spatial discretisation of the fluid governing equations. This has a number of advantages over finite difference or finite element methods. It has good conservation properties. It allows complicated computational domains to be discretised in a simpler way than the aforementioned methods (Fletcher, 1991).

The finite volume method exploits the divergence theorem of Gauss to reduce the spatial derivative terms of the volume integral form of the governing equations to surface integrals. This theorem can be considered as defining the average gradient of a scalar as a function of its values at the boundaries of the volume under consideration (Hirsch, 1992a).

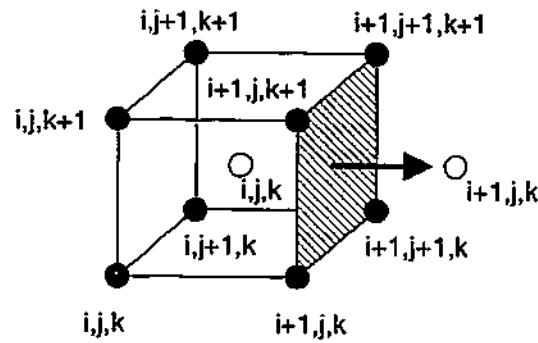


Figure 4.1: Discretisation in computational space.

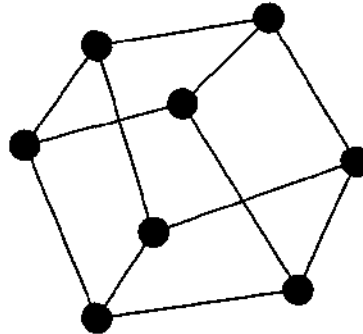


Figure 4.2: Geometry of a typical computational cell.

$$\int_V \left(\frac{\partial u_i}{\partial x_i} \right) dV = \oint_S u_i dS. \quad (4.1)$$

The calculation of the volume integral reduces to a summation of the momentum fluxes through the volume's surface.

$$\oint_S u_i dS = \sum_{sides} u_i S \quad (4.2)$$

The fluid governing equations may be rewritten in a flux formulation

$$\frac{d}{dt} (V_{ijk} w_{ijk}) + Q_{c,ijk} - Q_{\mu,ijk} = 0, \quad (4.3)$$

where $Q_{c,ijk}$ and $Q_{\mu,ijk}$ are the summations of the convective and viscous fluxes respectively. The fluxes are decomposed into convective and viscous terms as they considered separately in the time integration method.

$$Q_{c,ijk} = \sum_{k=1}^6 (f_c dS_x + g_c dS_y + h_c dS_z) \quad (4.4)$$

$$Q_{\mu,ijk} = \sum_{k=1}^6 (f_v dS_x + g_v dS_y + h_v dS_z) \quad (4.5)$$

The flow, convective and viscous vectors in Cartesian coordinates implemented in the code are,

$$\begin{aligned}
 \mathbf{w} &= \begin{pmatrix} \bar{\rho} \\ \bar{\rho}\hat{u} \\ \bar{\rho}\hat{v} \\ \bar{\rho}\hat{w} \\ \bar{\rho}E \end{pmatrix}, \quad \mathbf{f}_c = \begin{pmatrix} \bar{\rho}(\hat{u} - u_{\text{grid}}) \\ \bar{\rho}\hat{u}(\hat{u} - u_{\text{grid}}) + P \\ \bar{\rho}\hat{v}(\hat{u} - u_{\text{grid}}) \\ \bar{\rho}\hat{w}(\hat{u} - u_{\text{grid}}) \\ \bar{\rho}E(\hat{u} - u_{\text{grid}}) + P\hat{u} \end{pmatrix}, \\
 \mathbf{g}_c &= \begin{pmatrix} \bar{\rho}(\hat{v} - v_{\text{grid}}) \\ \bar{\rho}\hat{u}(\hat{v} - v_{\text{grid}}) \\ \bar{\rho}\hat{v}(\hat{v} - v_{\text{grid}}) + P \\ \bar{\rho}\hat{w}(\hat{v} - v_{\text{grid}}) \\ \bar{\rho}E(\hat{v} - v_{\text{grid}}) + P\hat{v} \end{pmatrix}, \quad \mathbf{h}_c = \begin{pmatrix} \bar{\rho}(\hat{w} - w_{\text{grid}}) \\ \bar{\rho}\hat{u}(\hat{w} - w_{\text{grid}}) \\ \bar{\rho}\hat{v}(\hat{w} - w_{\text{grid}}) \\ \bar{\rho}\hat{w}(\hat{w} - w_{\text{grid}}) + P \\ \bar{\rho}E(\hat{w} - w_{\text{grid}}) + P\hat{w} \end{pmatrix}, \\
 \mathbf{f}_\mu &= \begin{pmatrix} 0 \\ \hat{\tau}_{xx} \\ \hat{\tau}_{yx} \\ \hat{\tau}_{zx} \\ \hat{u}\hat{\tau}_{xx} + \hat{v}\hat{\tau}_{yx} + \hat{w}\hat{\tau}_{zx} + (\mu + \sigma^*\mu_T)\frac{\partial k}{\partial x} - q_x \end{pmatrix}, \quad (4.6) \\
 \mathbf{g}_\mu &= \begin{pmatrix} 0 \\ \hat{\tau}_{xy} \\ \hat{\tau}_{yy} \\ \hat{\tau}_{zy} \\ \hat{u}\hat{\tau}_{xy} + \hat{v}\hat{\tau}_{yy} + \hat{w}\hat{\tau}_{zy} + (\mu + \sigma^*\mu_T)\frac{\partial k}{\partial y} - q_y \end{pmatrix}, \\
 \mathbf{h}_\mu &= \begin{pmatrix} 0 \\ \hat{\tau}_{xz} \\ \hat{\tau}_{yz} \\ \hat{\tau}_{zz} \\ \hat{u}\hat{\tau}_{xz} + \hat{v}\hat{\tau}_{yz} + \hat{w}\hat{\tau}_{zz} + (\mu + \sigma^*\mu_T)\frac{\partial k}{\partial z} - q_z \end{pmatrix}.
 \end{aligned}$$

The total shear stress tensor which includes the turbulent stress tensor and viscous shear tensor is,

$$\hat{\tau}_{ij} = 2\mu \left(S_{ij} - \frac{1}{3} \frac{\partial \hat{u}_k}{\partial x_k} \delta_{ij} \right) + \tau_{ij}$$

and the heat flux vector,

$$q_j = - \left(\frac{\mu}{Pr_L} + \frac{\mu_T}{Pr_T} \right) \frac{\partial \hat{h}}{\partial x_j}.$$

Note that other variables are defined in Chapter 3.

Fluxes are calculated by averaging the cell centred values to the cell face and multiplying by the corresponding area vector. For example, the flux through the face in the positive i direction in computational space is shown in Figure 4.1. Mesh points are represented by filled spheres, whilst the cell centred flow variables are represented by empty spheres. The average of the two cell centred values is used to approximate the flux through the shaded face. The geometry of a typical cell of the discretised fluid field is shown in Figure 4.2. For a moving mesh, the extra flux due to the velocity of the cell face must also be accounted for in the calculation. The flux through common faces of cells need not be calculated twice, but may be added to one and subtracted from the other. This results in a compact implementation in the calculation of the viscous fluxes.

The coordinates of the cell centred values do not appear explicitly in the discretisation, nor in the implementation. Thus the variable is not necessarily attached to a fixed point within the cell volume and may be considered the average value of the variable over the entire cell volume (Hirsch, 1992a).

The viscous stress tensor is calculated through a dual application of the divergence theorem. Firstly the velocity and heat gradients are calculated at the cell vertices. This involves calculating the flux through the centre of the cells by multiplying the cell centred values by an average of the area vectors on either side of the cell. These fluxes are averaged to the cell face and then a summation is performed to calculate the gradients at the cell vertex.

Once the gradients have been calculated at the cell vertices, the second derivatives of the stress tensor may be calculated by another application of the Gauss formula. The gradient tensor is averaged to the cell faces, then multiplied by the corresponding area vector. The fluxes are summed over the cell volume resulting in the calculation of the viscous stress tensor at the cell centre (Liu, 1991).

4.1.2 Spatial Discretisation of k - ω Equations

The turbulence model equations closely resemble the Navier-Stokes equations, in that they involve first and second order spatial derivatives. Therefore a similar algorithm is used to solve the k - ω equations in a strongly coupled manner with the Navier-Stokes solver (Liu &

Zheng, 1994). It has proven to be an efficient and effective method for solving steady flow in turbine cascade passages (Liu & Zheng, 1994; Zheng & Liu, 1995; Liu & Zheng, 1996).

The method involves the serial evaluation of the eddy viscosity within the five stage solution scheme of the Navier-Stokes equations. A five stage Runge-Kutta scheme is also used for the solution of the turbulence equations. The turbulence variables of k and ω are also located at cell centres. This is different to the previous implementations (Liu & Zheng, 1994) due to stability issues with certain turbine cases and also a simplification of inter-block communication. With a cell vertex scheme, the cells at block interfaces must be averaged in some manner, increasing communication overhead and storage. Previously it was believed that a staggered implementation was more stable than a cell centred scheme, however the present implementation has been tested by other authors and is sufficiently stable (Yao *et al.*, 2000).

4.1.3 Time Discretisation

There are a range of methods for the accurate integration of time dependant problems. The method of lines (Fletcher, 1991) is used to reduce a partial differential equation from a non-linear partial differential equation to an ordinary differential equation, otherwise known as semi-discrete form.

$$\frac{dw}{dt} + R(w) = 0 \quad (4.7)$$

Since the equations are non-linear, they must be solved through an iterative technique. In general iterative techniques may be divided into implicit and explicit methods.

A major consideration in the solution of ordinary differential equations is stability, as it determines the rate of convergence of the iterative method and hence the solution time. Implicit methods usually have no stability limit however they require a large matrix inversion, or at the very least the solution of a tridiagonal system. For the multidimensional problem the matrix inversion may be avoided by splitting the problem into a number of 1-dimensional problems and solving in a number of steps. The alternating direction implicit method is an example which may be used for the solution of 3-dimensional systems of equations, requiring 3 steps per integration iteration. Explicit methods are restricted by stability and often require a prohibitive number of iterations for convergence.

A dual time stepping scheme (Jameson, 1991) is used to calculate the unsteady flow problem. This involves a steady state solver modified to compute a solution in a time accurate manner. Within a real time-step, the scheme is explicit and all the methods of convergence acceleration for steady state solutions may be employed. The time accuracy is gained through the inclusion of an unsteady source term. The method has shown to be effective for external flow simulations involving flow past an airfoil (Alonso & Jameson, 1994; Alonso, 1997;

Jameson, 1991), flows past wings (Liu *et al.*, 2000), and in turbomachinery simulations (Ji & Liu, 1999; Sadeghi & Liu, 2001a).

Following the Jameson and Alonso (Jameson, 1991; Alonso, 1997), the time derivative can be written as an operator,

$$D_t(\mathbf{w}^{(n+1)}V^{(n+1)}) + R(\mathbf{w}^{(n+1)}) = 0, \quad (4.8)$$

where D_t is a backward difference operator to order k . A second order backwards difference operator is

$$D_t(\mathbf{w}^{(n+1)}V^{(n+1)}) = \frac{3}{2\Delta t}\mathbf{w}^{(n+1)}V^{(n+1)} - \frac{2}{\Delta t}\mathbf{w}^{(n)}V^{(n)} + \frac{1}{2\Delta t}\mathbf{w}^{(n-1)}V^{(n-1)}. \quad (4.9)$$

Equation (4.8) can be discretised using this operator and rewritten in terms of source terms and residual,

$$\frac{3}{2\Delta t}\mathbf{w}^{(n+1)}V^{(n+1)} + \frac{E}{\Delta t} + R(\mathbf{w}^{(n+1)}) = 0, \quad (4.10)$$

where the source terms E ,

$$E = -2\mathbf{w}^{(n)}V^{(n)} + \frac{1}{2}\mathbf{w}^{(n-1)}V^{(n-1)}. \quad (4.11)$$

The implicit equations may be cast into a modified steady state form

$$\frac{\partial \mathbf{w}^{(n+1)}}{\partial t^*} + R^*(\mathbf{w}^{(n+1)}) = 0, \quad (4.12)$$

where the residual contains the source terms arising from the time discretisation and a steady state residual,

$$R^*(\mathbf{w}^{(n+1)}) = \frac{3}{2\Delta t}\mathbf{w}^{(n+1)} + \frac{1}{V^{(n+1)}} \left(\frac{E}{\Delta t} + R(\mathbf{w}^{(n+1)}) \right). \quad (4.13)$$

This equation may be marched in time explicitly, however this can lead to numerical instability if the ratio of quasi time step to real time step $\lambda = \frac{3\Delta t^*}{2\Delta t}$ becomes too small. This may be overcome by treating the time derivative implicitly,

$$(1 + \lambda)(\mathbf{w}^{(l+1)} - \mathbf{w}^{(l)}) + \Delta t^* R^*(\mathbf{w}^{(l)}) = 0. \quad (4.14)$$

Within each Runge-Kutta stage, the term $\mathbf{w}^{(l)}$ is the solution from the previous stage so that the scheme is implicit within a complete Runge-Kutta integration step.

The k - ω equations are discretised in time in a similar manner,

$$\frac{\partial \mathbf{k}^{(n+1)}}{\partial t^*} + R^*(\mathbf{k}^{(n+1)}) = 0, \quad (4.15)$$

however there are further implicit terms must also be included. These are discussed in Section 4.1.5 and relate to the stiffness of the k - ω model. For the k equation,

$$R^*(\rho k^{(n+1)}) = \frac{3\rho k^{(n+1)}}{2\Delta t + \Delta t^*(\alpha\Delta^+ + \beta^*\omega)} + \frac{1}{V^{(n+1)}} \left(-\frac{2}{\Delta t} \rho k^n + \frac{1}{2\Delta t} \rho k^{n-1} + R(\rho k^{(n+1)}) \right), \quad (4.16)$$

and the ω equation,

$$R^*(\rho\omega^{(n+1)}) = \frac{3\rho\omega^{(n+1)}}{2\Delta t + \Delta t^*(\alpha\Delta^+ + 2\beta^*\omega)} + \frac{1}{V^{(n+1)}} \left(-\frac{2}{\Delta t} \rho\omega^n + \frac{1}{2\Delta t} \rho\omega^{n-1} + R(\rho\omega^{(n+1)}) \right). \quad (4.17)$$

4.1.4 Time Stepping Scheme for Navier-Stokes Equations

Within the time accurate flow solver, a steady state solver is used to march the flow field in quasi-time. This solver involves a number of convergence acceleration techniques that allow the use of higher Courant numbers, thus increasing numerical efficiency and reducing solution time.

The Runge-Kutta scheme has been developed into an efficient method to solve the steady Euler equations (Jameson *et al.*, 1981). To take full advantage of a multigrid method the scheme should be effective in damping high frequency modes. A five stage scheme was found to be one of the most effective, as it allows the addition of the dissipative terms at alternate Runge Kutta stages to improve the high frequency damping properties and extend the stability region (Jameson & Schmidt, 1985). In effect, the scheme is tailored so that different schemes are selected for the convective terms that tend to be hyperbolic and the dissipative terms that are parabolic in nature. This scheme is implemented in the present method and has proven effective for the solution of the gas dynamic equations in different applications (Hirsch, 1992a).

The Courant Fredrich Lewy condition is the time step limit that is a result of the explicit time discretisation. This limits the rate at which the iterative method reaches a converged solution. In general, the lower this number, the more cycles required thus the longer the time period required for the computational method to obtain a solution. The Courant number of this scheme is $2\sqrt{2}$. This is higher than for other methods such as Leapfrog or MacCormack

schemes. Note that the present method differs from the traditional Runge-Kutta method in that the evaluations of intermediate stages are not stored separately. This is intended to conserve computer memory and still proves effective as the order of accuracy is not important, the requirement being that a steady state solution is obtained as quickly as possible.

Consider the semi-discrete form of the fluid governing equations

$$\frac{d\mathbf{w}}{dt} + R(\mathbf{w}) = 0, \quad (4.18)$$

where $R(\mathbf{w})$ is the residual

$$R(\mathbf{w}) = \frac{1}{V} \left(Q(\mathbf{w}^{(k)}) + \beta_k D(\mathbf{w}^{(k)}) + (1 - \beta_k) D(\mathbf{w}^{(k-1)}) \right). \quad (4.19)$$

and $Q(\mathbf{w}^{(k)})$ are the convective terms and $D(\mathbf{w}^{(k)})$ and $D(\mathbf{w}^{(k-1)})$ are dissipative terms.

Given that \mathbf{w}^n is the value of \mathbf{w} after n time steps, the general m stage scheme to advance to a time Δt^* is,

$$\begin{aligned} \mathbf{w}^{(0)} &= \mathbf{w}^{(l)} \\ (1 + \alpha_k \lambda) \mathbf{w}^{(k)} &= \mathbf{w}^{(0)} + \alpha_k \lambda \mathbf{w}^{(k-1)} - \alpha_k \Delta t^* R^*(\mathbf{w}^{(k-1)}) \\ \mathbf{w}^{(l+1)} &= \mathbf{w}^{(m)}, \end{aligned} \quad (4.20)$$

where the implicit terms due to the time accurate discretisation appear on the left hand side and the term $R^*(\mathbf{w}^{(k-1)})$ is the modified residual that includes the unsteady source terms. Note that the Runge-Kutta scheme is reformulated in Section 4.1.6 for the multigrid solver.

Local time steps are used, whereby the time step for each cell is calculated based on the Courant number of the each cell. At the expense of time accuracy, the solution rate of convergence is increased. The local time step is calculated through an approximation to the wave speed that accounts for hyperbolic convective terms (Liu, 1991).

$$\Delta t^* = \frac{\text{CFL} \cdot V}{(\Lambda_\xi + \Lambda_\eta + \Lambda_\zeta) + 2 \frac{\mu}{\rho V} (S_\xi^2 + S_\eta^2 + S_\zeta^2)} \quad (4.21)$$

The parabolic or viscous terms are also accounted for by the second term in the denominator. To aid stability, a pressure sensor is used to detect the presence of shock waves. In these regions the time step is reduced (Alonso, 1997).

$$\overline{\Delta t^*} = \frac{2\Delta t^*}{V_{i,j,k} + \mu_{i,j,k} + \kappa_{i,j,k}} \quad (4.22)$$

The pressure sensor is a normalised second difference of pressure in each coordinate direction,

$$v_{i,j,k} = \frac{p_{i+1,j,k} - 2p_{i,j,k} + p_{i-1,j,k}}{p_{i+1,j,k} + 2p_{i,j,k} + p_{i-1,j,k}},$$

$$\mu_{i,j,k} = \frac{p_{i,j+1,k} - 2p_{i,j,k} + p_{i,j-1,k}}{p_{i,j+1,k} + 2p_{i,j,k} + p_{i,j-1,k}},$$

$$\kappa_{i,j,k} = \frac{p_{i,j,k+1} - 2p_{i,j,k} + p_{i,j,k-1}}{p_{i,j,k+1} + 2p_{i,j,k} + p_{i,j,k-1}}.$$

4.1.5 Time Stepping Scheme for k- ω Equations

The major difference between the time stepping scheme for the Navier-Stokes equations and the turbulence model equations is the implicit treatment of the negative source terms.

The semi-discrete form of the k- ω equations is written

$$\frac{\partial}{\partial t}(\rho k) + R_k(\rho k, \rho \omega) = 0 \quad (4.23)$$

$$\frac{\partial}{\partial t}(\rho \omega) + R_\omega(\rho k, \rho \omega) = 0 \quad (4.24)$$

where R_k and R_ω are the residuals for k and ω respectively. The terms in the turbulence model equations may be collected into convective, dissipative and source terms (Liu & Zheng, 1994).

$$R_k(\rho k, \rho \omega) = \frac{1}{V}(C_k - D_k) - S_k \quad (4.25)$$

$$R_\omega(\rho k, \rho \omega) = \frac{1}{V}(C_\omega - D_\omega) - S_\omega \quad (4.26)$$

The convective and dissipative terms are integrated explicitly, however unlike the Navier-Stokes equations the dissipative terms are calculated at every Runge-Kutta stage in the 5 stage scheme. It has been found that in practical implementations of the k- ϵ that the negative source terms lead to large negative eigenvalues and hence a stiff system of equations and slow convergence. These terms include the Favre averaged Reynolds-stress tensor and dissipation terms. The effect of the time step restriction imposed by the negative source terms may be lessened by treating these terms implicitly within the Runge Kutta solution method. The source terms of equations 4.25 and 4.26 may be expanded

$$S_k = \mu_t P_d - \frac{2}{3}(\nabla \cdot \mathbf{u})(\rho k) - \frac{\beta^*}{\rho}(\rho \omega)(\rho k) \quad (4.27)$$

$$S_\omega = \alpha\alpha^* \rho P_d - \alpha \frac{2}{3} (\nabla \cdot \mathbf{u}) (\rho\omega) - \frac{\beta}{\rho} (\rho\omega)^2 \quad (4.28)$$

where

$$P_d = \frac{1}{2} (\epsilon_{11}^2 + \epsilon_{22}^2 + \epsilon_{33}^2) + \epsilon_{12}^2 + \epsilon_{13}^2 + \epsilon_{23}^2$$

$$\epsilon_{ij} = 2 \left(S_{ij} - \frac{1}{3} \frac{\partial u_k}{\partial x_k} \delta_{ij} \right)$$

The major production terms of equation 4.27 and 4.28 $\mu_t P_d$ and $\alpha\alpha^* \rho P_d$ are always positive. The dilation of pressure term $(\nabla \cdot \mathbf{u})$ may be positive or negative, depending on whether the flow is locally undergoing compression or expansion. This term is treated implicitly if it is negative and explicitly if positive by defining the following.

$$\Delta^+ = \max \left(0, \frac{2}{3} \nabla \cdot \mathbf{u} \right) \quad (4.29)$$

The time discretisation may now be formulated

$$[1 + \Delta t \Delta^+] [(\rho k)^{n+1} - (\rho k)^n] + \Delta t \frac{\beta^*}{\rho} [(\rho k)^{n+1} (\rho\omega)^{n+1} - (\rho k)^n (\rho\omega)^n] = -R_k^n \Delta t \quad (4.30)$$

$$[1 + \Delta t \alpha \Delta^+] [(\rho\omega)^{n+1} - (\rho\omega)^n] + \Delta t \frac{\beta^*}{\rho} [(\rho\omega)^{n+1} (\rho\omega)^{n+1} - (\rho\omega)^n (\rho\omega)^n] = -R_\omega^n \Delta t \quad (4.31)$$

The time discretisation is not time accurate, but is consistent. Time accuracy is not important in the steady state solver and only the steady solution is required within each real time step in time accurate simulations. Equation (4.30) is a nonlinear algebraic equation in terms of the new values $(\rho k)^{n+1}$ and $(\rho\omega)^{n+1}$. They may be solved using the quadratic root formula, but in this case the equations are linearised instead.

Define

$$\delta(\rho k)^n = (\rho k)^{n+1} - (\rho k)^n \quad (4.32)$$

$$\delta(\rho\omega)^n = (\rho\omega)^{n+1} - (\rho\omega)^n \quad (4.33)$$

then

$$\delta(\rho\omega)^n = \Delta t \frac{-R_\omega^n}{1 + \Delta t(\alpha\Delta^+ + 2\beta\omega^n)} \quad (4.34)$$

$$\delta(\rho k)^n = \Delta t \frac{-R_k^n}{1 + \Delta t(\alpha\Delta^+ + \beta^*\omega^n)} \quad (4.35)$$

4.1.6 Multigrid

The explicit scheme is subject to a time step constraint. One method of accelerating convergence is through the use of multiple grids. Initially this method was applied to the equations for potential flow. Subsequently they were used successfully in the solution of the Euler equations (Jameson, 1983).

The multigrid method involves the solution of the problem on an increasingly coarse grid. Multigrid increases the rate of convergence in a number of ways. Its application removes the low frequency spatial errors from the solution domain. The time stepping scheme is relatively efficient at removing high frequency spatial errors. When the solution is interpolated to a coarser grid, low frequency errors on the fine grid become high frequency errors on the coarse grid. Thus the application of the time stepping scheme to coarser grids removes these low frequency errors. For explicit methods, the speed at which disturbances may propagate through the flow-field is limited by the number of cells in any particular coordinate direction for a finite discretisation stencil. This speed of propagation may be accelerated through the use of coarser grids with smaller numbers of cells in each direction of the computational domain. Coarser grids also involve larger cells and given that the time step is governed by the Courant condition, larger local time steps may be used.

The coarser grids are generated by removing every second grid point, effectively doubling the mesh spacing. Flow variables are transferred to a coarser mesh by weighting each cell by its volume

$$\mathbf{w}_{2h}^{(0)} = \sum \frac{V_h \mathbf{w}_h}{V_{2h}}, \quad (4.36)$$

where the sum is over the eight cells of the finer grid within the single cell of the coarse grid. This conserves energy, momentum and mass.

A forcing function is defined

$$P_{2h} = \sum R_h(\mathbf{w}_h) - R_{2h}(\mathbf{w}_{2h}^{(0)}). \quad (4.37)$$

The Runge-Kutta scheme is formulated,

$$\mathbf{w}_{2h}^{(0)} = \mathbf{w}_{2h}^{(l)}$$

$$\begin{aligned} (1 + \alpha_k \lambda) w_{2h}^{(k)} &= w_{2h}^{(0)} + \alpha_k \lambda w_{2h}^{(k-1)} - \alpha_k \Delta t^* (R^*(w_{2h}^{(k-1)}) + P_{2h}) \\ w_{2h}^{(l+1)} &= w_{2h}^{(m)} \end{aligned} \quad (4.38)$$

Note that in the first Runge-Kutta step the addition of the forcing term P_{2h} cancels out the residual for the first stage. Thus the evolution of the coarse grid solution is driven by the fine grid residual. This process is performed on successively coarse grids. Once the coarsest grid is reached, the solution is interpolated back through the array of grids to the finest grid us trilinear interpolation. During this process of interpolation, no further application of the governing equations or time stepping scheme is performed. On the coarser grids, because the unsteady source terms are constant throughout a Runge-Kutta stage, they need not be added to the residual. This is due to the fact that they will be cancelled out by the second term in the forcing term P_h .

There are a number of different multigrid strategies. Two common ones are known as V and W cycle. The V-cycle is where each increasingly coarse grid is calculated for, then the solutions interpolated back to the finest grid. In a W-cycle, the finest grid solution is only calculated every second cycle through the grids. The W-cycle has proven more effective with regards to its convergence rate compared to the V-cycle for practical flows (Liu, 1991; Alonso, 1997). This is due to the fact that more iterations on the coarser grid appears to increase rates of convergence.

A similar algorithm is used for the k- ω solver.

4.1.7 Artificial Dissipation

In the solution of the Euler equations in the transonic and supersonic flow regimes, it is necessary to implement a discretisation that removes nonphysical oscillations from the flow domain. These oscillations lead to instability in the numerical method and stem from a number of sources including odd even decoupling due to the finite volume discretisation and oscillations in the region of large gradients found at stagnation points and in the region of shock waves. A number of solutions have been proposed including the addition of artificial viscosity in the form of second and fourth order terms (Jameson *et al.*, 1981), approximate Riemann solvers and other flux splitting schemes. The performance of these schemes is often problem dependant; where later developments perform better for some cases, the earlier schemes are more appropriate for others. Of major importance is that the scheme adds sufficient dissipation without adversely affecting the final solution.

The evaluation of the artificial viscosity at each time step adds to the overall computation time. Jameson proposed that this be frozen through the Runge Kutta scheme, however after experimentation an effective combination of Runge Kutta coefficients was chosen and the dissipation was calculated at alternate steps through the 5 step scheme. This resulted in a

robust scheme that minimised the appearance of high frequency errors in the steady state solution (Jameson & Schmidt, 1985).

There are a number of smoothing schemes implemented in the code, however only two have been applied herein. The first is the addition of artificial viscosity through the addition of second and fourth order terms to the governing equations and is referred to as a JST scheme after the original authors (Jameson *et al.*, 1981). The second involves adding artificial viscosity through a scheme that becomes upwind in supersonic regions through a flux limiter and is known as convective upwind split pressure or CUSP (Jameson, 1995a; Jameson, 1995b) scheme.

Extensive research has been undertaken into the mathematical formulation of non-oscillatory discretisation schemes (Jameson, 1995a). The applicability of the schemes is highly dependant on the flow configuration (Private communication, Liu). It has been shown that scalar dissipation can perform equally as well as more sophisticated splitting of the conservation laws such as through characteristic decomposition for resolution of laminar boundary layers (Tatsumi *et al.*, 1995). In theory, the CUSP scheme will capture a shock wave within a single interior point. According to Jameson (1995b), this is the simplest implementation with this property. The JST scheme is unable to capture shocks with this resolution and thus represents shock waves of greater width. In theory, strong shock waves may have a very small width, in the order of a few molecules. If weak shock waves are present, these are best captured with a characteristic method, as the front tends to be smeared by both the JST and CUSP schemes.

JST scheme

Originally the JST scheme was developed for the solution of the Euler equations. It is still applicable to high speed simulations involving the Navier-Stokes equations. While the governing equations include dissipative terms, they may not be sufficient to damp flow instabilities particularly in free stream regions away from solid boundaries. The scheme has been developed from its original form (Jameson *et al.*, 1981) to improve the scaling of the dissipative terms, although essentially the algorithm remains the same.

The scheme involves the addition of first and third order differences. The third order differences are distributed throughout that flow field and provide a background level of smoothing. Whilst this is sufficiently high to remove odd even decoupling it is insufficient to damp flow instabilities due to discontinuities such as shock waves. In the region of discontinuities the scheme uses a switch to detect high gradients and the more dissipative first order differences are applied to generate artificial viscosity (Jameson & Schmidt, 1985).

The dissipation is constructed as a dissipative flux for each cell face to preserve the conservation properties of the discretisation. These are summed over the faces of a cell to generate the dissipation for the cell flow variable at the cell centre through the finite volume

method (Jameson, 1983). The dissipation flux of the positive i cell face for the conservation equations,

$$d_{i+\frac{1}{2},j,k}(\mathbf{w}) = D^{(2)}(\mathbf{w}) + D^{(4)}(\mathbf{w}) \quad (4.39)$$

where the dissipative fluxes are made up of a blending of terms that result in second and fourth differences when the dissipative fluxes are summed over the finite volume cell.

$$D^{(2)}(\mathbf{w}) = \Lambda_{i+\frac{1}{2},j,k} \varepsilon_{i+\frac{1}{2},j,k}^{(2)} \Delta \mathbf{w}_{i+\frac{1}{2},j,k} \quad (4.40)$$

$$D^{(4)}(\mathbf{w}) = \Lambda_{i+\frac{1}{2},j,k} \varepsilon_{i+\frac{1}{2},j,k}^{(4)} (\mathbf{w}_{i+\frac{3}{2},j,k} - 2\mathbf{w}_{i+\frac{1}{2},j,k} + \mathbf{w}_{i-\frac{1}{2},j,k}) \quad (4.41)$$

where

$$\Delta \mathbf{w}_{i+\frac{1}{2},j,k} = \mathbf{w}_{i+1,j,k} - \mathbf{w}_{i,j,k}$$

An approximation is used for the spectral radii of the flux Jacobian matrix for the scaling of the dissipative terms (Jameson & Schmidt, 1985). For the local cell direction ξ in curvilinear coordinates this is estimated as (Liu, 1991)

$$\Lambda_{\xi,i+\frac{1}{2},j,k} = \frac{1}{2} (\Lambda_{\xi,i,j,k} + \Lambda_{\xi,i+1,j,k}) = |(\mathbf{u} - \mathbf{u}_{grid}) \cdot \mathbf{S}_{\xi}| + c|\mathbf{S}_{\xi}| \quad (4.42)$$

where \mathbf{S}_{ξ} is the area vector in the ξ direction.

The large aspect ratios found in boundary regions of the flow-field can lead to a large differences in the dissipation scales in different coordinate directions. To reduce this effect, the spectral radius is modified,

$$\Lambda_{\xi} = \lambda_{\xi} \Phi_{\xi} \quad (4.43)$$

where

$$\Phi_{\xi} = \left[1 + \left(\frac{\lambda_{\eta}}{\lambda_{\xi}} \right)^{\sigma} + \left(\frac{\lambda_{\zeta}}{\lambda_{\xi}} \right)^{\sigma} \right] \quad (4.44)$$

This improves the convergence properties of the scheme for computations involving stretched meshes.

The smoothing parameters are formulated

$$\varepsilon^{(2)} = k^{(2)} \max(v_{i,j,k}, v_{i+1,j,k}) \quad (4.45)$$

where the pressure sensor is a normalised second difference of pressure as defined in Section 4.1.4 and

$$\epsilon^{(4)} = \max(0, (k^{(4)} - \epsilon^{(2)})) \quad (4.46)$$

where the $k^{(4)}$ and $k^{(2)}$ are user specified parameters, ranging between zero and one.

The coefficients $\epsilon^{(2)}$ and $\epsilon^{(4)}$ are constructed so that the fourth differences are switched off in the regions of shock waves. This was found necessary to prevent overshoot and oscillation in the neighbourhood of shock waves (Jameson & Schmidt, 1985). Thus the scheme behaves locally first order in the neighbourhood of shock waves. Where the flow is varying smoothly the parameter $\epsilon^{(2)}$ is proportional to the square of the mesh width, while $\epsilon^{(4)}$ is of the order of one.

The dissipative fluxes at solid boundaries are set to zero to maintain conservation. The fluxes are constructed for all of the conservative variables in each coordinate direction and are added explicitly to the governing equations.

CUSP

A series of non-oscillatory schemes were developed in the first half of the 1990's. Liou and Steffen (Liou & Steffen, 1993) proposed a scheme that has the similar general form to the flux splitting of the CUSP scheme. A major difference between the CUSP scheme and the JST scheme is the use of flux limiters instead of a pressure switch.

The scheme involves the splitting of the governing equations into convective and pressure terms (Tatsumi *et al.*, 1995). For a one dimensional system, the Euler equations may be written

$$\frac{\partial \mathbf{w}}{\partial t} + \frac{\partial \mathbf{f}(\mathbf{w})}{\partial x} = 0 \quad (4.47)$$

where

$$\mathbf{w} = \begin{pmatrix} \rho \\ \rho u \\ \rho E \end{pmatrix}, \mathbf{f}(\mathbf{w}) = \begin{pmatrix} \rho u \\ \rho u^2 + p \\ \rho u H \end{pmatrix} \quad (4.48)$$

The CUSP scheme is constructed by splitting the dissipative fluxes into convective and pressure fluxes. This is convenient so that upwinding may be applied separately to the pressure terms. In supersonic flow, the pressure and convective terms have the same zone of dependence and may be treated in a similar method. However in subsonic flow, pressure waves must be allowed to travel in any direction. The application of an upwind method to these terms in subsonic flow will mean that the system will not have a proper zone of dependence. The scheme therefore is constructed to switch to an upwind scheme in supersonic regions.

Convective and pressure terms are split

$$f_c = u \begin{pmatrix} \rho \\ \rho u \\ \rho H \end{pmatrix}, f_p = \begin{pmatrix} 0 \\ p \\ 0 \end{pmatrix} \quad (4.49)$$

The dissipative fluxes for the convective terms and pressure terms are respectively

$$d_{c_{j+\frac{1}{2}}} = f_1(M) c_{j+\frac{1}{2}} \begin{pmatrix} \Delta \rho_{j+\frac{1}{2}} \\ \Delta \rho u_{j+\frac{1}{2}} \\ \Delta \rho H_{j+\frac{1}{2}} \end{pmatrix} \quad (4.50)$$

$$d_{p_{j+\frac{1}{2}}} = f_2(M) \begin{pmatrix} 0 \\ p_{j+\frac{1}{2}} \\ 0 \end{pmatrix} \quad (4.51)$$

The functions $f_1(M)$ and $f_2(M)$ are formulated so that the upwinding is appropriately implemented in the discretisation. So that these functions are smooth as the discretisation moves from subsonic to supersonic regions, a blend of quartic and linear functions is used.

$$f_1(M) = \begin{cases} a_0 + a_2 M^2 + a_4 M^4 & |M| < 1 \\ |M| & |M| > 1 \end{cases} \quad (4.52)$$

$$f_2(M) = \begin{cases} \frac{1}{2} M (3 - M^2) & |M| < 1 \\ \text{sign}(M) & |M| > 1 \end{cases} \quad (4.53)$$

Note that the diffusion remains positive for the convective terms when $M = 0$ so that it is active in stagnation regions. To preserve continuity of the function f_1 at a Mach number of unity, the coefficients are chosen $a_2 = \frac{3}{2} = -2a_0$, $a_4 = a_0 - \frac{1}{2}$. In practise it was found that for high speed flows $a_0 = \frac{1}{2}$ and for transonic flows $a_0 = \frac{1}{4}$. The diffusion for the convective terms is the same as that for the JST scheme with a modification of the scaling.

4.1.8 Residual Averaging

Another method is used to increase the rate of convergence of the fluid governing equations. The stability region of the multi-stage time integration scheme may be increased through the application of residual averaging. This increases the CFL number by replacing the residuals calculated through the Runge Kutta method with weighted averages of neighbouring residuals has been found to be particularly effective for solutions of the Euler equations (Jameson & Schmidt, 1985). This method was further developed for application to the Navier-Sokes equations by the inclusion of locally varying coefficients (Martinelli, 1987).

For a one-dimensional problem, consider the residual to be an average of itself and its

two neighbours,

$$\bar{R}_i = \varepsilon R_{i-1} + (1 - 2\varepsilon)R_i + \varepsilon R_{i+1}$$

If the factor $\varepsilon > \frac{1}{4}$ then there are Fourier modes that exist in residual space such that $\bar{R}_i = 0$ when $R_i \neq 0$. One method of avoiding this problem is to form the average in an implicit manner.

$$-\varepsilon \bar{R}_{i-1} + (1 + 2\varepsilon)\bar{R}_i - \varepsilon \bar{R}_{i+1} = R_i$$

It can be shown for an infinite interval, the tridiagonal system has the explicit solution

$$R_i = \frac{1-r}{1+r} \sum_{q=-\infty}^{\infty} r^q R_{i+q}, \quad \varepsilon = \frac{r}{(1-r)^2}, \quad r < 1$$

An expansion of the above sum demonstrates that in this form the residual for each cell is influenced by all residuals in the flow domain. To apply the scheme in multi-dimensions, an alternating direction implicit approach is taken,

$$(1 - \varepsilon_x \delta_{xx}^2)(1 - \varepsilon_y \delta_{yy}^2)(1 - \varepsilon_z \delta_{zz}^2)\bar{R}_{i,j,k} = R_{i,j,k}.$$

The coefficients for each coordinate direction are formulated based on a modified local wave speed and the ratio of CFL number to maximum allowable CFL number CFL^* , in the x-direction,

$$\varepsilon_x = \max \left(0, \frac{1}{4} \left\{ \frac{CFL}{CFL^*} [\lambda_x + \lambda_y + \lambda_z] \right\}^2 \right) \quad (4.54)$$

It has been found that implicit residual averaging can allow the use of Courant numbers three times higher than usually allowable, however in the present case this was close to twice for the calculation of the Navier-Stokes equations on a highly stretched grid. The residuals are smoothed at every Runge-Kutta stage for both the Navier-Stokes and the $k-\omega$ variables.

4.1.9 Boundary Conditions for Navier-Stokes Equations

The boundary conditions are the auxiliary data that help to provide a unique solution of the model equations and may be drawn from experimental or theoretical sources. They are particularly important in defining the flow conditions. There are a number of different types of boundary conditions applied in CFD. One is the far-field conditions where fluid crosses into or out of the flow domain. The second are solid surface boundary conditions, where the flow must be locally tangential to the boundary given that the boundary is impervious.

A third type is periodic conditions, mainly applied to flows that involve an array of profiles, such as a turbomachinery cascade.

Far field boundary conditions are the most difficult conditions to formulate and implement. Ideally they will prevent reflections of waves at the boundary whilst remaining relatively simple. The way in which far-field boundary conditions are applied depends on the model geometry. In field of aerospace CFD simulations may be classified as either external or internal flows. External flows generally involve the simulation of vehicles or parts of vehicles such as wings in flight and the edge of the computational domain may be many chords away from the body. The flow at an external boundary may enter or exit the flow domain. Depending on the direction of flow at the external boundary of a particular cell, inflow or outflow conditions are imposed. For compressible flow models the parameters of Mach number and Reynolds number are specified.

Internal flows are where the domain boundaries are well defined and usually involve flow that is bounded by solid surfaces. There are well defined and possibly multiple inlet and outlet planes. For simulations in turbomachinery, it is the usual practice to specify constant values of total temperature and pressure at the inlet with an average flow angle. An average value of the static pressure is imposed at the outlet, with the characteristic theory providing the variation about this average. For a given set of inlet conditions, the outlet conditions may be varied to produce completely different conditions within the turbine passage. One major difference from external flows is that usually the inlet velocity and outlet velocity are unknown initially – they are determined once the solution is found and are determined by the pressure gradient.

Giles (Giles, 1988; Giles, 1990) formulated boundary conditions applicable both to external and internal flows, in particular for turbomachinery. External flows such as airfoil simulations usually employ grids that extend to 30 - 50 chords from the airfoil surface. As waves propagate outwards from the airfoil surface the grid becomes coarser and eventually disturbances may be dissipated by numerical viscosity. In the case of turbomachinery however the inlet plane may be less than a chord length from the leading edge of a blade. Shock waves may exist if the flow is transonic. It is important though that boundary conditions be compatible with physical flow behaviour as they can have a dominating effect on accuracy, stability and convergence rate of the scheme (Hirsch, 1992b; Giles, 1988). In general numerical schemes require the values of all variables at boundaries. Boundary conditions may be classified as physical boundary conditions where flow conditions are transported from the boundary into the domain and the remaining variables are numerical boundary conditions that depend on the final solution and must be consistent with the physical properties of the flow. For one-dimensional compressible flows, three variables are required at each boundary. At the inlet two physical conditions are required and one numerical condition. At the outlet one physical condition is required and two numerical conditions (Hirsch, 1992b). For inter-

nal flows the inlet and outlet flow velocity magnitudes are unknown they may be determined by the inner flow.

To understand the far-field boundary conditions it is useful to consider the mathematical properties of the model governing equations. The numerical schemes and their properties for the Navier-Stokes equations are dominated by their hyperbolic character in time. This hyperbolic nature is also found in the Euler equations that are a subset of the Navier-Stokes equations. The Euler equations omit the effects of viscosity which simplifies analysis. Since the influence of viscous effects is much less in magnitude in far-field regions compared to the time dependent behaviour, the Euler equations are sufficient in describing flow behaviour. They involve both spatial and time characteristics and are classed as mixed or hybrid in type, depending on the Mach number and spatial direction under consideration. Therefore they may be in the hyperbolic or elliptic class of differential equations. Most importantly though they are dominated by their time dependent behaviour. As a consequence they admit wave like solutions, thus the methods of characteristics is useful for analysing the form of solutions and represent the essential aspects of inviscid flows (Hirsch, 1992a). The dominant property of both the mathematical description and numerical discretisation is convective in nature.

Non-reflecting boundary conditions can be derived for 1-dimensional flows using hyperbolic characteristic theory. For three-dimensional and two-dimensional flows the 1-dimensional theory can be applied in the normal direction, ignoring all tangential derivatives. This is the most commonly used boundary condition in unsteady calculations and is referred to as the quasi-one-dimensional or normal one-dimensional boundary conditions or method of characteristics (Giles, 1988).

The non-reflecting boundary condition expresses the physical boundary conditions under the requirement that the local perturbations propagated along incoming characteristics be made to vanish. The method is valid provided shock waves do not cross the boundary. Given that across a shock wave, if the shock is of strength ϵ , the Riemann variables change by an amount $O(\epsilon^2)$ through the shock and produce a reflection of this magnitude (Hirsch, 1992b).

In one-dimensional isentropic flows, the characteristics are constant along the associated characteristics in (x, t) space. Riemann variables are variables that may be characterised by a propagation speed or characteristic. When a variable is conserved during the propagation along a characteristic, it said to be invariant and is regarded as a Riemann invariant. Thus the application of the 1-dimensional characteristic equations at a boundary is equivalent to the use of Riemann invariants. The present formulation for of non-reflecting boundary conditions for the Euler equations was proposed by Jameson (Jameson, 1983).

The majority of viscous and inviscid aeroelastic computations implement 1-dimensional, non-reflecting boundary conditions as described by Giles (1990). The two-dimensional form of boundary conditions are not implemented in numerical models because they are known to show great benefit only in steady flow calculations (Isomura & Giles, 1998). However they

have been implemented in unsteady calculations for rotor stator interactions, where the inlet and outlet lengths are substantially shorter than a chord length (Sbardella & Peiro, 1997).

There are a number of conditions that may be imposed at the inlet:

1. Incoming characteristic: $u_{nB} + \frac{2c_B}{\gamma-1} = U_{n\infty} + \frac{2c_\infty}{\gamma-1}$
2. Outgoing characteristic: $u_{nB} - \frac{2c_B}{\gamma-1} = U_{ni} + \frac{2c_i}{\gamma-1}$
3. Far-field normal velocity: $u_{nB} = u_{n\infty}$
4. Far-field entropy: $S_B = S_\infty$
5. Far-field enthalpy: $H_B = H_\infty$
6. Far-field flow angles: $\alpha_B = \alpha_\infty, \beta_B = \beta_\infty, \gamma_B = \gamma_\infty$

To determine the inlet velocities, condition number 2. is used, coupled with the flow angles and constant enthalpy. The enthalpy is calculated from the local values of total temperature and total pressure. Thus the two physical conditions are the enthalpy and the flow angle and the numerical condition is obtained from the Riemann invariant. This satisfies the requirements for application of 1-dimensional boundary conditions.

At the outlet, two numerical conditions are required with one physical condition. The static pressure is specified at the outlet boundary and the outgoing characteristic equation is used to calculate the other conditions at the boundary, combined with the entropy that is extrapolated from inside the flow field to calculate the outlet density and sound speed.

Periodic boundary conditions can be implemented where it is assumed that a single blade passage represents all blades in the cascade or annulus. For steady calculations, fluxes are merely passed from one side of the domain to the other, taking into account the angle between periodic faces if the cascade is annular. However where periodicity is assumed in unsteady aeroelastic calculations and only one passage is used, the periodic boundary field variables will change depending on the stage within the oscillation cycle. Thus in the "direct store method", the periodic boundary values must be stored at each point in the cycle, which equates to the temporal linearisation of the lagged periodic boundary condition. This allows the modelling of any inter-blade phase angle with a single blade passage (Hwang & Yang, 1995; Abhari & Giles, 1997; Weber *et al.*, 1998). However, this method has been shown to produce different results compared to multiple passage calculations (Marshall & Imregun, 1996a).

Since the direct store method is not used in the present approach, as many passages must be modelled as there are different flow patterns in the cascade. This may be calculated by through 360/IBPA where the IBPA is specified in degrees. Spatially periodic boundary conditions are used at the boundary of the annulus segment in the present method.

Wall boundary conditions are applied by setting the boundary ghost cells. These cells lie beyond the flow domain. For the Euler equations, the normal velocity is equated to zero,

$$(u - u_{grid}) \cdot \mathbf{n} = 0, \quad (4.55)$$

and the density is extrapolated from within the domain. The normal momentum equation may be constructed through the streamline differentiation of the wall boundary condition (Rizzi, 1978). The pressure gradient obtained may be then used to calculate the total energy in the ghost cell. In Navier-Stokes simulations, the flow velocity at the boundary is set to zero by setting the velocities to the negative of those in the domain interior. The wall is adiabatic in that there is zero heat flux at the boundary.

4.1.10 Boundary Conditions for k - ω Equations

The boundary conditions are implemented as in previous versions of the code (Liu & Zheng, 1994).

Simulations involving the original free-stream conditions have been found to be sensitive to the free-stream level of turbulence dissipation rate ω (Menter, 1992), particularly in the case of free shear flows. The present implementation used that proposed by Menter, estimated for high Reynolds number boundary layer flows as

$$\omega_{\infty} = O\left(10 \frac{U_{\infty}}{L}\right) \quad (4.56)$$

The far-field boundary value of turbulence kinetic energy k is set at a very low level, but is not zero for numerical reasons.

Wall conditions are as originally prescribed (Wilcox, 1988). The exact solution of the ω equation within the viscous sub-layer is given as

$$\omega \sim \frac{6\nu_{wall}}{\beta_0 y^2}, \quad y^+ < 2.5 \quad (4.57)$$

Alternate conditions have been proposed by other authors (Wilcox, 2000; Menter, 1994) to improve the velocity distribution through the boundary layer. However the grid dependence of all Navier-Stokes simulations was investigated and the following implementation was found to be sufficient. This has also been found by other authors for relatively complex turbine configurations (Liu & Zheng, 1994). At the first grid point from the wall, the value of turbulence specific dissipation rate ω_{wall} is set based on the normal distance from the wall,

$$\omega_{wall} = \frac{6\nu_{wall}}{\beta y_n^2} \quad (4.58)$$

where y_n is the normal distance from the first grid point to wall. For multigrid calcu-

lations, the fine grid wall distance is used in the calculation of ω_{wall} on coarser grids. In all the simulations presented, the turbulence quantities are integrated to solid surfaces and no special functions are used in boundary layer regions to obtain theoretical boundary layer profiles.

4.2 Structural Model Discretisation

The simulation of the structural behaviour involves the equations governing the structural model that have been reduced to modal form. Each mode has an associated model equation which is solved to obtain the behaviour of the complete model. These equations are solved in a similar manner to the fluid model governing equations, with the same dual time discretisation and Runge-Kutta time stepping scheme.

The structural displacement vector is written as a summation of N modal shapes extracted from a finite element analysis of the structure.

$$h_s = \sum_{i=1}^N q_i \Phi_i \quad (4.59)$$

where Φ_i are the modal shapes. Equation (5.1) is further reduced to a first order system of equations for each i and integrated in time by a second-order fully implicit scheme.

$$\ddot{q}_i + 2\zeta_i \omega_i \dot{q}_i + \omega_i^2 q_i = Q_i \quad (4.60)$$

Following Alonso and Jameson (Alonso & Jameson, 1994), we assume

$$\begin{aligned} h_{1i} &= q_i \\ \dot{h}_{1i} &= h_{2i} \\ \dot{h}_{2i} &= Q_i - 2\zeta_i \omega_i h_{2i} - \omega_i^2 h_{1i} \end{aligned} \quad (4.61)$$

for each of the modal equations. Thus in matrix form:

$$\{\dot{H}_i\} = [A_i]H_i + \{F_i\}, \quad i = 1, 2 \quad (4.62)$$

where $\{H_i\} = \begin{Bmatrix} h_{1i} \\ h_{2i} \end{Bmatrix}$, $[A_i] = \begin{bmatrix} 0 & 1 \\ -\omega_i^2 & -2\omega_i \zeta_i \end{bmatrix}$ and $\{F_i\} = \begin{Bmatrix} 0 \\ Q_i \end{Bmatrix}$.
After proper diagonalisation, the above equation can be decoupled.

$$\frac{dz_{1i}}{d\tau} = \omega_i(-\zeta_i + \sqrt{\zeta_i^2 - 1})z_{1i} + \frac{(-\zeta_i + \sqrt{\zeta_i^2 - 1})}{2\sqrt{\zeta_i^2 - 1}} Q_i \quad (4.63)$$

$$\frac{dz_{2i}}{d\tau} = \omega_i(-\zeta_i - \sqrt{\zeta_i^2 - 1})z_{2i} + \frac{(\zeta_i + \sqrt{\zeta_i^2 - 1})}{2\sqrt{\zeta_i^2 - 1}}Q_i \quad (4.64)$$

In these equations, the time derivative operator is discretised by a second order accurate scheme for each mode

$$\frac{3z_{1i}^{n+1} - 4z_{1i}^n + z_{1i}^{n-1}}{2\Delta\tau} = \omega_i(-\zeta_i + \sqrt{\zeta_i^2 - 1})z_{1i}^{n+1} + \frac{(-\zeta_i + \sqrt{\zeta_i^2 - 1})}{2\sqrt{\zeta_i^2 - 1}}Q_i^{n+1} \quad (4.65)$$

$$\frac{3z_{2i}^{n+1} - 4z_{2i}^n + z_{2i}^{n-1}}{2\Delta\tau} = \omega_i(-\zeta_i - \sqrt{\zeta_i^2 - 1})z_{2i}^{n+1} + \frac{(\zeta_i + \sqrt{\zeta_i^2 - 1})}{2\sqrt{\zeta_i^2 - 1}}Q_i^{n+1} \quad (4.66)$$

The above equations are coupled with the time-marching of the Navier-Stokes equations and solved by a dual time stepping algorithm similar to that used for the fluid solver.

4.3 Parallel Computation Strategy

The motivation behind the development of computing systems for scientific and engineering applications is to reduce computation time and increase computational capacity. The reduction of computation time is gained through higher processor speed and improvement of system architecture. Increasing the system memory allows for the solution of larger problems, or the solution of problems at higher resolution or model complexity. Ultimately this results in better models and more realistic predictions or results.

Single processor vector supercomputers were popular in the 1980's. In the 1990's it was recognised that parallel architecture computers offer the promise of providing orders of magnitude greater computational power. One of the key advantages identified was the scalability of the systems, that is the performance of a multi-processor architecture increases linearly with the number of processors for a wide variety of problems. It was proposed that the computational requirements for solving the grand challenge large scale problems in industry the distributed memory, multiple instruction, multiple data machines are most likely to meet this challenge due to their scalability (Argarwal, 1992). The grand challenge equations are the most difficult and important equations that model scientific phenomena, including the Navier-Stokes equations.

4.3.1 Architecture of High Performance Computers

One of the significant differences between sequential programming and parallel processing is that it is necessary to have an understanding of the underlying computer architecture and numerical algorithm and the effect one has on the other for efficient operation. This is important in order to extract a significant fraction of the peak performance from the machine

(Emerson, 1996). The great effort that has been invested in the development of powerful computers has led to large number of different types of systems. The configuration or architecture of these machines is complex however it is useful to characterise them so that the structure of the simulation tool may be tailored in an appropriate manner.

One of the most widely used classifications of parallel architectures was provided by Flynn (Flynn, 1972). Known as Flynn's Taxonomy, it is based on the concept of a data and instruction stream. A data stream is a sequence of data that includes input and partial or temporary results. The instruction stream is a sequence of instructions as executed by the machine. The classification involves four major groups; single instruction and single data stream (SISD), single instruction and multiple data stream (SIMD), multiple instruction and single data stream (MISD) and multiple instruction and multiple data stream (MIMD).

Single instruction stream single data (SISD) organisation is found in the majority of conventional desktop computers, however rarely in modern large scale computers. Processor speed is limited by manufacturing techniques and the speed of light. Even though manufacturing technology is advancing to produce faster processors, parallelism has been introduced to further increase the efficiency of the computer beyond the restrictions of the SISD model.

The single-instruction multiple data (SIMD) classification is for computers otherwise known as vector or array processors. They have one instruction processing unit and several processing units and involve an array of processors that operate on a segment of a vector of data. Pipeline computers also fall within this category. An important characteristic of SIMD organisation is that the processor has access to all of the memory. The Multiple instruction single data (MISD) class of machines do not exist.

The final and most diverse group involves Multiple Instruction Multiple Data organisation. This group is subdivided into shared memory SM-MIMD systems and distributed memory DM-MIMD systems. Hybrids also exist, for example combining a number of SIMD processors to form a MIMD system, or SM-MIMD systems to create an DM-MIMD. Thus Flynn's Taxonomy isn't the most descriptive of classifications, however it remains the most widely used.

There are a number of strategies used to increase the power of the large scale system. Pipelining is where instructions are overlapped enabling the processor to produce a result every cycle, even for instructions that may require multiple clock cycles to be produced. Initialisation is required where the pipe is filled. Thus processor clock speed is not an accurate indication of processing speed as the use of a pipeline can significantly increase the processor work rate independently of the clock speed.

Toward the end of the 20th century, processor speed approximately doubles every 18 months, however this does not apply to memory access speed (Gustafson, 1998). Most arithmetic operations are executed in one or two clock cycles, but fetching data from memory could take 50 or 100 clock cycles. One of the most important strategies used to reduce the

effect of memory latency involves the caching of data and instructions in smaller and faster memory chips that are closer to the processor. Data that is used a number of times can be stored in the cache rather than main memory. Data can also be loaded into the cache in advance while the processor is performing operations on data from other parts of the cache. Thus memory is divided into a number of levels, some systems have a small and very fast primary cache and a slower but larger secondary cache.

Relatively slow memory fetch time also makes it difficult to evaluate system performance from fundamental measures such as clock speed and floating operations per second (FLOPS) (Gustafson, 1998). The memory size and memory organisation may become a major constraint on system performance – programs with small memory requirements may run much faster than those with large memory requirements. Performance is therefore application dependant as well as system dependant.

An important measure in the evaluation of computer performance is the execution time for a particular program (Allen *et al.*, 1996). This may be represented by the following equation in terms of n_i the number of instructions to be executed, the cycles required per instruction and the time per cycle.

$$T = n \times CPI \times t_{cycle} \quad (4.67)$$

The time required per instruction is purely determined by the engineering of the processing unit, whereas the other two parameters are affected by the type of architecture under consideration. Given that the technology of the processing unit is limited by the advance of manufacturing techniques, there has been a large effort to develop architectures to increase computer performance. Key to this is the concept of parallelism, be it within the processor or through collecting of processing units to form a single machine.

A number of different types of parallelism have been identified (Flynn, 1972). In particular there is program level parallelism, instruction level parallelism and arithmetic and bit level parallelism. All of these optimisations have the ability to affect the method of code implementation. Program level parallelism may be applied to different sections of a program, or a loop where each operation is independent of another within the loop. This will affect the implementation at the programming level. Instruction level parallelism is where an instruction may be divided into sub-operations and the operations overlapped, or individual instructions may be overlapped. Compilers are in general optimised to make best use of this parallelism and it does not impact on the implementation as the program level parallelism.

4.3.2 Parallel Performance

There are a host of parallel performance metrics, however the most frequently used is the *speed-up* S_n and *total efficiency* E_n (Drikakis, 1999).

$$S_n = \frac{t_1}{t_p} \quad (4.68)$$

$$E_n = \frac{t_1}{nt_p} \quad (4.69)$$

The parallel execution time is t_p and n is the number of processors. The definition of the sequential execution time t_1 is important as it can greatly affect the measures of performance. The *relative speed-up* is defined as where the sequential time is based on the speed of the parallel code on one processor and the *absolute speed-up* is where the sequential execution time is for the best sequential algorithm available. In the present context, the relative speed-up should be higher given that the implementation of the multiple block code tends to slightly increase the execution time and operation count. The absolute speed-up should emphasise how much faster a problem can be solved with parallel processing, while the relative speed-up will be more dependant on machine architecture.

An important factor in the parallel performance of an algorithm is the percentage of serial computation time versus the parallel computation time (Emerson, 1996). Amdahl's law (Amdahl, 1967) was first applied to vector systems, however it may equally be applied to parallel systems. Given that the fraction f is carried out on n processors and the other fraction of the computation occurs on a single processor ($1 - f$) (which includes time required for communication between processors), t_1 is the time taken on a single processor, the total time taken is given by

$$t = t_p + t_s = \frac{ft_1}{n} + (1 - f)t_1 \quad (4.70)$$

Ware's (Ware, 1973) law provides the speed-up in terms of fraction of parallel computation time f ,

$$S_n = \frac{t_1}{t_p} = \frac{n}{f + (1 - f)n} \quad (4.71)$$

Efficiency is given by,

$$E_n = \frac{S_n}{n} = \frac{1}{f + (1 - f)n} \quad (4.72)$$

For a large number of processors, the speed-up is bounded by

$$S_n \leq \frac{1}{1 - f} \quad (4.73)$$

This law has limited applicability. It is pessimistic in that even a small level of serial computation will lead to a low speed-up – few problems experience even a 100-fold speed-up. It has been found that the law does not take into account that the sequential part of

the computation may reduce in proportion as the problem size increases. This is true if the initialisation phase and message passing phase does not increase with the larger problem. Gustafson (Gustafson, 1998) found that to a first approximation, the parallel or vector part of a program scales with problem size. Times for vector start-up, program loading and input/output operations do not grow with problem size. Thus the amount of work done varies linearly with the number of processors. An alternative to Amdahl's law is provided as:

$$S_{\text{nscaled}} = n + s(1 - n) = n + (1 - f)(1 - n) \quad (4.74)$$

where $s = (1 - f)$ is the fraction of serial computation time. However there is still much debate of the usefulness of this model (Casavant *et al.*, 1996).

If experiments are used to determine the parallel performance of a particular parallel machine, performance metrics can be greatly affected by the machine architecture. Most high performance machines have memory that is divided into a hierarchy. Small but fast memory is located close to the processor, whereas lower level slower cache may be larger and further away. Access time for data in lower level cache and main memory is much slower than for the high level cache. Execution time can vary greatly, depending on the amount of memory used and the percentage of the data that fits in the faster memory. Speedup may increase due to different memory usage purely because the ratio of execution to communication time increases.

4.3.3 Parallelisation of CFD Codes

There are two major types of parallel processing models, the Single Program Multiple Data (SPMD) and the Multiple Program Multiple Data (MPMD) model. The most commonly used model for scientific computation is the SPMD (Emerson, 1996) model as they usually involve performing computations in an iterative manner on a relatively large set of data. The MPMD model is not applicable to CFD and the SPMD model is used in the present code.

The type of parallel implementation will depend on the configuration of the particular system. The compilers on some shared memory SM-MIMD machines can parallelise code automatically through compiler directives within the source code. This is one of the simplest methods of implementing a parallel solver, however it is limited to these types of machines and is not compatible with machines with distributed memory. A code suitable for the DM-MIMD may be run on a SM-MIMD machine, although it may not be optimal.

The method of domain decomposition is where the computational domain is divided into a number of blocks that can be allocated to processors of the a multiple processor system. Each processor performs the same types of computations on data, although different boundary conditions may be applied by each processor. In the present work, so that each block

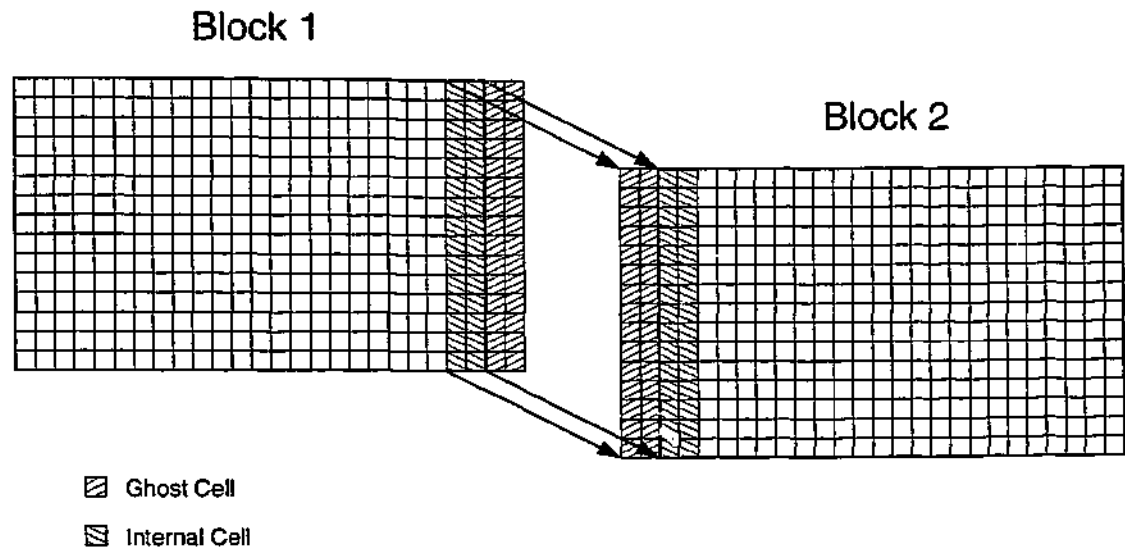


Figure 4.3: Transfer of boundary cells.

may be operated on in parallel, each cell must have access to two neighbouring cells at the edge of the domain in each coordinate direction of the computational domain due to the discretisation stencil. At the edges of a block ghost cells are required to hold the data of a neighbouring block from the previous time step, or for the boundary condition. The transfer of cells is demonstrated in Figure 4.3 in computational space for a 2-dimensional domain. The two internal rows adjacent to a boundary of block 1 are transferred to the ghost cells of block 2. Subsequently the internal cells of block 2 would be transferred to the ghost cells of block 1. This transfer of cells is performed at every time step or partial step. Where the blocks are allocated to the same processor and therefore share the same memory, the transfer may take place by copying from one memory location to the other. Where the blocks reside on different processors that do not share the same memory the transfer must occur through message passing.

Typical modern day distributed memory machines have multiple processors sharing common memory within a node, with the machine being made up of a large number of nodes. An optimal code for this type of architecture would be one that is parallel within each node using compiler directives, then use message passing between each cluster. Whilst it is significantly less complex to implement a parallel code through the use of compiler directives, it takes time for the system to initialise the parallel loop computation. This time must be compared for the time required for message passing. Efficiency gains may be negligible compared to the added complexity required for such a hybrid approach.

The method of code parallelisation is not a trivial one as it adds another level to code complexity and can vary in efficiency. There are many different standards and implementations that may be used, however the Message Passing Interface (MPI) has become one of the most popular. The majority of large, parallel computers support this standard, as do the

more economical PC based Beowulf clusters. Open MP is another standard, that makes use of compiler directives to parallelise loops within a shared memory system.

Load balancing is another important issue which relates to the distribution of the computational domain across the system. Ideally each processor would perform calculations on the same number of computational cells. However due to geometry this may not always be possible, particularly where the more sophisticated turbomachinery grid generators are used that provide better cell distributions in a geometric sense, but are poorer with regard to the domain decomposition. There may also be small regions of the flow field such as the tip gap that due to their geometry involve blocks with small numbers of cells. Thus it may be more efficient with regard to load balancing to allocate more than one block to a single processor.

There is a compromise between numerical efficiency and parallel efficiency. Parallel efficiency involves maintaining a high ratio between number of operations and size of communications. Numerical efficiency involves implementing the fastest converging numerical methods. Often these two counter each other, however in general the numerical efficiency is the most important consideration.

There are a number of important issues with regard to the parallel computations of large problems, some of which are considerations in the design of the implementation, others that are important in the problem setup at run time.

- Total efficiency increases for increasingly fine grids (computation time/communication time), as in general the number of operations increases proportional to the cube of the number of cells, whilst the relative size of the communication increases by six times the square of the number of cells.
- Total efficiency decreases for larger number of processors (Amdahl's law).
- Method of discretisation does not greatly affect total efficiency unless there is a large difference between communication size and thus communication time, although it affects numerical efficiency.
- The more model equations solved, the higher the total efficiency provided the increase in communication time is not proportional to the increase in computation time.
- The closer to cube in shape the computational blocks, the higher the parallel efficiency due to reduction of message size without changing of number of operations.
- Multigrid decreases parallel efficiency due to increased communication per grid point. However increased numerical efficiency overshadows this disadvantage.
- Poor load balancing can reduce parallel efficiency.

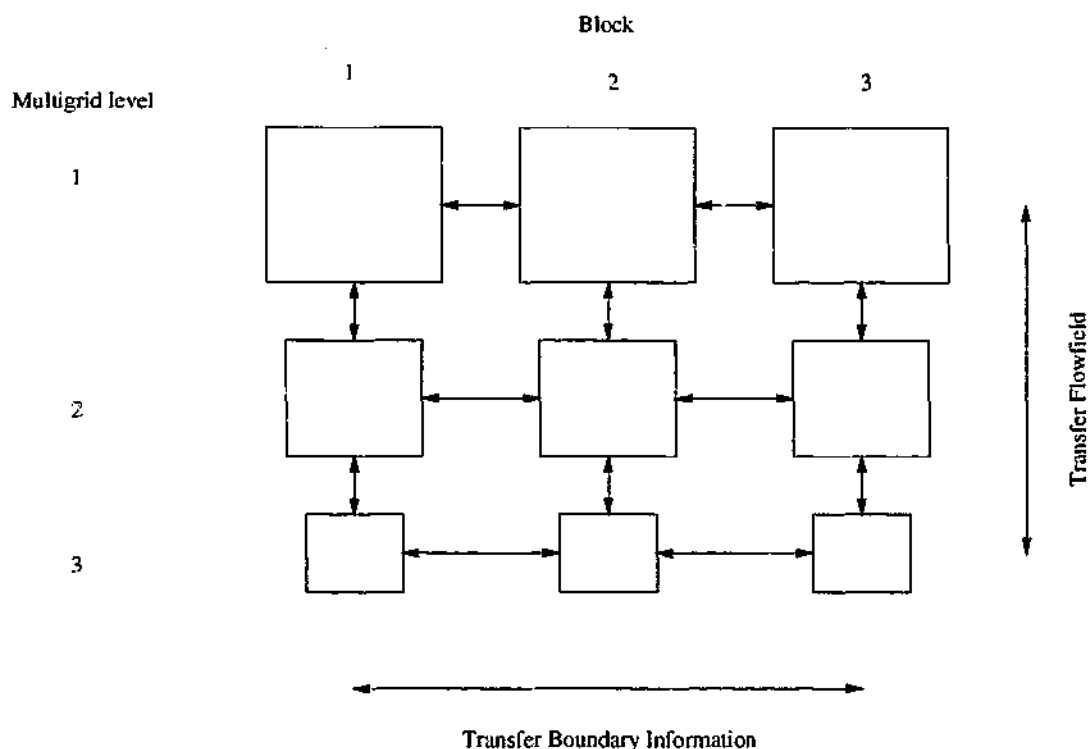


Figure 4.4: Communication between blocks and grids in multiblock code.

4.3.4 Implementation of Parallel Solver

The conventional method of domain decomposition of the structured grid is used to exploit the parallel computing systems that are presently available. An unstructured approach was taken to the method of decomposition in order to not restrict the topology and distribution of blocks. This allows for better load balancing where the computational geometry is restricted due to physical and geometrical considerations. While each block consists of a structured grid, the blocks can be connected to each other in an unstructured manner provided the mesh geometry is matched at the block interfaces. Thus the parallel topology is unstructured in that the block size and geometry in the computational domain does not have to be regular over the problem domain. This has implications for the data structure, outlined in the following sections.

Each fluid block is treated as a single object or entity. A schematic of the multi-block data structure is shown in Figure 4.4. A processor may be allocated more than one fine grid block and each fine grid block will have associated a number of coarser, multi-block grids. Computations are performed at each multigrid in parallel then copies the solution or interpolates the residual to the next multigrid level.

In keeping with the use of high levels of Fortran90 code, the communication module also exploits some of the more sophisticated MPI routines. The use of MPI derived types allows the direct access of memory for the transfer of data, reducing the number of copies required

during the communication of ghost cells. Due to the repetitive nature of the CFD computation, the "pipe-lining" of message passing calls, also known as persistent communication is implemented.

4.3.5 Data Structure

With the implementation of the parallel solver, the data structure was redesigned to allow for the unstructured domain decomposition approach and multiple block single process capability. Object oriented data constructs and matrix transformations are introduced to allow for more efficient allocation of memory and a more compact implementation.

A similar structure has been implemented for a general multigrid solver (Numerich *et al.*, 1998), although there are some major difference as this solver assumed the problem domain is regular and rectangular and decomposition may be performed automatically. The present method is not limited to this structured block topology. In the general multigrid solver, it was found that Co-Array Fortran, an extension of Fortran-95, was equally efficient as MPI over a small number of processors. However it became much more efficient over a much larger number of processors, is much easier to implement than MPI calls and does not require access to the large MPI library. The problem with using such a Fortran extension is that this is only available on large parallel computers with shared memory. It cannot be used on the DM-MIMD systems, therefore is less portable. Portability was a major consideration in the development of the present code, thus MPI was chosen as the most portable standard.

Fortran 90 has a number of developments that are improvements from the former versions of Fortran. The major differences is the ability to allocate array sizes at run time and the introduction of object oriented data constructs such as derived types and pointer arrays. These features have been exploited to reformulate the data structure in a manner better suited to parallel processing. A major drawback of using these features is that it is often more difficult to debug due to the use of pointer variables.

All the quantities are stored for each multigrid level which means that they do not have to be swapped. This is the reason that each multigrid level in Figure 4.4 is shown as an individual block. If stored in structured arrays, the dimensions of all arrays would have to be the same for all multigrid levels, as different sizes cannot be allocated for different array indices. The use of Fortran90 derived types allows each block involving a single multigrid level to be treated as an entity. The arrays within the entity may be allocated to the exact size required without regard to the size of other blocks.

All variables required for each block are contained within a single array of block derived types, the first index being for the local block number and the second for the multigrid level. All variables are associated with a pointer and this pointer is set to the variables on the required block by a single subroutine call. The variables stored within a block include the flow

quantities, grid geometry and grid velocity, turbulence quantities and boundary condition information.

4.3.6 Boundary Conditions

Due to the increase in complexity of the geometric modelling introduced by the multiple block implementation, it was decided to formulate a general way of handling block boundaries. Consider a single block in the computational domain. The ghost cells that surround the computational block are updated either by applying a boundary condition or transferring values from neighbouring blocks as shown in Figure 4.3. There are two planes of cells required for each face for the flow quantities due to the artificial viscosity and the $k-\omega$ equations for the calculation of the dissipative terms at the cell vertices.

Each block face may be subdivided into sub-domains, or subfaces. There are a number of restrictions on the specification of subfaces; they must be rectangular in computational space and they must have corners that are defined on the coarsest multigrid level. Multiple blocks may interface with a single block face by defining the appropriate subfaces on the blocks, however this may not be used with the present moving grid implementation. In the code, interpolation for the moving grid is performed by defining the movement of block corners only – the generation of the spring network for subface block topology is more complex, as is the interpolation for a face containing a number of subfaces that interface with multiple blocks.

A subface is defined as another object in the data structure. This is used for the interface between the present block and another block, or a region to which a single boundary condition is to be applied. These objects are cycled through each time the boundary of the blocks are to be updated, upon which communication is effected or a boundary condition is applied. So that separate boundary conditions are not required for each coordinate direction, subface objects are transformed into a single coordinate system. This increases code complexity marginally. However it maintains that the code that is relatively compact. The structured cell numbering within each block is unimportant as transformations are used to re-orient the face so that the numbering matches with the neighbouring face. For example for a C-grid where a single block is wrapped around the blade, at the interface downstream of the trailing edge the cell numbering will be different on the upper and lower blocks, thus requiring re-orientation of the 2-dimensional arrays. Where meshes are required in tip gap regions, transformations must be used due to the nature of the structured grid. The nature of the tip gap mesh is discussed in Chapter 6.

4.4 Moving Grid

The movement of the fluid boundary requires the fluid computational mesh be somehow adapted to the new geometry. A number of researchers have coupled the fluid solver with a grid generator to regenerate the grid at each time step. Clearly the optimal method would be one that required the least computational effort whilst maintaining grid regularity. Grid regularity is particularly important in Navier-Stokes computations where the aspect ratio of cells close to the solid boundary is high.

Given that the original grid is close to optimal and the structural deformations are not too large, an interpolation method such as transfinite interpolation (TFI) is more efficient compared to iterative grid generation methods. The method has the advantage that only the location of the corners of each computational block are defined for the cell geometries on the block faces to be maintained across block boundaries with the displacement of the corner points.

The method has been used for an incompressible flow solver, whereby the block corners were located globally by modelling the whole flow-field as an elastic solid (Jenssen *et al.*, 1998). The finite element method was used to solve the static problem and locate block corners. This was intended to maintain grid regularity over the entire flow domain. It has also been employed for aeroelasticity in turbomachinery simulations where time linearised fluid models were used (Holmes & Lorence, 1998). In a more general application, the aeroelastic problem was regarded as the solution of three sets of equations. They include the equations governing the fluid, the equations governing the structure and third set governing the deformation of the mesh (Farhat *et al.*, 1998). The equation governing the mesh deformation may be regarded as a pseudo-structural problem, where field variables such as grid elasticity and density are used to maintain mesh regularity. These methods may be more sophisticated than is necessary where small deformations are involved.

The method used herein is through the use of Batina's (Batina, 1990) spring analogy to locate block corners (Wong *et al.*, 2000). This is equivalent to the above, however the solution of the static equilibrium equations are less complicated to implement. Note that the present implementation is less sophisticated than that used in by Wong *et al.* (2000), as the mixed block boundary conditions have not been allowed for in the moving mesh method, and grid blending is not used at block corners. It was found that these were unnecessary for the geometries of the cases presented.

4.4.1 Transfinite Interpolation

The grid for each computational block is regenerated independently of other blocks, on the local processor. The arc length method of transfinite interpolation has been used by other authors in similar applications (Jones & Samareh-Abolhassani, 1995; Wong *et al.*, 2000).

In this case it is used to regenerate the grid of a single hexahedral block. The displacement of the block corners or whole surfaces is first calculated and this is used to interpolate the position of the new grid.

This method may be broken down into a number of steps.

1. Calculate edge and corner deformations.
2. Parameterise points on block surface.
3. Perform 1-dimensional, 2-dimensional and 3-dimensional TFI of the deformations.
4. Add the deformations to the original grid to obtain the final mesh.

Edge and corner deformations are calculated through the structural solver or specified by input parameters. The parameterisation of the mesh involves the taking of differences in each direction in computational space. Each direction is considered separately, the parameterised coordinates for the I -direction, J -direction and K -directions are denoted F , G and H respectively. For example, in the I -direction the arc length and parameterised coordinate:

$$SF_{j,k} = \sum_{i=1}^{imax} \sqrt{(x_{i+1,j,k} - x_{i,j,k})^2 + (y_{i+1,j,k} - y_{i,j,k})^2 + (z_{i+1,j,k} - z_{i,j,k})^2}$$

$$F_{i,j,k} = \frac{\sqrt{(x_{i,j,k} - x_{i-1,j,k})^2 + (y_{i,j,k} - y_{i-1,j,k})^2 + (z_{i,j,k} - z_{i-1,j,k})^2}}{SF_{j,k}} + F_{i-1,j,k}$$

The 1-dimensional TFI in the K -direction to calculate the deformation of an edge $\Delta E_{1,1,k}$ is given by

$$\Delta E_{1,1,k} = (1 - H_{1,1,k})\Delta P_{1,1,1} + H_{1,1,k}\Delta P_{1,1,kmax}$$

The deformations of the corner points at each end of the edge are $\Delta P_{1,1,1}$ and $\Delta P_{1,1,kmax}$. For a surface, the 2-d TFI is defined for a surface in the $I = 1$ plane,

$$\begin{aligned} \Delta S_{1,j,k} = & A_{1,j,k}\Delta E_{1,j,1} + B_{1,j,k}\Delta E_{1,j,kmax} + \\ & C_{1,j,k}\Delta E_{1,1,k} + D_{1,j,k}\Delta E_{1,jmax,k} - \\ & A_{1,j,k}C_{1,j,k}\Delta P_{1,1,1} - B_{1,j,k}C_{1,j,k}\Delta P_{1,jmax,1} - \\ & A_{1,j,k}D_{1,j,k}\Delta P_{1,1,kmax} - B_{1,j,k}D_{1,j,k}\Delta P_{1,1,kmax} - \\ & B_{1,j,k}D_{1,j,k}\Delta P_{1,jmax,kmax} \end{aligned}$$

The blending functions are related to the parameterisation of the grid:

$$A_{1,j,k} = 1 - \eta_{1,j,k}$$

$$B_{1,j,k} = \eta_{1,j,k}$$

$$C_{1,j,k} = 1 - \xi_{1,j,k}$$

$$D_{1,j,k} = \xi_{1,j,k}$$

where

$$\begin{aligned}\zeta_{1,j,k} &= 1 - (G_{1,j,kmax} - G_{1,j,1})H_{1,jmax,k} - H_{1,1,k} \\ \xi_{1,j,k} &= \frac{G_{1,j,1} + H_{1,1,k}(G_{1,j,kmax} - G_{1,j,1})}{\zeta_{1,j,k}} \\ \eta_{1,j,k} &= \frac{H_{1,1,k} + G_{1,j,1}(H_{1,jmax,k} - H_{1,1,k})}{\zeta_{1,j,k}}\end{aligned}$$

The volumes are constructed in a number of steps, combining point-wise, edgewise and surface-wise deformations.

$$\Delta x_{i,j,k} = X1 + X2 + X3 - X12 - X13 - X23 + X123$$

where

$$X1 = (1 - F_{i,j,k})\Delta S_{1,j,k} + F_{i,j,k}\Delta S_{imax,j,k}$$

$$X2 = (1 - G_{i,j,k})\Delta S_{i,1,k} + G_{i,j,k}\Delta S_{i,jmax,k}$$

$$X3 = (1 - H_{i,j,k})\Delta S_{i,j,1} + H_{i,j,k}\Delta S_{i,j,kmax}$$

$$\begin{aligned}X12 &= (1 - F_{i,j,k})(1 - G_{i,j,k})\Delta E_{1,1,k} + (1 - F_{i,j,k})G_{i,j,k}\Delta E_{1,jmax,k} + \\ &F_{i,j,k}(1 - G_{i,j,k})\Delta E_{imax,1,k} + F_{i,j,k}G_{i,j,k}\Delta E_{imax,jmax,k}\end{aligned}$$

$$\begin{aligned}X13 &= (1 - F_{i,j,k})(1 - H_{i,j,k})\Delta E_{1,j,1} + (1 - F_{i,j,k})H_{i,j,k}\Delta E_{1,j,kmax} + \\ &F_{i,j,k}(1 - H_{i,j,k})\Delta E_{imax,j,1} + F_{i,j,k}H_{i,j,k}\Delta E_{imax,j,kmax}\end{aligned}$$

$$\begin{aligned}X23 &= (1 - G_{i,j,k})(1 - H_{i,j,k})\Delta E_{i,1,1} + (1 - G_{i,j,k})H_{i,j,k}\Delta E_{i,1,kmax} + \\ &G_{i,j,k}(1 - H_{i,j,k})\Delta E_{i,jmax,1} + G_{i,j,k}H_{i,j,k}\Delta E_{i,jmax,kmax}\end{aligned}$$

$$X123 = (1 - F_{i,j,k})(1 - G_{i,j,k})(1 - H_{i,j,k})\Delta P_{1,1,1} + (1 - F_{i,j,k})(1 - G_{i,j,k})H_{i,j,k}\Delta P_{1,1,kmax} +$$

$$(1 - F_{i,j,k})G_{i,j,k}(1 - H_{i,j,k})\Delta P_{1,jmax,1} + (1 - F_{i,j,k})G_{i,j,k}H_{i,j,k}\Delta P_{1,jmax,kmax} + \\ F_{i,j,k}(1 - G_{i,j,k})(1 - H_{i,j,k})\Delta P_{imax,1,1} + F_{i,j,k}(1 - G_{i,j,k})H_{i,j,k}\Delta P_{imax,1,kmax} + \\ F_{i,j,k}G_{i,j,k}(1 - H_{i,j,k})\Delta P_{imax,jmax,1} + F_{i,j,k}G_{i,j,k}H_{i,j,k}\Delta P_{imax,jmax,kmax}$$

In the implementation, the surfaces and edges are objects and as such derived types are used to store the deformations of the coordinates.

4.4.2 Multi-block Moving Grid

In a large multi-block problem, there are block corners that do not correspond with a stationary or moving solid surface. One possible solution is to fix the location of these corners, however this may result in a loss of grid regularity. To avoid this problem, a hypothetical network of springs is generated for the whole network of blocks (Wong *et al.*, 2000).

Initially an unstructured grid network is constructed on the root processor. This contains nodal locations for each block corner and the connecting node information. Each spring runs along the edge of a block and connects two corners. There are also springs in the diagonal direction across the block. The stiffness of each spring is inversely proportional to the length of each block side or diagonal.

$$k_{i+\frac{1}{2}} = \frac{1}{[(x_{i+1} - x_i)^2 + (y_{i+1} - y_i)^2 + (z_{i+1} - z_i)^2]^{\frac{p}{2}}}$$

The variable p controls the stiffness of the springs; the higher the value of p the stiffer the springs connecting the blocks and the more constrained the block corners. Block corner positions are determined by a solution of the static equilibrium problem.

At the predictor step, the new displacements are approximated:

$$\begin{aligned} (\bar{\delta x})_{i,j,k} &= 2(\delta x)_{i,j,k}^n - (\delta x)_{i,j,k}^{n-1} \\ (\bar{\delta y})_{i,j,k} &= 2(\delta y)_{i,j,k}^n - (\delta y)_{i,j,k}^{n-1} \\ (\bar{\delta z})_{i,j,k} &= 2(\delta z)_{i,j,k}^n - (\delta z)_{i,j,k}^{n-1} \end{aligned}$$

The corrector step is given by

$$\begin{aligned} (\delta x)_{i,j,k}^{n+1} &= \frac{k_{i+\frac{1}{2},j,k}(\bar{\delta x})_{i,j,k} + \dots + k_{i,j,k-\frac{1}{2}}(\bar{\delta x})_{i,j,k-1}}{k_{i+\frac{1}{2},j,k} + \dots + k_{i,j,k-\frac{1}{2}}} \\ (\delta y)_{i,j,k}^{n+1} &= \frac{k_{i+\frac{1}{2},j,k}(\bar{\delta y})_{i,j,k} + \dots + k_{i,j,k-\frac{1}{2}}(\bar{\delta y})_{i,j,k-1}}{k_{i+\frac{1}{2},j,k} + \dots + k_{i,j,k-\frac{1}{2}}} \end{aligned}$$

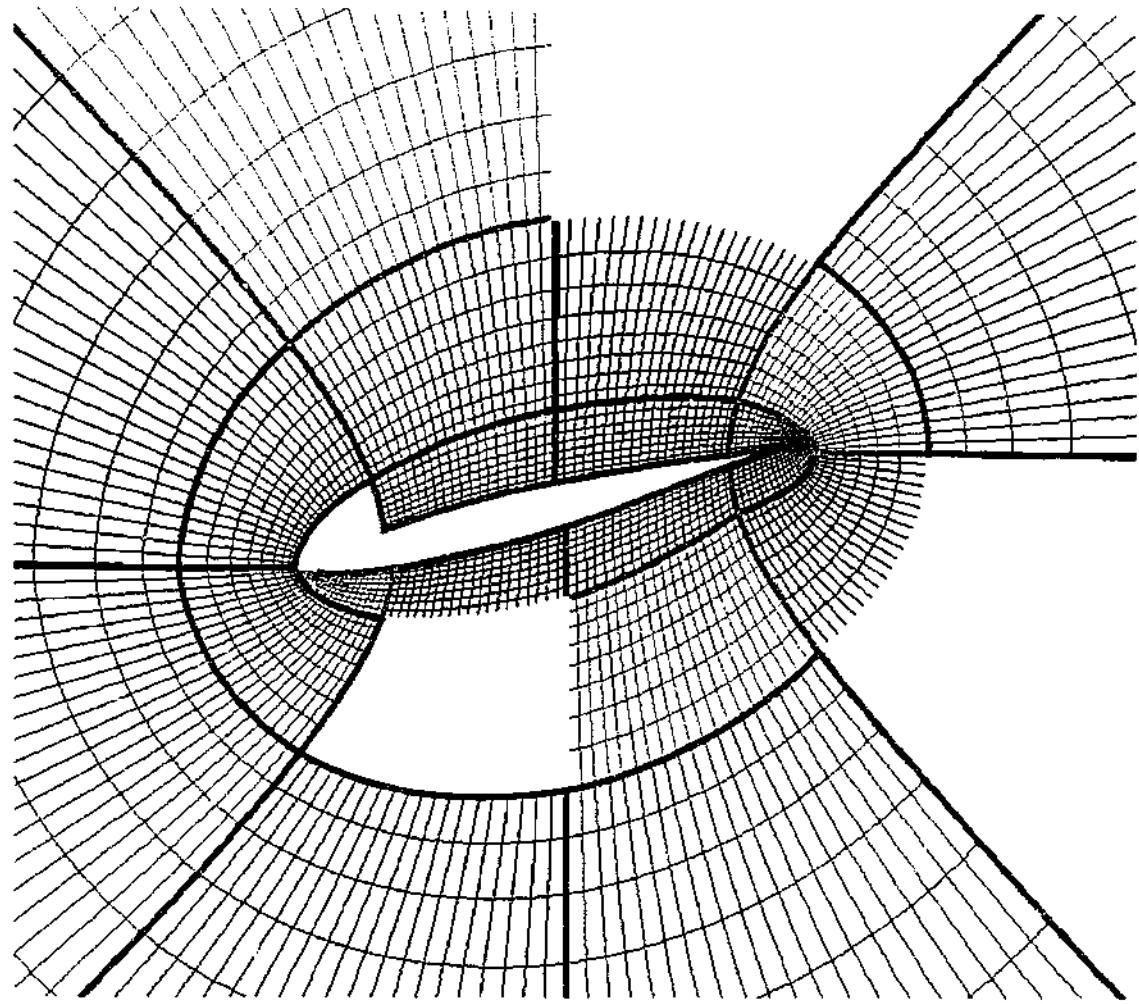


Figure 4.5: Deformed mesh for NACA64A010.

$$(\delta z)_{i,j,k}^{n+1} = \frac{k_{i+\frac{1}{2},j,k}(\bar{\delta z})_{i,j,k} + \dots + k_{i,j,k-\frac{1}{2}}(\bar{\delta z})_{i,j,k-1}}{k_{i+\frac{1}{2},j,k} + \dots + k_{i,j,k-\frac{1}{2}}}$$

The predictor and corrector scheme is applied in an iterative manner until the system is in static equilibrium. Once the new corner displacements are calculated, they are broadcast to each corresponding block.

The solution time required for the mesh regeneration is small compared to the time required for solution of the Navier-Stokes equations and turbulence model. An example of the deformed mesh for the NACA64A010 airfoil is shown in Figure 4.5. Note that although the deflection of the airfoil is much larger than considered in any of the validation test problems, it demonstrates the effectiveness of the moving mesh implementation.

4.5 Coupling and Model Integration

As discussed in Chapter 2, often in the modelling of aeroelastic problems the method of sub-cycling is appropriate due to the different rates of convergence of the structural and fluid domains. Usually more iterations are performed on the fluid field per real time step. The solution process is illustrated in Figure 4.6. One real time step is made up of a number of sub-cycles. Within a structural sub-cycle, the position of the structure is updated a number of times. For the fluid field, a number of iterations are required before the pressure field at the structural interface changes enough to influence the structural model. The optimal number of cycles for each field is problem dependant, however for the Isogai model presented in Chapter 5, 10 multigrid cycles were performed per structural iteration and 5 structural cycles were performed per real time step.

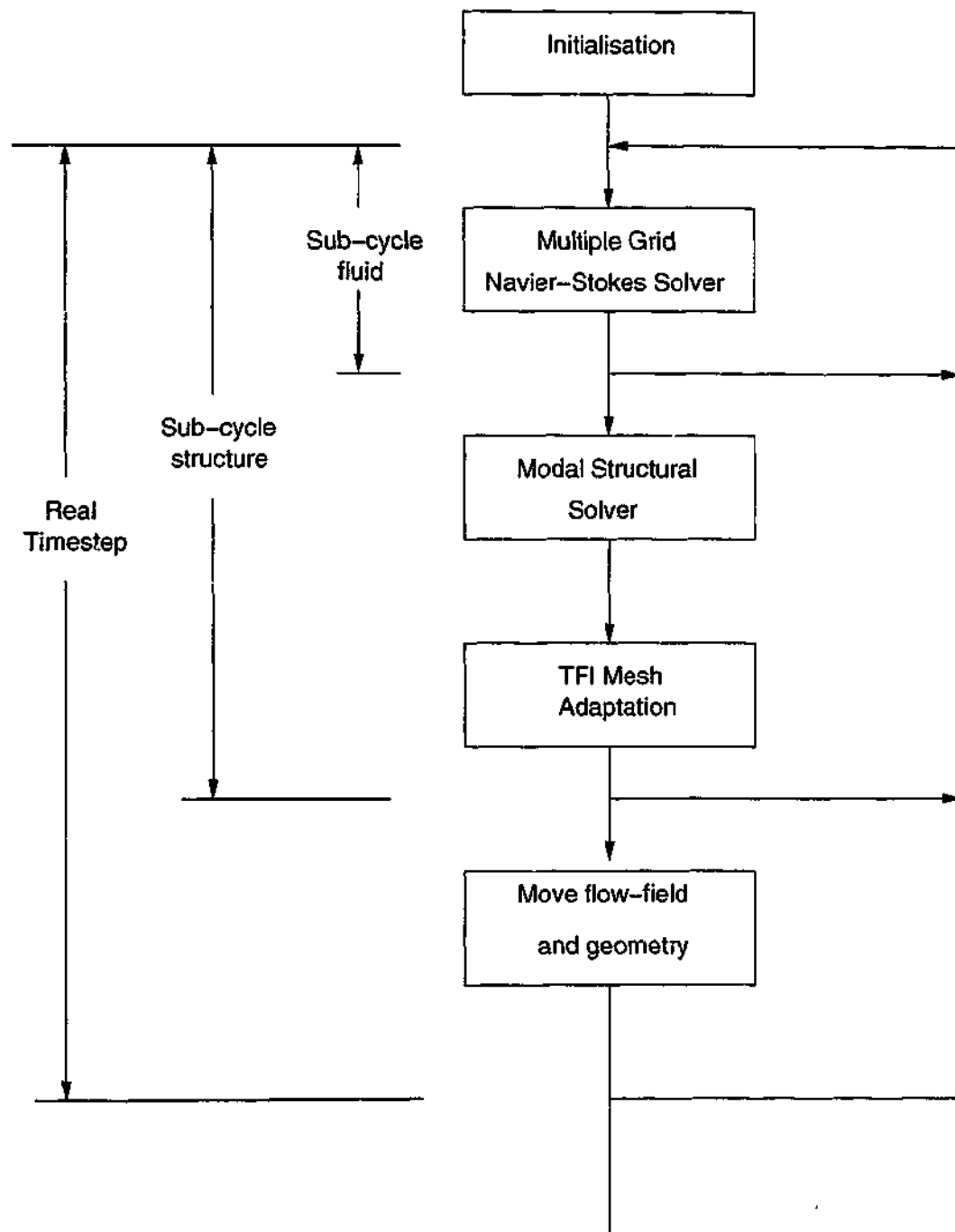


Figure 4.6: Integration of fluid and structure models.

Chapter 5

Validation of Computational Model

During the course of research a code has been developed to model unsteady gas and structural dynamics. With the implementation of the new routines it was necessary to test or validate the code. This helps to identify errors in the implementation that may not be obvious when the code is applied to more complex geometries. Test or validation cases are intended to be as simple as possible whilst at the same time providing data that may be compared with existing experimental or theoretical results. The ideal case is where a physical flow process can be isolated and analysed in comparison with experiment or theory.

The majority of the validation cases have been used by other authors with similar algorithms. However it is useful as it provides an estimate of the code's ability to model flow and the magnitude of deviation from experimental measurements. This also develops confidence in the predictions made for the more complex cases that are considered herein.

5.1 Laminar Flat Plate

The classical, theoretical analysis of 2-dimensional boundary layer flow involves flow over a flat plate for both laminar and turbulent flow regimes (White, 1994). In the case of laminar flow the boundary layer equations may be used to approximate the Navier-Stokes equations. Blasius derived an exact solution for the velocity and showed that the velocity profile is a function of the dimensionless variable η .

$$\frac{u}{U_\infty} = f'(\eta) \quad \eta = y\sqrt{\frac{U_\infty}{\nu x}}$$

This leads to an analytic solution for the skin friction c_f .

$$c_f = \frac{0.664}{\sqrt{Re_x}}$$

The flat plate is modelled by a 2-dimensional rectangular domain with an inlet and an outlet at the two sides and the plate at the top and bottom, separated by a distance of 50% of plate chord. The plate leading edge is 10% of chord from the inlet and the outlet is at the plate trailing edge. Periodic boundary conditions were applied at the top and bottom of the domain between the inlet and the plate trailing edge and slip conditions were applied to the boundaries in the span-wise direction, orthogonal to the plane of the flow. The mesh of dimensions $448 \times 160 \times 2$ was generated by stretching in the direction parallel to the flow and the cross-flow direction with cells concentrated at the plate leading edge and surface. Flow conditions were a Reynolds number of 53131 and an outlet Mach number of 0.3. The computational grid was divided into 16 blocks, 4 blocks in the flow direction and 4 in the cross-flow direction. Post-processing involved transforming from a multiple block domain to a single block domain before calculating flow properties.

A comparison is made between the computed and theoretical skin friction for the laminar regime in Figure 5.1. The Blasius equation may be integrated numerically to provide a relationship between velocity profile and a non-dimensional distance from the wall (White, 1994). The deviation between theory and the computed result at the leading edge of the plate may be attributed to the discontinuity in velocity and the singularity in the analytical solution of the Navier-Stokes equations at this point. Toward the trailing edge the skin friction is over predicted. This is probably due to the effects of blockage of the boundary layer and the axial pressure gradient. A comparison of velocity profile through the boundary layer for various axial positions along the plate is made with the analytic solution in Figure 5.2. The largest discrepancy is found at the middle region of the boundary layer and this may once again be due to boundary layer blockage effects. Other potential sources of deviation include a small compressibility of the flow and the effects of the artificial dissipation scheme. The JST artificial dissipation scheme was used for the present simulation.

5.2 Turbulent Flat Plate

The turbulent flat plate is similar to the laminar flat plate, in that it is one of the simplest ways to investigate 2-dimensional boundary layer flows. With the development of the flow solver from single block to multiple block, it was necessary to change the storage of the turbulence quantities from cell vertex to cell centred. It was also necessary to check that the results for the simulations were continuous over block boundaries.

The smooth flat plate in the turbulent regime may be analysed based on the momentum integral equation of boundary-layer theory. This provides a relationship between the characteristic parameters of the boundary layer, between the displacement thickness, momentum thickness and shear stress at the wall. The same law of velocity distribution in a pipe leads to the same velocity distribution in the boundary layer of a flat plate which is found to be in

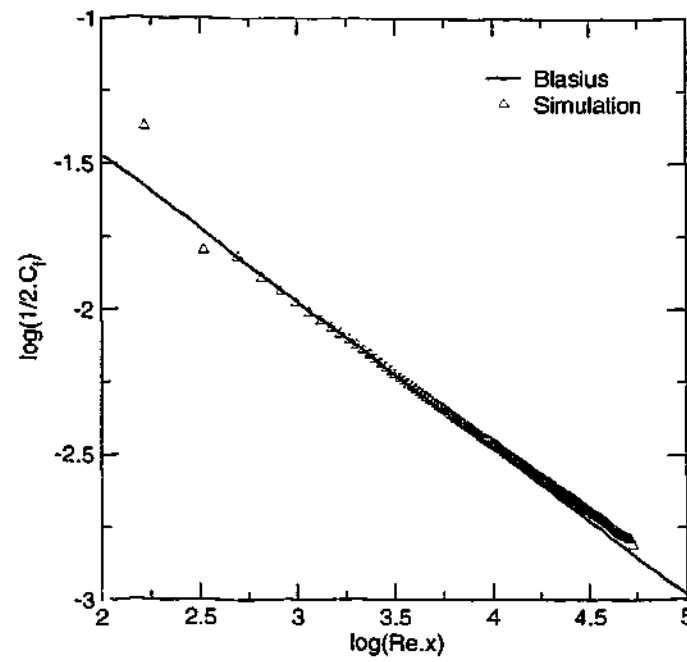


Figure 5.1: Skin friction coefficient for a flat plate for laminar flow regime.

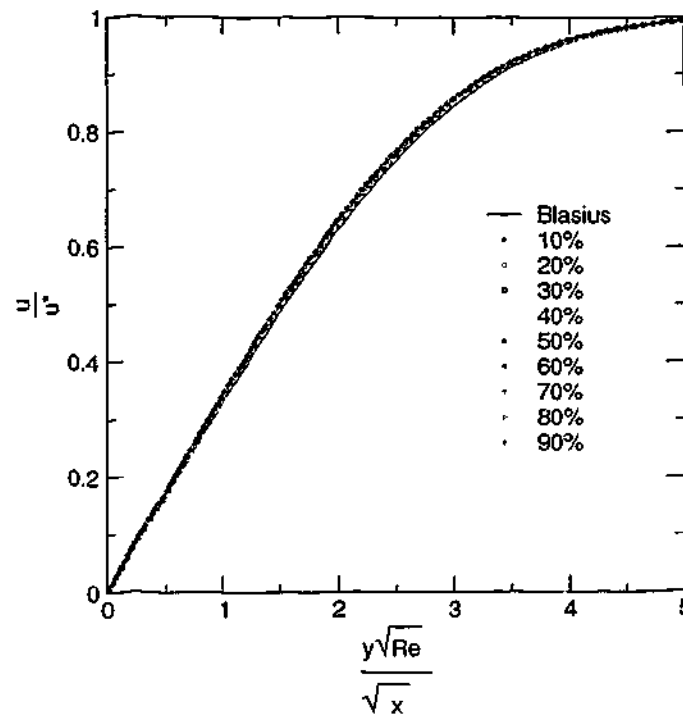


Figure 5.2: Boundary layer profile for a flat plate in laminar regime and theory.

agreement with experimental measurements (Schlichting, 1968). The skin friction is given by Prandtl

$$c_f = \frac{0.074}{(Re \cdot x)^{1/2}}.$$

The velocity distribution through the boundary layer is also developed from pipe flow theory and may be approximated by the function

$$\frac{u}{U_\infty} \approx \frac{1}{\kappa} \ln \frac{yu^*}{\nu} + B,$$

where $\kappa = 0.41$ and $B = 5.0$ (White, 1994).

The geometry of the simulation was similar to the laminar flat plate, except that the stretching distribution for the mesh was slightly different. The Reynolds number was $Re = 4.53 \times 10^5$. The same mesh dimensions of $448 \times 160 \times 2$ were used and divided into 16 blocks, 4 blocks in the flow direction and 4 in the cross-flow direction. One of the block boundaries was positioned at approximately $y^+ = 2$. A comparison of the skin friction in Figure 5.3 provides a reasonable match with theory, except for close to the plate leading edge. The deviation in gradient of the skin friction may be due to blockage effects. The velocity profile in Figure 5.4 also compares well, except for the profiles at 10% and 90% from the leading edge. Deviations in these regions are probably due to proximity to the domain boundaries. The profile of the inner layer region is consistent with the logarithmic law of the wall.

5.3 Isolated cylinder

The behaviour of the low Reynolds number, unsteady cylinder flow that exhibits a vortex street is well documented. It is a useful case to check the implementation of the time-accurate solver.

A four block O-grid was generated with the far-field boundary approximately 50 diameters from the cylinder surface. The far-field was placed at this distance to avoid interaction with the cylinder flow. The code may only calculate for 3-dimensional mesh geometries, so 2 cells were used in the span-wise direction. The Mach number of the compressible solver was in the region of 0.2 as at this Mach number the effects of compressibility are assumed to be negligible. A number of parameters have been compared with those from experiment (Barkley & Henderson, 1996) and other simulations (Reichl, 2001) in Table 5.1 for a Reynolds number of 190.

The drag coefficient C_D is the time average value, and the coefficients C'_D and C'_L are the

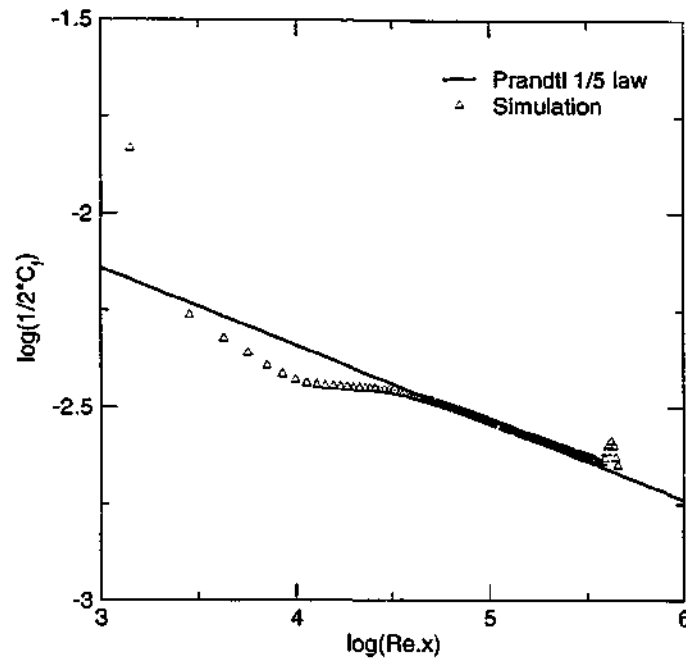


Figure 5.3: Skin friction coefficient for a flat plate with $k-\omega$ turbulence model simulation and theory.

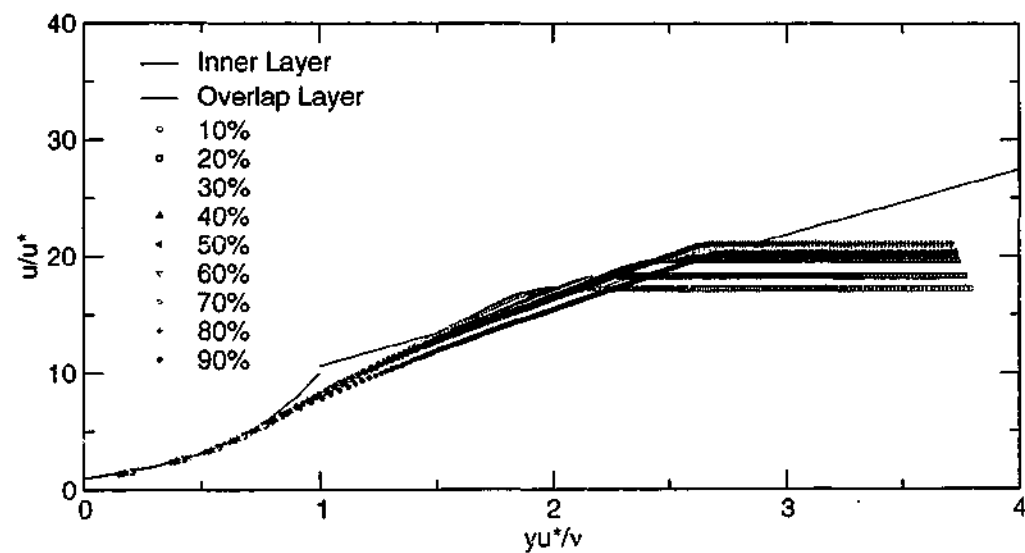
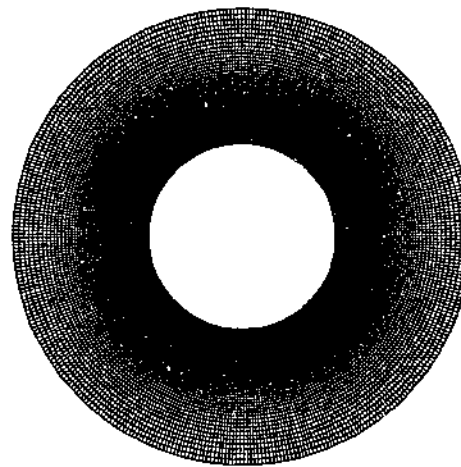


Figure 5.4: Boundary layer profile for a flat plate with $k-\omega$ turbulence model simulation and theory.

| | C_D | C'_D | C'_L | Strouhal |
|--|-------|--------|--------|----------|
| Barkley & Henderson (1996) | 1.344 | 0.0293 | 0.465 | 0.195 |
| Reichl (2001) | 1.335 | 0.0262 | 0.435 | 0.191 |
| JST, mesh $384 \times 192 \times 2$, 60 time steps | 1.257 | 0.0249 | 0.431 | 0.192 |
| JST, mesh $384 \times 192 \times 2$, 40 time steps | 1.256 | 0.0236 | 0.421 | 0.191 |
| CUSP, mesh $384 \times 192 \times 2$, 40 time steps | 1.269 | 0.0251 | 0.419 | 0.193 |
| JST, mesh $256 \times 128 \times 2$, 40 time steps | 1.261 | 0.0245 | 0.426 | 0.194 |
| JST, mesh $192 \times 96 \times 2$, 40 time steps | 1.245 | 0.0257 | 0.433 | 0.192 |

Table 5.1: Comparison of circular cylinder simulation parameters.

Figure 5.5: Inner mesh for isolated cylinder of dimensions $384 \times 198 \times 2$.

RMS values for unsteady drag and lift respectively. In the first column, the number of time steps is the approximate number of implicit time steps per shedding period. The Strouhal number was calculated for the simulations by fitting a cubic polynomial to the four closest points to a minimum and maximum of the lift coefficient in the shedding cycle and interpolating the extrema. The time difference between successive extrema may be calculated and thus the Strouhal number – this is the method advocated by Reichl (2001) for calculating the Strouhal number for numerical simulations of cylinder shedding flows.

The inner part of the mesh for the finest mesh of dimensions $384 \times 198 \times 2$ is shown in Figure 5.5. A plot of the instantaneous vorticity is shown in Figure 5.7 and the time evolution of the unsteady lift and unsteady drag for the finest JST simulation is shown in Figure 5.6. The simulation reached a periodic state after 10 shedding periods.

A small variation in the unsteady parameters may be observed over the different smoothing schemes and mesh geometries. Compared to the other numerical simulations, the quantity exhibiting the largest deviation is the average drag coefficient. Overall the comparison demonstrates the ability of the code to simulate unsteady flows, in particular the predicted

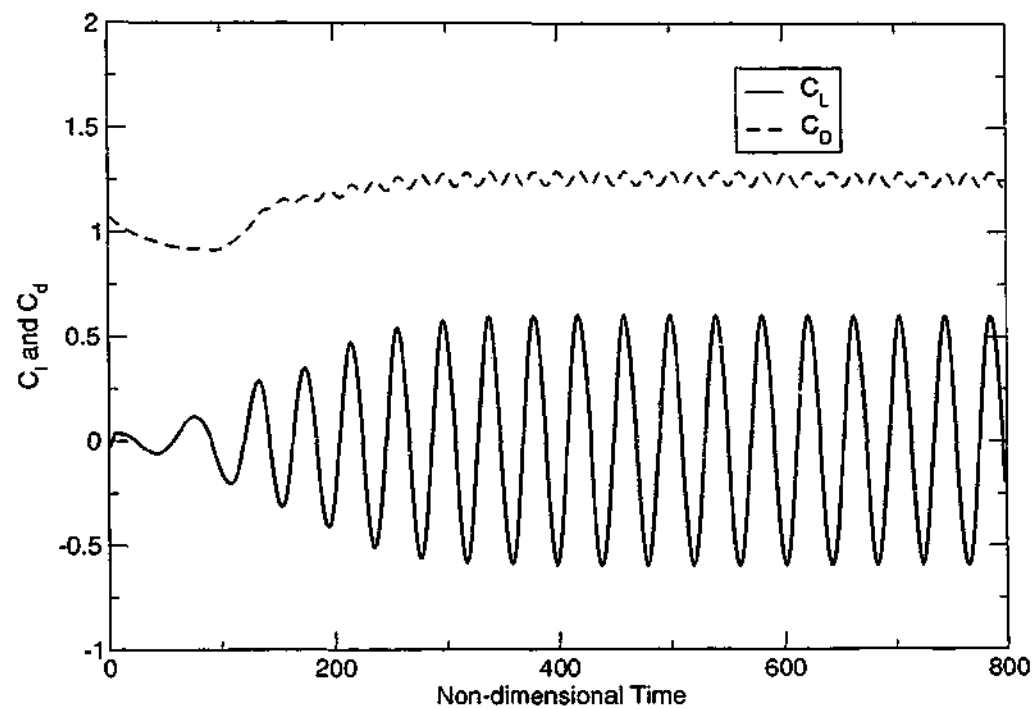


Figure 5.6: Time evolution of unsteady lift and unsteady drag for circular cylinder.



Figure 5.7: Vorticity plot for isolated cylinder at $Re = 190$.

Strouhal number. There is however a 7% difference in the drag coefficient - this could be due to the flow compressibility.

5.4 Isolated Airfoil

The circular cylinder provides a useful comparison with experimental, unsteady data. However most turbine configurations involve flow in the high subsonic and transonic flow regimes. A number of unsteady experimental measurements have been made for the NACA64010 airfoil in forced oscillation (Davis, 1982). This provides a useful test of the moving grid and unsteady implementation under flow conditions that are closer to those found in a turbine passage.

The 2-dimensional configuration involves the NACA64010 airfoil that is forced to oscillate about a pitching axis at quarter chord. Simulation conditions are free-stream $Ma_\infty = 0.796$, static temperature $T_\infty = 300^\circ K$, reduced frequency $k_c = 0.202$ and an oscillation amplitude of $\Delta\alpha = 1.01^\circ$. The experimental Reynolds number was $Re = 12.56 \times 10^6$.

A 2-dimensional grid was generated for the NACA64A010 profile using "nearly" conformal mapping (Thompson *et al.*, 1985). It is difficult to generate an O-grid for the airfoil case using conventional finite difference methods coupled with systems of equations, due to the discontinuity of the airfoil surface at the trailing edge. Conformal mapping involves a coordinate transform so that the mesh may be generated in a more regular domain. The airfoil surface is mapped to a near circle through a Karman-Trefftz transformation, effectively smoothing out the trailing edge region in the transformed plane. Stretching functions are used to distribute the mesh points in this coordinate system. Upon transformation back to geometric space, a smooth grid is produced. The mesh was generated by a code written by Jameson and has been used for simulations in other work (Alonso & Jameson, 1994).

5.4.1 Steady and Inviscid Simulations

A 3-dimensional grid is produced by stacking the 2-dimensional mesh in the span-wise direction. The inner region of the $160 \times 32 \times 2$ mesh used for the inviscid calculations is shown in figure 5.8. The far-field is placed at about 25 chords from the airfoil surface and is approximately circular. Far-field boundary conditions are applied at the outer regions, whilst tangential inviscid conditions are applied at the boundaries in the span-wise direction and at the airfoil surface.

To investigate the validity of the moving mesh algorithm, three different configurations were chosen. The first involves a four block mesh that rotates rigidly with the airfoil. Secondly, the outer boundary is fixed, and the TFI routines are used to adapt a four block mesh to the movement of the airfoil. The third configuration involves 32 computational blocks

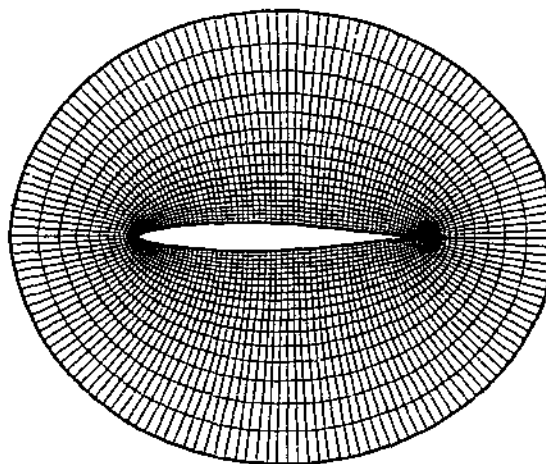


Figure 5.8: Inner region of mesh used for inviscid simulation of NACA64A010 airfoil.

and the spring network is used to locate block corners, with TFI to regenerate the mesh. The 32 block mesh has eight blocks in the circumferential direction and 4 in the radial direction. Results for unsteady lift are close to being identical and are compared in Figure 5.9. The dimensions of the mesh are denoted in the legend, the number of blocks is the first dimension, then the number of cells in the i direction, the j direction and k direction respectively.

The accuracy of the temporal and spatial discretisation of the numerical algorithm was investigated through analysis of the L2 norm. The L2 norm was calculated by taking the square root of the average of the square of the differences between a quantity and a reference quantity for a series of spatial or temporal resolutions. The gradient of the log of the metric versus the log of the L2 norm over the different resolutions in time or space provides an indication of the accuracy of the discretisation.

For the investigation of spatial accuracy, differences were defined as being between the surface pressure coefficient and some reference solution. Given that the exact solution for this problem is not known, three different reference solutions were used. The first was calculated through Richardson extrapolation of the calculated surface pressure coefficients for the two finest grids. The next was the next successively fine grid in the grid sequence. In another the finest grid solution was taken as the reference.

Coarser grids were generated by removing every other point in both coordinate directions in the plane of the airfoil. The finest grid was $256 \times 256 \times 2$. Successively coarse grids were of dimension $128 \times 128 \times 2$ and so on. All simulations were performed on a single block grid. The maximum residual of the simulation reduced by four orders magnitude for the CUSP smoothing and five orders for JST. It was found that sufficient resolution could not be provided for a high subsonic airfoil case with a shock at mid-chord. Resolution was required in two different regions – mid-chord and at the leading edge and this could not be provided

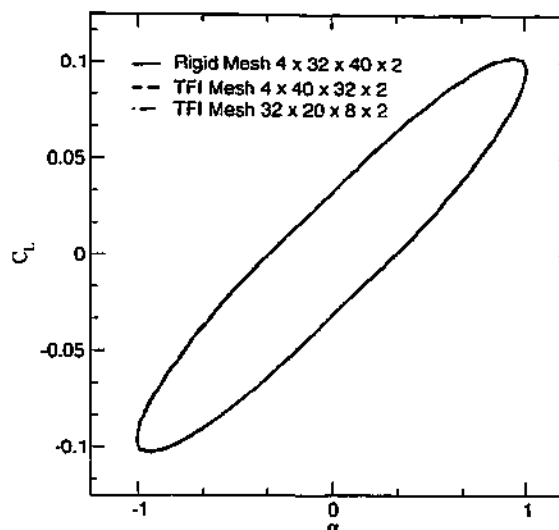


Figure 5.9: Validation of moving mesh implementation with NACA64A010 airfoil.

by the present grid generation method. Thus the lower far-field Mach number of $Ma_\infty=0.5$ was used in the present simulations. The grid was concentrated toward the leading edge and the trailing edge point was excluded from the calculation of the L2 norm, as the sharp trailing edge led slow convergence in this region. Figure 5.10 is a comparison between JST and CUSP smoothing schemes. The slope of these lines is of the order of 2.

The pressure distribution for the two dissipation schemes for a far-field Mach number of $Ma_\infty=0.5$ is compared with experiment for the two smoothing schemes in Figure 5.11. Note that the shock resolution for the CUSP scheme appears to be higher, in that the gradient of the pressure coefficient is higher in the region of the shock wave. The overshoots before and after the shock in the pressure coefficient are also less significant for the CUSP scheme.

The temporal accuracy was investigated for the second order accurate implicit operator. This investigation involved a comparison of the unsteady lift for the airfoil throughout the pitching cycle. For the comparison, four different simulations were used, the finest having 128 steps per period. The coarser simulations in time used half the number of time steps of the finer time resolutions. This case exhibited a temporal accuracy of approximately 2.5.

A comparison was also made between the unsteady lift coefficients for the two smoothing schemes and this is shown in Figure 5.13. The differences in shock resolution and the fact that it is the shock movement that produces the hysteresis in the unsteady lift coefficient produces a significant disparity between the two schemes in unsteady simulations of high subsonic and inviscid flow. This highlights the importance of resolving the flow phenomena to obtain more realistic simulation results.

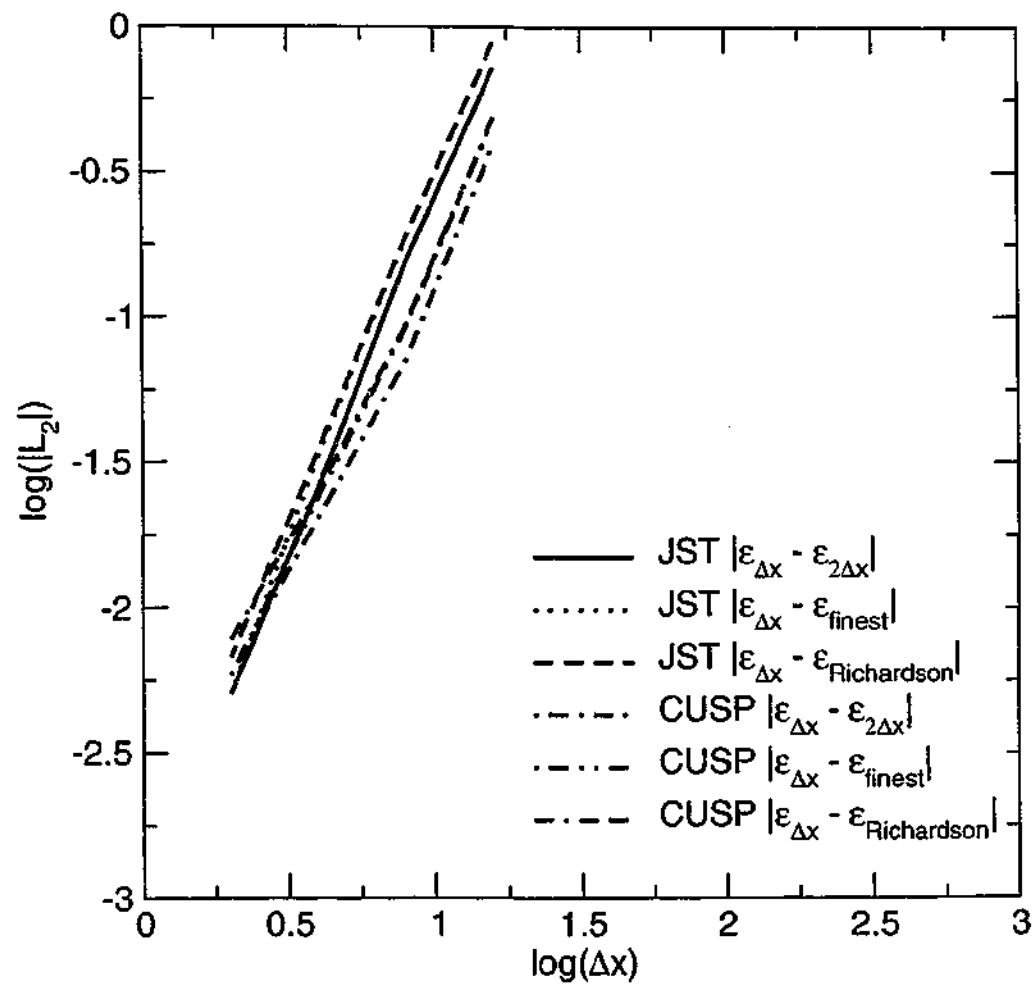


Figure 5.10: Spatial resolution study for NACA64A010 airfoil.

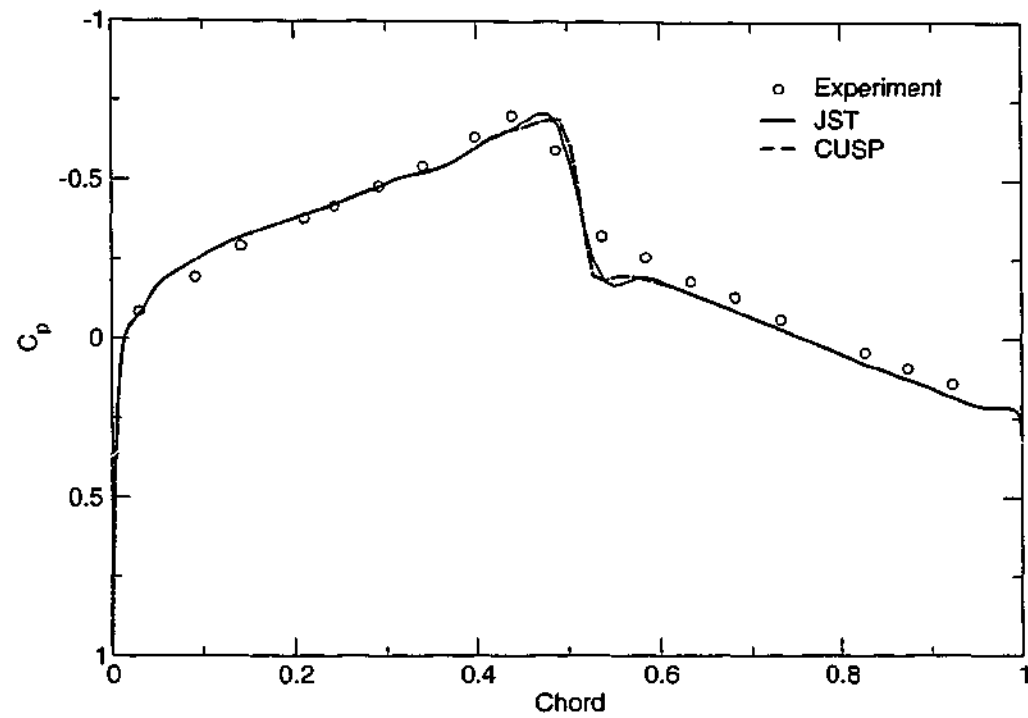


Figure 5.11: Spatial resolution study for NACA64A010 airfoil.

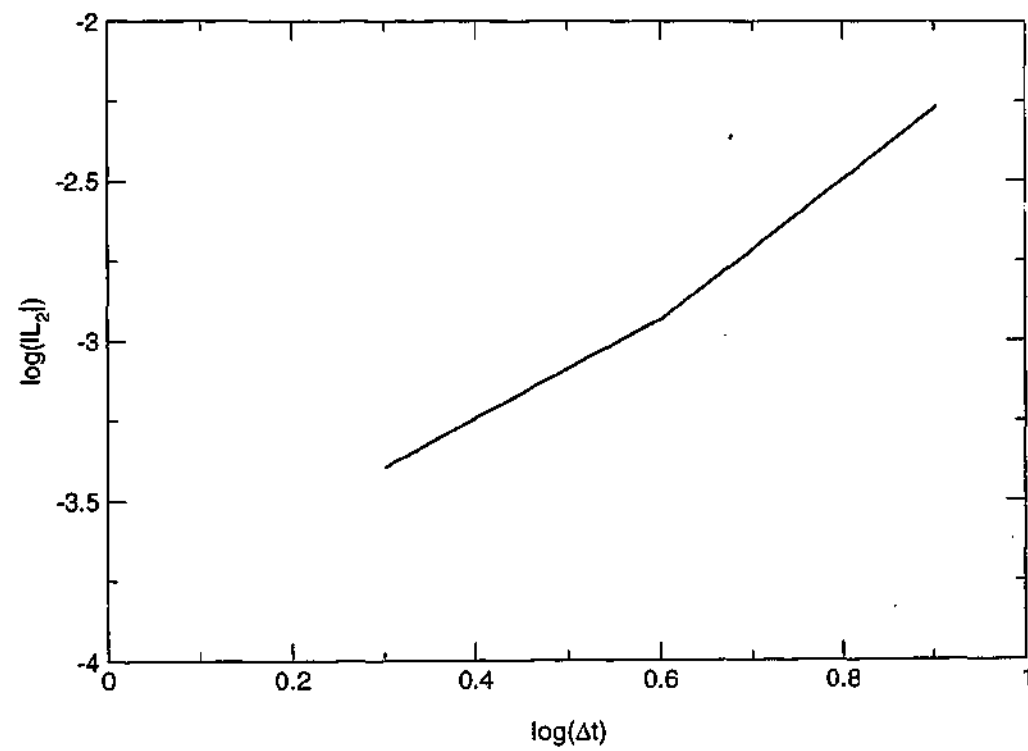


Figure 5.12: Temporal resolution study for NACA64A010 airfoil.

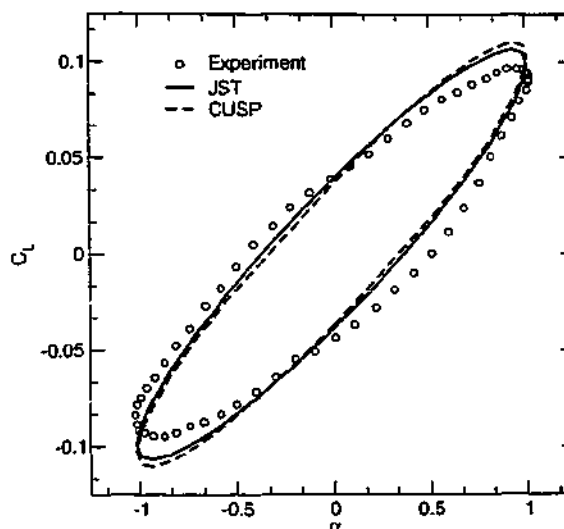


Figure 5.13: Comparison of smoothing schemes for NACA64A010 airfoil.

5.4.2 Navier-Stokes Simulations

This is the first case used to test the unsteady implementation of the turbulence model. The Navier-Stokes simulations for the NACA64A010 airfoil required a grid different to that used in the inviscid simulations. The number of cells was doubled in the radial direction and the grid is further refined in the proximity of the airfoil surface. Although it is recommended that the mesh spacing at the surface of a body should have $y^+ < 1$, this was not found to be necessary for this particular case. A number of meshes of different dimensions were used, including $64 \times 160 \times 8$ and $97 \times 160 \times 8$ and $128 \times 160 \times 8$. All produced similar results for unsteady lift coefficient. A comparison between the Navier-Stokes, inviscid simulations and experiment is shown in Figure 5.14.

5.5 Naca64 in Coupled Simulation

The modelling of coupled aeroelasticity requires the simulation of the interaction of an elastic member with an unsteady flow. One of the simplest examples is Isogai's wing model (Isogai, 1979; Isogai, 1981), a 2-dimensional NACA64A010 airfoil that has been studied numerically by a number of authors (Alonso & Jameson, 1994; Liu *et al.*, 2000). The structural response is determined by integrating the coupled model structural equations given the instantaneous lift and moment on the airfoil that is provided by the flow solver. In terms of the aeroelastic model classification, this is a partially integrated approach where sub-cycling of the fluid is employed.

The model of the wing is shown in Figure 5.15. A torsion spring is connected to the pitching axis and a linear spring is connected to the plunging axis of the NACA64010 airfoil

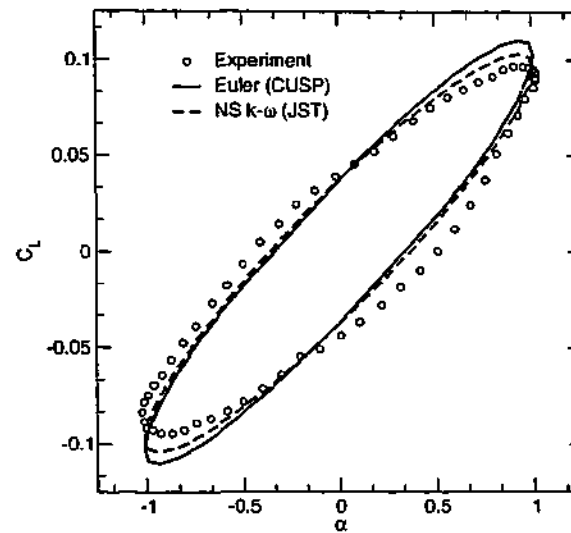


Figure 5.14: Validation of unsteady $k-\omega$ implementation with NACA64A010 airfoil.

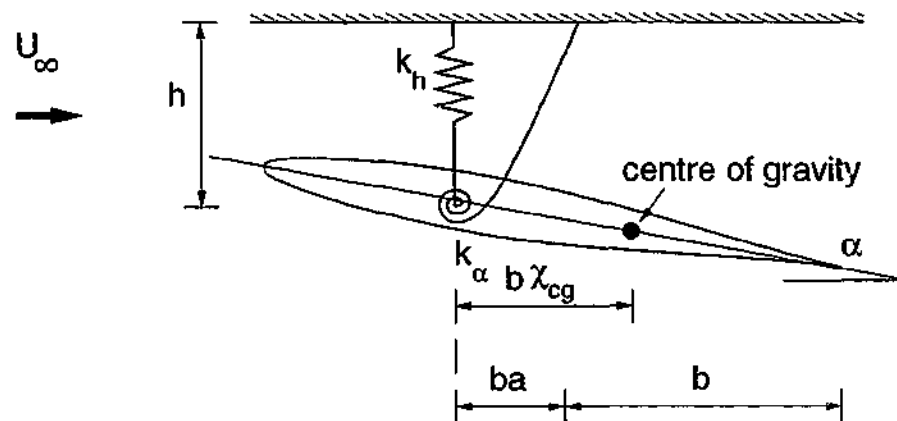


Figure 5.15: Isogai wing model

section. In this particular model, the pitching axis is well forward of the airfoil leading edge. This configuration leads to structural instabilities typically found in the swept back wings of fighter planes (Isogai, 1981). The wall at the top of Figure 5.15 is to indicate that the springs are attached to a stationary reference plane and the wall plays no role in the fluid model. The airfoil is isolated in that the far-field boundaries are approximately 25 chords from the airfoil surface. The model involves a mass ratio of $\mu_m = 60$ m, natural frequencies $\omega_\alpha = 100$ rad/s and $\omega_h = 100$ rad/s, distance from pitching axis to leading edge $a = -2.0$ m. The distance between the centre of gravity and the pitching axis is $\chi = -0.2$ m and b is the semichord, or half the true chord.

The structural model is similar to the simple spring mass problem, involving one equation for the linear inertial terms and another for rotational inertia.

$$m\ddot{h} + S_\alpha\ddot{\alpha} + k_h h = -L$$

$$S_{\alpha}\ddot{h} + I_{\alpha}\ddot{\alpha} + k_{\alpha}\alpha = M$$

These equations may be decoupled using modal analysis discussed in Section 3.2.2. This results in two second order differential equations in modal coordinates,

$$\ddot{q}_i + \omega_i^2 q_i = Q_i \quad (5.1)$$

where the modal coordinates are obtained by multiplying by the corresponding mode shape that involves the normalised mass matrix. The second order differential equation is further reduced to two first order equations that are solved using the structural solver.

The section is held by a pin at the torsion axis and forced for one period of oscillation whereupon the pin is released and the amplitudes of pitching and plunging are observed. The behaviour depends on the non-dimensional parameter of flutter velocity that contains the mass ratio and the reduced frequency,

$$V_f = \frac{U_{\infty}}{b\omega_{\alpha}\sqrt{\mu}} = \frac{1}{k_{\alpha}\sqrt{\mu}} \quad (5.2)$$

During the investigation, the parameter of flutter velocity was varied while the far-field Mach number was kept constant. Other geometric parameters such as wing chord, rotation axis, moment of inertia and hence mass also remained constant. Effectively this is equivalent to changing the spring constant k_{α} , or the stiffness of the spring mass system. The behaviour of the configuration is dominated by the ratio of the aerodynamic force to the combined force due to the spring and mass inertia. Given the natural frequency of the spring on the torsional axis,

$$\omega_{\alpha} = \sqrt{\frac{k_{\alpha}}{I_{\alpha}}}$$

the flutter velocity in terms of the spring constant and flow parameters is

$$V_f = \frac{\sqrt{\rho_{\infty}U_{\infty}}}{b\sqrt{\frac{m}{\pi b^2}}} \cdot \sqrt{\frac{I_{\alpha}}{k_{\alpha}}} \quad (5.3)$$

If one holds the Mach number constant and thus the flow parameters, an increase in the flutter velocity leads to a lower spring constant, thus there is less spring force to resist the instability provided by the force of the fluid. A decrease in this parameter increases the spring force and increases the stabilising effect of the spring. If the square of the flutter velocity is regarded, and the force due to aerodynamics is considered proportional to the free stream dynamic pressure and the force due to the spring is proportional to the spring constant,

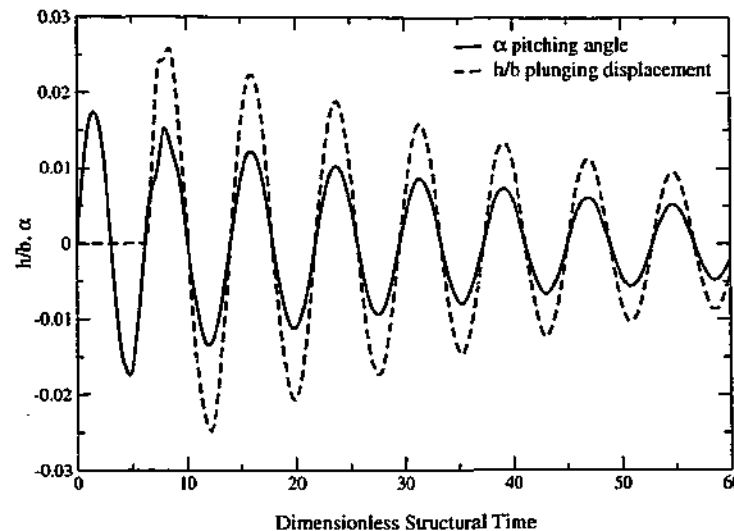


Figure 5.16: Coupled simulation for NACA64A010 airfoil – damped configuration $Ma_\infty = 0.825$, $V_f = 0.530$.

$$V_f^2 = \frac{\rho_\infty U_\infty^2 r_\alpha^2 b^2 \pi}{k_\alpha} \propto \frac{\text{Aerodynamic force}}{\text{Spring force}}$$

Once again this assumes that the parameters of semi-chord length and distance between the airfoil centre of gravity to rotation axis remain unchanged.

However there is not a simple one-to-one relationship between Mach number and flutter velocity for flutter boundary over the whole parameter space. This is due to the way in which the two degrees of freedom couple at particular Mach numbers. An example of neutrally stable, unstable and damped configurations and results are shown in Figures 5.16 to 5.18.

A plot of the predicted flutter boundary of the configuration is shown in Figure 5.19, the point at which the configuration changes from being stable to unstable. This result compares well with results from other authors (Alonso & Jameson, 1994).

This case was also computed with the Navier-Stokes and $k-\omega$ flow model. A comparison between the flutter boundary for the inviscid and viscous simulations is shown in Figure 5.20. It appears that the inclusion of viscous effects tends to damp the system, leading to a higher flutter boundary curve. Thus a lower spring force is required at lower Mach numbers for system stability.

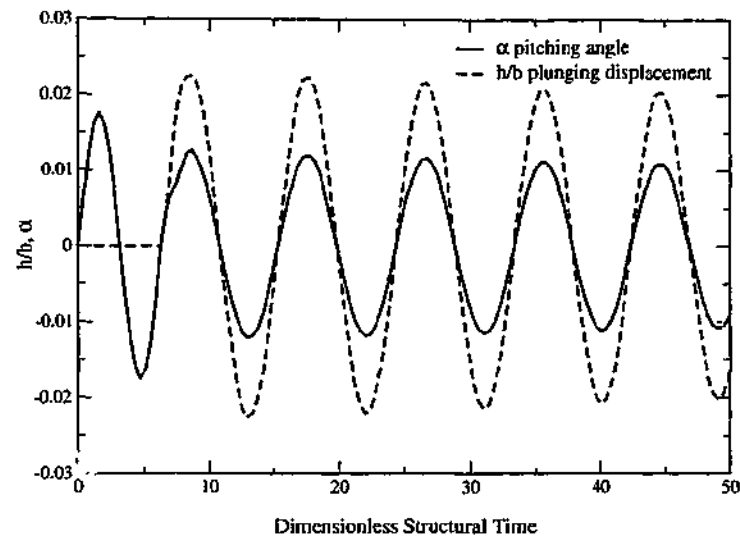


Figure 5.17: Coupled simulation for NACA64A010 Airfoil – stable configuration $Ma_\infty = 0.825$, $V_f = 0.630$.

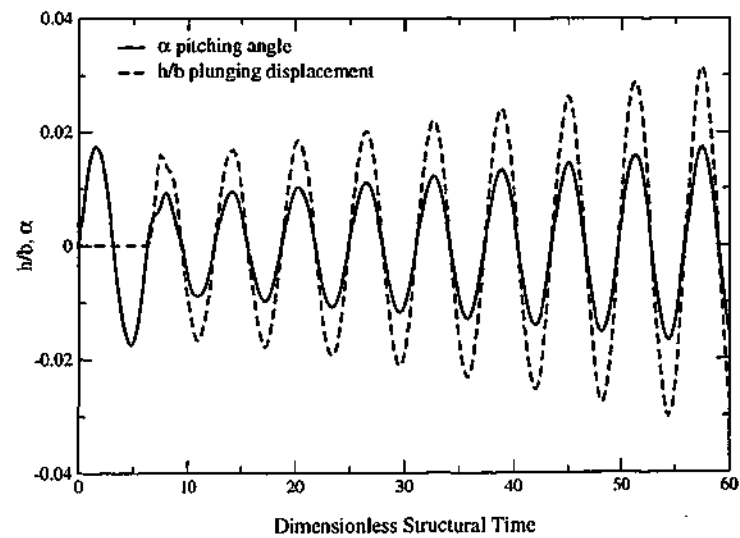


Figure 5.18: Coupled simulation for NACA64A010 Airfoil – unstable configuration $Ma_\infty = 0.825$, $V_f = 0.725$.

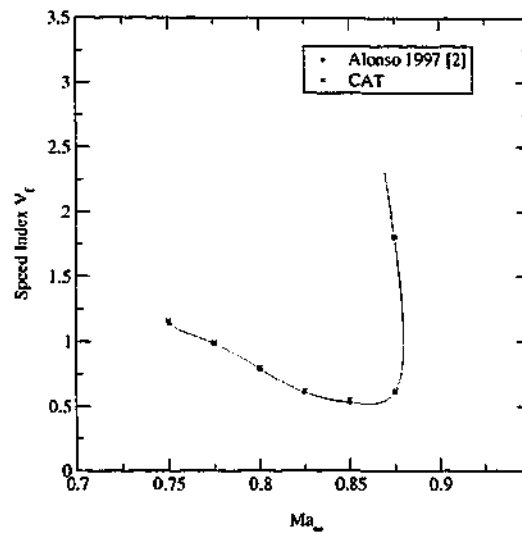


Figure 5.19: Flutter boundary for Isogai wing mode with Euler flow model.

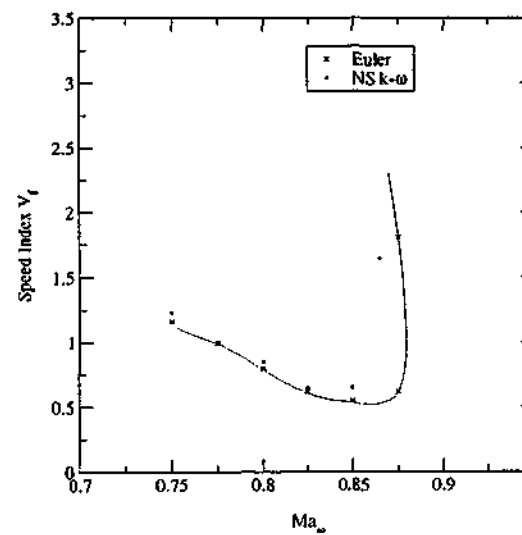


Figure 5.20: Comparison of flutter boundary for Isogai case for different flow models.

5.6 Grid Independence

An important aspect of numerical simulation is the dependence of the result on the grid geometry. For high resolution studies that are independent of the grid, a certain number of points are required in regions of high gradients of the flow quantities. In inviscid simulations performed in the transonic or supersonic regimes, often shock-waves are present. There are high gradients in the region of the shock front and stagnation points; to resolve both the shock position and shock strength the grid must be sufficiently fine in these regions.

The level of resolution of flow features will depend on the parameter under investigation. For example, the flutter boundary of the coupled case in Section 5.5 can be computed successfully with a relatively coarse grid. However where the unsteady lift of the airfoil is compared to experiment in the previous section, more grid resolution is required.

Where the effects of viscosity are included in the simulation, boundary layers form in regions close to solid bodies. High gradients exist in the cross-stream direction both in flow variables and turbulence quantities. In fact, for perfectly smooth walls, the value of the rate of turbulence dissipation ω becomes singular. Discontinuities can exist over turbulent and non-turbulent interfaces such as found in jet flow.

After over a decade of use, it has been found that where the k - ω model is integrated through the viscous sublayer, the distance of the first point from the wall should be such that $y^+ < 1$ (Wilcox, 2000). Grid resolution studies were performed on all of the cases presented to ensure that the parameter under consideration was relatively grid insensitive. The value of y^+ was varied above and below unity and results compared. For the higher speed flows such the isolated airfoil with an $Ma = 0.7$ and for the turbine cases an exit $Ma = 1.3$, $y^+ = 5$ was sufficient for a grid independent solution.

Other flow structures may also be sensitive to grid resolution. Stream-wise secondary flows such as hub and casing vortices may dissipate down stream if they are not sufficiently resolved. It is possibly the most difficult to ensure the resolution of these types of flow features as they are 3-dimensional and may migrate away from the boundaries toward the mid-passage region. These regions are usually the least well resolved, due to the constraints on processing and memory. Even with fine meshes that approach the capability of computational resources available it may be difficult to resolve all flow features of interest.

5.7 Parallel Performance

As discussed in Section 4.3.2, there are many different methods of evaluating the parallel efficiency of a computational implementation. The efficiency of the algorithm may be tested through experimentation with different parallel topologies for a particular problem. It is also interesting to compare the performance of the different flow models. Parallel performance

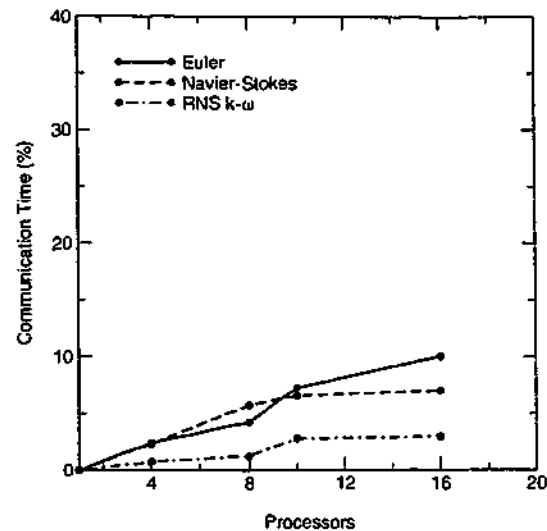


Figure 5.21: Communication time for different flow models.

may be model and geometry dependent.

The investigation involved the Euler, Navier-Stokes and RANS solver with $k-\omega$ turbulence model. The case was the flat plate geometry from Section 5.1. All simulations used the same grid dimensions and parallel topology, except the stretching was different in the case of the laminar and turbulent flows. The same number of multi-grid cycles were also used. Results are listed for each simulation in Table 5.2.

Tests were made on the computational facility used for the majority of simulations investigated in this work – the Compaq Alpha National Facility at the Australian National University in Canberra. This machine has a peak rating of almost 1 Teraflop and involves a cluster of 480, 1 GHz processors.

As shown in Figure 5.21, for the simpler models, the percentage of communication time increases by up to four times compared to the RANS solver. This is a substantial difference – clearly an increase in communication efficiency would have a great effect on the inviscid flow solver, particularly if the computational blocks are small. However the gains in increasing communication efficiency for the RANS solver would be marginal. This is shown where communication time as a percentage of total simulation time is plotted against the number of processors in Figure 5.21. The computer architecture involved nodes of 4 processors, thus the ten processor simulations may not have had exclusive access to nodes, so the timing results may have been affected by sharing resources with other processes.

Methods of evaluating the parallel performance of a code are discussed in Section 4.3.2. The relative speed-up is a metric that describes the wall time required for a simulation, given that the time required for the parallel algorithm running on a single processor is known. Timing results in Table 5.2 are used to calculate the speed-up for the simulation in Table 5.3.

In Section 4.3 it was noted that the computer hardware architecture can have a significant

| Procs | Time/proc | Total Time (s) | Comm Time (%) | Time (s)/ (points*steps) |
|----------------------|-----------|----------------|---------------|--------------------------|
| Euler Solver | | | | |
| 1 | 15600 | 15600 | 0 | 2.72×10^{-5} |
| 4 | 3003 | 12012 | 2.4 | 2.10×10^{-5} |
| 8 | 1363 | 10904 | 4.2 | 1.90×10^{-5} |
| 10 | 1113 | 11130 | 7.2 | 1.94×10^{-5} |
| 16 | 617 | 9872 | 10.0 | 1.72×10^{-5} |
| Navier-Stokes Solver | | | | |
| 1 | 20548 | 20548 | 0 | 3.56×10^{-5} |
| 4 | 5652 | 22608 | 2.3 | 3.94×10^{-5} |
| 8 | 2599 | 20792 | 5.7 | 3.62×10^{-5} |
| 10 | 2160 | 21600 | 6.5 | 3.77×10^{-5} |
| 16 | 1034 | 17216 | 7.0 | 3.30×10^{-5} |
| RANS Solver | | | | |
| 1 | 38746 | 38746 | 0 | 6.76×10^{-5} |
| 4 | 10279 | 41116 | 0.708 | 7.17×10^{-5} |
| 8 | 4601 | 36808 | 1.23 | 6.42×10^{-5} |
| 10 | 4221 | 42210 | 2.75 | 7.36×10^{-5} |
| 16 | 1911 | 30576 | 2.95 | 5.33×10^{-5} |

Table 5.2: Statistics for speed performance of code.

impact on parallel performance and performance metrics. Given that the problem is of fixed size, by increasing the number of processors each processor has smaller memory requirements. A larger percentage of the total data fits within the faster memory and thus execution time decreases (Foster, 1995).

There appears to be a large increase in communication time for the Euler simulation. This may be due to the fact the execution time has decreased due to cache effects and thus communication becomes a much larger portion of total execution time. The relative speed-up shown in Figure 5.22 experiences super-linear scaling, or speed-up that is greater than linear. This is most likely due to cache effects. Another method of calculating speed-up is Ware's law which is based purely on the parallel and serial execution time of an individual simulation. This model is bounded by Amdahl's law and is pessimistic in its estimate of maximum speed-up achieved. A less pessimistic model is provided by Gustafson and these two are compared in Figure 5.23. Whilst both laws do not suffer from the super-linear speed-up of the traditional measure it can be difficult to decide which is more useful. Ware's law is clearly more sensitive to the fraction of parallel execution time and thus to parallel inefficiencies. The two dominant factors on speed-up in this experiment appear to be cache effects and fluid model type. Both appear to have a significant impact on the ratio of communication to computation. This is inverse – a decrease in the number of processors for fixed problem size

leads to a decrease in the effects of cache, therefore a scalability that is closer to ideal. An increase in the complexity of the fluid model leads to an increase in scalability, provided the increase in communication time does not increase by the same amount. In general, computation would increase proportionally to the number of cells in volume of each computational block, whereas communication would increase proportional to the number of cell surfaces of the block.

| Procs | Relative Speed-up | Fraction Parallel | Ware's Law | Bound | Gustafson's Law |
|----------------------|-------------------|-------------------|------------|-------|-----------------|
| Euler Solver | | | | | |
| 4 | 5.2 | 0.976 | 3.73 | 42 | 3.93 |
| 8 | 11 | 0.956 | 6.11 | 23 | 7.69 |
| 10 | 14 | 0.913 | 5.61 | 12 | 9.22 |
| 16 | 25.3 | 0.866 | 5.31 | 7 | 13.98 |
| Navier-Stokes Solver | | | | | |
| 4 | 3.6 | 0.974 | 3.62 | 39 | 3.92 |
| 8 | 7.9 | 0.937 | 5.55 | 16 | 7.56 |
| 10 | 9.5 | 0.926 | 6.00 | 14 | 9.33 |
| 16 | 19.9 | 0.900 | 6.4 | 10 | 14.50 |
| RANS Solver | | | | | |
| 4 | 3.76 | 0.99 | 3.88 | 100 | 3.97 |
| 8 | 8.42 | 0.98 | 7.02 | 50 | 7.86 |
| 10 | 9.2 | 0.97 | 7.87 | 33 | 9.73 |
| 16 | 20.3 | 0.97 | 11.03 | 33 | 15.55 |

Table 5.3: Speed-up of code using various methods.

The evaluation of parallel performance can be important if the simulation tool is used repeatedly on large problems. In this case efficiency is important and improvements can increase its effectiveness. Of primary importance in this study is the ability to model complex physics rather than to produce an optimal parallel algorithm, thus performance considerations are secondary to the analysis of results of the simulations. However the simulations considered herein allow for tightly coupled parallel computation and thus provide excellent efficiencies compared to other problems and methods.

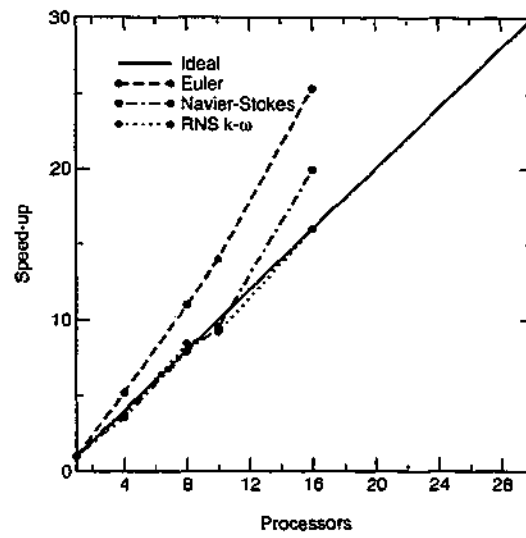


Figure 5.22: Traditional speed-up for different flow models.

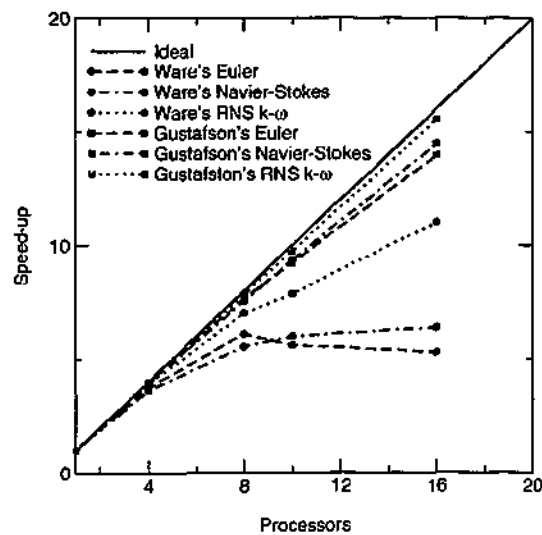


Figure 5.23: Other methods of calculating speed-up for different flow models.

Chapter 6

Turbine Cascade Simulations

This chapter discusses the application of the computational model to turbomachinery cascade flows, following the development and validation that has been described in the previous sections. Before the presentation of results typical cascade flow phenomena are discussed. Simulation results are compared with experimental measurements where they are available. Differences between existing models and experimental results are discussed, as well as the deviations of the approach over less complex models.

6.1 Modelling Considerations and Flow Physics

There are a number of important features in turbomachinery flows that contribute to loss and impact blade loading. These are found in both steady and time-averaged flow, and flow involving unsteady and time dependent behaviour. Given their potential importance in understanding the mechanisms behind aeroelastic flows it is instructive to first consider the different types of important flow structures found in turbomachinery cascades.

For configurations with supersonic axial outlet conditions impinging shocks and choked flow are important in determining the flow behaviour and its effects on structural members. Secondary flows such as passage vortices and stagnation point vortices increase blockage through the cascade. A poor modelling approach can also adversely affect simulation results. Thus, the independence of the simulation results on model parameters is ensured through investigations on the effects of grid density and turbulence quantities.

6.1.1 Computational Grid

A number of different types of meshes are employed in the simulation of turbomachinery flows. Terms structured and unstructured when applied to computational meshes define the way in which the computational domain is stored in memory. A structured mesh is made up of multidimensional arrays of hexahedral or quadrilateral cells. An unstructured grid may

be considered as a vector of tetrahedral or triangular cells. Structured grids are classified by their cell shape and global layout. Commonly used varieties include the straight H-grid that involves planes of nodes orthogonal to the machine axis, the orthogonal H-grid where the grid points are almost orthogonal at the blade surface and retain the H pattern, and the C-grid and the O-grid that both wrap around the blades. The advantages of the structured approach is that they may be better optimised for computation due to the fact that neighbouring cells in the computation are also neighbours in memory space. The mapping of the computational domain is much more easily handled. The computational meshes themselves may also be more easily and quickly generated and may more simply undergo resolution studies. The major disadvantage is that they often unnecessarily resolve parts of the flow-field or provide cells that are of undesirable geometry. Unstructured grids provide more regular cell shapes, however tetrahedral cells provide a reduced order of accuracy compared to the hexahedral cells usually used in structured meshes. Hybrid grids are also employed, that use structured meshes in boundary regions and unstructured meshes between far-field boundaries to outside boundary layers.

In the present approach, two different types of meshes have been used. The first is an orthogonal H-grid and the second a hybrid H-O mesh. These are first generated in 2-dimensions around the blade profile, then stacked in the span-wise direction. For the orthogonal H-grid, a straight H-grid is used to generate the initial mesh, then the orthogonal mesh is generated by using the spring network analogy. An example of the tip gap region of a typical grid is shown in Figure 6.1, for the Standard Test Case 4. Hyperbolic stretching functions are used to distribute the cells on the blade surface and geometric functions are used to distribute the grid in the pitch-wise direction. In the case of annular geometry, two meshes are generated for the hub and casing and then the 3-dimensional mesh is created by interpolation between the two.

The second type of mesh is an O-H hybrid grid, where the inner region wraps around the blade. The region between the O-mesh and the periodic boundaries is connected by an H-mesh. Initially 12 mesh blocks are generated, each involving local block numbering that does not necessarily coincide with neighbouring block. To the author's knowledge this mesh represents the state-of-the-art in structured meshes for turbomachinery.

The O-H mesh has a number of advantages over the orthogonal H-mesh. Later in this section this will be demonstrated through a comparison of simulation results. The O-H mesh provides a better distribution of cells – comparatively less cells are generated in the inlet region, with more cells in the mid-passage region. The orthogonal H-grid has highly sheared cells in the throat region – this can lead to poor resolution due to extremely slow convergence. However, the O-H grid provides regular cell shapes throughout the computational domain. A disadvantage of the O-H mesh is the non-aligned coordinate systems from block to block. This introduces added complexity to both the implementation and the specification

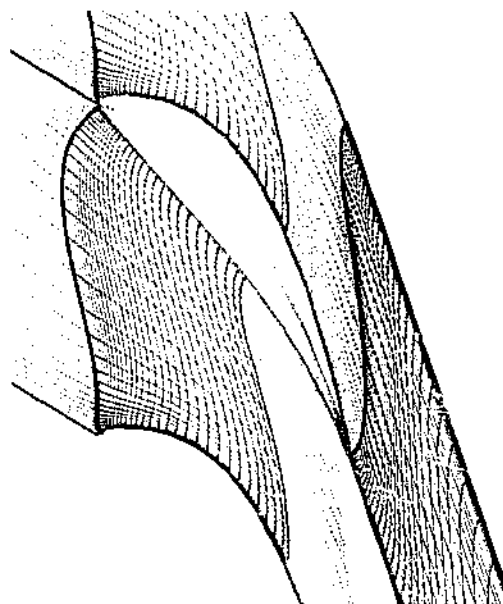


Figure 6.1: Mesh in tipgap region of the He Cascade

of boundary conditions. Cell counts are similar between the two, as is the time required for simulation. It was found that there was little difference between simulations for either of the meshes for the subsonic cases, but significant differences arose between results for the transonic cases that will be examined in later sections.

In a number of the simulations, the tip gap is also modelled. Tip gap models that obviate the need for detailed modelling of the region have been developed for compressors (van Zante *et al.*, 2000). Compressor blades have little or no camber and tend to have very little depth. The researchers modelled the tip gap without a grid, by assuming orifice flow with no change in mass or momentum or energy. For the compressor cases investigated this provided results sufficiently similar to simulations involving a tip gap mesh. However, turbine blades are highly cambered and relatively thick – the selection of flow direction over the tip is not obvious. Thus this model was not considered for the present turbine simulations.

The grid for the tip gap region between the blade tip and the casing was generated using the spring network approach between the mesh points defined on the surface of the blade. This provided a mesh that was similar in geometry to other numerical simulations of tip gap flow (Tallman & Lakshminarayana, 2001a; Tallman & Lakshminarayana, 2001b). An example for the He Cascade is shown in Figure 6.1. Note that the grid is relatively coarse in the pitch direction, however the structured grid limits the number of grid points. It is believed that the resolution in the pitch-wise direction is sufficient for the present work.

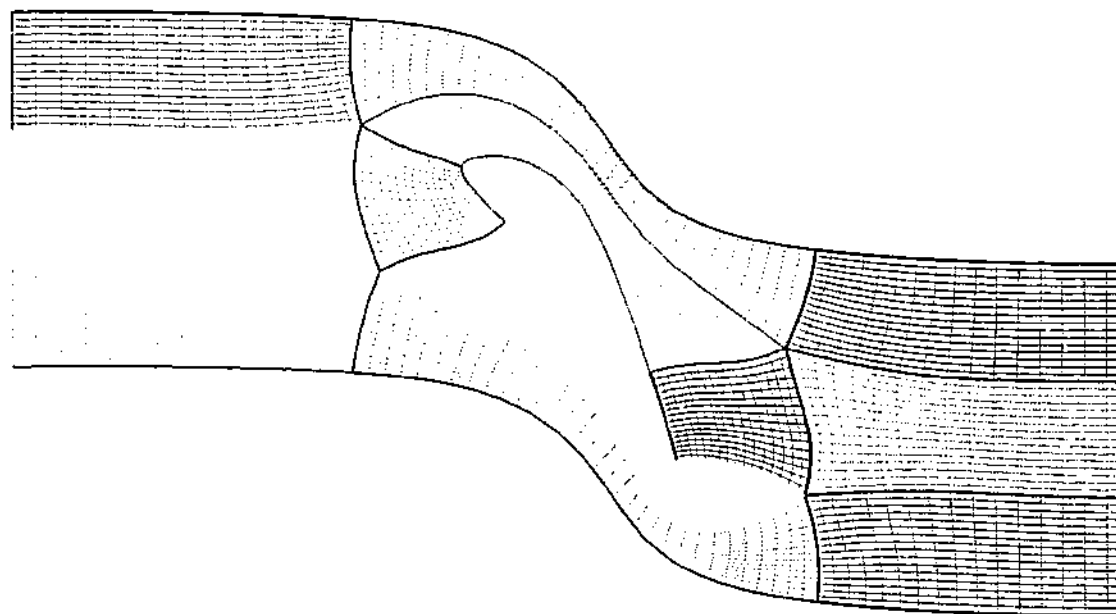


Figure 6.2: O-H grid for Standard Test Case 4 profile for Euler simulations.

6.1.2 Vortex Structures

Most vortex structures in turbomachinery cascades are classified as secondary flows, in that they influence the flow in the plane normal to the stream-wise direction. Separation on the blade surface may exist and can lead to undesirable aeroelastic effects, however these are not referred to as secondary flows herein. A thorough description of secondary flows in turbomachinery cascades is provided by Langston (1980) and also Sieverding (1985). A number of theories have been proposed as to the nature of the secondary flows; the more recent ones include vortices due to two different phenomena. They differ in their description of the position of these vortices and their interaction as the flow moves through the cascade passage.

Typical models for vortex structures in a turbomachinery cascade are shown in Figures 6.3 – 6.5. The stagnation vortex, also known as a horse-shoe vortex, wraps around the leading edge of the blade near the passage walls. It is a result of the boundary layer of the end-walls meeting the blade leading edge in a similar phenomenon to the case of a cylinder on a flat plate (Sierverding, 1985). Upstream of the blade leading edge a cross-flow vorticity component exists due to the boundary layer profile. As this boundary layer meets the leading edge the vorticity field is reorganised in such a way that the vortex lines are stretched and turned around the obstacle. The cross-flow lines of vorticity are turned so that they are in the stream-wise direction and intensify due to further stretching.

The horseshoe vortex has been identified by Gaugler and Russell (1984) through flow visualisation in a linear cascade of inlet guide vanes that have a similar profile to those used

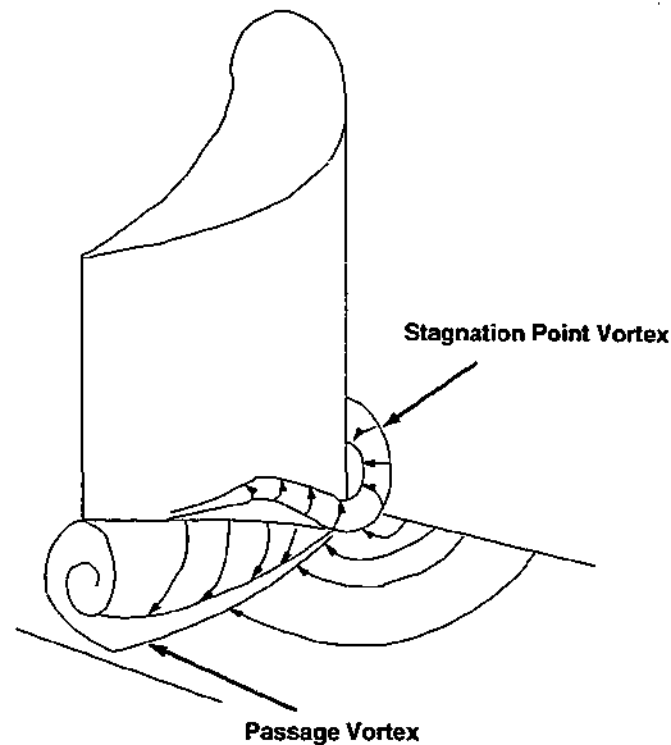


Figure 6.3: Sketch of viscous flow structures in a typical turbine cascade (Sieverding, 1985).

in the present simulations. About three rotations of the pressure-side vortex can be discerned from the Helium bubbles used to visualise the flow, by the time it reaches the mid-chord region. The authors note that the vortex core flow has moved about two thirds of the way toward the suction-side of the neighbouring blade at the trailing edge plane. Moore (Moore & Ransmayr, 1984; Moore & Smith, 1984) performed an experiment on a cascade in which he found that the pressure-side leg of the horseshoe vortex was entrained and distributed throughout the passage vortex by the time it had reached the passage exit plane. The suction-side vortex, however, was convected around the centre of the passage vortex.

The horseshoe vortex was not identified at the 0.4 chord region in an experiment by Sieverding et al. (1984) in an annular cascade and they state that they do not expect a distinct vortex except for the region close to the leading edge due to the fact that its sense of rotation coincides with the passage vortex. A detailed analysis of the horseshoe vortex has been performed by Ishii and Honami (Ishii & Honami, 1986) for turbulent flow of a low speed flow. They identify three smaller vortices in this type of flow, a separation vortex and counter vortex upstream of the horseshoe vortex and a corner vortex downstream of the horseshoe vortex.

The passage vortex is due to the turning of the flow by the cascade. The flow may be reduced to a simple flow with circular streamlines in order to understand the source of this flow structure (Gostelow, 1984). Consider a flow where all streamlines are circles centred

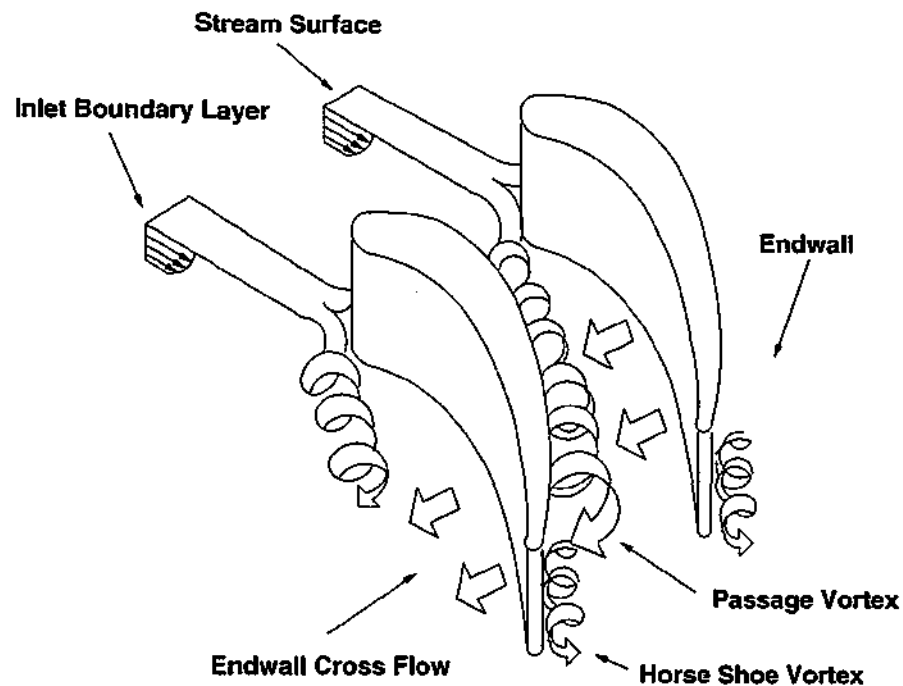


Figure 6.4: Sketch of viscous flow structures in a typical turbine cascade (Langston, 1980).

on a common axis of symmetry. If the motion is to remain purely rotatory, with the radial component of velocity zero, the circumferential pressure gradient is also zero. Thus the radial variation in pressure simply supplies the force necessary to maintain the circular path of the fluid particles (Batchelor, 1981). If the radius of the stream lines is R and the vector \mathbf{n} is normal to the streamlines, the radial equation of motion in cylindrical coordinates reduces to

$$\frac{dp}{dn} \approx \frac{\rho U^2}{R}.$$

In a linear cascade, the pressure gradient at the end wall is approximately the same as that at the mid-span – the pressure gradient is almost constant through the boundary layer. However, the velocity at the end-wall is much lower. Thus the streamlines closest to the end-walls turn at a smaller radius resulting in a velocity component normal to the stream-wise direction away from the pressure-side and toward the suction-side. This leads to what is known as over-turning at the end-walls. As a result there is a velocity component perpendicular to the stream-wise direction, causing a roll up of the shear layer in this region.

One of the more recent reviews of cascade flow behaviour (Sierverding, 1985) describes the interaction of the horse shoe vortices with the passage vortex. This updated model is shown in Figure 6.5. The pressure-side and suction-side legs of the horseshoe vortex (denoted H_p and H_s , respectively) are connected by the stream surface SS_1 . This stream surface

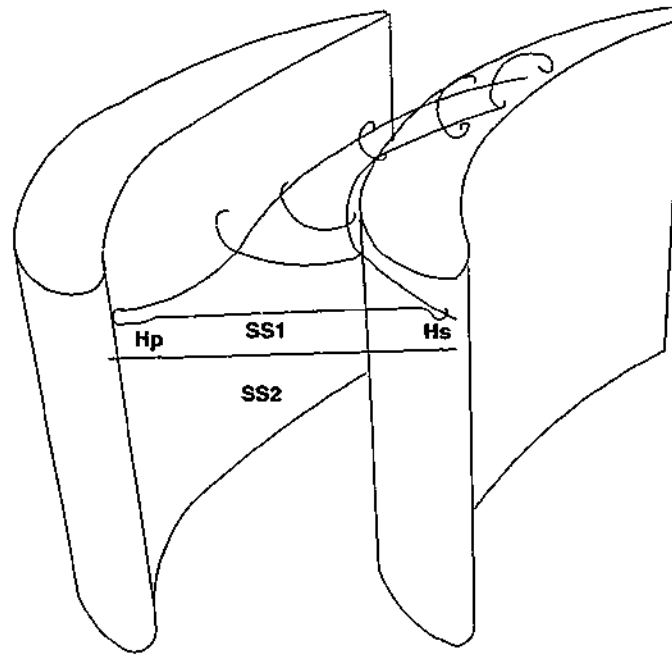


Figure 6.5: Sketch of interaction of passage and horseshoe vortex (Sieverding, 1985).

is inside the wall boundary layer. Another stream surface is shown outside the end-wall boundary layer – SS_2 . As the flow moves downstream of the leading edge, both stream surfaces start to rotate.

The pressure-side leg of the horseshoe vortex remains at the centre of this rotation, whilst the suction-side leg rotates around at some radius from the centre. Thus the pressure-side leg is at the centre of the passage vortex, while the suction-side leg H_p wraps around this core. This is consistent with the observations of Moore and Smith (Moore & Smith, 1984). The position of the suction-side leg of the horse shoe vortex depends on the flow conditions in the cascade and cascade geometry. However, in cascade experiments it has been difficult to trace its path through the cascade due to the strong acceleration and therefore stretching that it experiences at the front portion of the blade, then the strong interaction with the passage vortex in the region toward the trailing edge.

Annular cascades are slightly different to linear cascades in the comparative strength of the secondary flows at the hub and casing. Observations have been made of the passage vortex in an annular cascade of blades without a tip clearance (Sieverding *et al.*, 1984). Sieverding *et al.* note that one can expect different strengths of passage vortex at the hub and casing can be attributed to the different blade loading due to the radial pressure gradient distribution. This is observed through their analysis of the pitch-wise integrated flow angle.

6.1.3 Transonic Flow

Transonic turbine cascade flow has some different characteristics from cascades at subsonic conditions. Shock waves and the choking of the passage change both the steady and the aeroelastic loading distributions on the surface of the blade. The movement of shock waves on the blade surface causes oscillations in the local pressure coefficient and interactions of shock waves with the boundary layer can cause separation.

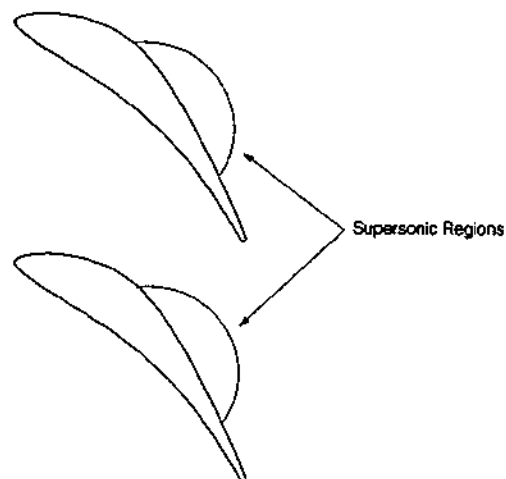
The flow behaviour dependence on Mach number is shown diagrammatically in Figure 6.6. This figure has been drawn based on Schlieren photos from the Standard Test Case 4 report (Bölcs & Fransson, 1986) and from other sources (Baines & Moheban, 1989; Gostelow, 1984). The Standard Test Case 4 profile is used in the present example. In cascades of blades that are convex on the blade suction-side in the region of the trailing edge, expansion shocks are possible in this neighbourhood (Gostelow, 1984). Note that the blade profile beyond the throat region has very little curvature, thus one would not expect expansion waves in this case.

In Figure 6.6(a), which is at high subsonic Mach number, regions on the suction-side of the blade become supersonic.

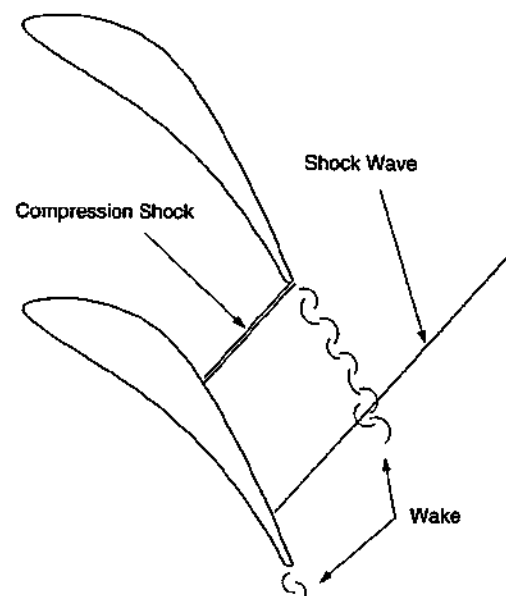
A further increase of outlet Mach number leads to choking of the passage as shown in Figure 6.6(b). A weak compression shock wave extends from the trailing edge of the upper blade to the mid-chord region of the lower blade. The condition where the passage is just choked is a particularly unpredictable flow regime that can lead to time non-linear flow effects where aeroelastic effects are considered. These have been investigated by a number of researchers (Sadeghi & Liu, 2001b; Bendiksen, 2000). Prediction of flow in this regime by time linearised methods is highly inaccurate due to the non-linear nature in time of the blade displacement. There is the possibility of the blade oscillating about mean position different to the undisturbed position, where every second blade passage is choked.

As the outlet Mach number increases the first compression shock becomes stronger, moves downstream and is more oblique to the suction-side surface. Reflections may arise from the suction surface at the point of impingement of the first compression shock as shown in Figure 6.6(c). These reflections may further reflect from the wake of the neighbouring blade.

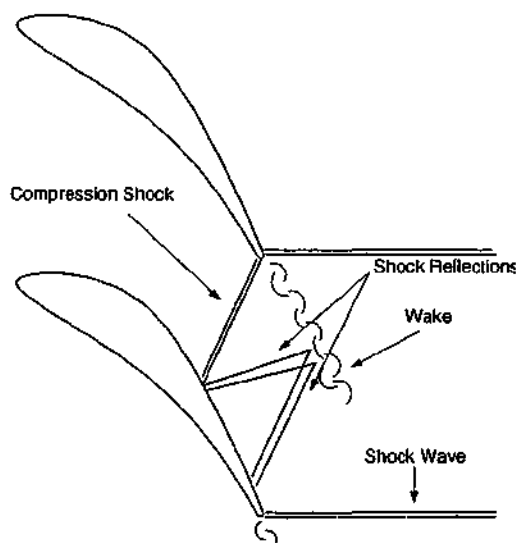
The final diagram in Figure 6.6(d) shows an even higher outlet Mach number. The impingement of first compression shock has moved further aft and reflections are possibly stronger. At the trailing edge the shock has also gained in strength and has become more oblique. The strength of this shock wave may cause separation on the blade suction-side near the trailing edge. This is due to the strong, adverse pressure gradient setup by the shock front. Separation of this nature may cause a number of undesirable effects in terms of aeroelasticity. It will cause a thickening of the wake region and can lead to large fluctuations in pressure in the wake. The shock wave may oscillate in position due to shedding leading to



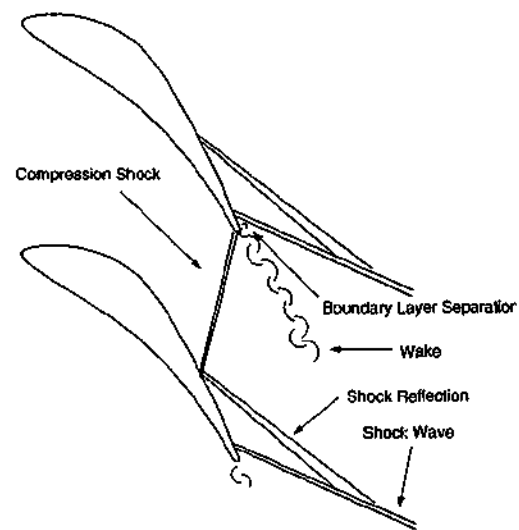
(a) High subsonic conditions, outlet $Ma_{i2} = 0.9$.



(b) Supersonic outlet conditions, outlet $Ma_{i2} = 1.02$.



(c) Supersonic outlet conditions, outlet $Ma_{i2} = 1.2$.



(d) Supersonic outlet conditions, outlet $Ma_{i2} = 1.4$.

Figure 6.6: Sketch of passage flow at different outlet conditions.

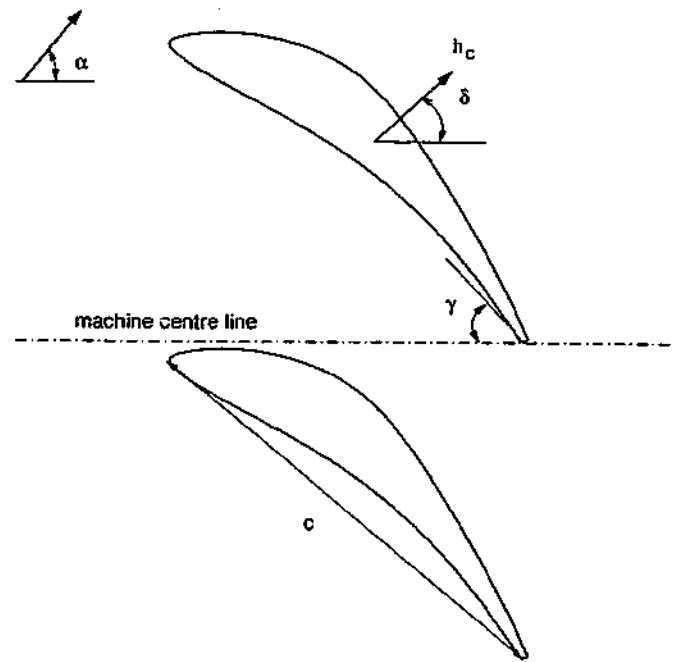


Figure 6.7: Nomenclature for aeroelastic turbomachinery simulations.

large oscillating forces at the blade trailing edge.

6.1.4 Aeroelastic Configuration

Where the energy method has been applied to turbomachinery cascade configurations, a nomenclature has been developed to describe the cascade geometry and vibration mode. This began with the development of the Standard Test Configurations for aeroelasticity in turbomachinery (Bölcs & Fransson, 1986). The nomenclature in the present investigation uses the same symbols, however operates in the reference frame of the machine axis rather than the blade chord.

For translational mode shapes, such as those used to model blade bending modes, the blade displacement h_c is non-dimensional with blade chord. Other important parameters include the inlet flow angle α and the blade displacement angle δ which are both with respect to the machine centre line.

6.2 He Cascade

The first of the turbine cascade configurations considered is a single blade oscillating in a contoured channel with low subsonic, incompressible flow conditions. Comprehensive, 3-dimensional surface measurements have been taken by Bell and He (Bell & He, 1997; Bell & He, 1998) on this experimental configuration including an investigation into the effects of

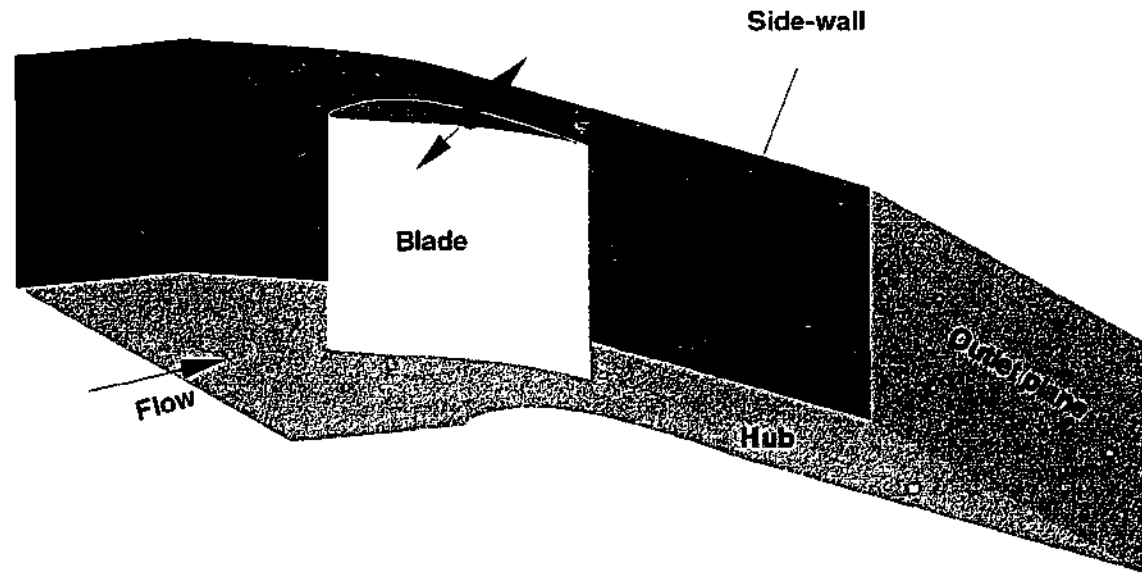


Figure 6.8: Configuration of the cascade of Bell and He (1997).

varying tip gap clearance (Bell & He, 2000).

The configuration is shown in Figure 6.8. A bending mode is simulated by attaching the hub end of the blade to a hinge and moving the blade tip in an oscillatory motion at a specific amplitude. The blade's displacement is prescribed by a sinusoidal signal at a particular reduced frequency. Passage flow is well subsonic and almost incompressible at an inlet Mach number of $Ma = 0.1$. Experimental measurements were taken at a number of span-wise locations, however only those at 10%, 50% and 90% span were considered in the present investigation. The turbine blade is prismatic and there are two passages above and below the blade. The side-wall shown in Figure 6.8 in dark blue was contoured to the blade shape and inflow and out flow angles to simulate a turbine cascade – the side-wall on the side of the blade closest of the viewer has been omitted for clarity. The green area is the cascade hub which is planar as is the cascade casing, which is not shown. The design of the blade profile is such that the flow deflection angle is restricted to reduce the strength of blade secondary flows.

A summary of flow conditions used in the present simulations is tabulated in Table 6.1 and the geometry is summarised in Table 6.2. Note that the only major difference between the experimental conditions and those in the simulation is the outlet Mach number. The compressible solver has extremely slow convergence at very low Mach number due to the effects

| Condition | Experiment | Simulation |
|--|-------------------|-------------------|
| Typical Reference Velocity | 33.4 m/s | |
| Bending mode direction | 35.5° | 35.5° |
| Bending mode amplitude at tip | 0.055 Chord | 0.055 Chord |
| Bending mode amplitude at hub | 0.006 Chord | 0.006 Chord |
| Reynolds number (referenced to outlet velocity) | 4.5×10^5 | 4.5×10^5 |
| Outlet Mach number | 0.1 | 0.3 |

Table 6.1: Parameters for He Cascade

| | |
|--------------------|-------|
| Blade chord | 0.2 m |
| Aspect ratio | 1.0 |
| Solidity | 1.35 |
| Blade inlet angle | 25.0° |
| Blade outlet angle | 74.3° |
| Inlet flow angle | 31.0° |
| Nominal exit flow | 71.3° |

Table 6.2: Cascade, blade and flow geometry

of incompressibility on the algorithm. Therefore the outlet Mach number was increased to $Ma_{is2} = 0.3$. In this regime the effects of compressibility are still low enough to have a negligible effect on simulation results.

The geometry of the cascade was modelled through an orthogonal H grid, a cross-section of which is shown in Figure 6.1. The inlet and outlet region extends 1 axial chord upstream and downstream of the blade respectively as in the experiment, the inlet plane having the same geometry as the inlet traverse plane. The same span was also used as the experiment for the height of the cascade and the side-walls were modelled as solid walls.

6.2.1 Steady Simulations

An investigation was undertaken into the effects of model parameters on the characteristics of the simulated cascade. This included a study into the effects of grid resolution, inlet turbulence quantities and geometric configuration. These results are compared with experiment.

A grid resolution study was performed in 2-dimensions for the Navier-Stokes simulations. For this study, the computational mesh included 8 cells in the third dimension and the slip boundary condition was imposed on the walls in the span-wise direction. In Figure 6.9, the effect of variation in mesh distribution is investigated whilst the number of mesh nodes is kept constant – note that the mesh size in the contour legend is the number of cells in the axial, span-wise and pitch-wise directions respectively. Figure 6.10 is another grid study, whereby a fine grid of $160 \times 256 \times 8$ in the axial, pitch-wise and span-wise directions was initially generated. Coarser grids are created by removing every second point. The differences

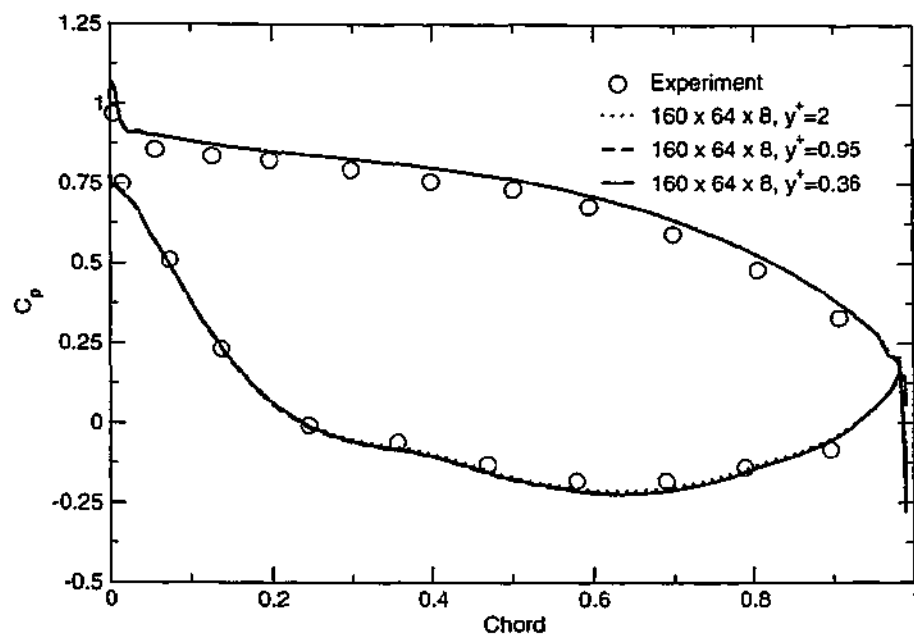


Figure 6.9: He Cascade – 2-dimensional simulation test for grid dependency of grid cluster.

between pressure coefficient for the different grids is deemed to be small enough for a grid geometry of $160 \times 64 \times 8$ with the geometry of the grid point adjacent to the blade surface such that $y^+ < 1$ as recommended (Wilcox, 2000). It is assumed that in the 3-dimensional simulations that this distribution when applied in the span-wise direction also provides a grid independent solution for the Navier-Stokes simulations at the hub and casing. It was found for higher Reynolds number cases that the restriction on $y^+ < 1$ for the grid point adjacent to the wall may be relaxed.

The differences between 3-dimensional and 2-dimensional models on surface pressure coefficient are also investigated. In Figure 6.11 a comparison of simulations shows some difference in pressure coefficient on the blade suction-side. However, the presence of secondary flows, typically about 10% from the end-walls, has little effect on the span-wise variation of the surface pressure coefficient in the simulation as shown in Figure 6.12. The experimental results displayed greater variation between these span-wise positions.

Secondary flows can be visualised in the passage through fluid stream-lines or path-lines in unsteady flow. The commercial plotting package Tecplot was used to generate path-lines, through its predictor corrector algorithm. A rake line is specified within the fluid field and the program defines a number of evenly spaced points over the line. From each of these points, the local vector field is used to define the initial direction of the streamline. The path-lines are then generated by taking small spatial increments along the vector and using the vector at the new position to define the next segment of the path-line. The path-lines may be integrated in both the upstream and downstream directions.

The stream-wise vorticity was plotted to identify the hub vortex recirculation in front of

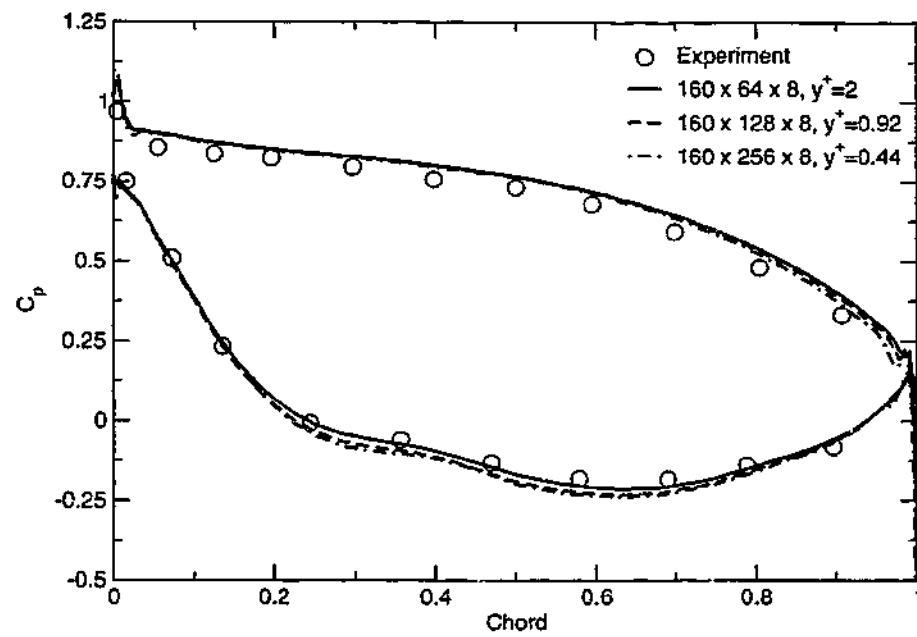


Figure 6.10: He Cascade – 2-dimensional simulation test for grid dependency of grid density.

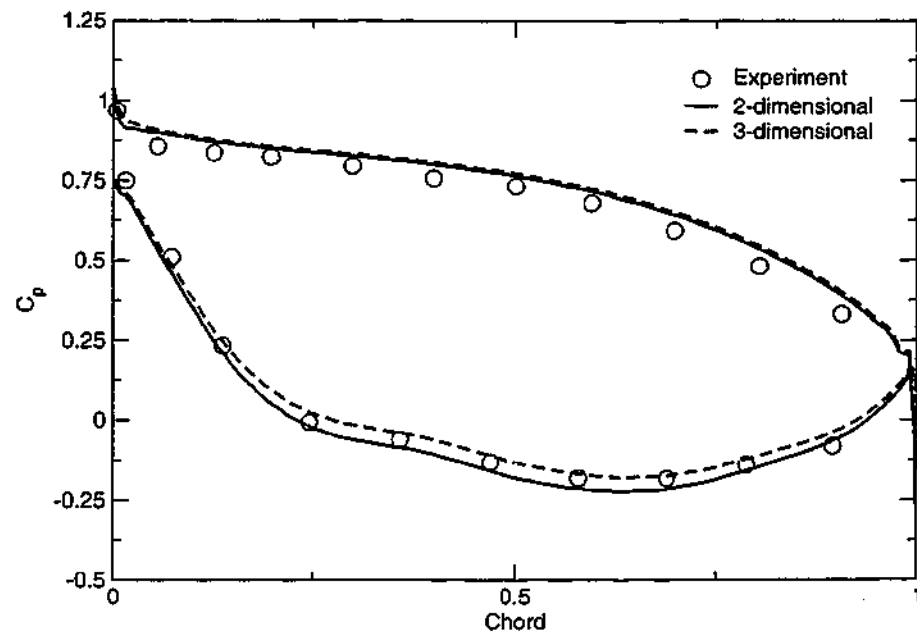


Figure 6.11: He Cascade, significance of endwall flows on steady pressure coefficient distribution at mid-span without tip clearance model.

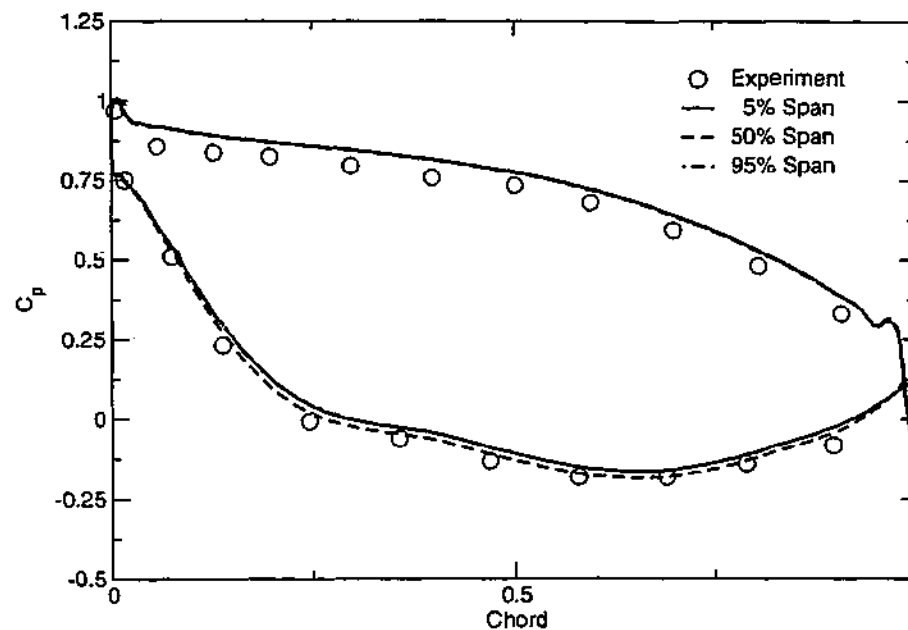


Figure 6.12: He Cascade, significance of endwall flows on steady pressure coefficient distribution across blade span, without tip clearance model.

the blade leading edge. While the vortex was small in size in this region it could be identified by a clear peak in the vorticity. Stream-lines were integrated through the flow field on both sides of the leading edge stagnation line to locate both the pressure-side and suction-side legs of the vortex shown in Figure 6.13. Stream-lines were placed at increasing distance from the hub in colour order yellow, pink, green, dark blue and light blue.

On the pressure-side the over-turning of the flow away from the pressure-side and toward the side wall can be observed. However, there is no clear roll up of the stream lines on the pressure-side. On the suction-side there is also over-turning of the flow close to the hub. Once again there is little roll up. It would seem that the horse shoe vortex is weak in this case.

In axial turbomachinery, often a gap exists between the ends of the blades and casing. This introduces a number of phenomena not present in shrouded assemblies. The two major effects is the blockage due to the tip vortex which is a result of the tip leakage flow, and the unloading of the blade in the tip region.

The resolution required for the tip gap region was investigated by varying the number of cells in the span-wise direction and comparing with the experimental measurements of pressure coefficient at 90% span, for a tip clearance of 1.5% chord. This case was chosen as it represents the largest gap considered and thus it is expected that if the resolution is sufficient for this case it is also sufficient for the cases with a smaller tip gap. For the present simulations it was decided that 32 cells was sufficient to resolve the tip clearance flow. Comparisons are made in Figure 6.14. The same number of cells and cell distribution is maintained in the

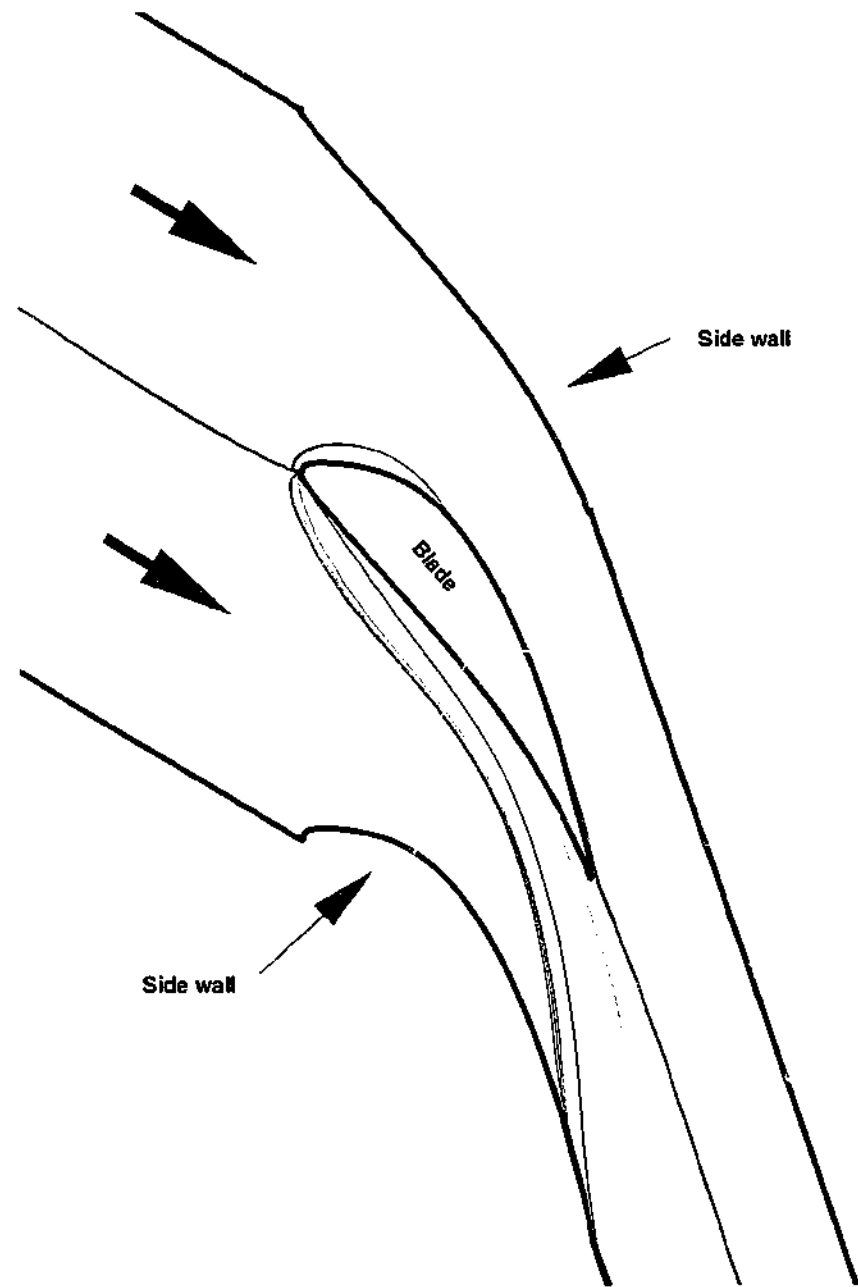


Figure 6.13: He Cascade and stream-lines in horseshoe vortex flow in the hub region.

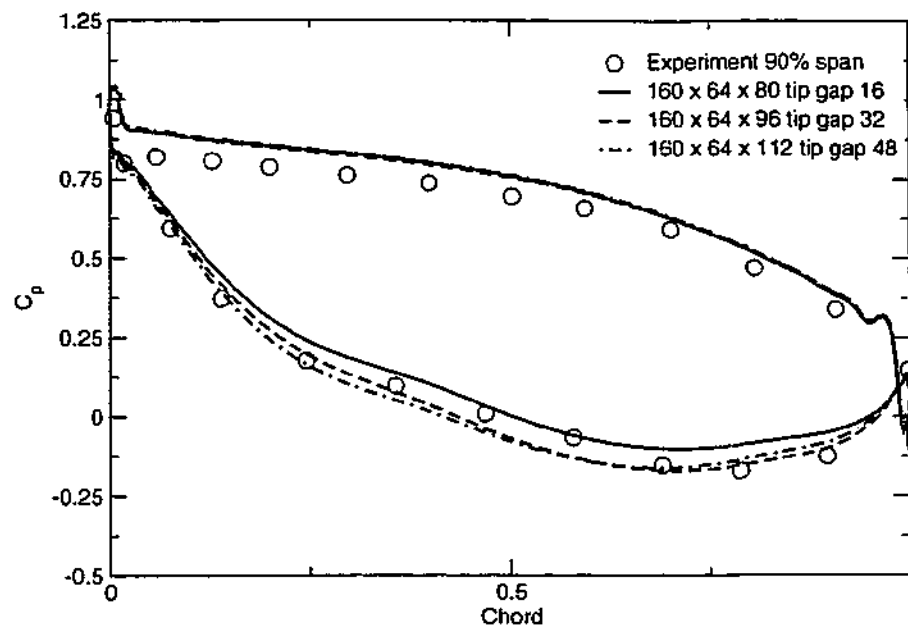


Figure 6.14: He Cascade grid dependence study for tip gap configuration – pressure coefficient at 90% span.

span-wise direction to the top of the blade – only the number of cells in the gap is varied.

The turbulence model also has the potential to affect simulation results. It has been found by a number of researchers (Menter, 1992; Wilcox, 2000) that a particular issue with the $k-\omega$ model is that the level of free-stream turbulence dissipation rate ω can have a large effect on the spreading rate of free shear flows. Whilst the present investigations involve internal and therefore wall bounded flows, free vortices may be affected by this quantity where they lie beyond the wall boundary layers.

Menter (1992) found that for solutions of the defect layer equations the free-stream values of ω were most influential at the boundary layer edge – this is the region closest to the secondary flows. For free shear layers Menter found that the velocity profile was found to be more affected by free-stream values and has a much larger spreading rate as the free-stream ω decreases. The present flow cannot be classified as either a free shear flow or a boundary layer flow, however it should be noted that the local value of ω at vortex cores was close to the free-stream values. Regions of low ω may be dependent on free-stream values. The specification of far-field ω is given by Menter (1992) as a function of inlet velocity and a length scale (see Section 4.1.10). In the present investigation this length scale was set at smaller values to increase the level of ω at the inlet.

The tip gap vortex was the feature of most interest so this was chosen to investigate the effect of the inlet turbulence length scale. Two different positions were chosen, one at 90% axial chord and the other just downstream of the trailing edge at 110% axial chord from the leading edge. The circulation around the tip vortex was calculated at these stations through

| Inlet Turbulence Length Scale | Inlet ω_1 | $\Gamma_s \cdot \mathbf{n}$ at 90% Chord | $\Gamma_s \cdot \mathbf{n}$ at 110% Chord |
|-------------------------------|--------------------|--|---|
| 0.2 | 1.85×10^4 | -10.40 | -8.86 |
| 0.1 | 3.7×10^4 | -10.25 | -8.75 |
| 0.02 | 1.85×10^5 | -10.31 | -8.71 |

Table 6.3: Tip vortex and dependence on inlet turbulence length scale.

the integration of the stream-wise vorticity,

$$\Gamma_s = \int_{\Delta S} \omega_s dS.$$

This is calculated over a closed contour of vorticity in the region of the tip vortex, with the same level of vorticity contour for the different inlet turbulence levels and a comparison is shown in Table 6.3. Note that the normal of the plane of integration is not coincident with the stream-wise direction, nor the axis of the vortex, but the machine axis. It is shown that the inlet turbulence level ω_1 has little impact on the strength of the tip clearance vortex in this case.

For steady simulations, Bell and He (Bell & He, 2000) found that the tip leakage flow had a considerable impact on the surface pressure coefficient at 90% span. A comparison is made between experimental measurements and simulation results in Figure 6.15. The pressure coefficient is over predicted a little on the pressure-side compared with experiment as in all of the other steady simulations presented. On the suction-side the leakage flow has less impact on span-wise variation in pressure distribution between 10% and 50% span in the simulation than in the experiment. The overall trend on the suction-side compares well with the experimental measurements.

The effect of varying the tip clearance was also investigated in the present simulations by the comparison in Figure 6.16 of the steady pressure coefficient with no tip gap model, a tip gap of 0.5% chord, 1.0% chord and 1.5% chord. The trends between experiment and simulations agree well, although the pressure coefficient on the pressure-side is over predicted once again in the simulations.

The effect of different tip gap ratios on the tip leakage vortex for the simulations is demonstrated in Figure 6.17. Figure 6.17(a) is for a tip gap ratio of 0.5% chord and Figure 6.17(b) for a tip gap of 1.5% chord. There are a number of notable differences between the two. The larger tip gap has a larger diameter vortex and the turning of the stream-lines appears to continue much further down stream, indicating a stronger vortex behaviour. The tip vortex on the right appears to remain attached to the blade longer. In the left hand case it appears that only those stream-lines at the centre of the vortex, originating close to the blade leading edge, continue the vortical motion well downstream from the trailing edge. The

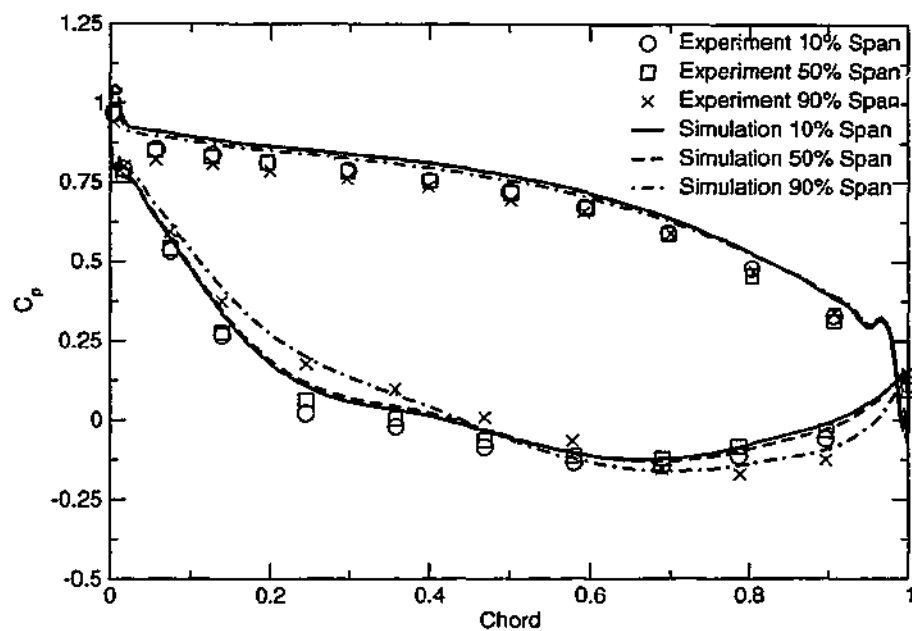


Figure 6.15: He Cascade span-wise pressure coefficient distribution for tip gap of 1.5% chord.

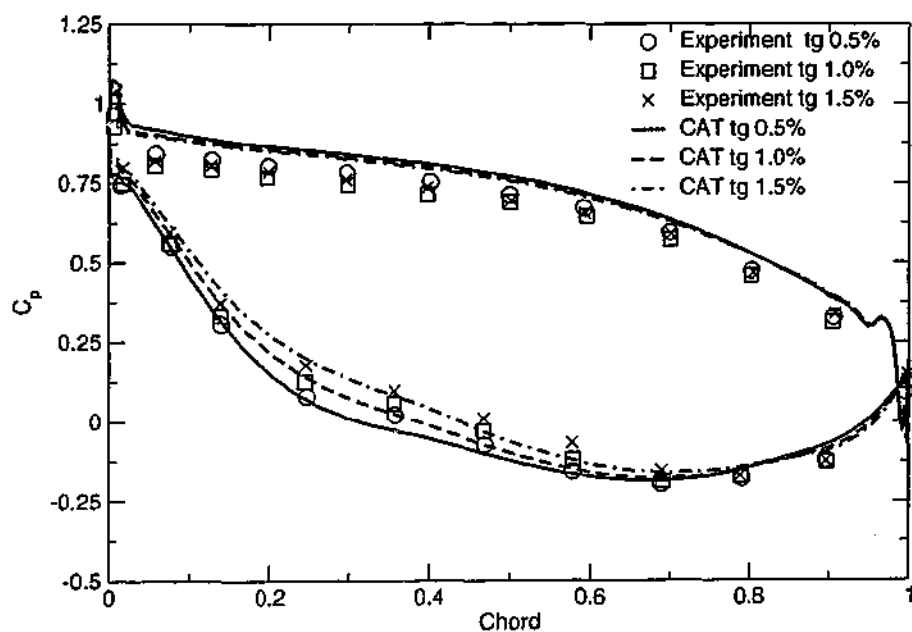


Figure 6.16: He Cascade comparison of surface pressure coefficient for different tip gaps at 90% span.

green stream-lines, crossing the tip just aft of the mid chord region, undergo little rotation in the smaller tip gap case. However, in the right hand figure, these lines are entrained in the central vortex motion even before the flow passes the trailing edge.

There are few descriptions of the nature of the tip leakage vortex in the literature. Recently, the different types of roll-up in the tip vortex have been classified by Tallman and Lakshminarayana (Tallman & Lakshminarayana, 2001a). In particular they sought to find a physical explanation for the behaviour of the tip leakage vortex. They conclude that the convection of vorticity plays a significant role in the development of the tip gap vortex and also that a shear jet model is invalid for certain tip clearance flows. It will be argued that the jet shear model is adequate in describing the present flow and that their classification of different types of vortex flow is ambiguous.

They classify three types of roll-up in the tip vortex. The first two types involve the flow over the tip at the forward part of the blade. Consider the velocity profile at the exit of the tip gap region shown in Figure 6.18 at quarter chord. Some of the contours in the tip gap region have been omitted for clarity. Vorticity at the blade tip side has the same sense of rotation as the tip gap vortex. Flow at the outer boundary involves vorticity of opposite sign. They separate the two different types of roll-up, type one and two, due to the differences in sign of vorticity at the exit of the tip gap region from which the stream-lines originate. They point out that the flow close to the blade tip has the same vorticity as the tip vortex and therefore rolls up in the centre of the vortex. They contend the flow close to the casing however has the opposite vorticity and therefore it resists rolling into the leakage vortex and is gradually entrained around the outside of the leakage vortex downstream of the trailing edge, but does not roll up inside the passage. In their case the tip gap flow at the casing appears to avoid the tip vortex completely, travelling through the passage slightly below and outside the tip vortex.

They argue that for the tip flow to follow the jet model some of the bulk flow, that has not passed over the gap, must be entrained in the vortex formed at the edge of the shear layer of the jet flow. In their investigations they fail to find streamlines that move through the passage and do not pass over the blade tip, that are involved in the roll-up of the tip vortex.

Their description does not coincide what is observed in the present simulations. The plan view and side view of three stream-lines are shown in Figure 6.19(a) and Figure 6.19(b), respectively. The red stream-line enters the tip gap close to the blade leading edge. At the tip gap exit, it is very close to the blade tip and beyond this region it rolls into the tip vortex. The blue stream-line represents passage flow that is entrained into the tip gap vortex due to the shearing of the jet-like flow. It passes close to the blade at the leading edge and follows the contour of the blade, before rolling into the tip vortex. Whilst it begins close to the core of the tip vortex it moves radially outwards as it is convected downstream. Once again, this stream-line could not be located in the simulations performed by Tallman et al (Tallman &

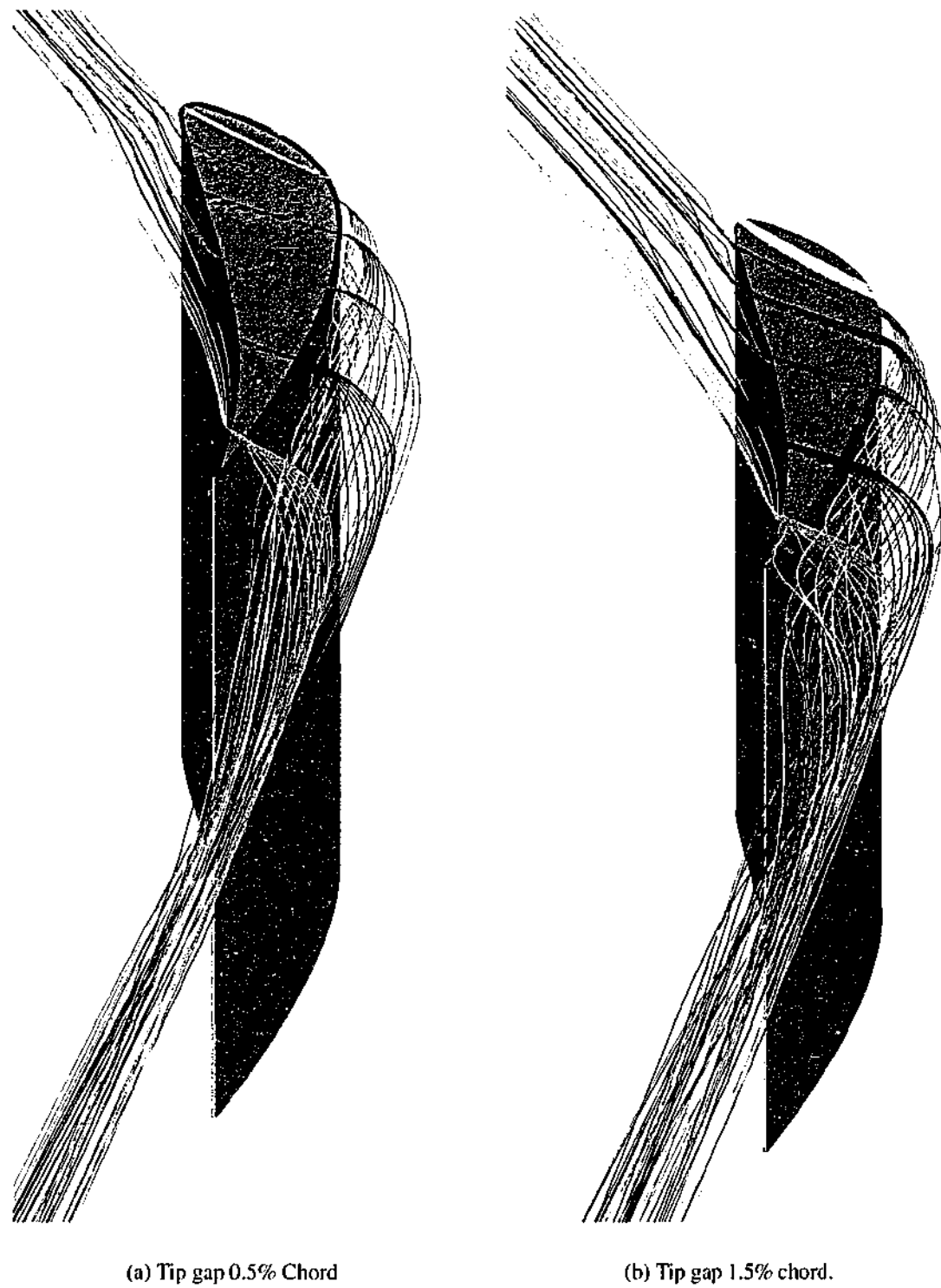


Figure 6.17: He Cascade stream-lines through tip gap region for two different tip gap lengths.

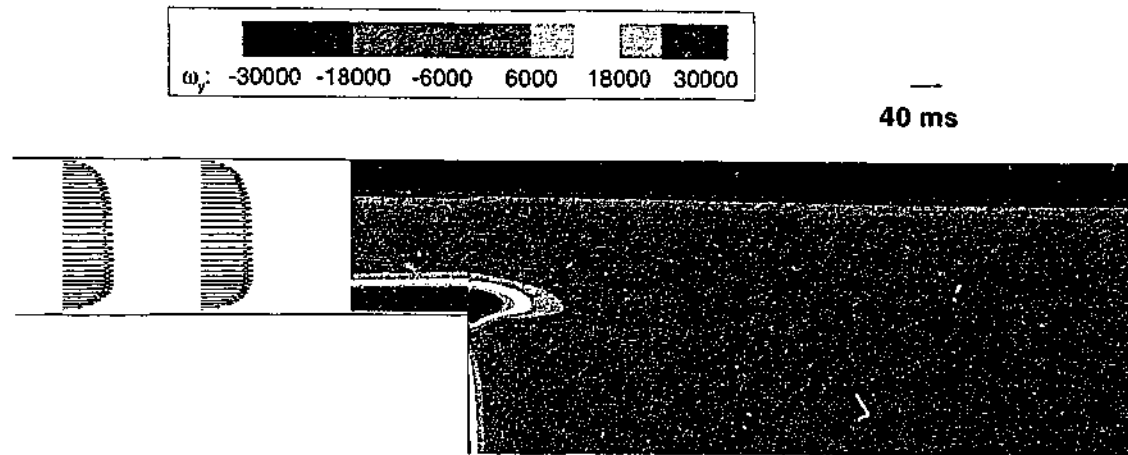


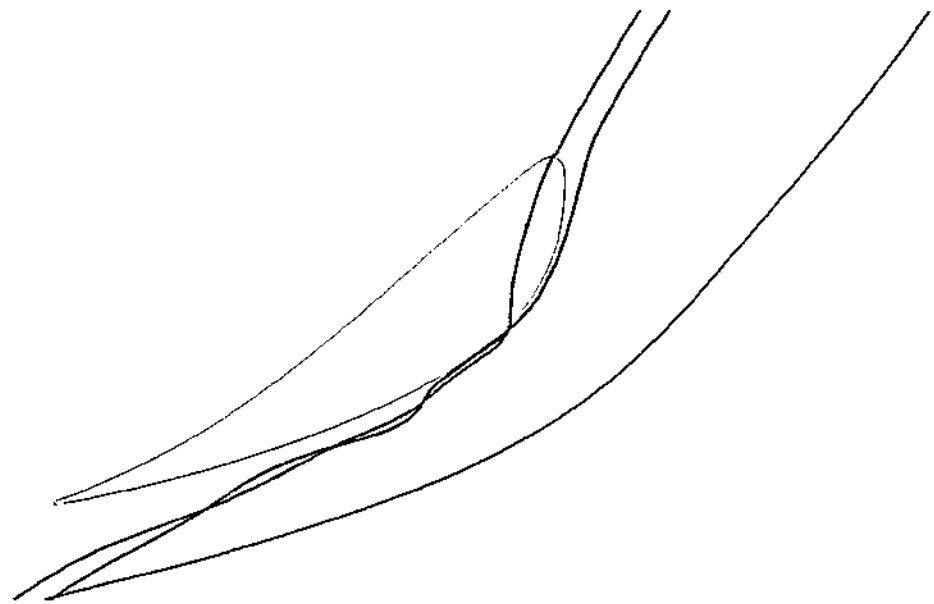
Figure 6.18: He Cascade velocity profile in tip region and vorticity at exit of tip section at 25% chord.

Lakshminarayana, 2001a).

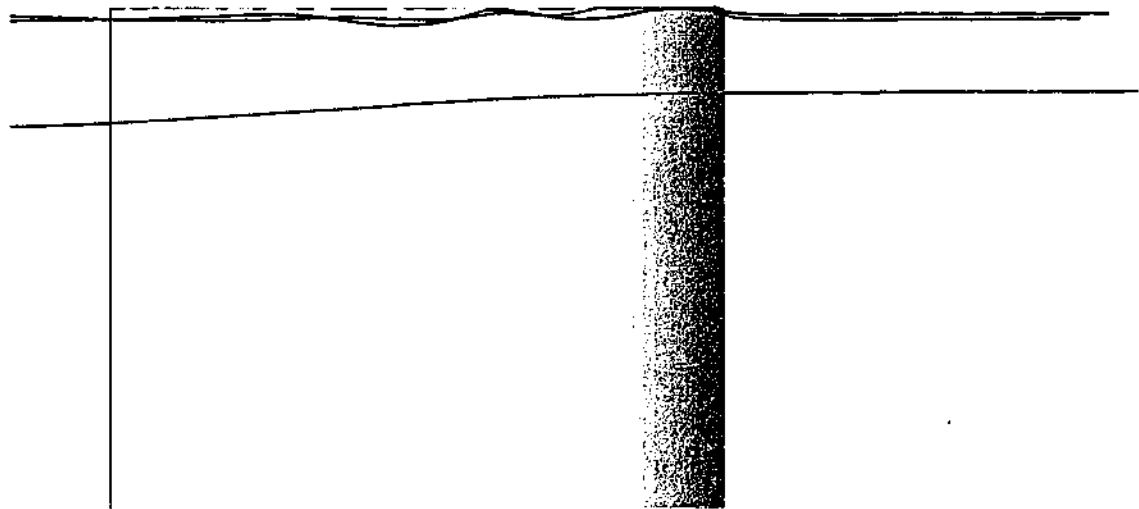
Tallman's analysis is applied to the present flow in Figure 6.20. In Figure 6.20(a) streamlines pass through the tip clearance region forward of mid-chord. Each group of streamlines passed through the same axial and pitch-wise location on the middle of the blade tip and divided into two colours, based on their proximity to the blade tip. For example, the light blue streamlines follow the flow in the span-wise half of the tip gap closest to the casing wall, the dark blue streamlines follow the span-wise half of the tip gap closest to the blade tip. Further downstream the light blue streamlines wrap around the outside of the tip vortex, whilst the dark blue streamlines remain in the vortex centre. Figure 6.20(b) shows streamlines in the portion of the tip gap downstream of the mid-chord region. Once again streamlines are separated into colours depending on their span-wise position in the clearance region.

In Tallman et al's analysis, type 3 roll up is separated from type one and type two due to the fact that these streamlines do not divide depending on their proximity due to their position at the blade tip exit. The present flow differs from this analysis as shown in 6.20(b). A number of the red and the blue streamlines separate from the rest of the group as they travel through the vortex.

In the present example, the organisation of the streamlines within the vortex may be explained due to their proximity to the blade trailing edge, and the vortex dynamics are impacted little by the vorticity from the tip gap flow. A comparison of two different flows is shown in Figures 6.21(a) and 6.21(b). The first is under the conditions found in the experiment with non-slip boundaries at all solid walls. The second has a slip condition applied at the casing boundary – there is no casing boundary layer. The streamlines over the blade tip behave in a similar manner between the two configurations, even though the streamlines exiting the gap close to the casing have vorticity of the same sign at the exit as the flow close



(a) Plan view.



(b) Side view.

Figure 6.19: He cascade, entrainment of passage flow in tip vortex for tip gap of 1.5% chord.

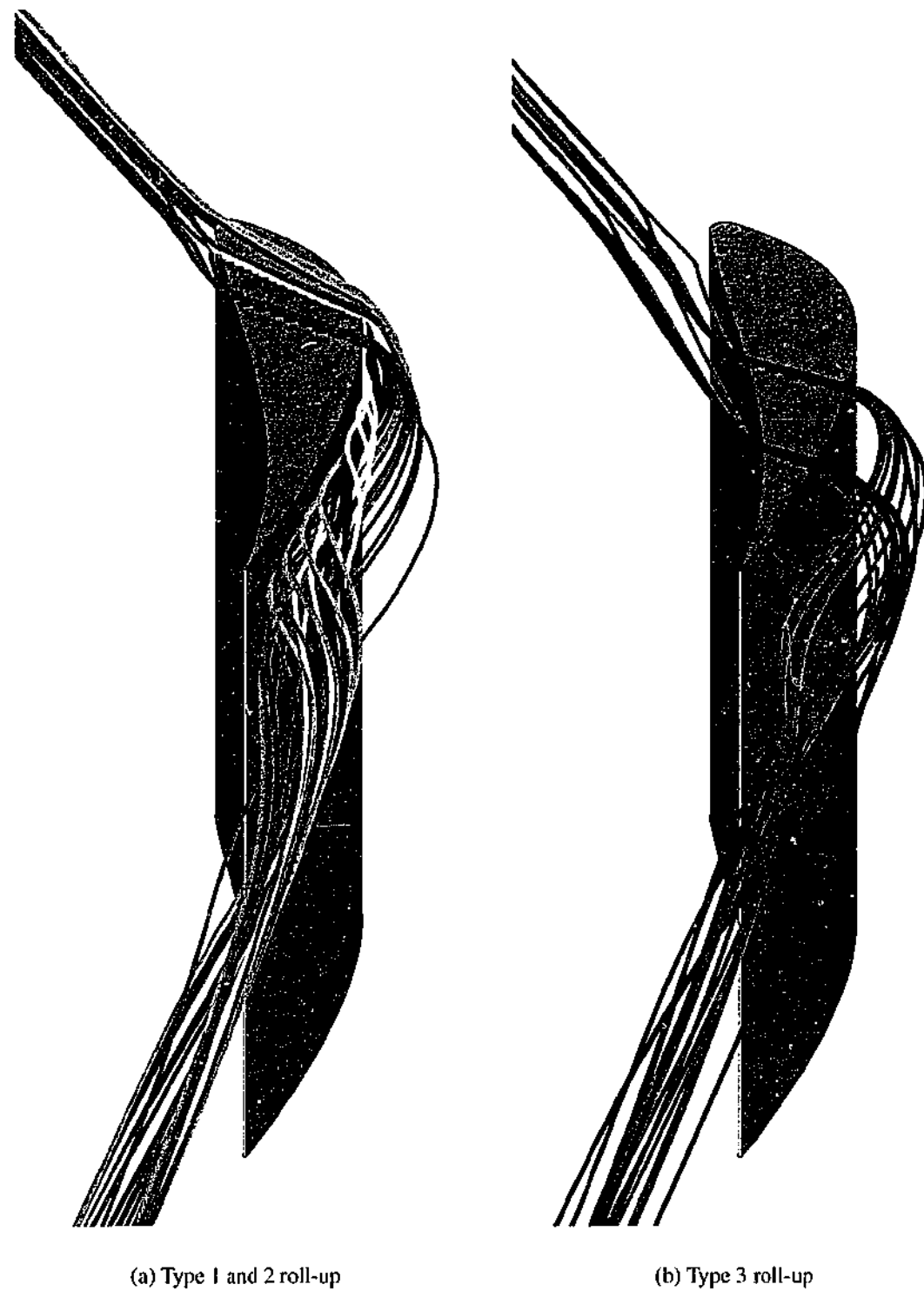


Figure 6.20: He Cascade, classification of different types of tip vortex roll up, with streamlines through tip gap region for tip gap of 1.5 % chord.

to the blade tip.

It appears that the casing boundary layer flow increases the strength of the tip vortex. This is probably due to the fact that the slower moving flow in the boundary layer is more influenced by the secondary flow.

The tip gap leakage vortex is predominantly an inviscid phenomenon that may be considered to have properties similar to a two dimensional jet flow at a solid boundary. The presence of viscosity has a number of effects on the leakage flow and tip vortex. The casing boundary layer decreases flow velocity and makes it more susceptible to entrainment, compared to flow away from the boundary. It causes blockage in the tip gap region, therefore limiting the mass flow through the tip gap and thus the strength of the tip vortex. Finally, viscous forces dissipate the energy in the leakage vortex and reduce its strength as it moves downstream, both before and after the trailing edge.

The classification of the stream-lines into different types depending on the vorticity at the tip exit seems arbitrary, particularly considering the continuous nature of the flow field and lack of flow discontinuities. The location of the stream-lines within the tip gap is important in determining the position of the stream-lines and their location once they become involved in the tip vortex. At the tip exit, the closer the stream-lines are to the casing, or the further down stream they exit the gap, the larger the radius at which the streamlines are located in the tip vortex.

The effects of the tip leakage model on surface pressure coefficient for the simulation are illustrated by comparisons of complete blade surface distributions of the steady pressure coefficient on the blade suction-side, in Figure 6.22. The most obvious effect of the increase in tip gap is the reduction of the steady pressure coefficient over the whole blade. There are also local effects close to the tip gap where the steady pressure coefficient decreases significantly. Thus the tip leakage has the effect of increasing the variation in pressure coefficient across the blade in the span-wise direction, as one may expect.

Although the tip leakage flow affects the steady blade loading, it is not obvious how the unsteady loading will be influenced. The consequences of the tip leakage flow on the unsteady aeroelastic behaviour of the cascade will be investigated in the following section. It has been shown that the presence of the tip gap vortex causes blockage in the passage and passage flow moves towards the mid-chord region. The extent of this blockage and its effect on the aeroelastic configuration needs to be quantified.

6.2.2 Aeroelastic Simulations

As described earlier this case involves a rigid bending mode of blade oscillation, with the parameters defined in Table 6.1. Investigations involve three different tip gap models. First the effect of including the tip gap in the model configuration is examined, then the effect of

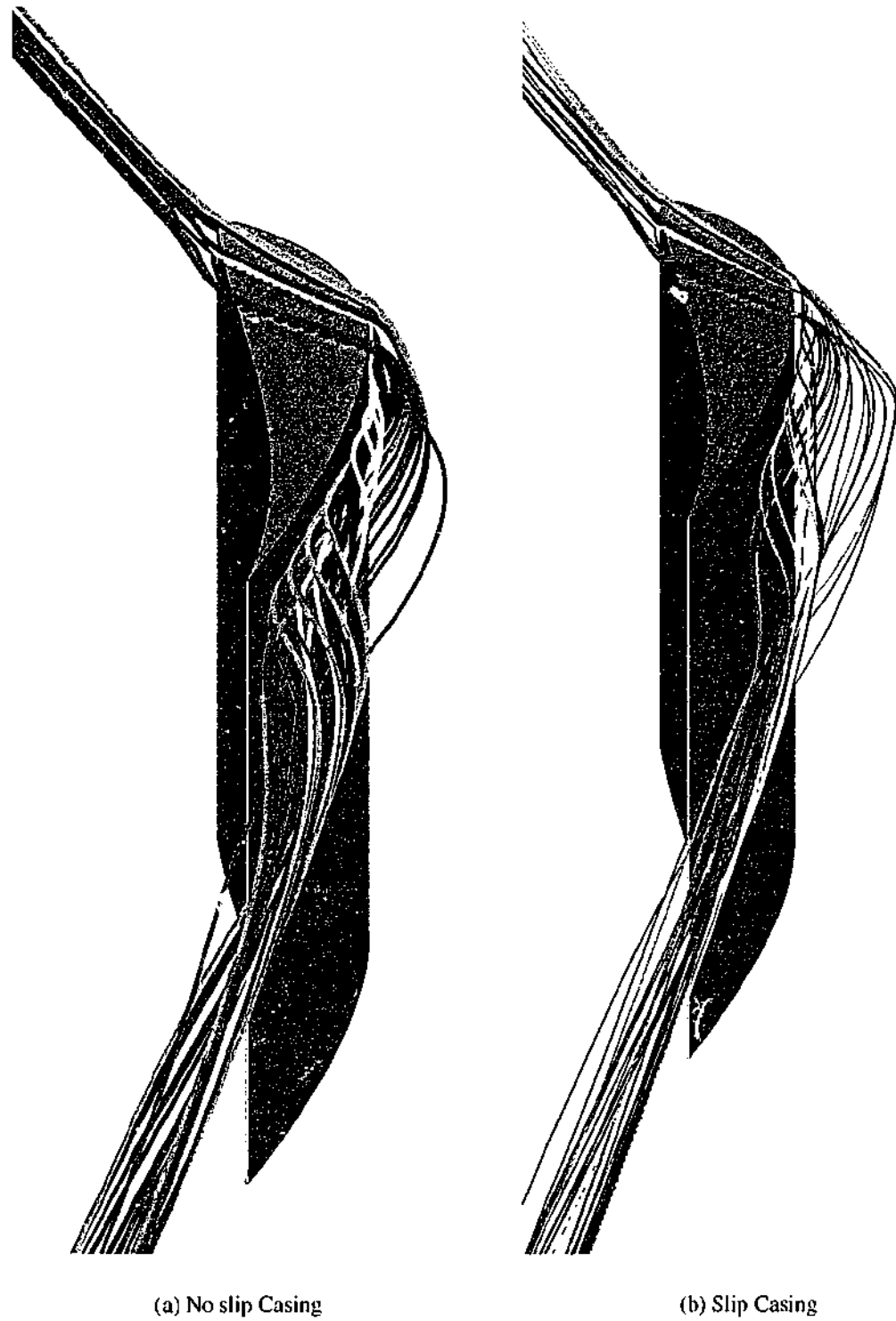

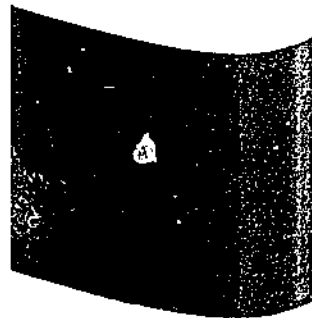



Figure 6.21: He Cascade, type 1 and 2 roll-up with different casing boundary conditions for tip gap of 1.5 % chord.



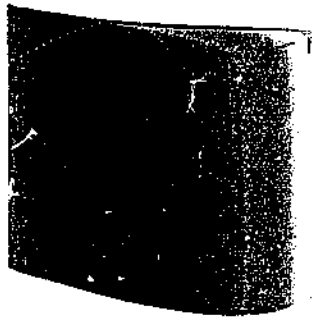
C_p : -0.2 -0.1 0.0 0.1 0.2 0.3 0.4 0.5 0.6 0.7 0.8 0.9 1.0




(a) No tip gap.



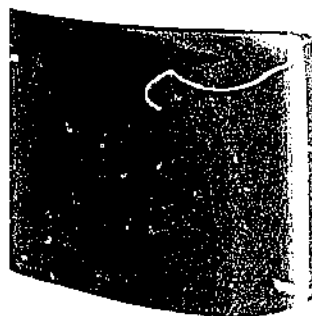
C_p : -0.2 -0.1 -0.0 0.1 0.2 0.3 0.4 0.5 0.6 0.7 0.8 0.9 1.0



(b) Tip gap 0.5 % chord.



C_p : -0.2 -0.1 -0.0 0.1 0.2 0.3 0.4 0.5 0.6 0.7 0.8 0.9 1.0



(c) Tip gap 1.5 % chord.

Figure 6.22: He Cascade. comparison of steady pressure coefficient on blade.

varying the tip gap is investigated. Finally the damping coefficient for the different tip gap results is compared with experiment.

The 3-dimensional mode was realised through different oscillation amplitudes at the hub and blade tip. In the simulation this was modelled through a span-wise variation in oscillation amplitude, which was assumed to be a pure translation in a plane orthogonal to the span-wise direction. Where a tip gap was modelled, the tip gap clearance was maintained as constant throughout the blade movement. In the experiment there may have been some variation in tip clearance through the oscillation due to the fact that the blade tip displacement follows a circular path in plane normal to the axial direction.

The simulation of the unsteady flow involved two different models, one with the same tip clearance as in the experiment, the other without the tip gap. A reduced frequency of $k_c = 0.125$ was chosen for comparison with the experimental investigation into tip gap flow behaviour. Note that in the experiment the reduced frequency is defined with respect to chord rather than semi-chord as in this case.

A comparison between experimental results for unsteady pressure is made in Figures 6.23 – 6.26. Bell and He (Bell & He, 2000) found that the magnitude of the unsteady pressure coefficient increased in the region between the mid-chord and the trailing edge of the suction-side at 90% span, for increasing tip gap. The introduction of the tip gap in the model appears to have a similar effect in the simulated results as the effect of increasing the tip gap in the experiment. The largest deviations between the two simulations in Figure 6.23 is in the mid-chord region at 90% span. The simulation under predicts the unsteady pressure magnitude compared to the experiment at 20% chord across the span, except for the 10% span position. Towards the blade trailing edge the unsteady pressure is also under predicted on the blade suction-side.

Chord-wise distributions of the phase of the unsteady pressure for the blade suction-side at different span-wise positions are shown in 6.24. The phase of the unsteady pressure compares well with experiment, except for at 10% span. The inclusion of the tip gap model reduces the phase variation along the chord of the blade on the suction-side. The largest deviations in phase in the experiment for different tip gaps were also observed in the region from mid-chord to the trailing edge.

In the comparison for the pressure-side in Figure 6.25 there is less difference between the simulation results with and without the tip gap model. The magnitude of the pressure coefficient on the forward part of the blade is under predicted at all span-wise locations. The phase of the unsteady pressure compares better with experiment than for the suction-side, except for the 10% span position. This displays the largest deviation in phase for both the suction and pressure surfaces.

The effect of the size of tip clearance on the aeroelastic simulations is investigated and also compared with the experimental measurements. Simulations were performed at a re-

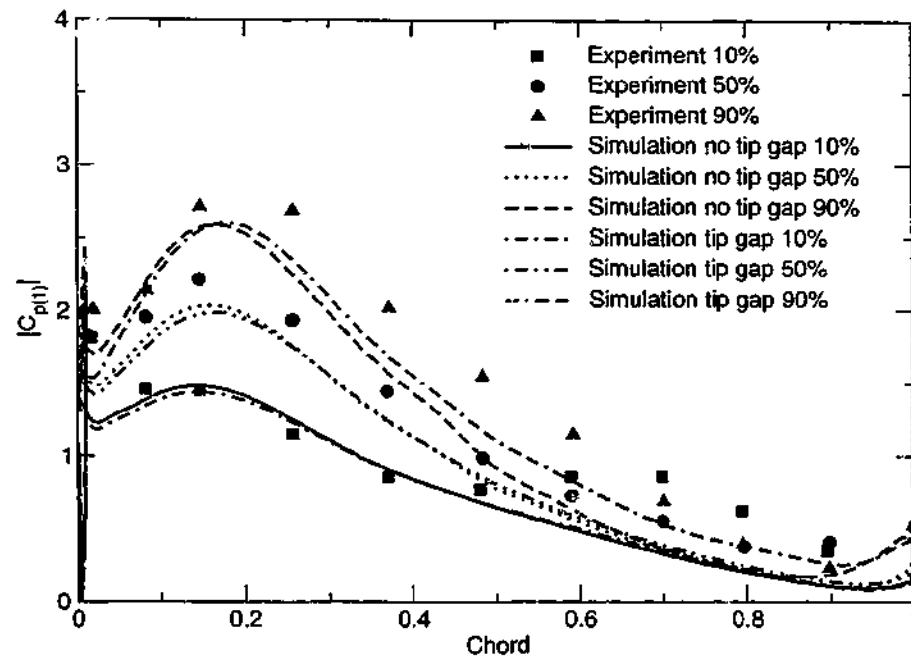


Figure 6.23: He Cascade, comparison of magnitude of first harmonic of unsteady pressure coefficient with experiment for suction surface $k_c = 0.125$.

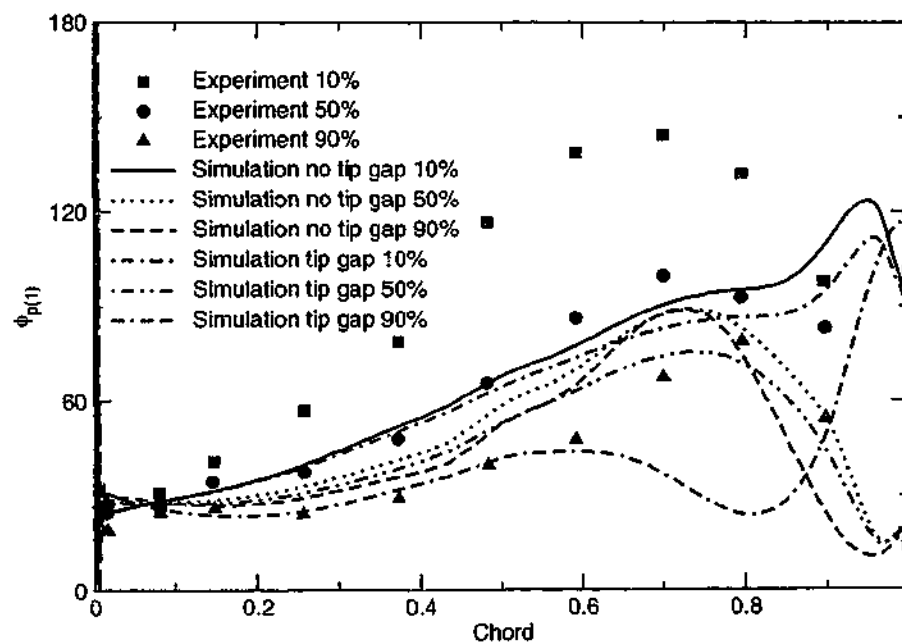


Figure 6.24: He Cascade, comparison of phase of first harmonic of unsteady pressure coefficient with experiment for suction surface $k_c = 0.125$.

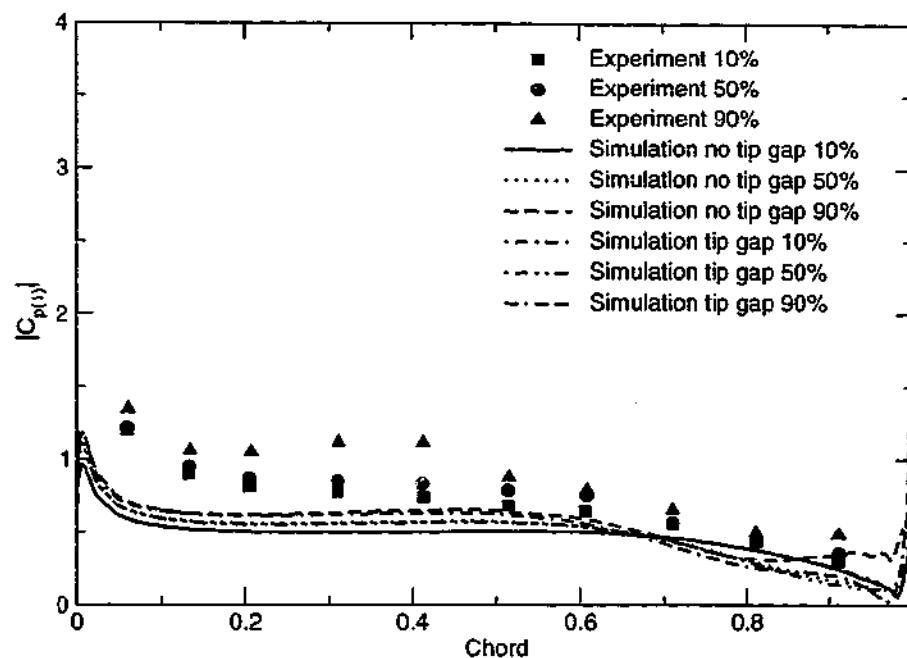


Figure 6.25: He Cascade, comparison of magnitude of first harmonic of unsteady pressure coefficient with experiment for pressure surface $k_c = 0.125$.

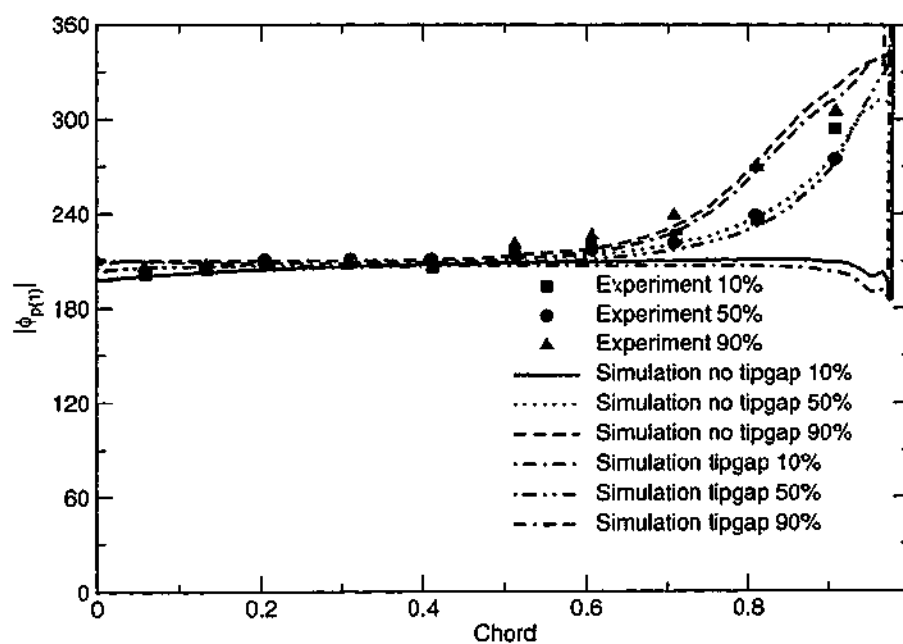


Figure 6.26: He Cascade, comparison of magnitude of first harmonic of unsteady pressure coefficient with experiment for pressure surface $k_c = 0.125$.

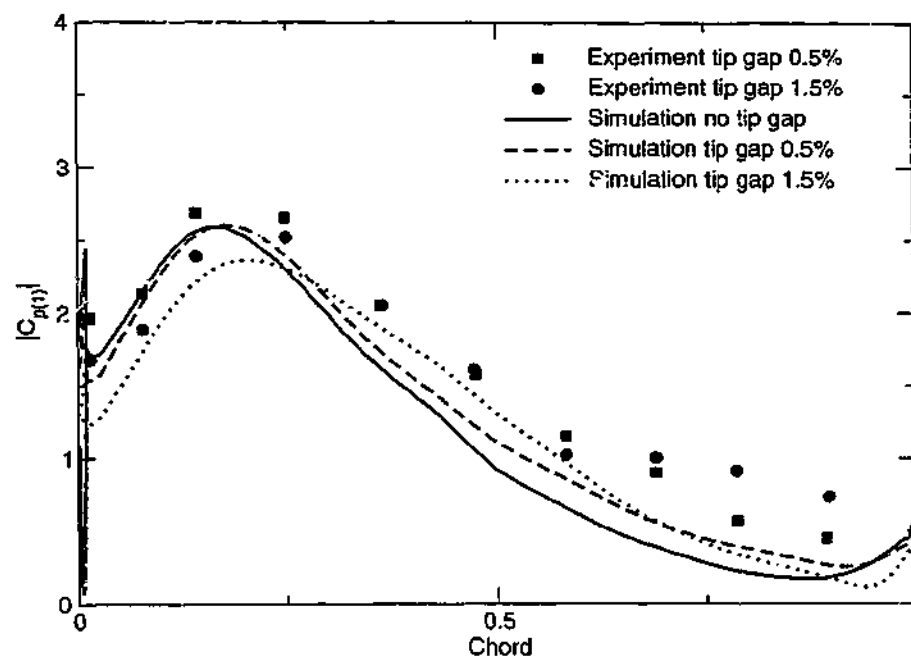


Figure 6.27: He Cascade, comparison of magnitude of first harmonic of unsteady pressure coefficient at 90% span with experiment for suction surface $k_c = 0.125$ for different tip gaps.

duced frequency of $k_c = 0.125$ for a configuration with no tip gap model, a tip gap of 0.5% chord and 1.5% chord. Figure 6.27 compares results for the suction-side at 90% span. For the unsteady pressure magnitude, a similar trend may be observed with experiment, although the magnitude is under predicted across the whole blade. The simulation results are closest to experiment for the tip gap of 1.5% chord. The largest deviations in unsteady pressure magnitude between the experimental results on the blade suction-side occur for the 1.5% case at the trailing edge, and the other simulation cases at mid-chord. For the simulations, there is a larger difference between the magnitude of the 1.5% tip clearance case compared to the other two simulation results for the first half of the blade.

Differences in phase for both the simulations and the experiment for the blade suction-side are most significant from the mid-chord region to the trailing edge, as shown in Figure 6.28. However, in the region between mid-chord and the trailing edge, the simulations with the tip gap model predict the phase significantly closer to the experimental results when compared to the simulation without a tip gap. The pressure side results are much more similar in terms of magnitude, as shown in Figure 6.29, although there are significant deviations in the trailing edge region.

The blade surface distribution of unsteady pressure magnitude has been plotted in Figure 6.30 for the suction-side. Once again the three different models are compared – no tip gap, 0.5% chord gap, and 1.5% chord gap. The signature of the tip vortex can be observed for the two cases involving the tip gap model. The reduction in unsteady pressure magnitude with increasing tip gap across the blade surface is obvious. It appears that in the 1.5% gap

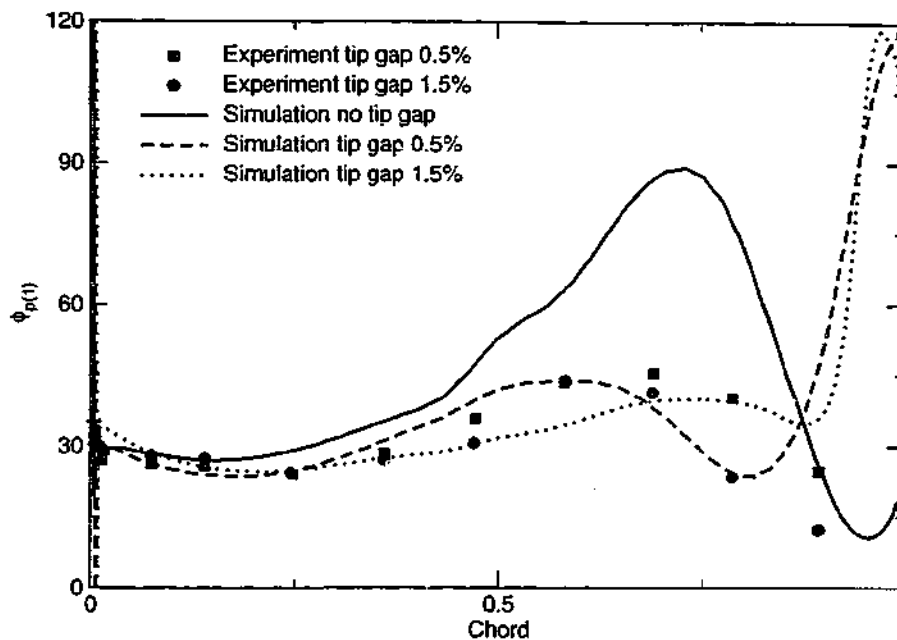


Figure 6.28: He Cascade, comparison of phase of first harmonic of unsteady pressure coefficient at 90% span with experiment for suction surface $k_c = 0.125$ for different tip gaps.

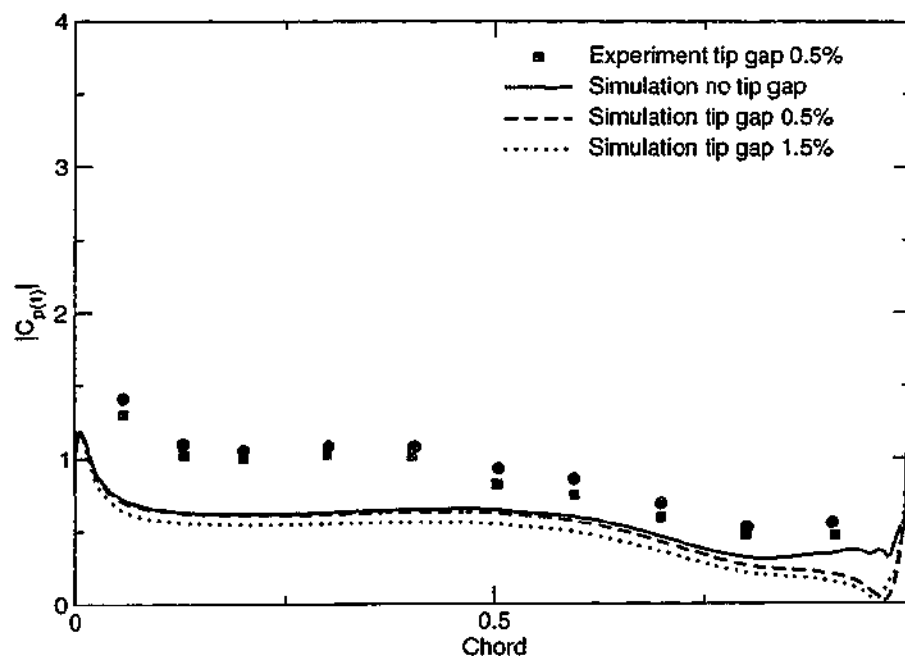


Figure 6.29: He Cascade, comparison of magnitude of first harmonic of unsteady pressure coefficient at 90% span with experiment for pressure surface $k_c = 0.125$ for different tip gaps.

| Case | Experiment damping Ξ | Simulation damping Ξ |
|--------------------|--------------------------|--------------------------|
| No tip gap | – | 0.52 |
| Tip gap 0.5% Chord | 0.422 | 0.456 |
| Tip gap 1.5% Chord | 0.422 | 0.421 |

Table 6.4: He Cascade, variation of damping with tip gap at $k_c = 0.125$.

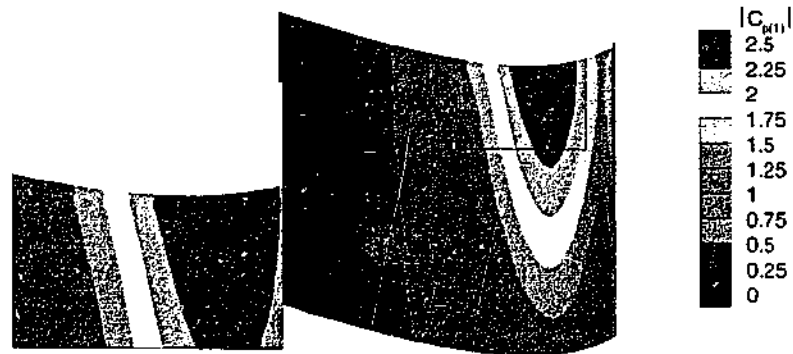
case the local impact on the unsteady blade loading is more significant and is lower in the span-wise direction.

A distribution plot was also generated for the unsteady pressure phase and compared between the different models in Figure 6.31. The differences between the model predictions for phase are significant from the blade mid-chord to the blade trailing edge, as observed in the chord-wise plots. It is interesting that while in the plot of magnitude the existence of the tip vortex is obvious in the peak unsteady pressure region, it is not so in the phase distributions. However, there is evidence of a passage vortex in the simulation without the tip gap modelled, near the blade tip at 75% chord. In the simulations with a tip gap, the signature of the tip gap flow only becomes evident towards the trailing edge.

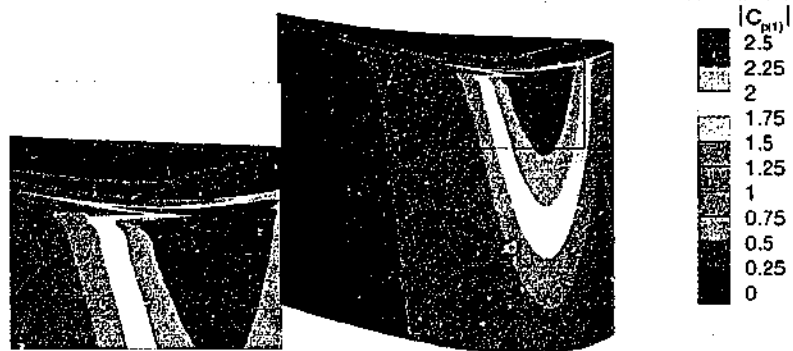
A decrease in phase is observed with an increase in tip gap length for the after part of the blade. In a case that is close to the stability limit, this could make a stable configuration unstable. In some particular cases, the inclusion of a tip model in the simulation could be important due to this effect. The impact of this difference in phase on the damping coefficient will be investigated later in this chapter.

The damping coefficient was calculated for the simulations to provide an indication of the effect of the tip gap on the aeroelastic stability of the configuration. This is compared with the damping coefficients calculated in the experiment (Bell & He, 2000) in Table 6.4. Note that the experimental results have been multiplied by the blade span, as damping coefficient calculated in the paper was not non-dimensional and has the units of m^{-1} . As in the experiment, the different tip gaps for the simulation provide a similar damping coefficient. However, there is a significant difference between simulation results with and without the tip gap model. This is due to the differences in unsteady pressure magnitude at mid-chord and, perhaps more importantly, the phase towards the blade trailing edge on the blade suction-side.

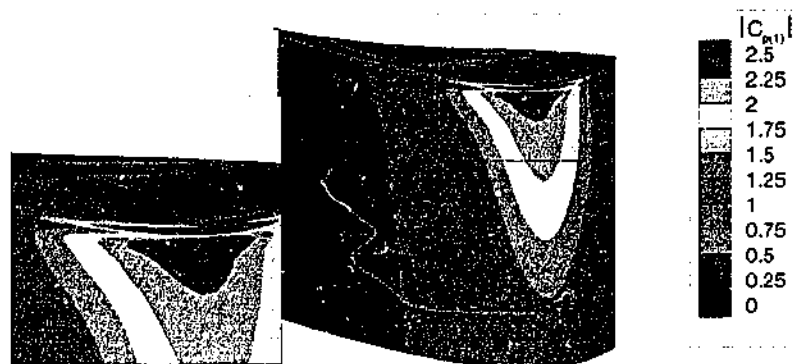
A number of trends were found in the simulation results. The net effect of tip clearance flow on the aeroelastic configuration is to increase the span-wise variation in unsteady pressure magnitude, particularly on the blade suction-side. Locally the tip gap flow introduces a local maximum and minimum in the tip gap region to the unsteady pressure magnitude on the suction-side. However over the whole blade, the unsteady pressure magnitude is reduced. There was little effect noted on the blade pressure-side of a variation in tip gap length. A significant variation in phase was observed on the blade suction-side, from mid-chord to the



(a) No tip gap.

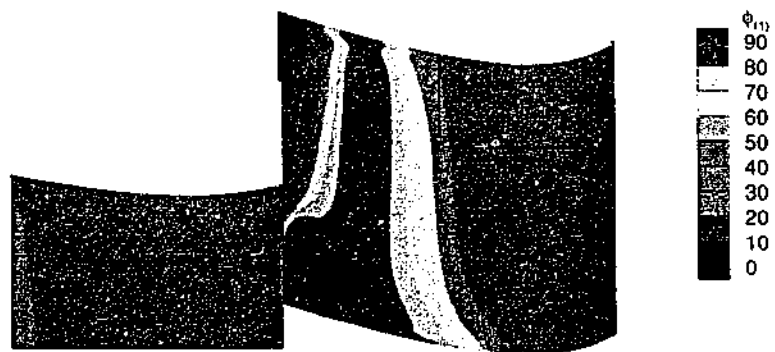


(b) Tip gap 0.5 % chord.

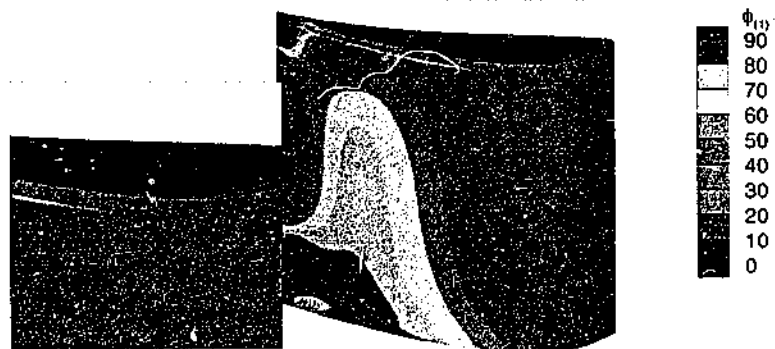


(c) Tip gap 1.5 % chord.

Figure 6.30: He Cascade, comparison of unsteady pressure coefficient magnitude on suction-side of blade, $k_c = 0.125$ for different tip models.



(a) No tip gap.

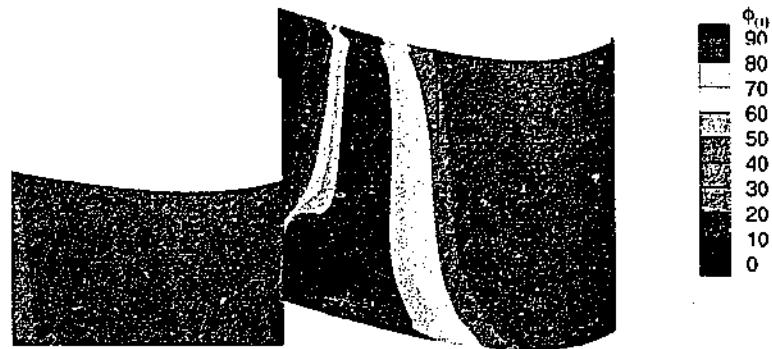


(b) Tip gap 0.5 % chord.

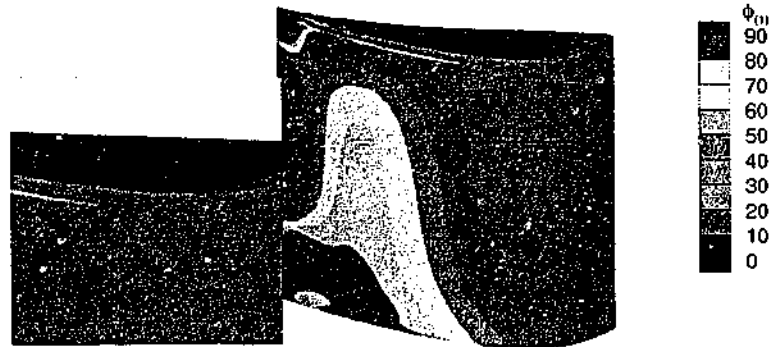


(c) Tip gap 1.5 % chord.

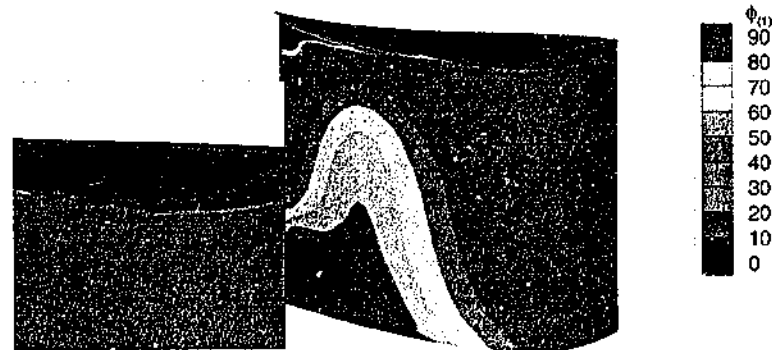
Figure 6.31: He Cascade, comparison of unsteady pressure coefficient phase on suction-side of blade, $k_c = 0.125$ for different tip models.



(a) No tip gap.



(b) Tip gap 0.5 % chord.



(c) Tip gap 1.5 % chord.

Figure 6.31: He Cascade, comparison of unsteady pressure coefficient phase on suction-side of blade, $k_c = 0.125$ for different tip models.

blade trailing edge.

A number of comparisons have been made between the linear cascade aeroelastic case, between experiment and simulation with different tip gap lengths. The results are summarised as follows:

- The suction-side pressure coefficient at 90% span for different tip gap lengths compares well between experiment and simulation for the steady configuration.
- Differences were proposed between the description of the tip gap flow compared to those given by Tallman and Lakshminarayana (2001a). The behaviour of the present tip gap flow may be best described by a jet flow close to a solid boundary.
- The unsteady pressure magnitude results for the simulations compare well in trend for a reduced frequency of $k_c = 0.125$.
- The signature of the tip vortex was evident in blade surface plots of magnitude and phase. For the $k_c = 0.125$ case the vortex moved lower down the blade with increasing tip gap length, and increasing axial chord position on the blade.
- While there was some difference found between experiment and simulation for unsteady pressure magnitude, the damping coefficient compares well with experiment for a $k_c = 0.125$. The simulations with a tip gap compare more favourably with experiment.

6.3 Standard Configuration 4

The second of the turbine cascades is subject to flow in the high subsonic and the transonic flow regimes. As discussed in Section 6.1.3, this flow regime involves important phenomena that have the potential to influence the aeroelastic configuration, including shock waves and shock-induced boundary layer interaction.

A comprehensive set of measurements were performed on the annular cascade at Lausanne Institute of Technology or *École Polytechnique Fédérale de Lausanne* (EPFL) (Bölcs & Fransson, 1986). The experiment involved an annulus of blades vibrating at a prescribed reduced frequency, the vibration of each blade set at a particular inter-blade phase angle. Subsequently 3-dimensional data has been made available for the flow (Ott, 1998) and the 3-dimensional geometry of the vibration mode shape (Ott, 2002). The case is known as Standard Configuration 4 (STCF 4), and is one of the 11 standard, aeroelastic turbine test cases (Bölcs & Fransson, 1986; Fransson & Verdon, 1991).

Data for the blade geometry is listed in Table 6.5. Blade profiles are described as being typical of modern free standing turbine blades. Blade thickness and camber is relatively

| | |
|--------------------|-------------------|
| Blade chord | 0.072 m |
| Aspect ratio | 1.8 |
| Solidity | 0.76 (at midspan) |
| Blade outlet angle | 72.4° |
| Inlet flow angle | 44.1° |
| Stagger angle | 56.5° |

Table 6.5: Blade and flow geometry for Standard Configuration 4

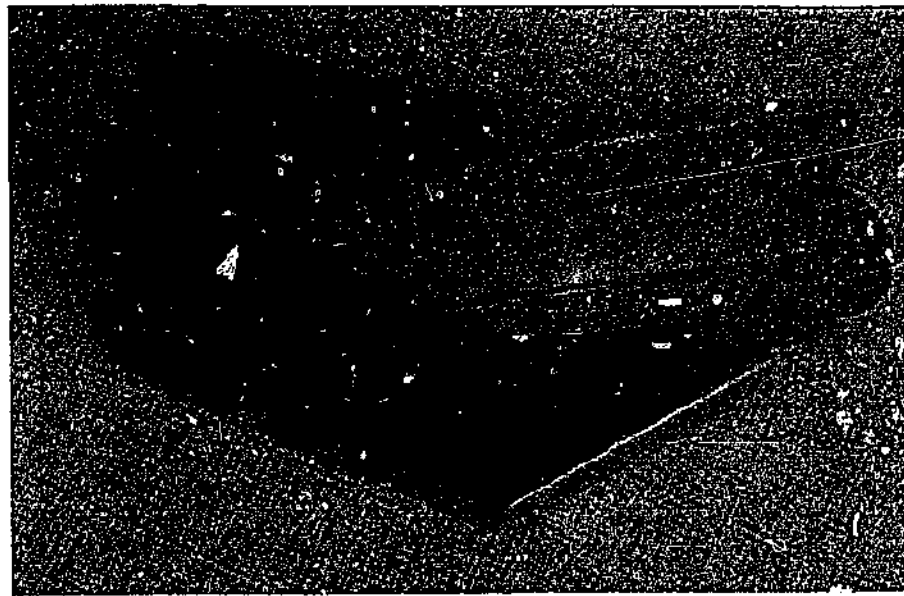


Figure 6.32: Standard Test Case 4 blade from experimental facility (Ott, 2002).

high. Some of the tests were performed under transonic flow conditions; at the inlet the flow is low subsonic and at the outlet it is supersonic in the axial direction. Typically these types of blades exhibit a flutter instability in the first bending mode. This is simulated in the experiment by a translation in the cylindrical coordinate system of the prismatic blade at a prescribed displacement angle. A blade from the rig is shown in Figure 6.32 – note the hub shroud to reduce end-wall leakage.

The mode shape of vibration in the experiment has been estimated by taking the mid-span amplitude and assuming a pivot point at 0.0885 m from the axis of the facility. The spring body assembly for the experimental rig is shown in Figure 6.33. In this figure, the radiating spokes form the springs, the large blocks and the blades (not shown) are the masses for the system. The pivot point for each blade is estimated as being at the centre of the spring section (Ott, 2002).

The experimental rig is described as an annular cascade of turbine blades meaning that that the rig is non-rotating. The full annulus allows for the measurement of all possible inter-blade phase angles without any of the approximations to flow periodicity made in linear cascades. Figures 6.34 and 6.35 show the cascade assembly. There is no structural inter-

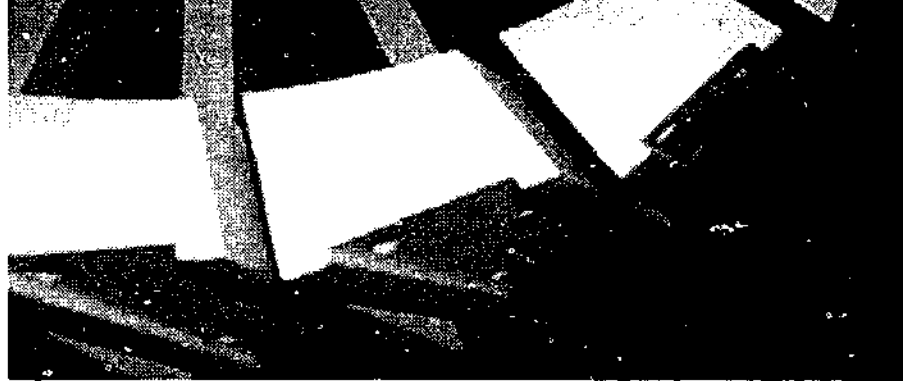


Figure 6.33: Standard Test Case 4 spring mass assembly in experimental facility (Ott, 2002).

ference for the flow between the blade tips and casing. A significant lip exists on the hub shroud.

6.3.1 Simulation Model

The present simulations involve two different geometric configurations. The first is a 2-dimensional cascade, the geometry of which is a 2-dimensional projection of the annular cascade onto a cylinder of constant radius that bisects the blades at mid-span of the experimental rig. The second involves 3-dimensional annular blade passages which is as similar as possible to the rig. The inlet and outlet plane lie one axial chord upstream and downstream of the blade's leading and trailing edges, respectively.

Differences in geometry:

- Hub leakage shroud not modelled.
- Surface on blade and side-walls assumed to be hydraulically smooth.
- The tip clearance varies, depending on the blade number. The casing is oval by 0.1 mm and it is estimated that the tip clearance is between 0.25 mm and 0.3 mm. In the simulation the clearance is set at 0.3 mm where it is modelled.
- There is a slight chamfer on the blade tip edges, that is not modelled.

Differences in flow conditions:

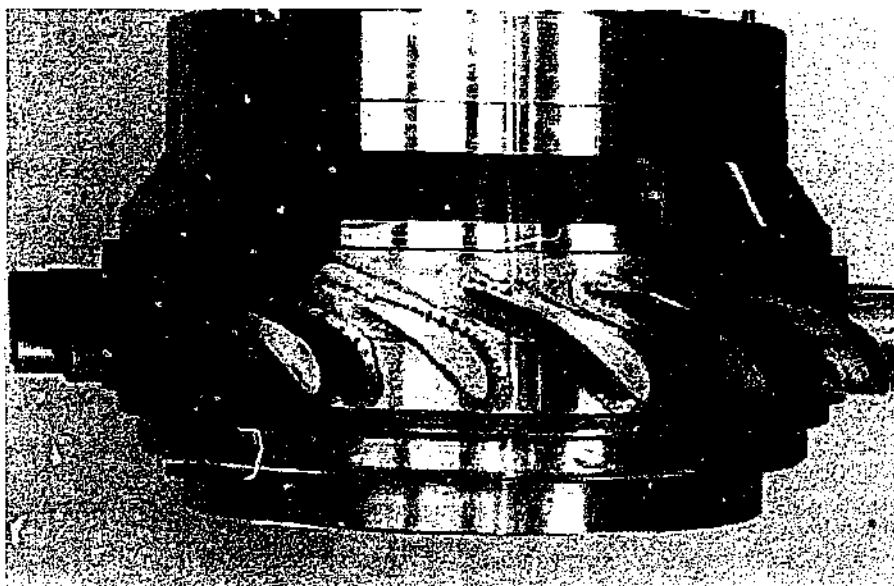


Figure 6.34: Standard Test Configuration 4 annular cascade assembly (Ott, 2002).



Figure 6.35: Close up of Standard Test Configuration 4 annular cascade assembly (Ott, 2002).

- The inlet plane in the simulation is specified at 1 axial chord upstream of the blade leading edge; in the experiment inlet plane measurements are made at 13% of axial chord upstream of the blade.
- Inlet total pressure span-wise distribution is specified as a constant, taking the same value as the circumferential average at mid-span at the inlet measurement plane in the experiment.
- Inlet flow angle is also prescribed from the experiments in the same manner as the inlet total pressure for the subsonic test. For the transonic test, this is specified to obtain the same blade loading as the experiment.
- The outlet plane is 1 axial chord down-stream from the trailing edge; the experimental measurement plane is 1.61 axial chords down-stream of trailing edge.
- The outlet static pressure profile is specified in the span-wise direction. As with the inlet total pressure distribution, no pitch-wise variation is specified; all other quantities are extrapolated from the interior of the domain.
- Boundary layers on the blade and side-walls are assumed to be fully turbulent.
- Hub leakage flow is not modelled.
- The boundary layers on the side walls at the inlet are assumed to be of negligible thickness.
- The inlet total temperature was not indicated in the experiment; this was set at standard conditions.
- An ideal gas was modelled, in the experiment air was the working fluid.
- The typical inlet turbulence length scale was not specified in the experimental report, nor was the inlet intensity level. This was assumed to be the order of the blade length and 0.1 respectively, as used by other researchers in the simulation of turbomachinery cascades (Liu *et al.*, 1998a; Garg & Ameri, 2001).

The inlet plane was positioned through a number of considerations. In the experimental results, no data was provided regarding the condition of the hub and casing boundary layer at the inlet. It was not possible to generate an acceptable mesh with an inlet length of 0.13 axial chord as in the experiment. Small inlet disturbances can adversely affect the solution process causing divergence of the numerical algorithm. These effects are usually reduced by moving the inlet away from the blade leading edge. Boundary layer suction was performed in the experiment 2.34 axial chord lengths upstream of the cascade so the thickness of the boundary layers at the inlet of the simulation domain are assumed to be small.

| Condition | Test 552 | Test 627 |
|-----------------------------------|----------------------|-----------------------|
| Bending mode direction | 63° | 63° |
| Bending mode amplitude at hub | NA | 3.0×10^{-3} |
| Bending mode amplitude at midspan | 3.0×10^{-3} | 3.8×10^{-3} |
| Bending mode amplitude at casing | NA | 4.68×10^{-3} |
| Reynolds number | 8.2×10^5 | 5.6×10^5 |
| Inlet Mach number | 0.28 | 0.19 |
| Outlet Mach number | 0.9 | 0.85 |
| Reduced frequency | 0.107 | 0.1187 |

Table 6.6: Aeroelastic configuration parameters for high subsonic tests for Standard Configuration 4.

6.3.2 High-subsonic Cases

In this section two different cases are considered in the high-subsonic regime. The first is for validation purposes and is a 2-dimensional configuration, involving an outlet Mach number of 0.9. The second is a 3-dimensional configuration for which inlet and outlet plane conditions are available and is characterised by an outlet Mach number of 0.85. Conditions for both cases are listed in Table 6.6. Significant differences between the two experimental results exist, even though they involve similar conditions.

The importance of including the effects of viscosity is examined through comparisons of Euler and RANS simulations and through the modelling of tip gap flow. The blade surface unsteady pressure distributions are compared for two different interblade phase angles; the simplest from a modelling perspective at $IBPA = 180^\circ$ and the second at $IBPA = -90^\circ$. At the second IBPA the configuration exhibits an aeroelastic instability – this is important from a design perspective. Parameters for the steady and aeroelastic cases are listed in Table 6.6.

Steady Simulations

As done previously the suitability of the mesh was investigated. The grid convergence of the Navier-Stokes simulations was only performed for 2-dimensional configurations, with the mid-span conditions for Test 627. It was found that a mesh of 160 cells in the axial direction and 64 cells in the blade to blade direction was sufficient to provide grid convergence, with a $y^+ < 3$ at mid-chord on the suction-side. Simulations were also performed on a finer grid with a $y^+ < 1$, however this produced a variation in the steady pressure coefficient of less than 1 percent. The number of cells was doubled in the axial direction but this made little difference to the steady surface pressure coefficient. Based on the 2-dimensional grid convergence studies, a mesh of $160 \times 64 \times 64$ in the axial, pitch-wise and span-wise directions, respectively, is used for 3-dimensional Navier-Stokes simulations. The largest grid involved approximately 2.6 million points distributed over 32 computational blocks. A typical mesh for a four passage, 3-dimensional Euler simulation for an interblade phase angle

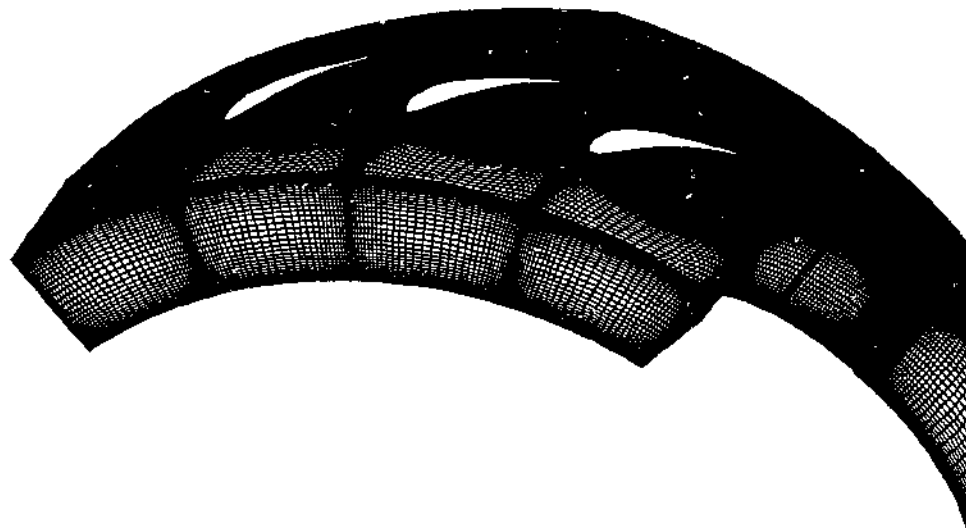


Figure 6.36: Typical mesh for a four passage, 3-dimensional Euler simulation.

of 90 degrees is shown in Figure 6.36.

The steady pressure coefficient is shown for the 3-dimensional cascade simulation at mid-span of Test 627 and compared with experiment in Figure 6.37. The Navier-Stokes results under-predict the suction over the back portion of the blade suction-side, while the inviscid result under-predicts the suction in the mid-chord region. The reason for this deviation is not obvious, but maybe due to a combination of the presence of the boundary layer on the blade and the end-walls.

A plot of passage Mach number distribution at mid-span for an annular cascade configuration with a tip gap model is shown in Figure 6.38. Flow conditions are subsonic throughout the entire passage. This has important implications for the aeroelastic configuration – a choked passage leads to coupling between the blades due to the passage shock wave and an entirely different unsteady pressure distribution, particularly for the mid-chord region of the blade suction-side.

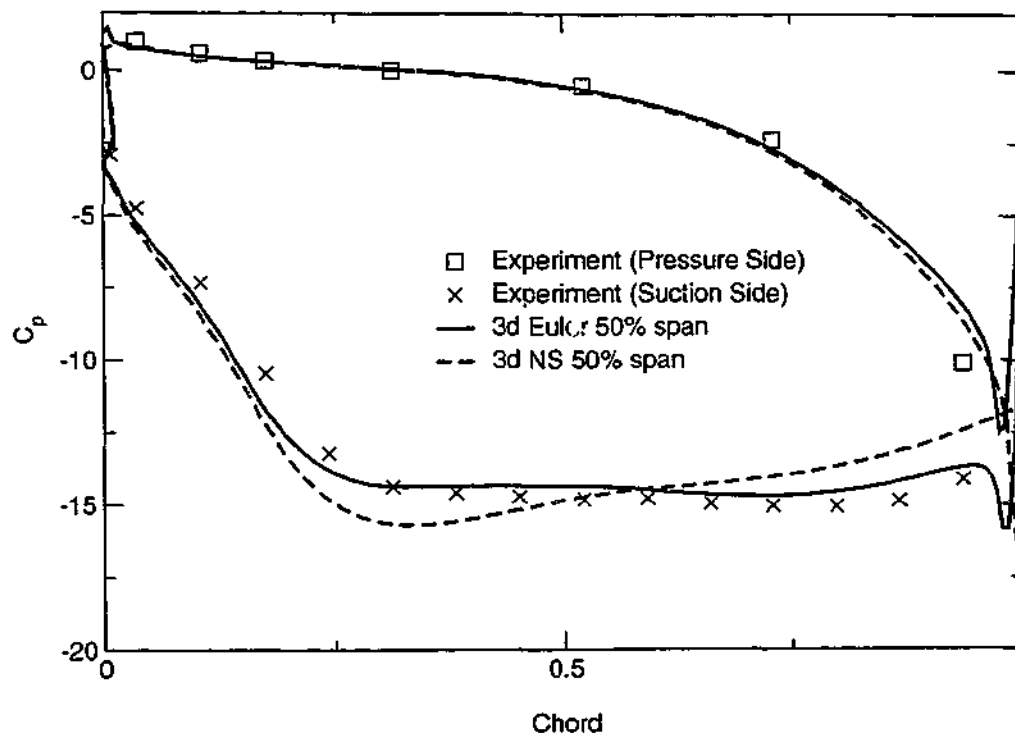


Figure 6.37: Steady surface pressure coefficient.

Aeroelastic Simulations

The investigation into the aeroelastic configuration involved two different cases, with the conditions listed in Table 6.6. For all of the simulations, time step was such that 32 steps were used per period of oscillation. For temporal convergence the simulation was integrated for 4 periods, except for the tip gap simulations which required 6.

The first case was also simulated by other authors (Grüber & Carstens, 1998). Note that there is a slight difference in reduced frequency and inflow Reynolds number between the other simulations and the present simulations as these were the conditions quoted in the updated experimental report (Fransson & Verdon, 1991). The simulation model involved a two passage, 2-dimensional cascade and an inter blade phase angle of 180° . The Navier-Stokes and $k-\omega$ flow solver was used and slip boundary conditions were applied to the end-walls in the span-wise direction. A comparison between experimental results (Bölcs & Fransson, 1986) and simulated results for unsteady pressure magnitude and unsteady pressure phase is shown in Figures 6.39 and 6.40 respectively.

There is some discrepancy between the simulated results and experiment, particularly in the unsteady pressure magnitude at 20% chord on the blade suction-side. However, these results are very close to the 2-dimensional Navier-Stokes simulations presented by Grüber and Carstens (1998).

The second case, Test 627, has a lower outlet Mach number than Test 525. The 3-

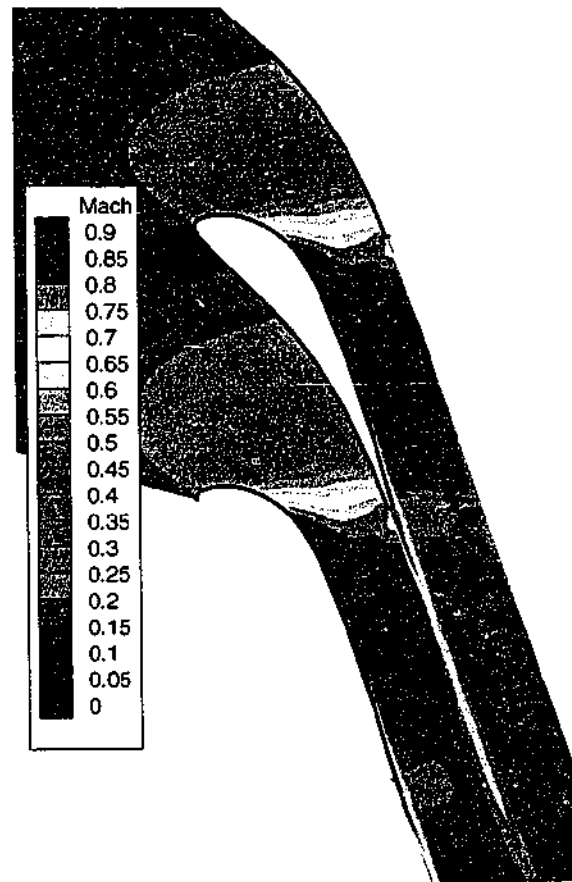


Figure 6.38: STCF 4 Test 627, Mach number distribution for simulation with Navier-Stokes model in passage at mid-span.

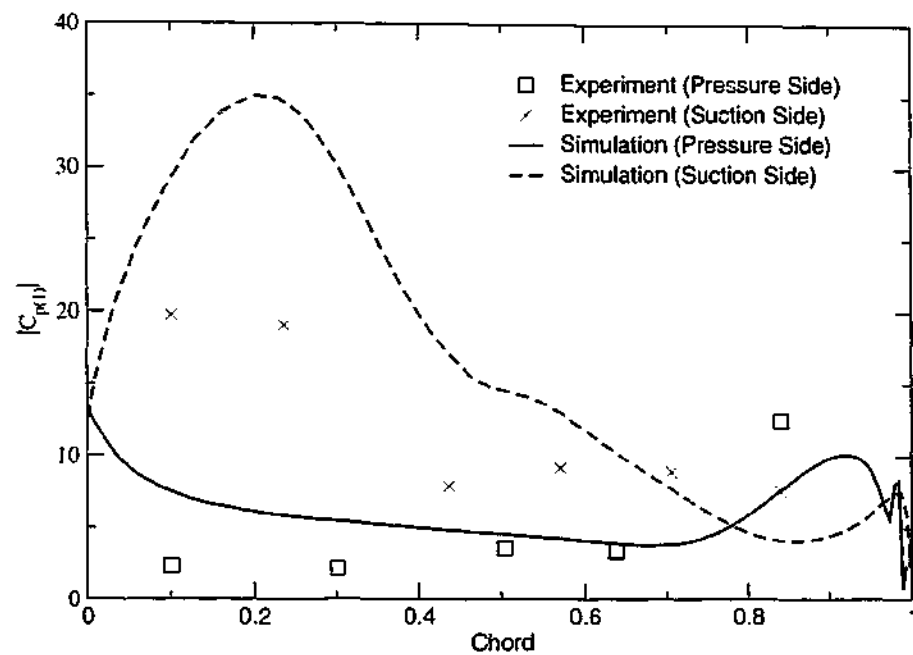


Figure 6.39: STCF 4, Test 552, $IBPA = 180^\circ$ first harmonic of unsteady pressure coefficient magnitude.

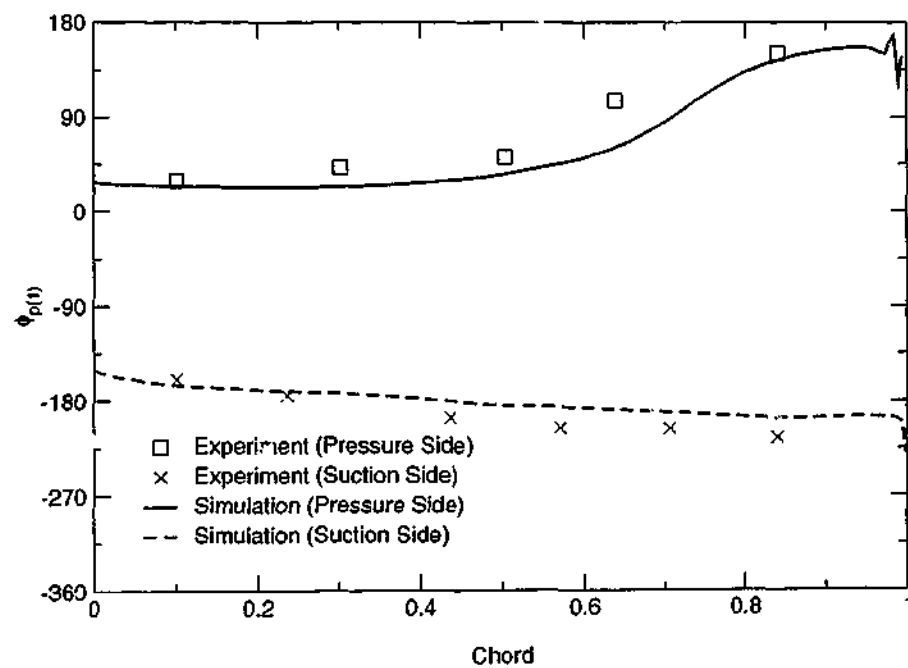


Figure 6.40: STCF 4, Test 552, $IBPA = 180^\circ$ first harmonic of unsteady pressure coefficient phase.

dimensional flow conditions were available for this case, allowing for 3-dimensional simulations. For the 3-dimensional results, the reference pressure for the unsteady pressure is at mid-span on the inlet plane and the reference amplitude is at mid-span on the blade.

Simulations were performed for a number of different configurations. As a reference, 2-dimensional simulations for both the inviscid and Navier-Stokes flow model were undertaken. The 3-dimensional simulations involved the Euler flow model, the Navier-Stokes solver with $k-\omega$ turbulence model, and the Navier-Stokes model with the tip gap modelled. Comparisons are made between these cases at different span-wise locations, between the Euler and Navier-Stokes simulations and experiment at 50% and 10% span, and with the Navier-Stokes simulations with and without the tip gap model at 90% span. These comparisons exhibit the largest differences between simulation configurations.

A comparison between the unsteady pressure coefficient for the two different flow models, and the 2-dimensional and 3-dimensional configuration is made in Figures 6.41 – 6.43. Where the amplitude is highest on the suction-side at 20% chord there is a deviation between the simulations and experiment in the order of 15–30%. This is less than the previous case, Test 525. None of the simulations exhibit a local maximum in the magnitude of unsteady pressure coefficient found in experimental measurements in the region of mid-chord. Predictions for phase compare well with experiment close to the leading edge on both the suction-side and pressure-side. The 2-dimensional simulations predict similar unsteady pressure magnitude to the 3-dimensional simulation, and are almost identical in phase.

There is a significant difference in the predictions of the phase angle for the surface pressure coefficient on the blade suction-side in Figure 6.43, in particular for the region between mid-chord and the trailing edge. This feature in the experimental results coincides with a maximum in the magnitude of the unsteady pressure coefficient that is also not observed in the simulation.

The experimental results are consistent with choked or close to choked conditions in the passage. The Mach distribution of the Navier-Stokes simulation of the passage in Figure 6.38 shows that the Mach number is no higher than 0.8 close to the trailing edge on the blade pressure-side. The Test 525, which was discussed earlier in this section, has a higher outlet Mach number than the present Test 627. Therefore one would expect if the Test 627 passage was choked, the passage of Test 525 would also be choked. Consequently Test 525 should exhibit a similar phase change on the blade suction-side as Test 627 due to the impingement of the passage shock. As is shown in Figure 6.40, this is not the case, thus there appears to be some inconsistency in the experimental measurements. The behaviour of the unsteady pressure phase on the blade suction-side is similar to other tests at higher outlet Mach number conditions, one of which will be examined later in this chapter.

The largest difference between the Euler and Navier-Stokes simulations is in the prediction of the unsteady pressure magnitude on the blade suction-side. The profiles are similar in

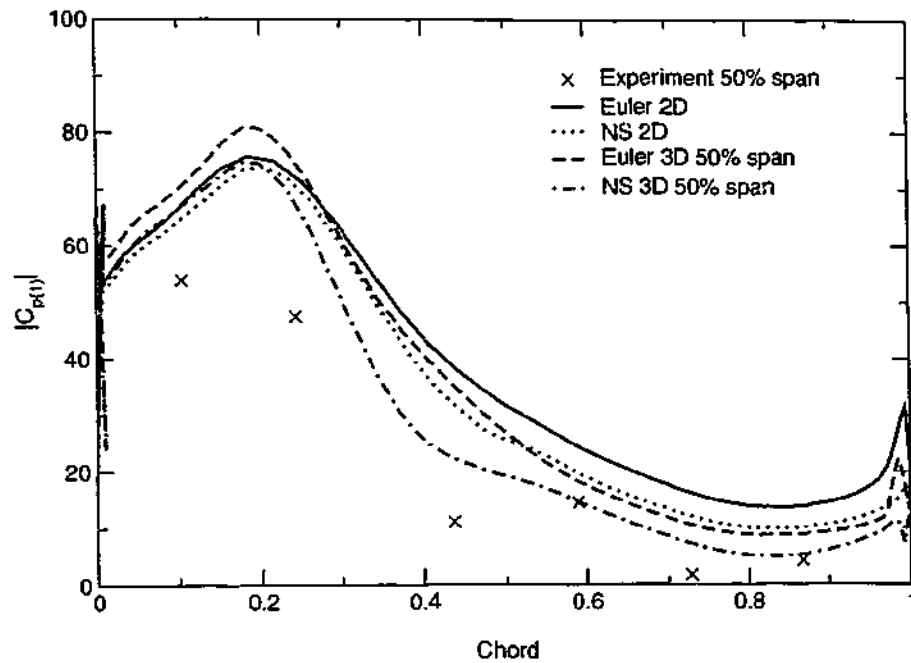


Figure 6.41: STCF 4, $IBPA = 180^\circ$, first harmonic magnitude of unsteady pressure coefficient on suction-side at mid-span.

shape and differences in phase only become apparent towards the trailing edge on the blade suction-side.

One of the most significant differences between the 3-dimensional Euler and Navier-Stokes simulations was found at 10% span, on the blade suction-side. Figures 6.44 and 6.45 show the Euler and Navier-Stokes results at 10% span. There is a local maximum in the Euler simulation at 50% chord which is not present in the Navier-Stokes result. Flow conditions in the Euler simulation at this span-wise position are close to choke – much closer than for the Navier-Stokes simulation.

The deviations in phase for blade suction surface are minor in Figure 6.45. This suggests that for the inviscid simulation it appears that the close to choked conditions affect the magnitude of the unsteady pressure coefficient first, before influencing its phase. The influence of the hub secondary flows on the Navier-Stokes results is difficult to gauge – this done more easily through complete surface distributions.

The tip gap effects are investigated through comparisons of unsteady pressure coefficient at 90% span. This is in the region of the casing secondary flow, but below the localised effects of the tip vortex. Figures 6.46 – 6.47 compare Navier-Stokes simulations with and without the tip gap model. Results with and without the tip gap model are similar, with the largest differences on the suction-side at 20% chord at the peak unsteady pressure, and mid-chord. Whereas the subsonic case in Section 6.2 exhibited a significant rise in the unsteady pressure magnitude at mid-span with the tip gap, this is not observed for this case.

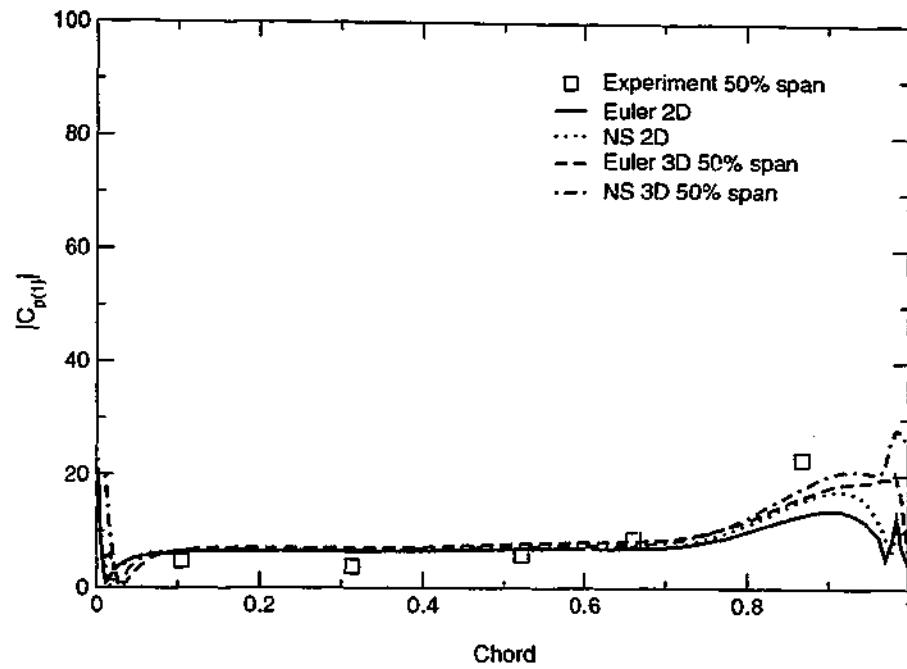


Figure 6.42: STCF 4, $IBPA = 180^\circ$, first harmonic magnitude of unsteady pressure coefficient on pressure-side at mid-span.

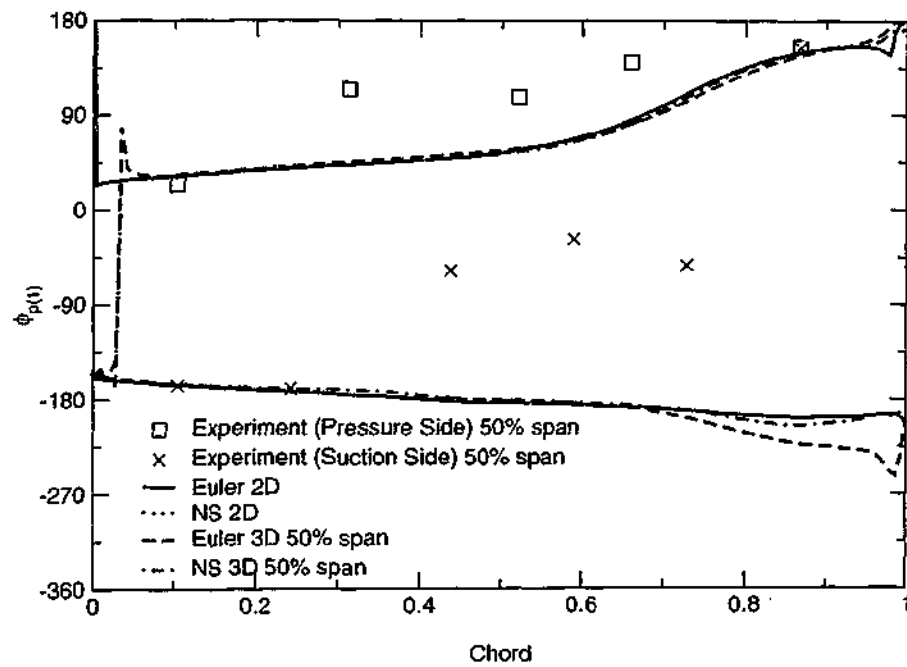


Figure 6.43: STCF 4, $IBPA = 180^\circ$, phase of first harmonic of unsteady pressure coefficient at mid-span.

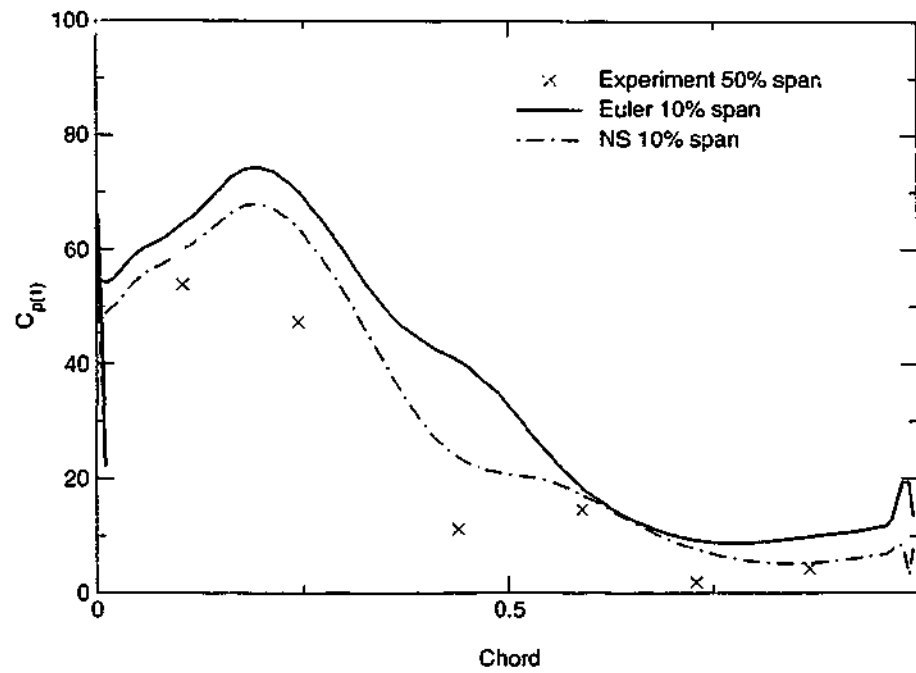


Figure 6.44: STCF 4, $IBPA = 180^\circ$, first harmonic magnitude of unsteady pressure coefficient on suction-side at 10% span.

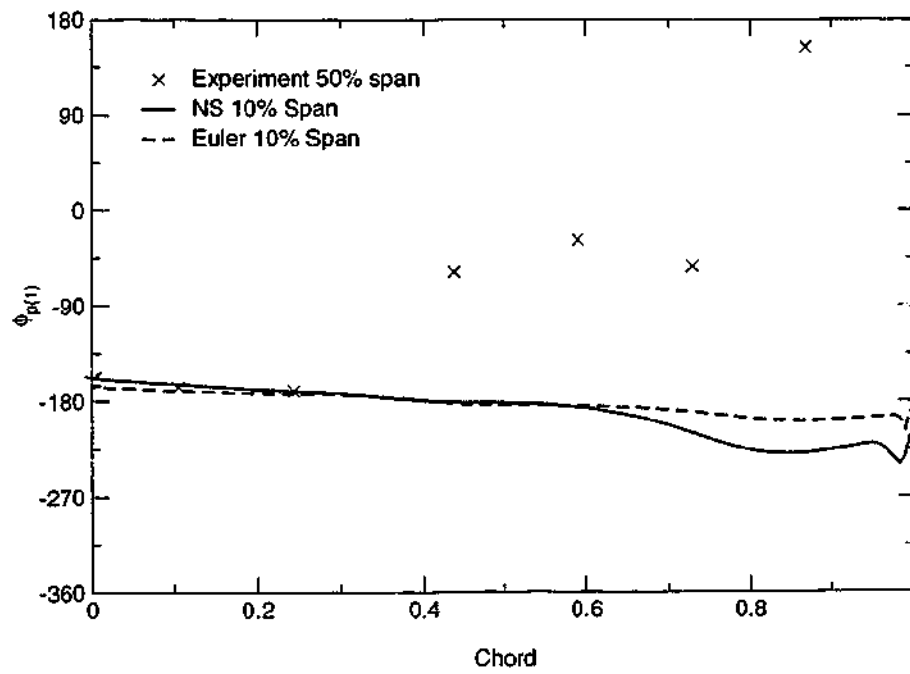


Figure 6.45: STCF 4, $IBPA = 180^\circ$, phase first harmonic of unsteady pressure coefficient on suction-side at 10% span.

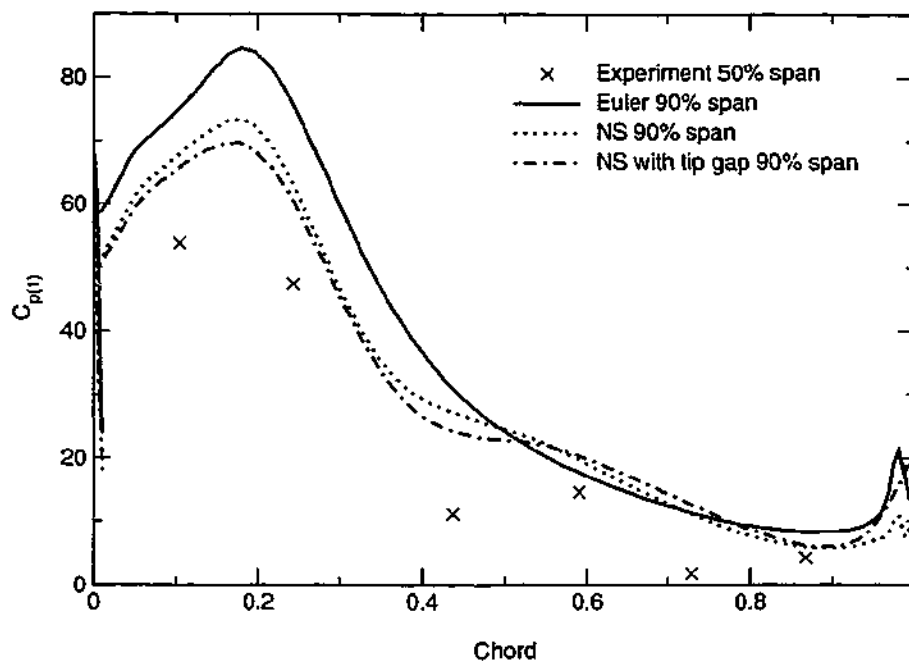


Figure 6.46: STCF 4, $IBPA = 180^\circ$, first harmonic magnitude of unsteady pressure coefficient on suction-side at 90% span.

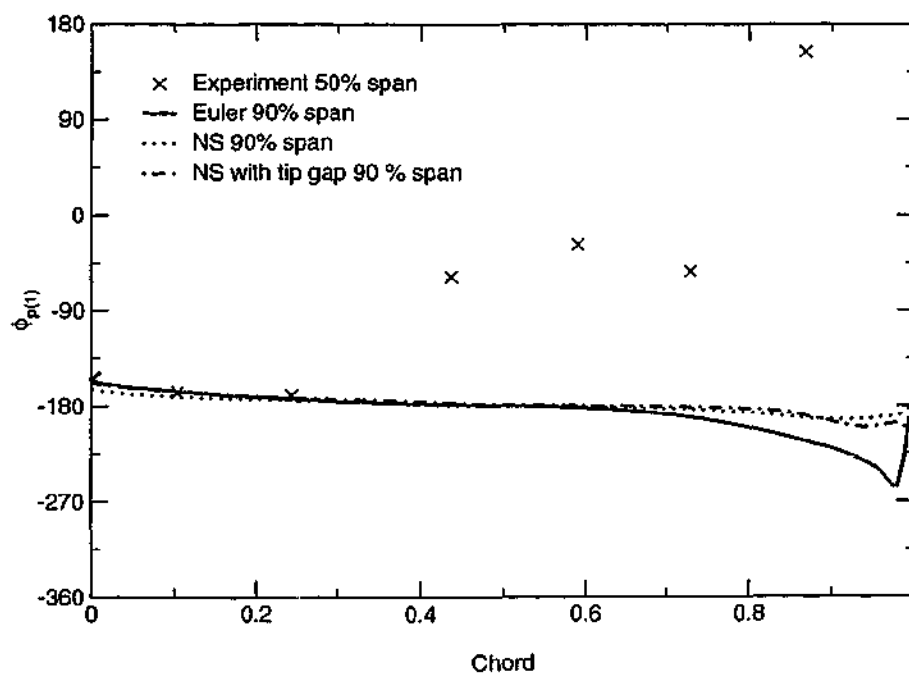


Figure 6.47: STCF 4, $IBPA = 180^\circ$, phase of first harmonic of unsteady pressure coefficient on suction-side at 90% span.

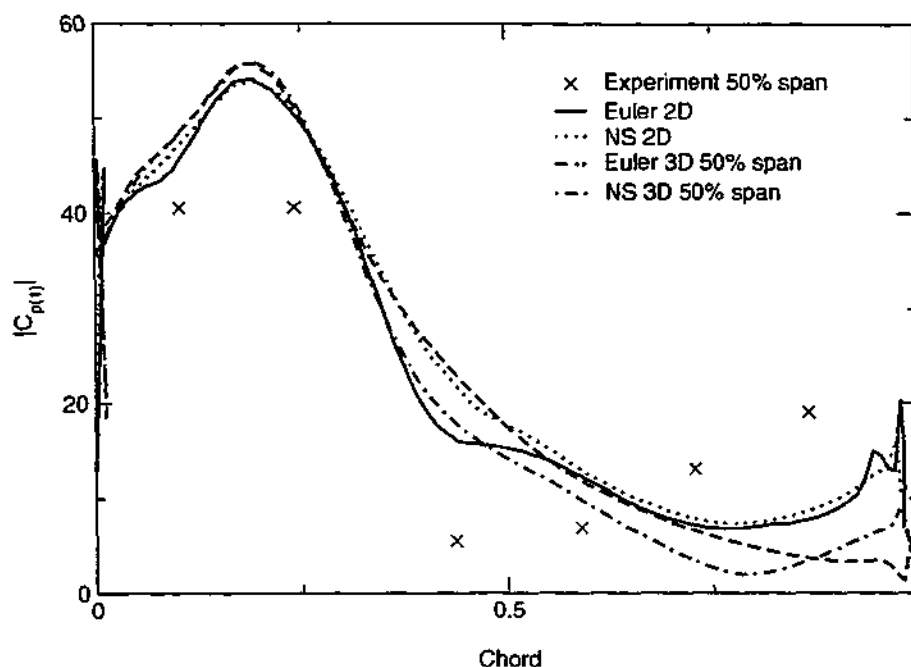


Figure 6.48: STCF 4, $IBPA = 270^\circ$, first harmonic magnitude of unsteady pressure coefficient on suction-side at mid-span.

At an $IBPA = 270^\circ$ the aeroelastic configuration exhibits instability in the experimental measurements. The same simulations were performed for this inter-blade phase angle as for the 180° case. Once again results are compared for the different flow models and geometric configurations, in Figures 6.48 – 6.51. In a similar way to the 180° case, the simulations over predict the peak unsteady pressure at 20% chord when compared to experimental measurements on the blade suction-side. Results for phase in Figure 6.50 and Figure 6.51 compare well close to the leading edge, however there are discrepancies in the mid-chord region. The experimental results for the suction-side in Figure 6.50 are similar to those at higher outlet Mach number where the passage is choked. The dip in phase at 60% chord is not a feature of the experimental results at the higher outlet Mach number of 0.9 from Test 525 (Bölcs & Fransson, 1986). This suggests a similar inconsistency in flow conditions in the experiment as in the $IBPA = 180^\circ$ case.

The differences between the Navier-Stokes and Euler simulations, and also the geometric models is less than for the $IBPA = 180^\circ$. The largest differences are at the blade trailing edge on the suction-side, for both unsteady pressure magnitude and phase. These are probably due once again to the influence of the boundary layers in the case of the Navier-Stokes simulations.

Figure 6.52 shows a comparison of the unsteady pressure coefficient between the Euler, Navier-Stokes and Navier-Stokes with tip gap simulations. The contours of pressure magnitude have the same levels for all of the results shown in the figure. In the case of the

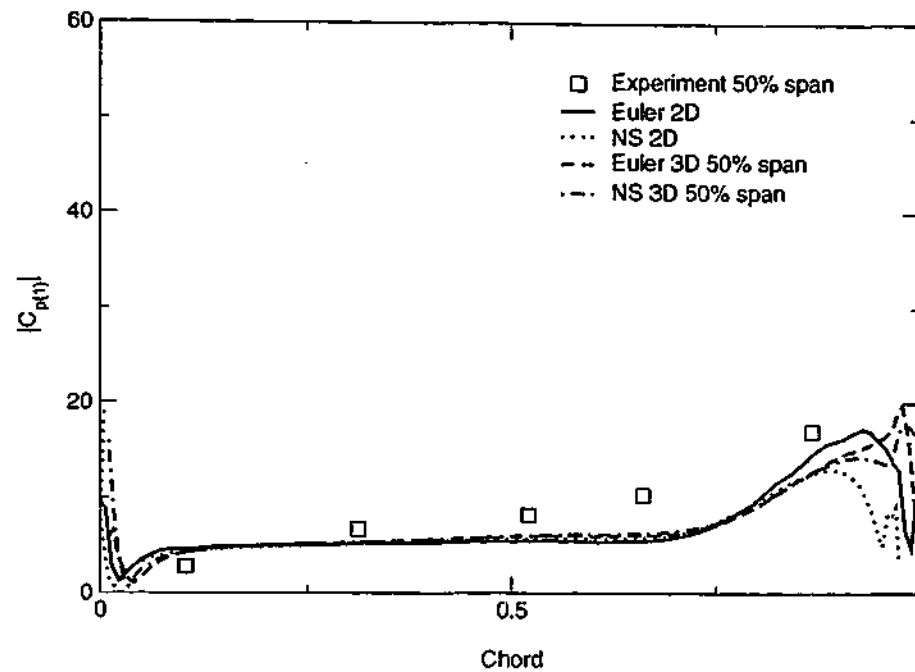


Figure 6.49: STCF 4, $IBPA = 270^\circ$, first harmonic magnitude of unsteady pressure coefficient on pressure-side at mid-span.

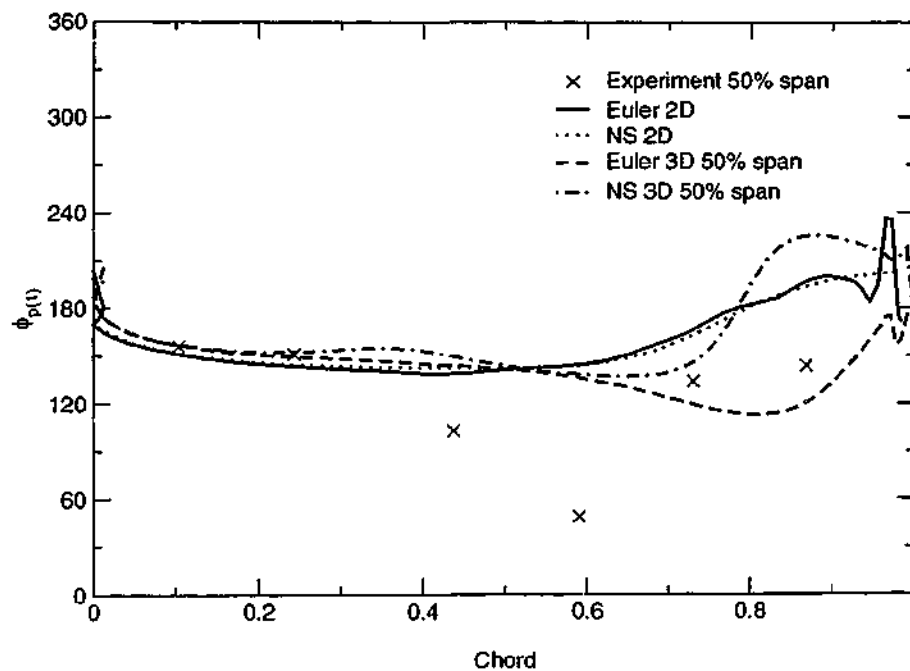


Figure 6.50: STCF 4, $IBPA = 270^\circ$, phase of first harmonic of unsteady pressure coefficient on suction-side at mid-span.

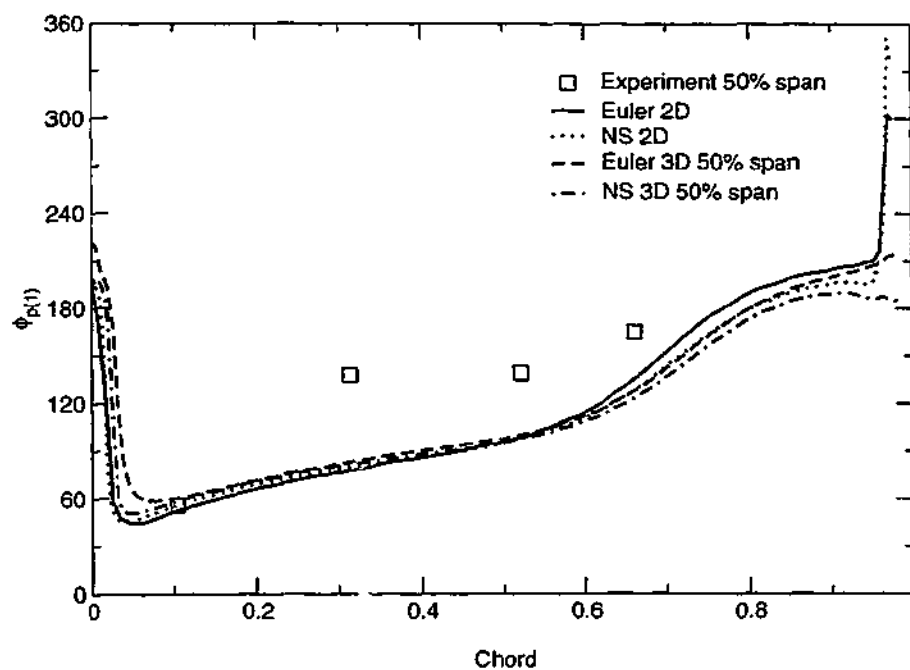


Figure 6.51: STCF 4, $IBPA = 270^\circ$, phase of first harmonic of unsteady pressure coefficient on pressure-side at mid-span.

Euler simulation in Figure 6.52(a), the distribution varies little with span-wise position. The variation observed in the chord-wise distribution at mid-chord at 10% span is not obvious, although variation towards the trailing edge in the hub region is obvious.

The distribution for the unsteady pressure coefficient for the Navier-Stokes simulation without a tip gap is shown in Figure 6.52(b). This shows significantly more variation of surface pressure with span compared to the inviscid simulation, particularly towards the blade tip. The impression of the passage vortex can be observed at 90% span, particularly towards the trailing edge region. It is also evident in the plot of phase in Figure 6.53(b). Less distinct is the passage vortex at 10% span, close to the cascade hub. The relative impact of the hub and casing passage vortices on the blade may be attributed to the different magnitudes of blade vibration in these two regions. The relative strength of the hub passage vortex and casing passage vortex is similar, based on the fact that the flow velocity is also similar.

In the bottom of Figure 6.52, the unsteady pressure magnitude for the Navier-Stokes simulation with a tip gap is shown. There are two major differences between this figure and the one above involving the Navier-Stokes simulation without the tip gap. The signature of the leakage vortex may be observed in the close-up of the tip region towards the front of the blade as a dip in the unsteady pressure. Towards the trailing edge, the passage vortex also causes a dip in the unsteady pressure coefficient, at about 90% span. This dip is much less than in the simulation without the tip gap. Thus the tip leakage flow appears to reduce the effects of the passage vortex on the unsteady pressure, either causing it to migrate away from

the blade surface or by reducing its strength. The decrease in the influence of the passage vortex on the unsteady pressure coefficient magnitude is also reflected in the plot of phase in Figure 6.53(c).

The overall difference between the simulations with and without a tip gap on the blade suction-side is that the unsteady pressure magnitude on the blade in the simulation without the tip gap is more uniform over the span in the forward part of the blade. Conversely, the simulation with the tip gap has a more uniform distribution of unsteady pressure magnitude in the region after mid-chord, as the effects of the casing passage vortex on the unsteady pressure is much less significant.

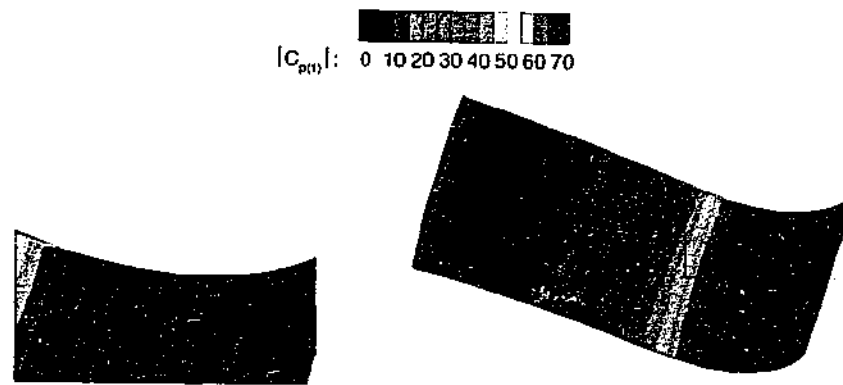
It is interesting to note the higher impact of passage vortices on the blade surface unsteady pressure in this case, compared to the low subsonic case of Section 6.2. This is mainly due to the different turning angles of the blade profiles – the relatively low turning angle of the low subsonic case results in secondary flows that are much weaker and thus have less impact on the unsteady surface pressure for the aeroelastic configuration.

Aeroelastic Work

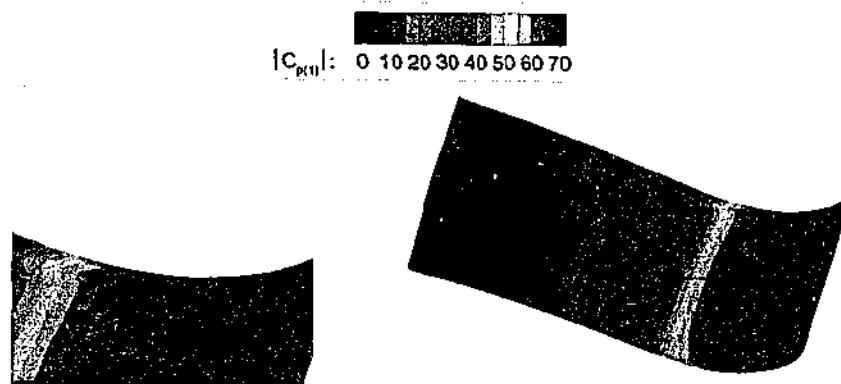
To understand the unsteady blade loading in terms of aeroelasticity, blade surface pressures were integrated over the displacement cycle to gauge the stability of the configuration, using the energy method. Comparisons are made with experiment in Figure 6.54 for the different flow models and geometric configurations. A positive damping coefficient indicates a stable configuration and conversely a negative coefficient is unstable. Even though there are discrepancies between simulation and experiment, the predictions of damping coefficient compare well.

For the present case all the flow models and geometries predicted a similar damping coefficient, except for the 3-dimensional Euler simulations. Thus, the simplest model is able to predict a similar aeroelastic stability of this configuration at the given flow conditions. This is significant when simulation times and resource requirements are compared. The most sophisticated of the models for an inter-blade phase angle of 180 degrees was the 3-dimensional geometry with tip gap and Navier-Stokes flow model. The simplest model considered was with the 2-dimensional configuration with the Euler flow model. The former required 200 times the CPU time, 2.5 times the number of processors and 20 times the memory as the latter.

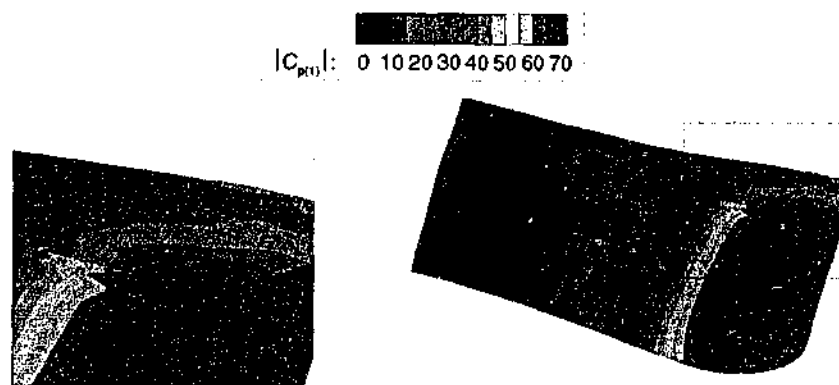
The most significant 3-dimensional effects were found to be due to the choking of the flow close to the cascade hub. This effect will be investigated in the following section for flow conditions at higher outlet Mach number.



(a) Inviscid, Euler simulation.

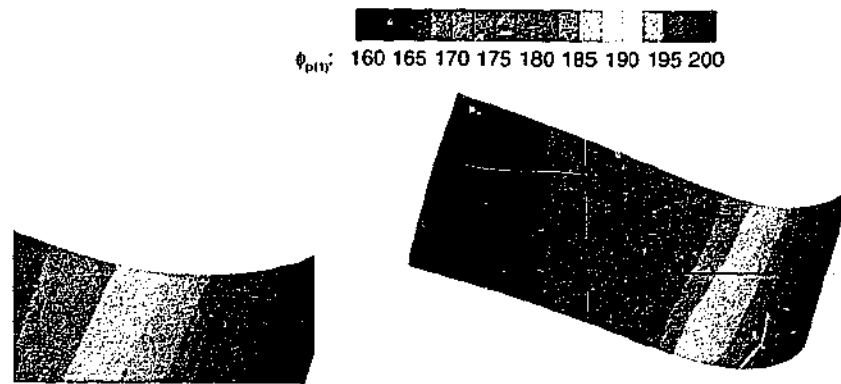


(b) Navier-Stokes simulation without tip gap model.

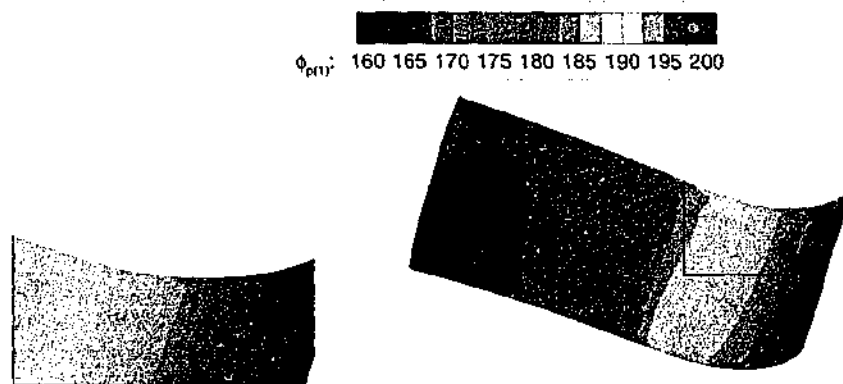


(c) Navier-Stokes simulation with tip gap model.

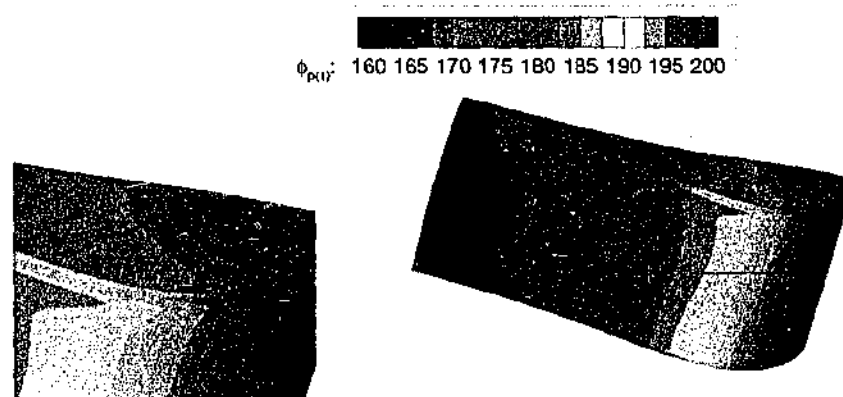
Figure 6.52: STCF 4, $IBPA = 180^\circ$, first harmonic magnitude of unsteady pressure coefficient on suction for different models.



(a) Inviscid, Euler simulation.



(b) Navier-Stokes simulation without tip gap model.



(c) Navier-Stokes simulation with tip gap model.

Figure 6.53: STCF 4, $IBPA = 180^\circ$, phase of first harmonic of unsteady pressure coefficient on suction for different models.

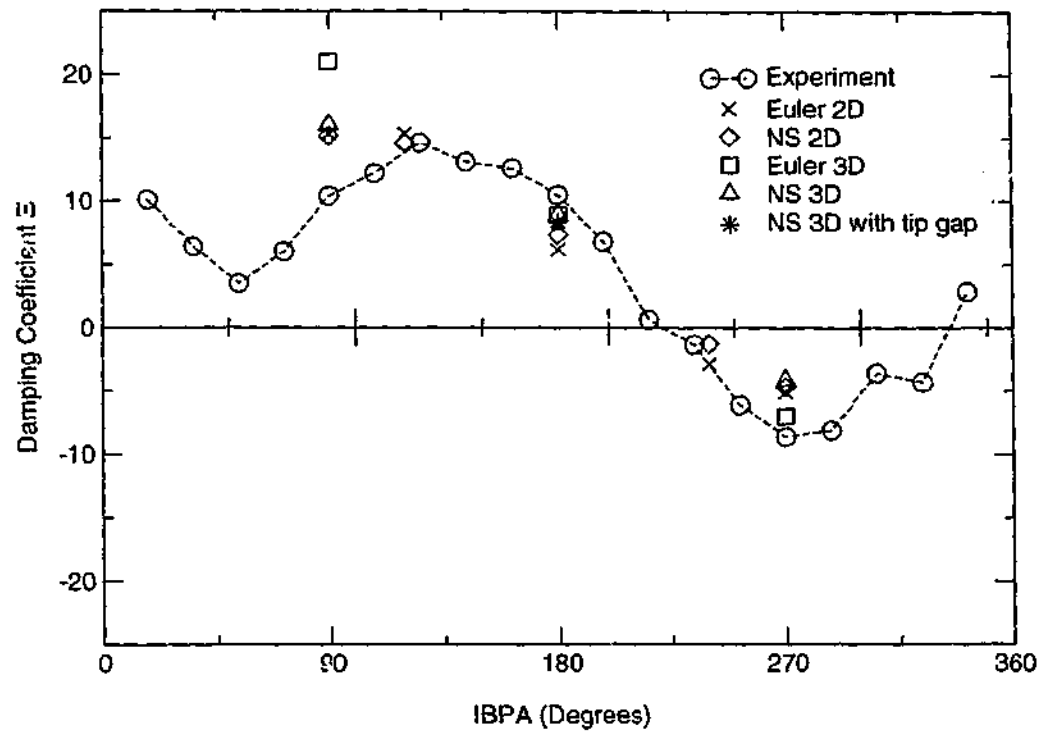


Figure 6.54: STCF 4, Test 627, damping coefficient for different configurations over a range of inter-blade-phase-angles.

6.3.3 Transonic Cascade

This test is known as Test 628 and involves the same geometry as Test 627, with different flow conditions and displacement amplitude – these are tabulated in Table 6.7. The most significant difference is the supersonic outlet conditions, leading to transonic flow within the turbine cascade passage. Visualisation of the flow in the form of Schlieren photographs was performed by the researchers. They identify the presence of a relatively strong passage shock. As with Test 627, the aeroelastic characteristics of this case will be investigated through 2-dimensional and 3-dimensional, Euler and Navier-Stokes simulations.

| Condition | Experiment |
|-----------------------------------|-----------------------|
| Typical Reference Velocity | 65 m/s |
| Bending mode direction | 63.0° |
| Bending mode amplitude at hub | 3.15×10^{-3} |
| Bending mode amplitude at midspan | 4.03×10^{-3} |
| Bending mode amplitude at casing | 4.91×10^{-3} |
| Reynolds number | 5.9×10^5 |
| Outlet Mach number | 1.43 |
| Reduced frequency | 0.0779 |

Table 6.7: Aeroelastic parameters for Standard Configuration 4, Test 628.

Steady Flow

During a grid dependence study it was found that whilst the orthogonal H-grid was adequate for modelling the subsonic cases, it had some major deficiencies when applied to the modelling of transonic cascade flow. A comparison between the passage Mach number distribution and cell distribution for 2-dimensional steady simulations with an outlet Mach number of 1.4 is shown in Figure 6.55 for the two different types of mesh geometries. Each mesh has a comparable cell count, with the O-H grid having 152 cells and the orthogonal H-grid having 160 cells on the blade surface, respectively. The most notable difference is the resolution of the trailing edge shock. The wake region in the case of the orthogonal H-grid is also less distinct. This was the most compelling reason for the use of the O-H mesh for the modelling of this flow regime. It was suspected that the low resolution of this region could lead to inaccuracies in the reproduction of the unsteady flow field close to the trailing edge.

An O-H mesh was further refined in the throat region, which led to better resolution of the passage shock. A simulation involving the new mesh of four times the number of cells exhibited shock-induced boundary-layer separation at about 70% of chord on the blade suction-side. A mesh of twice the density was produced involving 85000 cells per span-wise plane and 736 cells on the blade surface, displayed little further change in results. The surface pressure coefficient for these two meshes is shown in Figure 6.56. There is some difference in the separation region, however the distribution through the passage shock at 70% chord is similar between the two simulations.

To obtain a similar blade loading to experiment, the inlet flow angle was increased from -12 to -26 degrees. It is assumed that the average values measured in the experiment at 10% axial chord from the leading edge were under the influence of the blade and that since the inlet of the cascade in the simulation was further upstream a different flow angle was appropriate.

Pseudo-Schlieren distributions of the simulated flow field may be represented by contours of density gradient (defined as $\nabla\rho$). They are useful for identifying shock features, wake regions and boundary layers in compressible flow. Comparisons of this quantity for the coarse and fine meshes showed that they were similar for the 2-dimensional simulations, with little difference between the flow features. The plot in Figure 6.57 showing the trailing edge region of the two dimensional simulation, shows the flow separation on the blade suction-side. The contours of Mach number are plotted and the streamlines help to identify the separation zone.

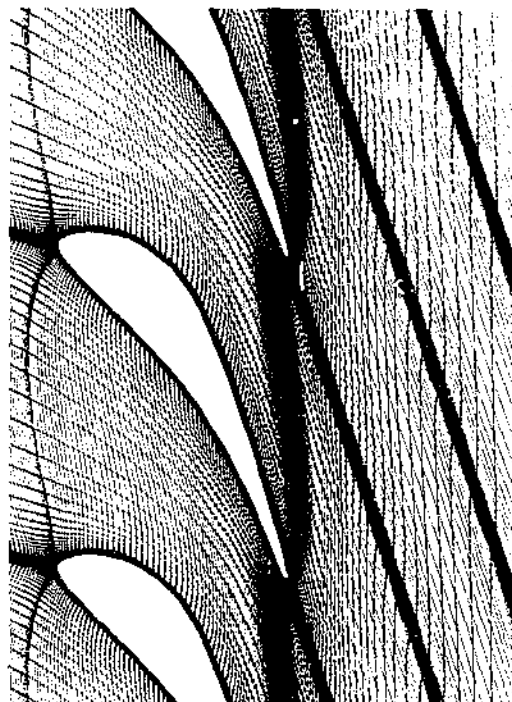
A comparison of the surface pressure coefficient at mid-span for the 3-dimensional, the 2-dimensional Navier-Stokes and Euler simulations is made in Figure 6.58. Both Navier-Stokes simulations predict the impingement of the passage shock on the blade suction-side at about 65% chord, with the position predicted by the 2-dimensional simulation slightly forward of that predicted by the 3-dimensional simulation. The 2-dimensional Euler simulation



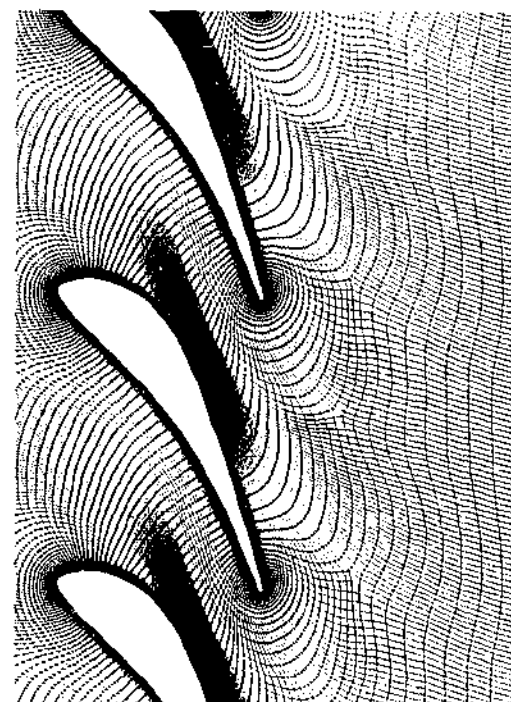
(a) Orthogonal H-grid Mach distribution.



(b) Hybrid O-H grid Mach distribution.



(c) Orthogonal H-grid.



(d) Hybrid O-H grid

Figure 6.55: Comparison of transonic flow fields for two different mesh geometries.

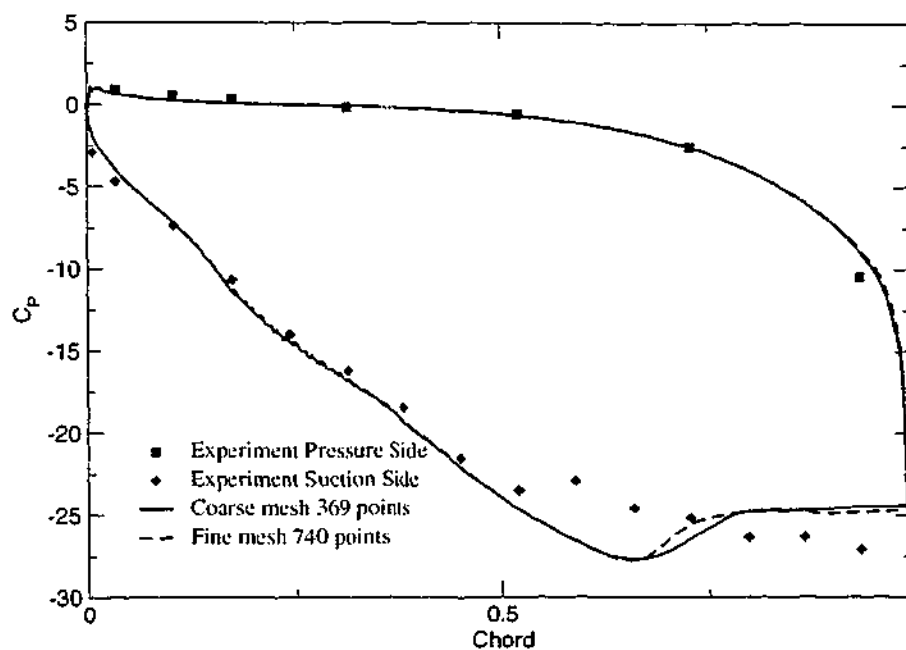


Figure 6.56: Grid dependency of 2-dimensional grid for Test 628.

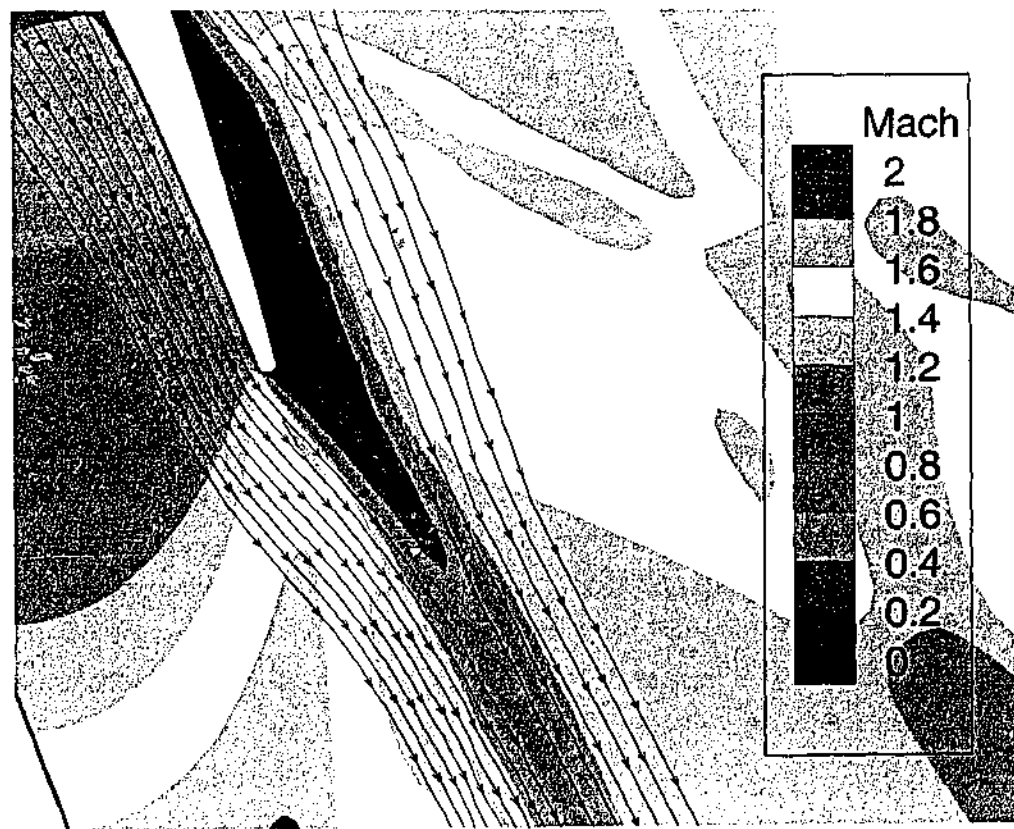


Figure 6.57: STCF 4, Test 628, separation region on trailing edge of blade for 2-dimensional simulation.

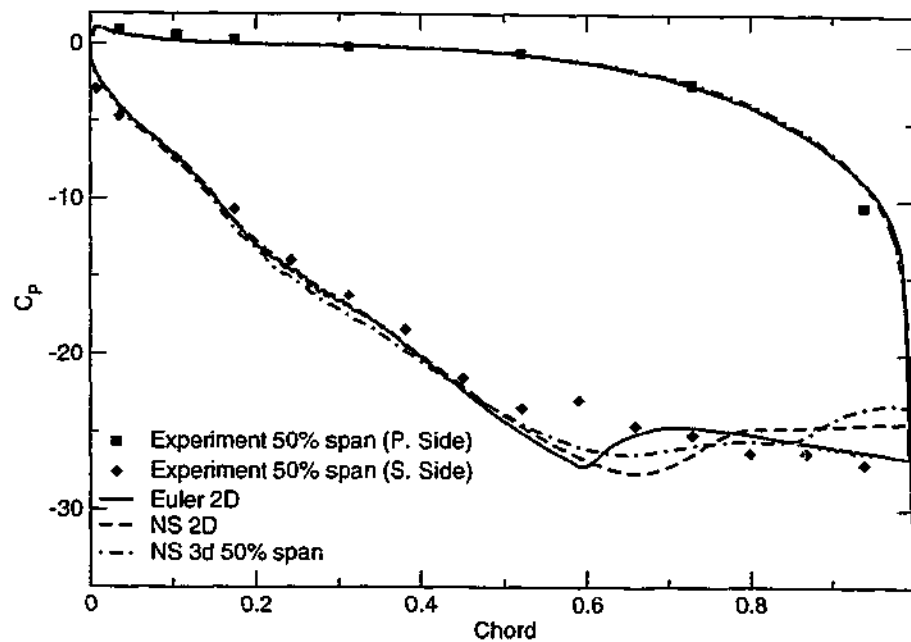


Figure 6.58: STCF 4, Test 628, comparison of steady pressure coefficient for the 2-dimensional and 3-dimensional simulations.

predicts the shock impingement further forward again, at 60% chord. In the experimental results shown in the same figure, it appears that the passage shock impinges on the blade at 50% of chord, given that the passage shock is identified by a local minimum in the surface pressure coefficient. It is not obvious whether the experimental results involve a separation zone at the trailing edge. Experiments in a linear cascade at the higher outlet Mach number of 1.68 (Böles & Fransson, 1986) show what appears to be a separated zone after the passage shock on the suction-side in a plot of surface isentropic Mach number.

The Schlieren distributions in Figure 6.59 were calculated for the 2-dimensional and 3-dimensional Navier-Stokes simulations to identify differences between the two results. The Schlieren distribution for the 3-dimensional case is at mid-span. The flow is quite complex and involves a number of different phenomena. Both the 2-dimensional and 3-dimensional simulations exhibit similar features although the geometry is different.

In the 2-dimensional case the point of flow separation coincides with the passage compression shock at about 70% chord. An oblique shock wave emanates from the separation point at -30 degrees from the machine axis. The shear layer is thick on the outside of the separation bubble, much thicker than on the blade surface before the point of separation. Another oblique shock wave extends from the blade trailing edge towards the outlet at an angle of -20 degrees from the machine axis. The wake is characterised by a fork like region, extending in the flow direction from the trailing edge.

The 3-dimensional simulations differ in the point of separation and the geometry of the shock waves. The passage shock is also visible but does not coincide with the sepa-

ration point on the blade suction-side – the flow separates further down stream at about 85% chord. A shock wave also occurs at the point of separation at a similar angle to that in the 2-dimensional case.

A 3-dimensional contour plot of steady pressure coefficient for the blade suction-side is shown in Figure 6.60. In the trailing edge region of the blade in the figure, the green region represents the separation bubble – this is where the flow has negative axial velocity at the first mesh point adjacent to the blade surface. The pressure distribution varies significantly in the span-wise direction from mid-chord towards the trailing edge, as does the size of the separation bubble. Upon inspection, the flow in the circumferential plane at the 25% span region more closely resembles the 2-dimensional simulation compared with the mid-span 3-dimensional distribution.

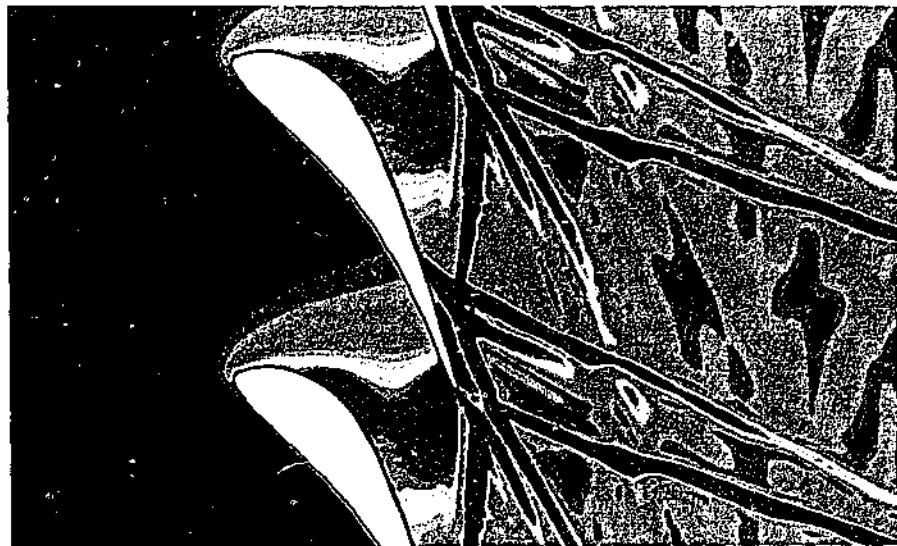
The span-wise variation in pressure coefficient is also compared with experimentally measured values in Figure 6.61. Once again, the impingement of the passage shock on the blade suction-side is identified by a local minimum in the pressure coefficient, in the neighbourhood of mid-chord. The point of impingement of the passage shock in the simulation is 70% chord at 25% span, 65% chord at mid-span and 55% chord at 75% span. It is more difficult to identify the position of the shock in the experimental measurements due to a lack of resolution. At 25% span the shock may be at about 65% chord, at mid-span at 50% chord and at 75% span at 45% chord. The simulation predicts a shock position that is 10% further aft on average than the experiment. Therefore, the in-passage flow conditions in the simulations are at higher Mach number than in the experiment.

There are some differences between the steady simulations, between the 2-dimensional and 3-dimensional simulations, and also with experiment. The next section investigates the way in which these differences affect the results for the simulations of the aeroelastic configuration. The surface pressure distribution for the 3-dimensional case does not vary linearly with span, as it does for the subsonic case. Therefore 2-dimensional geometries will not describe sufficiently similar flow conditions. The way in which this affects the aeroelastic stability of the configuration is investigated in the following section.

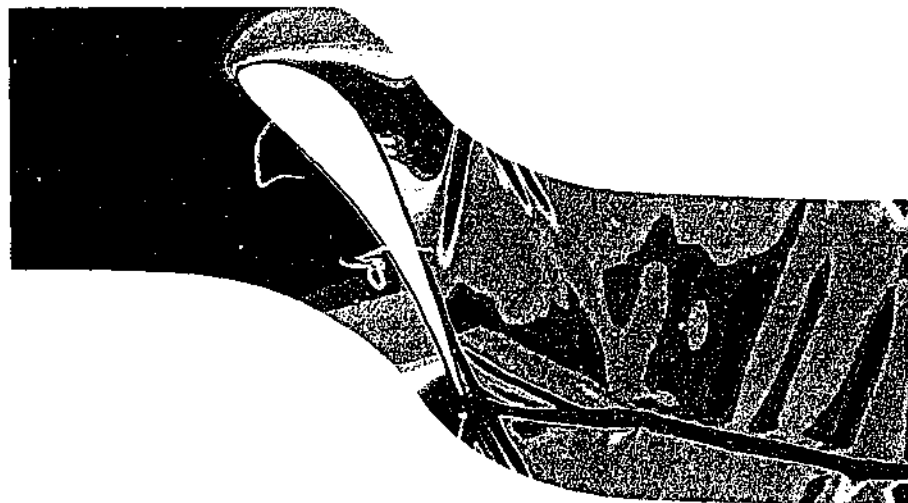
Aeroelastic Simulations

Due to the higher density of the mesh required to resolve the passage shock, only an inter-blade phase angle of 180 degrees is investigated for this Test, given the limits of the available computer resources. Significant differences were found in the flow features and steady pressure distribution for this test between different models and geometries. Once again different flow models and geometries are compared.

A comparison is made between Euler and Navier-Stokes simulations for 2-dimensional and 3-dimensional simulation models in Figures 6.62 – 6.64. For the peak unsteady pressure on the blade suction-side at 20% chord, there is some deviation between the 2-dimensional



(a) 2-dimensional simulation.



(b) 3-dimensional simulation, at mid-span.

Figure 6.59: Comparison of Schlieren plots.

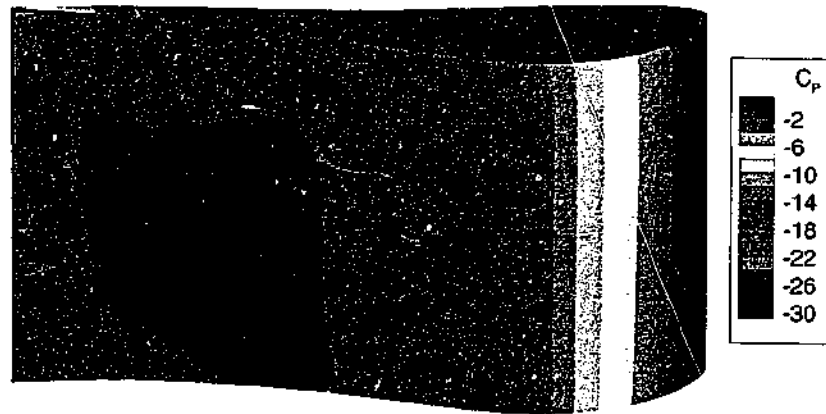


Figure 6.60: STCF 4, Test 628, steady pressure coefficient and separation bubble on suction-side of the 3-dimensional simulation.

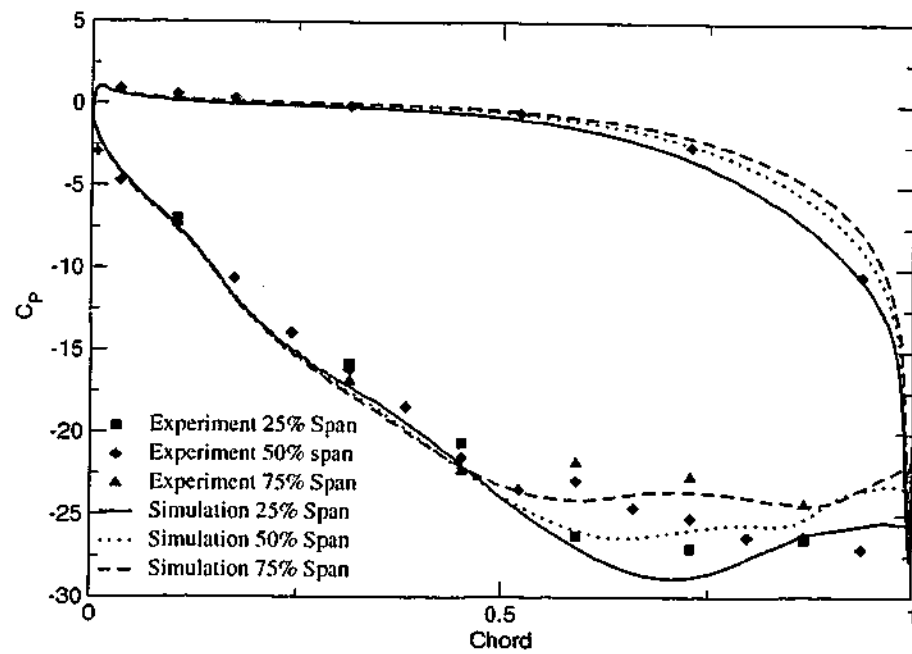


Figure 6.61: STCF 4, Test 628, the span-wise distribution of steady pressure coefficient on blade surface.

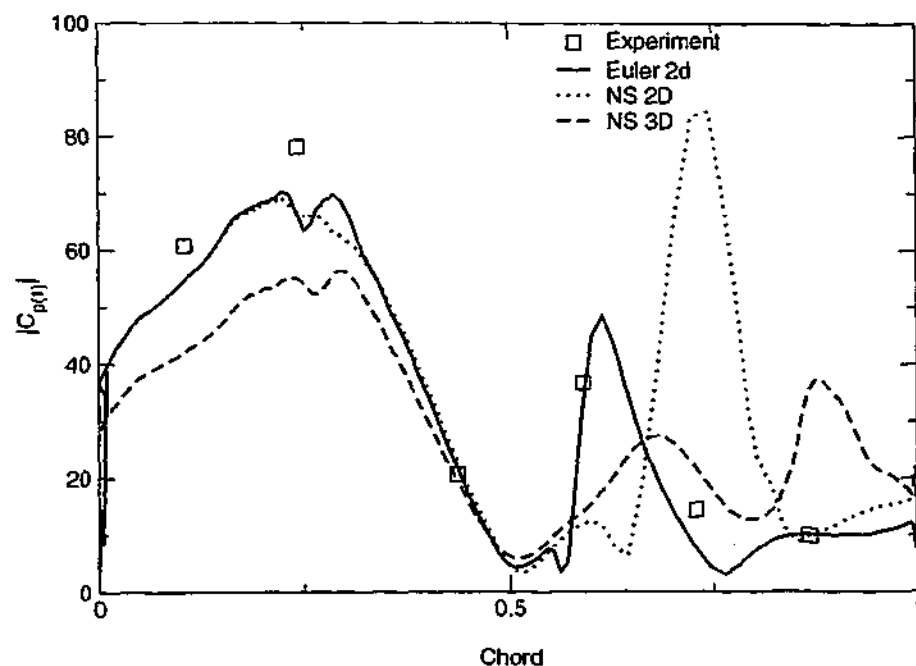


Figure 6.62: STCF 4, Test 628, $IBPA = 180^\circ$, first harmonic magnitude of unsteady pressure coefficient on suction-side at mid-span.

and 3-dimensional geometries. In the forward half of the blade, the predictions of unsteady pressure phase compare well with experiment for both models and both surfaces.

Beyond mid-chord on the blade suction-side, however, there are more significant differences. The passage shock is evident in the experiment and simulation results by a local maximum on the blade suction-side between 60% and 70% chord. The 2-dimensional Euler simulation predicts the shock impingement position closest to the experiment as it did in the steady simulations. For the 2-dimensional Navier-Stokes simulations it is difficult to distinguish between the shock impingement and the separation point at 70% chord. The 3-dimensional Navier-Stokes simulation predicts the impingement at about 65% chord as in the steady simulation. The flow separation is the cause of the second maximum at about 85% chord.

On the blade pressure side, the magnitude of the pressure coefficient in Figure 6.63 compares well with experiment up until the midchord region. Beyond the mid-chord region, all of the simulations underpredict the magnitude, by more than 50% close to the trailing edge.

There are significant differences in phase in Figure 6.64 for the flow models on the blade suction-side towards the trailing edge, however the 3-dimensional result gives the best prediction of phase in this region. In the experiment, the phase on the blade suction-side returns to similar values to the forward section after the neighbourhood of the passage shock, whereas both 2-dimensional fluid models predict a phase almost half a cycle from the experimentally measured value.

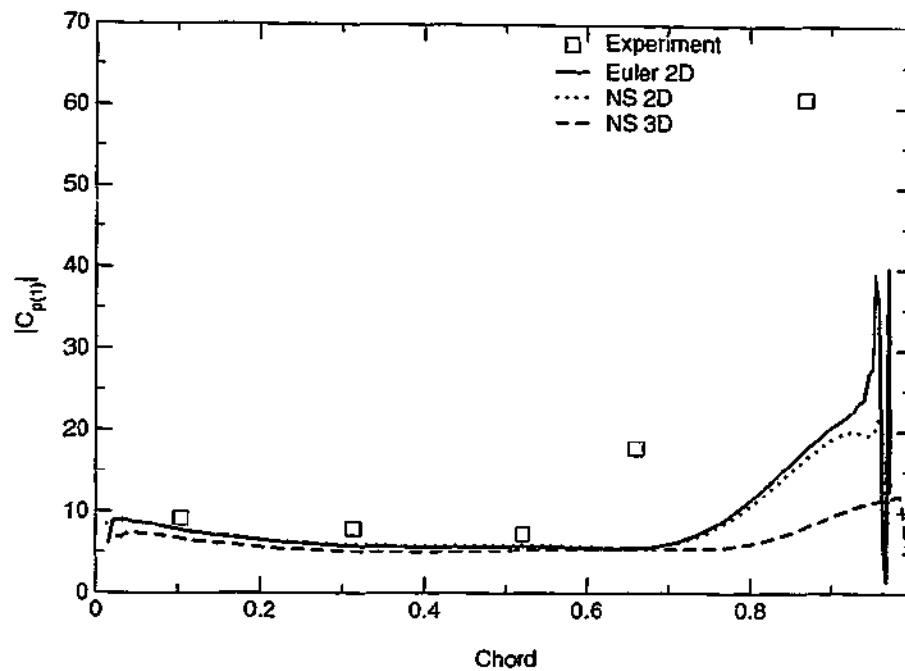


Figure 6.63: STCF 4, Test 628, $IBPA = 180^\circ$, first harmonic magnitude of unsteady pressure coefficient on pressure-side at mid-span.

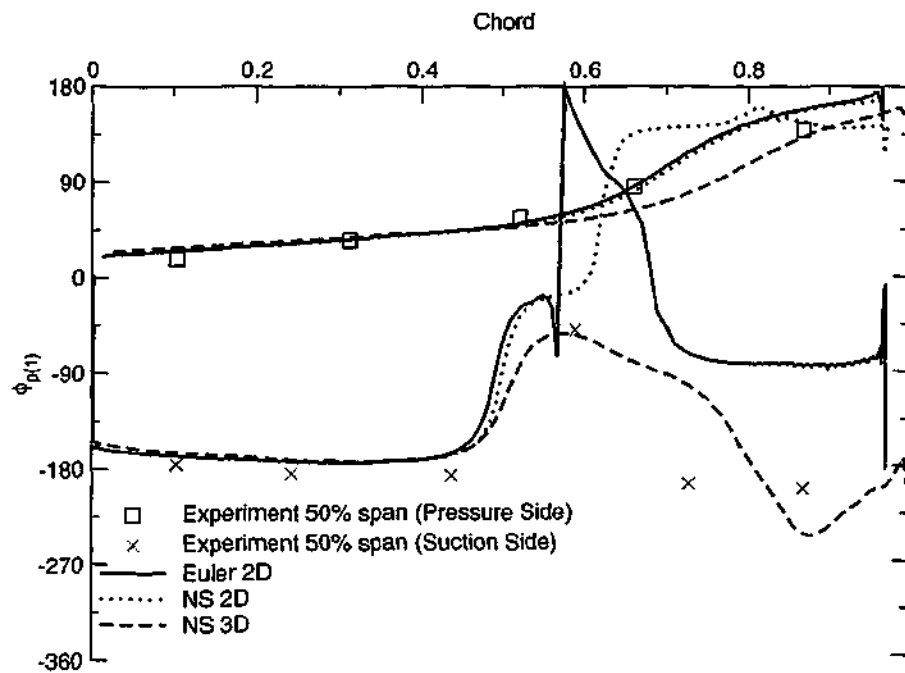


Figure 6.64: STCF 4, Test 628, $IBPA = 180^\circ$, phase of first harmonic of unsteady pressure coefficient at mid-span.

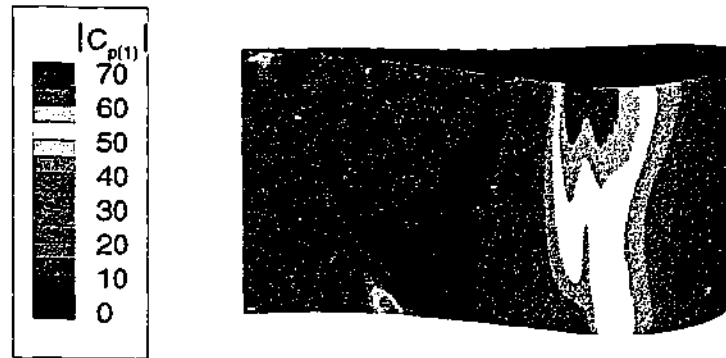


Figure 6.65: STCF 4, Test 628, $IBPA = 180^\circ$, blade unsteady surface pressure magnitude distribution.

The distribution on the blade of the unsteady pressure and phase for the 3-dimensional Navier-Stokes simulation is shown in Figures 6.65 and 6.66. The separation line is visible in both plots towards the blade trailing edge. The impingement of the passage shock is also visible in the plot of phase, as a local maximum at 70% chord. Due to the span-wise distribution of the unsteady pressure, it is doubtful whether a 2-dimensional simulation could reproduce the distribution at a particular span, as is supported by the 2-dimensional simulations presented.

Given that only one inter-blade phase angle was considered, it is difficult to draw conclusions on the predictive ability of the simulations in terms of the damping coefficient. Nonetheless, a comparison is made between the different configurations for damping coefficient in Figure 6.67. Even though the 3-dimensional Navier-Stokes simulation predicts a significant difference in the peak unsteady pressure magnitude at 20% chord, the damping coefficient it predicts is closest to experiment since the damping coefficient is mostly determined by phase angle.

Clearly, the shock induced boundary layer separation or any other flow separation on the blade suction-side cannot be well predicted by the inviscid simulations. However it is not clear whether this behaviour should be expected at these flow conditions. The prediction of flow separation involves characteristics that probably cannot be predicted by the present flow models due to the following reasons:

- Separation point position, existence of bubble – affected by turbulence model and resolution of viscous passage flow.
- Width of unsteady pressure spike from passage shock, due to lack of mesh resolution.

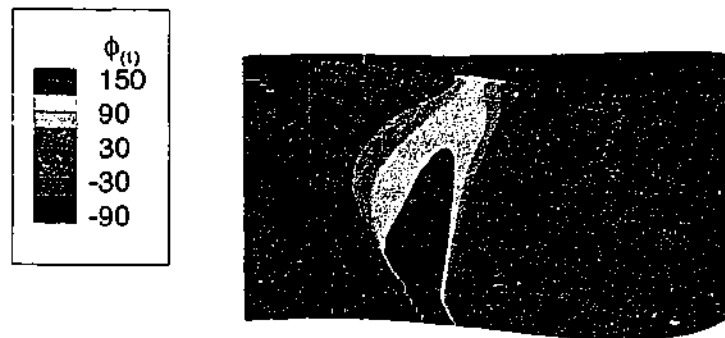


Figure 6.66: STCF 4, Test 628, $IBPA = 180^\circ$, blade unsteady surface pressure phase distribution.

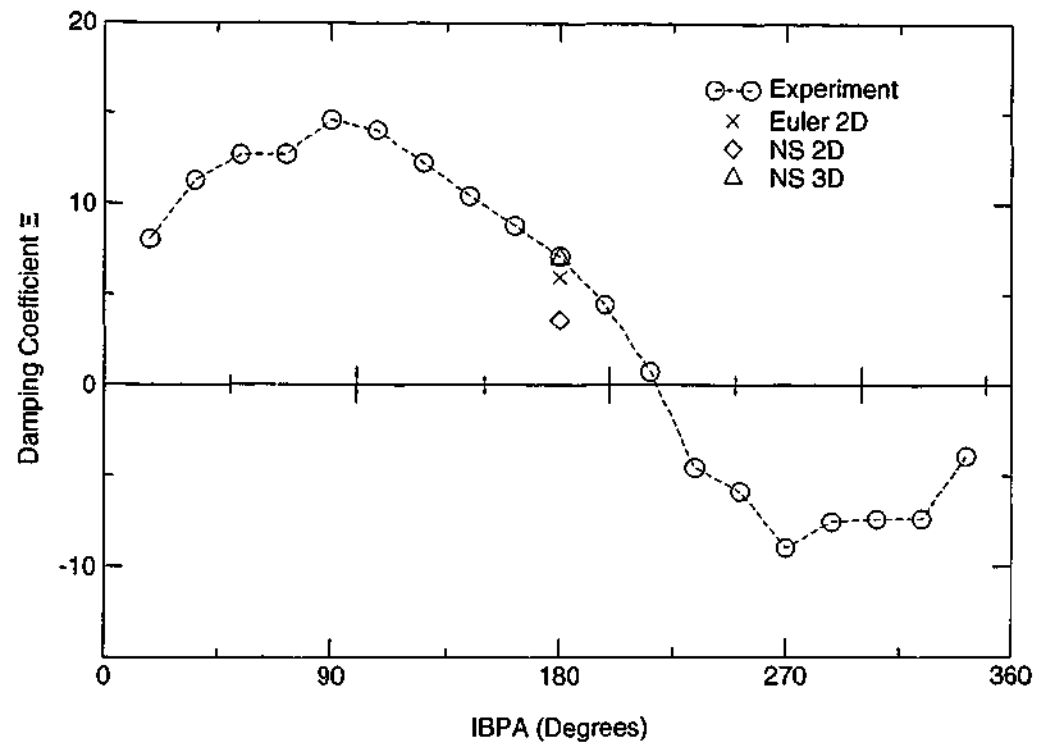


Figure 6.67: STCF 4, Test 628, damping coefficient for different simulations compared with experiment.

- Shedding due to flow separation.
- Amplitude of unsteady pressure across shock.

Shedding of the separation bubble could lead to further increases in the unsteady pressure, movement of the passage shock and differences in phase in the separated region. This probably cannot be resolved by the present spatial and temporal resolution. Different behaviour could occur depending on the phase of the shedding with respect to the blade motion.

The suitability of the turbulence model under the present conditions needs to be better understood. Other authors have investigated the performance of turbulence simulations with separated flow with mixed results (Fransson *et al.*, 1998).

The design engineer may not be interested in the behaviour of the separated flow. However the point of onset of flow separation may be important so that it can be avoided. In the present case it is possible that shock-induced boundary-layer separation is predicted where in reality it would not occur. Deficiencies in the turbulence model could be an important factor in determining the appearance of the separated flow, however other factors could be as equally important, such as the detailed specification of flow conditions at the boundaries. This includes effects such as leakage at hub shrouds and the flow conditions at the simulation inlet and outlet planes.

Chapter 7

Conclusions and Future Work

A computational tool has been developed to simulate 3-dimensional transonic, viscous and unsteady flow. The important requirements of the implementation included a flexible parallel solution capability, so that well resolved studies into aeroelastic cascade simulations could be undertaken. The code was developed from a single passage and single block, steady Navier-Stokes solver with the $k-\omega$ turbulence model.

During the development of the code, the data structure was completely restructured to make it suitable for a multiple block solution method. This was combined with the extensive use of high level data structures in Fortran-90 for a more object oriented approach. A number of high level message passing structures were also used in keeping with the data structure. An unstructured approach to the multiblock method provided flexibility and allowed the use of the latest structured turbomachinery meshes and the simulation of tip gap regions. This resulted in a sophisticated, efficient and compact implementation.

With the implementation of the unsteady routines, the data structure and the multiple block and parallel method, each component was validated through comparison with theoretical, experimental and other numerical results. This provided the confidence in the method so that it could be applied to the more complicated turbomachinery configuration.

The parallel efficiency of the implementation was investigated. Traditional methods indicated super scalar speed-up, where the sum of the computation time for the parallel simulation was less than for a simulation on a single processor. This is not unusual and is due to the computer architecture. Gustafson's and Ware's laws were also used to evaluate parallel efficiency. While these no longer indicated super-scalar speed-up, it is difficult to establish the most useful measure. A single coefficient is not sufficient to represent and analyse the complexities that implementation and architecture impose on parallel efficiency.

The importance of viscous flow behaviour on aeroelasticity has been investigated through the simulation of a number of turbine cascade configurations, under different flow regimes. The cases were selected due to the availability of 3-dimensional experimental results.

The nature of the behaviour of the tip gap flow for the low-subsonic cascades was in-

investigated and compared with other simulation results. It was found that the present tip gap flow may be described as being similar to a jet flow model, something disputed by other researchers for another turbine cascade configuration. Results with the tip gap model exhibited significant local variations in the steady pressure coefficient in the neighbourhood of the blade tip and an overall decrease in blade loading.

Aeroelastic simulations were undertaken for different tip gap lengths for the low-subsonic case. The trend of the magnitude of unsteady pressure compared well with the experimental observations. As with the steady simulations, the tip gap flow imposed local variations in the unsteady pressure close to the blade tip. Configuration aeroelastic stability was also investigated through the damping coefficient. This compared well with experiment for the simulations with the tip gap and the simulation without the tip gap model tended to over predict the damping coefficient.

The behaviour of aeroelastic configurations involving high subsonic and transonic flow was investigated through the simulation of Standard Configuration 4 at a number of different conditions. Viscous effects and cascade configuration geometry were examined through the comparison of 3-dimensional and 2-dimensional geometries, and Euler and Navier-Stokes results for a range of inter-blade phase angles. While the tip gap model did not significantly change the overall aeroelastic behaviour of the simulated configuration, it did have a discernible impact on the distribution of the unsteady pressure on the blade surface. In the Navier-Stokes simulations without the tip gap, the signature of the casing vortex was clearly observed towards the blade trailing edge on the suction side. For the unsteady pressure distribution for the simulation with the tip gap model, the effect of the passage vortex was less evident. Thus the tip gap leakage reduces the impact of the passage vortex on the unsteady pressure distribution for the simulation.

The 2-dimensional simulations made adequate predictions of the unsteady pressure and damping coefficient that were similar to the 3-dimensional simulations. Thus 3-dimensional effects were insignificant in this case.

The flow behaviour in cascade simulations in the transonic regime differs from the high-subsonic case due to the presence of the passage shock. The grid resolution and geometry required for the simulation of this case necessitated the use of an O-H mesh, rather than the orthogonal H mesh used for the other turbomachinery simulations. Highly 3-dimensional flow features were noted in both the steady and unsteady surface pressure distributions. Inviscid Euler and Navier-Stokes simulations were performed and significant differences existed between the two, and 3-dimensional Navier-Stokes simulations. Shock boundary interaction caused separation of the boundary layer towards the blade trailing edge; this was the most significant physical difference between the three simulations. This type of behaviour cannot be predicted by an inviscid model. It also results in a highly 3-dimensional flow in the annular cascade, thus 2-dimensional Navier-Stokes configurations are also not suitable

for analysis. The 3-dimensional Navier-Stokes simulation provided a prediction of phase the closest to the experiment of the configurations, although the shock position and peak unsteady pressure magnitude deviated from the experimental results. Nonetheless, the 3-dimensional Navier-Stokes simulation provided a prediction of damping coefficient closest to experiment, for an inter-blade phase angle of $IBPA = 180^\circ$.

The simulations of transonic cascade flow may be beyond the prediction capability of the present Navier-Stokes flow model. Shock boundary layer interaction is a very challenging phenomenon to model due to uncertainties in turbulence modelling, particularly for the unsteady periodic flow investigated in Chapter 6. The shedding of the separation bubble behind the shock may cause a different unsteady surface pressure distribution, and this is not predicted by the present simulations.

Further work needs to be undertaken to understand how well the present implementation simulates shock boundary layer interaction. This may concentrate on the turbulence model, for more simple configurations. The predictive capability for the turbulence model under strong adverse pressure gradient, conditions which are found on the suction side of the blade, are still under question. This issue requires further research.

Simulations have been undertaken of the behaviour of aeroelastic configurations of turbomachinery cascades. These have been compared with experiment and a number of different aspects of cascade flow has been discussed. Their effect on the aeroelastic characteristics of the cascade has been investigated. Whilst the present approach may be beyond the sophistication required for parameter studies used in industry, it provides a starting point for the understanding of the flow phenomena. The 2-dimensional investigations could be used in parameter studies, and the 3-dimensional approach used to validate particular cases of interest.

References

- Abhari, R. S., & Giles, M. 1997. A Navier-Stokes analysis of airfoils in oscillating transonic cascades for the prediction of aerodynamic damping. *Journal of Turbomachinery*, **119**, 77-84.
- Adamczyk, J. J., Stevans, W., & Jutras, R. 1982. Supersonic stall flutter of high-speed fans. *ASME Journal of Engineering Power*, **104**, 675-682.
- Allen, Richard C., et al. 1996. *Computer science education project*. Computer Science Education Project. <http://csep1.phy.ornl.gov>.
- Alonso, Juan, & Jameson, Antony. 1994 (Jan.). Fully-implicit time-marching aeroelastic solutions. *In: AIAA 32nd Aerospace Sciences Meeting*. AIAA. 94-0056.
- Alonso, Juan Jose. 1997 (June). *Parallel computation of unsteady and aeroelastic flows using an implicit multigrid-driven algorithm*. Ph.D. thesis, Princeton University.
- Amdhal, G. 1967. Validity of the single processor approach to achieving large scale computing capabilities. *Afips conference proceedings*, 483-485.
- Argarwal, R. K. 1992. *Parallel computers and large problems in industry*. Elsevier Science Publishers.
- Ayer, T. C., & Verdon, J. M. 1998. Validation of a nonlinear unsteady aerodynamic simulator for vibrating blade rows. *Journal of Turbomachinery*, **120**(Jan.).
- Baines, N. C., & Moheban, M. 1989. Transonic flow through turbine cascades. *Chap. 20 of: Encyclopedia of fluid mechanics*, vol. 8. Gulf Publishing Company.
- Baldwin, B. S., & Barth, T. J. 1991 (Jan.). A one-equation turbulence transport model for high Reynolds number wall bounded flows. AIAA. AIAA-91-610.
- Baldwin, Barrett, & Lomax, Harvard. 1978 (Jan.). Thin layer approximation and algebraic model for separated turbulent flows. *In: AIAA 16th Aerospace Sciences Meeting*. AIAA. AIAA-78-257.

- Barkley, D., & Henderson, R. D. 1996. Three-dimensional floquet stability analysis of the wake of a circular cylinder. *Journal of Fluid Mechanics*, **322**, 215–241.
- Batchelor, G. K. 1981. *An introduction to fluid dynamics*. Vol. 1. London: Cambridge University Press.
- Batina, J. T. 1990. Unsteady Euler airfoil solutions using unstructured dynamic meshes. *AIAA Journal*, **28**(8), 1381–1388.
- Bell, D. L., & He, L. 1997. Three dimensional unsteady pressure measurements for an oscillating turbine blade. In: *International gas turbine & aeroengine congress & exhibition*. ASME. 97-GT-105.
- Bell, D. L., & He, L. 1998. Three dimensional unsteady flow around a turbine oscillating in bending mode = an experimental and computational study. Pages 53–66 of: Fransson, T. (ed), *Unsteady Aerodynamics and Aeroelasticity of Turbomachines*. Kluwer Academic Publishers.
- Bell, David L., & He, Li. 2000. Three-dimensional unsteady flow for an oscillating turbine blade and the influence of tip leakage. *ASME Journal of Turbomachinery*, **122**(Jan.), 93–101.
- Bendiksen, O. O. 1986. Role of shocks in transonic/supersonic compressor rotor flutter. *AIAA Journal*, **24**(July), 1179–1186.
- Bendiksen, Odvar O. 2000. Transonic bending flutter in rotors and cascades. Pages 791–802 of: Ferrand, Pascal, & Aubert, Stephane (eds), *Unsteady aerodynamics, aeroacoustics and aeroelasticity of turbomachines*. Presses Universitaires de Grenoble.
- Böles, A., & Fransson, T. H. 1986. *Aeroelasticity in turbomachines: Comparison of theoretical and experimental cascade results*. Lausanne: EPFL.
- Carta, F. O. 1967. Coupled blade-disk-shroud flutter instabilities in turbojet engine rotors. *Journal of Engineering for Power*, **89**, 419–426.
- Casavant, Thomas L., Tvrđik, Pvael, & Plasil, Frantisek. 1996. *Parallel computers: Theory and practice*. Washington: IEEE Computer Society Press.
- Cebeci, T., & Smith, A. M. 1974. *Recent developments in turbomachinery aeroelasticity*. Academic Press.
- Chaderjian, Neal M., & Guruswamy, Guru P. 1992. Transonic Navier-Stokes computations for oscillating wings using zonal grids. *Journal of Aircraft*, **29**(3), 326–334.

- Chew, J. W., Marshall, J. G., Vahdati, M., & Imregun, M. 1998. Part-speed flutter analysis of a wide-chord fan blade. *Pages 707–724 of: Fransson, T. (ed), Unsteady Aerodynamics and Aeroelasticity of Turbomachines*. Kluwer Academic Publishers.
- Chima, Roderick V. 1996. Application of the $k-\omega$ model to quasi-three dimensional turbomachinery flows. *Journal of Propulsion and Power*, **12**(6), 1176–1179.
- Collar, A. 1947. The expanding domain of aeroelasticity. *Journal of the Royal Aeronautical Society*, **51**, 1–34.
- Cunningham, H. J., Batina, J. T., & Benett, R. M. 1988. Modern wing flutter analysis by computational fluid dynamics methods. *Journal of Aircraft*, **25**(10), 962–968.
- Davis, S. S. 1982 (Aug.). *NACA64A010 oscillatory pitching*. Tech. rept. AGARD. AGARD-R-702.
- Dixon, S. L. 1998. *Fluid mechanics and thermodynamics of turbomachinery*. Butterworth-Heinemann.
- Doi, Hirofumi, & Alonso, Juan. 2002. Fluid/structure coupled aeroelastic computations for transonic flows in turbomachinery. *In: Proceedings of asme turbo expo 2002*. GT-2002-30313.
- Drikakis, D. 1999. *Parallelisation of CFD methods for incompressible and compressible flows*. Witpress.
- Ekaterinaris, J., & Platzer, M. 1996. Numerical investigation of stall flutter. *ASME Journal of Turbomachinery*, **118**(Apr.), 197–203.
- Ekaterinaris, J. A., & Menter, F. R. 1994. Computation of oscillating airfoil flows with one- and two-equation turbulence models. *AIAA Journal*, **32**(12), 2359–2365.
- Emerson, D. R. 1996. *Introduction to parallel computing: Architecture and algorithms*. Dordrecht: Kluwer Academic Publishers.
- Farhat, C., Lesoinne, M., & Tallec, P. 1998. Load and motion transfer algorithms for fluid/structure interaction problems with non-matching discrete interfaces: Momentum and energy conservation, optimal discretization and application to aeroelasticity. *Computer Methods in Applied Mechanics and Engineering*, **157**, 95–114.
- Farhat, Charbel, Lesoinne, Michel, & Maman, Nathan. 1995. Mixed explicit/implicit time integration of coupled aeroelastic problems: Three-field formulation, geometric conservation and distributed solution. *International Journal for Numerical Methods in Fluids*, **21**, 807–835.

- Fleeter, Sanford. 1977. Aeroelasticity research for turbomachinery applications. *Journal of Aircraft*, **16**(5), 320-326.
- Fletcher, Clive A. J. 1991. *Computational techniques for fluid dynamics*. Vol. 1. Berlin: Springer-Verlag.
- Fletcher, Clive A. J. 1997. *Computational techniques for fluid dynamics*. Vol. 2. Berlin: Springer-Verlag.
- Flynn, Michael J. 1972. Some computer organizations and their effectiveness. *IEEE transactions on computers*, **21**(9), 948-959.
- Foster, Ian. 1995. *Designing and building parallel programs*. New York: Addison-Wesley.
- Fransson, T. H., & Verdon, J. M. 1991 (Sept.). Update report on standard configurations for the determination of unsteady flow through vibrating axial-flow turbomachine cascades. In: *Sixth International Symposium on Unsteady Aerodynamics, Aeroacoustics and Aeroelasticity of Turbomachines and Propellers*.
- Fransson, T. H., Joecker, M., Bölcs, A., & Ott, P. 1998. Viscous and inviscid linear/nonlinear calculations versus quasi-3d experimental data for a new aeroelastic turbine standard configuration. In: *ASME Turbo Expo 1998*. ASME. 98-GT-490.
- Fransson, Torsten H. (ed). 1998. *Unsteady aerodynamics and aeroelasticity of turbomachines*. Dordrecht: Kluwer Academic Publishers.
- Garg, Vijay K., & Arneri, Ali A. 2001. Two-equation turbulence models for prediction of heat transfer on a turbine blade. *International Journal of Heat and Fluid Flow*, **22**, 593-602.
- Gaugler, R. E., & Russell, L. M. 1984. Comparison of visualised turbine endwall secondary flows and measured heat transfer patterns. *Journal of Engineering for Gas Turbines and Power*, **106**(Jan), 168-172.
- Giles, M. B. 1990. Nonreflecting boundary conditions for Euler calculations. *AIAA Journal*, **28**(12), 2050-2058.
- Giles, Michael. 1988 (Feb.). *Non-reflecting boundary conditions for the euler equations*. Tech. rept. MIT. CFDL-TR-88-1.
- Goldstein, M. E., Braun, W., & Adamczyk, J. J. 1977. Unsteady flow in a supersonic cascade with strong in-passage shocks. *Journal of Fluid Mechanics*, **83**, 569-604.
- Gostelow, J. P. 1984. *Cascade aerodynamics*. Oxford: Pergamon Press.

- Gropp, W., Lusk, E., Doss, N., & Skjellum, A. 1996. A high-performance, portable implementation of the MPI message passing interface standard. *Parallel computing*, **22**(6), 789–828.
- Gropp, William D., & Lusk, Ewing. 1996. *User's guide for mpich, a portable implementation of MPI*. Mathematics and Computer Science Division, Argonne National Laboratory. ANL-96/6.
- Grüber, B., & Carstens, V. 1998. Computation of the unsteady transonic flow in harmonically oscillating turbine cascades taking into account viscous effects. *Journal of Turbomachinery*, **120**(Jan.), 104–111.
- Gustafson, John L. 1998. *Making computer design a science instead of an art*. Boston: Kluwer Academic Publishers.
- Hall, K. C., & Crawley, E. F. 1989. Calculation of unsteady flows in turbomachinery using linearised Euler equations. *AIAA Journal*, **27**(6), 777–787.
- Hall, Kenneth C., & Clark, William S. 1993. Linearized euler predictions of unsteady aerodynamics loads in cascades. *AIAA Journal*, **31**(3), 540–550.
- Hall, Kenneth C., Thomas, Jeffrey P., & Dowell, Earl H. 2000. Proper orthogonal decomposition technique for transonic unsteady aerodynamic flows. *AIAA Journal*, **38**(10), 1853–1862.
- He, L. 1998. Unsteady flow in oscillating turbine cascades: Part 2 – computational study. *Journal of Turbomachinery*, **120**, 269–275.
- He, L., & Ning, W. 1998. Nonlinear harmonic analysis of unsteady transonic inviscid and viscous flows. *Pages 183–193 of: Fransson, T. (ed), Unsteady Aerodynamics and Aeroelasticity of Turbomachines*. Kluwer Academic Publishers.
- Henkes, R. A. W. M. 1997. Comparison of turbulence models for attached boundary layers relevant to aeronautics. *Applied Scientific Research*, **57**, 43–65.
- Hilbert, G. R., Ni, R., & Nakashi, R. K. 1997. Forced response prediction of gas turbine rotor blades. *In: Proceedings of the ASME Aerospace Division*, vol. 55. ASME.
- Hirsch, Charles. 1992a. *Numerical computation of internal and external flows*. Vol. 1. Chichester: John Wiley and Sons.
- Hirsch, Charles. 1992b. *Numerical computation of internal and external flows*. Vol. 2. Chichester: John Wiley and Sons.

- Hoehn, Wolfgang, & Fransson, Torsten H. 1998. Flutter analysis of two-dimensional viscous subsonic and transonic flow in turbomachines using the advection upstream splitting method. *Pages 195–210 of: Fransson, T. (ed), Unsteady Aerodynamics and Aeroelasticity of Turbomachines.* Kluwer Academic Publishers.
- Holmes, D. G., & Lorence, C. B. 1998. Three dimensional linearized Navier Stokes calculations for flutter and forced response. *Pages 211–224 of: Fransson, T. (ed), Unsteady Aerodynamics and Aeroelasticity of Turbomachines.* Kluwer Academic Publishers.
- Huenecke, Klaus. 2000. *Jet engines : fundamentals of theory, design and operation.* USA: Motorbooks International.
- Hwang, C. J., & Yang, S. Y. 1995. Euler solutions for transonic oscillating cascade flows using dynamic triangular meshes. *Journal of Turbomachinery*, **117**, 393–400.
- Imregun, M. 1998. Recent developments in turbomachinery aeroelasticity. *Computational Fluid Dynamics '98*, 524–533.
- Ishii, J., & Honami, S. 1986. A three-dimensional turbulent detached flow with a horseshoe vortex. *Journal of Engineering for Gas Turbines and Power*, **108**, 125–130.
- Isogai, K. 1979. On the transonic-dip mechanism of flutter of a sweptback wing. *AIAA Journal*, **17**(7), 793–795.
- Isogai, K. 1981. On the transonic-dip mechanism of flutter of a sweptback wing: Part ii. *AIAA Journal*, **19**(7), 1240–1242.
- Isomura, K., & Giles, M. B. 1998. A numerical study of flutter in a transonic fan. *Journal of Turbomachinery*, **120**(July).
- Jameson, A., Schmidt, W., & Turkel, E. 1981 (June). Numerical solutions of the Euler equations by finite volume methods using Runge-Kutta time-stepping schemes. *In: AIAA 14th Fluid and Plasma Dynamics Conference.* AIAA.
- Jameson, Antony. 1983. Solution of the euler equations for two dimensional transonic flow by a multigrid method. *Applied mathematics and computation*, **13**, 327–355.
- Jameson, Antony. 1991 (June). Time dependent calculations using multigrid, with applications to unsteady flows past airfoils and wings. *In: AIAA 10th computational fluid dynamics conference.* AIAA.
- Jameson, Antony. 1995a. Analysis and design of numerical schemes for gas dynamics 1. artificial diffusion, upwind biasing, limiters and their effects on multigrid convergence. *International Journal of Computational Fluid dynamics*, **4**, 171–218.

- Jameson, Antony. 1995b. Analysis and design of numerical schemes for gas dynamics 2. artificial diffusion and discrete shock structure. *International Journal of Computational Fluid dynamics*, 5, 1–38.
- Jameson, Antony, & Schmidt, Wolfgang. 1985. Some recent developments in numerical methods for transonic flows. *Computer methods in applied mechanics and engineering*, 51, 467–493.
- Jenssen, Carl B., Kvamsdal, Trond, Okstad, Knut M., & Amundsen, Jorn. 1998. *Parallel methods for fluid-structure interaction*. Springer Verlag.
- Ji, Shanhong, & Liu, Feng. 1999. Flutter computation of turbomachinery cascades using a parallel unsteady Navier-Stokes code. *AIAA Journal*, 37(3), 320–327.
- Johnson, D. A., & King, L. S. 1985. A mathematically simple turbulence closure model for attached and separated turbulent boundary layers. *AIAA Journal*, 23(11), 1684–1692.
- Jones, W. T., & Samareh-Abolhassani, J. 1995. A grid generation system for multi-disciplinary design optimization. AIAA. AIAA-95-1689-CP.
- Kahl, G. 1998. Structural mistuning and aerodynamic coupling in turbomachinery bladings. Pages 335–346 of: Fransson, T. (ed), *Unsteady Aerodynamics and Aeroelasticity of Turbomachines*. Kluwer Academic Publishers.
- Kim, Chang Sung, Kim, Chongam, & Rho, Oh Hyun. 2000. Parallel computations of high-lift airfoil flows using two-equation turbulence models. *AIAA Journal*, 38(2), 1360–1368.
- Kruse, M. J., et al. 1997. *Forces response analysis of gas turbine rotor blades using CFD-based aeroelastic tools*. ASME.
- Lane, Frank. 1956. System mode shapes in the flutter of compressor blade rows. *Journal of the Aeronautical Sciences*, Jan., 54–66.
- Langston, L. S. 1980. Crossflows in a turbine passage. *Journal of Engineering for Power*, 102(Oct), 866–874.
- Lauder, B. E., & Spalding, D. B. 1972. *Mathematical models of turbulence*. Academic Press.
- Lindquist, D. R., & Giles, M. B. 1994. Validity of linearized unsteady Euler calculations with shock capturing. *AIAA Journal*, 32(1), 46–53.
- Liou, M. S., & Steffen, C. J. 1993. A new flux splitting scheme. *Journal of Computational Physics*, 107(1), 23–39.

- Liu, F., Jameson, A., & Jennions, I. K. 1998a. Computation of turbomachinery flow by a convective-upwind-split-pressure (cusp) scheme. *In: 36th aerospace sciences meeting and exhibit*. AIAA.
- Liu, F., Cai, J., Zhu, Y., Wong, A. S. F., & Tsai, H. M. 2000 (Jan.). Calculation of wing flutter by a coupled CFD-CSD method. *In: 38th Aerospace Sciences Meeting and Exhibit*. AIAA. AIAA-2000-907.
- Liu, Feng. 1991 (May). *Numerical calculation of turbomachinery cascade flows*. Ph.D. thesis, Pinceton University.
- Liu, Feng, & Zheng, Xiaoqing. 1994. Staggered finite volume scheme for solving cascade flow with a $k-\omega$ turbulence model. *AIAA Journal*, **32**(8), 1589–1597.
- Liu, Feng, & Zheng, Xiaoqing. 1996. A strongly coupled time-marching method for solving the Navier- Stokes and $k-\omega$ turbulence model equations with multigrid. *Journal of Computational Physics*, **128**, 289–300.
- Liu, Feng, Jennions, Ian K., & Jameson, Antony. 1998b (Jan.). Computation of turbomachinery flow by a convective-upwind-split- pressure (CUSP) scheme. *In: 36th Aerospace Sciences Meeting and Exhibit*. AIAA. AIAA-98-0960.
- Mabey, D. G., Ashill, P. R., & Welsh, B. L. 1987. Aeroelastic oscillations caused by transitional boundary layers and their attenuation. *Journal of Aircraft*, **24**(7), 463–469.
- Marshall, J. G., & Giles, M. B. 1998. Some applications of a time linearized Euler method to flutter and forced response in turbomachinery. *Pages 225–240 of: Fransson, T. (ed), Unsteady Aerodynamics and Aeroelasticity of Turbomachines*. Kluwer Academic Publishers.
- Marshall, J. G., & Imregun, M. 1996a (June). An analysis of the aeroelastic behavior of a typical fan-blade with emphasis on the flutter mechanism. *In: International Gas Turbine and Aeroengine Congress and Exhibition*. ASME. 96-GT-78.
- Marshall, J. G., & Imregun, M. 1996b. A review of aeroelasticity methods with emphasis on turbomachinery applications. *Journal of Fluids and Structures*, **10**, 237–267.
- Martinelli, Luigi. 1987 (Oct.). *Calculations of viscous flows with a multigrid method*. Ph.D. thesis, Pinceton University.
- Martinez-Sanchez, M., Jaroux, B, Song, S. J., & Yoo, S. 1995. Measurement of turbine blade-tip rotordynamic excitation forces. *Journal of Turbomachinery*, **117**, 384–392.

- McCarter, Andrew A., Xiao, Xinwen, & Lakshminarayana, Budugur. 2001a. Tip clearance effects in a turbine rotor: Part ii – velocity field and flow physics. *ASME Journal of Turbomachinery*, **123**(Apr.), 305–313.
- McCarter, Xinwen Xiao Andrew A., Xiao, Xinwen, & Lakshminarayana, Budugur. 2001b. Tip clearance effects in a turbine rotor: Part i – pressure field and loss. *ASME Journal of Turbomachinery*, **123**(Apr.), 296–304.
- McMullen, Mathew, Jameson, Antony, & Alonso, Juan. 2001 (Jan.). Acceleration of convergence to a periodic steady state in turbomachinery flows. *In: 39th AIAA Aerospace Sciences Meeting and Exhibit*. AIAA.
- Menter, F. R. 1992. Influence of freestream values on k - ω turbulence model predictions. *AIAA Journal*, **30**(6), 1657–1659.
- Menter, F. R. 1994. Two-equation eddy-viscosity turbulence models for engineering applications. *AIAA Journal*, **32**(8), 1598–1605.
- Mikolajczak, A. A., Arnoldi, R. A., Snyder, L. E., & Stagardter, H. 1975. Advances in fan and compressor blade flutter analysis and predictions. *Journal of Aircraft*, **12**(4), 325–332.
- Moore, J., & Ransmayr, A. 1984. Flow in a turbine cascade: Part 1 – losses and leading edge effects. *Journal of Engineering for Gas Turbines and Power*, **106**(Apr), 400–408.
- Moore, J., & Smith, B. L. 1984. Flow in a turbine cascade: Part 2 – measurement of flow trajectories by ethylene detection. *Journal of Engineering for Gas Turbines and Power*, **106**(Apr), 409–413.
- Neilson, Robert M. 1912. *The steam turbine*. London: Longmans Green and Co.
- Ning, W., & He, L. 1998. Computation of unsteady flows around oscillating blades using linear and nonlinear harmonic Euler methods. *Journal of Turbomachinery*, **120**, 508–514.
- Nowinski, M., & Panovsky, J. 1998. Flutter mechanisms in low pressure turbine blades. *In: Fransson, T. (ed), Unsteady Aerodynamics and Aeroelasticity of Turbomachines*. Kluwer Academic Publishers.
- Numerich, Robert W., Reid, John, & Kim, Kieun. 1998. *Parallel methods for fluid-structure interaction*. Springer Verlag.
- Obayashi, S., & Guruswamy, G. P. 1992. Unsteady shock-vortex interaction on a flexible delta wing. *Journal of Aircraft*, **29**(5), 790–798.

- Ott, Peter. 1998 (August). *Update of stcf 4*. Tech. rept. École Polytechnique Fédérale de Lausanne, <http://www.egi.kth.se/ekv/research/stcf/>. Accessed 4th March 2001.
- Ott, Peter. 2002 (August). *Information for 3d computations of the stcf 4 test cases*. Tech. rept. LTT-02-04. École Polytechnique Fédérale de Lausanne.
- Parker, R. 1997. Aeroacoustics. *International Journal of Fluid Dynamics*, 1(May).
- Piperno, Serge. 1997. Explicit/implicit fluid/structure staggered procedures with a structural predictor and fluid subcycling for 2d inviscid aeroelastic simulations. *International Journal for Numerical Methods in Fluids*, 25, 1207–1226.
- Piperno, Serge, Farhat, Charbel, & Larrouturou, Bernard. 1995. Partitioned procedures for the transient solution of coupled aeroelastic problems. part i: Model problem, theory and two-dimensional application. *Computer Methods in Applied Mechanics and Engineering*, 124, 79–112.
- Queutey, Emmanuel Guilmineau Patrick. 1998. Numerical study of dynamic stall on several airfoil sections. *AIAA Journal*, 37(1), 128–130.
- Rao, S. S. 1989. *The finite element method*. 2 edn. Oxford: Pergamon Press.
- Rao, S.S. 1995. *Mechanical vibrations*. 3 edn. Massachusetts: Addison Wesley Publishing Co.
- Reichl, Paul. 2001 (July). *Flow past a cylinder close to a free surface*. Ph.D. thesis, Monash University.
- Richardson, Alex. 1911. *The evolution of parson's steam turbine*. London: Engineering House.
- Rizzi, A. 1978. Numerical implementations of solid-body boundary conditions for the euler equations. *ZAMM*, 58, 301–304.
- Sadeghi, M., & Liu, F. 2001a. Computation of mistuning effects on cascade flutter. *AIAA Journal*, 39(1), 22–28.
- Sadeghi, Mani, & Liu, Feng. 2001b. Investigation of non-linear flutter by a coupled aerodynamics and structural dynamics method. AIAA. AIAA 2001-0573.
- Sayma, A., Vahdati, M., Green, J., & Imregun, M. 1998. Whole-assembly flutter analysis of a low pressure turbine blade. Pages 347–359 of: Fransson, T. (ed), *Unsteady Aerodynamics and Aeroelasticity of Turbomachines*. Kluwer Academic Publishers.

- Sbardella, L., & Peiro, J. 1997 (June). Numerical simulations of stator-rotor interaction in a turbine stage. *In: Proceedings of ceas international forum on aeroelasticity and structural dynamics.*
- Schiano, Pasquale. 1994. *Parallel computing in aerospace: status, needs and trends.* John Wiley and Sons.
- Schlichting, Herman. 1968. *Boundary-layer theory.* New York: McGraw-Hill.
- Shibata, T., & Kaji, S. 1998. Role of shock structures in transonic rotor flutter. *Pages 733–747 of: Fransson, T. (ed), Unsteady Aerodynamics and Aeroelasticity of Turbomachines.* Kluwer Academic Publishers.
- Shiratori, T., Matshushita, M., & Noguchi, Y. 1998. Periodic fluctuation of shock waves in transonic cascade flows. *In: Fransson, T. (ed), Unsteady Aerodynamics and Aeroelasticity of Turbomachines.* Kluwer Academic Publishers.
- Sieverding, C. H. 1985. Recent progress in the understanding of secondary flows in turbine blade passages. *Journal of Engineering for Gas Turbines and Power*, **107**(April), 248–257. ASME.
- Sieverding, C.H., Hove, W. Van, & Boletis, E. 1984. Experimental study of the three-dimensional flow field in an annular turbine nozzle guide vane. *Journal of Engineering for Gas Turbines and Power*, **106**(apr), 437–444.
- Smati, L., Aubert, S., Ferrand, P., & Massão, F. 1998. Comparison of numerical schemes to investigate blade flutter. *In: Fransson, T. (ed), Unsteady Aerodynamics and Aeroelasticity of Turbomachines.* Kluwer Academic Publishers.
- Srinivasan, A. V. 1997. Flutter and resonant vibration characteristics of engine blades. *Journal of Engineering for Gas Turbines and Power*, **119**(Oct.).
- Srivastava, R., & Reddy, T. S. R. 1995. *Aeroelastic analysis of ducted rotors.* ASME.
- Tallman, J., & Lakshminarayana, B. 2001a. Numerical simulation of tip leakage flows in axial flow turbines, with emphasis on flow physics: Part I – effect of tip clearance height. *Journal of Turbomachinery*, **123**(Apr), 314–323.
- Tallman, J., & Lakshminarayana, B. 2001b. Numerical simulation of tip leakage flows in axial flow turbines, with emphasis on flow physics: Part II – effect of outer casing relative motion. *Journal of Turbomachinery*, **123**(apr), 324–333.
- Tatsumi, S., Martinelli, L., & Jameson, A. 1995. Flux-limited schemes for the compressible Navier-Stokes equations. *AIAA Journal*, **33**(2), 252–261.

- Thompson, Joe F., Warsi, Z.U.A., & Mastin, C. Wayne. 1985. *Numerical grid generation*. New York: North-Holland.
- Toro, E. F. 1997. *Approximate riemann solvers and numerical methods for fluid dynamics*. Vol. 1. Berlin: Springer Verlag.
- Vahdati, M., & Imregun, M. 1996. An application of the ICED-ALE methodology to integrated nonlinear aeroelasticity analyses. *Engineering Computations*, 14(3), 281–305.
- Vahdati, M., Sayma, A. I., & Imregun, M. 1999 (Mar.). Viscous flutter calculations for a fan assembly using hybrid grids. *Pages 353–363 of: IMECH Conference Transactions*. 3rd European Conference on Turbomachinery. C557/114/99.
- van Zante, Dale E., Strazisar, Anthony J., Wood, Jerry R., Hathaway, Michael D., & Okiishi, Theodore H. 2000. Recommendations for achieving accurate numerical simulation of tip clearance flows in transonic compressor rotors. *ASME Journal of Turbomachinery*, 122(Oct.), 733–742.
- Verdon, Joseph. 1993. Review of unsteady aerodynamic methods for turbomachinery aeroelastic and aeroacoustic applications. *AIAA Journal*, 31(2), 235–250.
- Ware, W. 1973. The ultimate computer. *IEEE spectrum*, Mar., 89–91.
- Watkins, W. B., & Chi, R. M. 1989. Noninterference blade vibration measurement system for gas turbine engines. *Journal of Power and Propulsion*, 5(6), 727–730.
- Weber, S., Gallus, H. E., & Peitsch, D. 1998. Numerical solution of the Navier Stokes equations for unsteady and unstalled and stalled flow in turbomachinery cascades with oscillating blades. *Pages 477–491 of: Fransson, T. (ed), Unsteady Aerodynamics and Aeroelasticity of Turbomachines*. Kluwer Academic Publishers.
- White, Frank M. 1994. *Fluid dynamics*. New York: McGraw-Hill.
- Whitehead, D. S. 1959. Vibration of cascade blades treated by actuator disc methods. *Proceedings of the institution of mechanical engineers*, 173(21), 555–563.
- Wilcox, D. C. 1988. Reassessment of the scale-determining equation for advanced turbulence models. *AIAA Journal*, 26(11), 1299–1310.
- Wilcox, D. C. 1994. *Turbulence modeling for CFD*. DCW Industries Inc.
- Wilcox, D. C. 2000. *Turbulence modeling for CFD*. DCW Industries Inc.
- Wolff, J. M., & Fleeter, S. 1995. *Nonlinear oscillating cascade transonic aerodynamic inviscid-viscous analysis*. ASME.

- Wong, A. S. F., Tsai, H. M., Cai, J., Zhu, Y., & Liu, F. 2000 (Jan.). Unsteady flow calculations with a multi-block moving mesh algorithm. *In: 38th Aerospace Sciences Meeting and Exhibit*. AIAA. AIAA-2000-1002.
- Yao, Jixian, Jameson, Antony, Alonso, Juan, & Liu, Feng. 2000 (Jan.). Development and validation of a massively parallel flow solver for turbomachinery flows. *In: AIAA 38th Aerospace Sciences Meeting*. AIAA. AIAA-00-0882.
- Zheng, Xiaoqing, & Liu, Feng. 1995. Staggered finite volume scheme for solving Navier-Stokes and $k-\omega$ turbulence model equations. *AIAA Journal*, 33(6), 991-998.
- Zienkiewicz, O. C., & Taylor, R. L. 1991. *The finite element method*. Vol. 2. London: MacGraw-Hill Book Company.